The Chemistry of *S* = 2 Nonheme Oxoiron(IV) Complexes

A THESIS SUBMITTED TO THE FACULTY OF THE GRADUATE SCHOOL OF
THE UNIVERSITY OF MINNESOTA
BY

Mayank Puri

IN PARTIAL FULFILLMENT OF THE REQUIREMENTS
FOR THE DEGREE OF
DOCTOR OF PHILOSOPHY

Prof. Lawrence Que, Jr., Advisor

May 2016

Acknowledgements

The support of others has been so important to me throughout my time in graduate school. I hope I can do some justice in the next few paragraphs for thanking those who have helped, encouraged and guided me over the last six years. In case it gets long-winded and confusing, I'll just say it clearly – thank you all through and through.

First, I want thank my PhD advisor, Larry Que. The excitement and knowledge Larry brings to research is infectious and made our everyday conversations memorable. It is Larry who really taught me how to think like a scientist, design elegant experiments and tell a good story with the results. His keen ability to take a seemingly failed piece of data and turn into a valuable insight has always amazed me. Finally, I look back fondly on the freedom Larry gave me in the lab, which ultimately helped me understand and appreciate the creativity that defines chemistry. My time under his mentorship is something I will always be grateful for and never forget.

My lab mates in the Que group were the glue that held my graduate school experience together. You are wonderful friends and incredible scientists, and it has been an honor to work with all of you.

When I first started, the postdoc powerhouse of Drs. Aidan McDonald, Genqiang Ken Xue, Kathy Van Huevelen, V.K.K .Praneeth and Matt Cranswick taught me the ways of the lab and helped me get my projects up and running. Aidan's wit and deep knowledge of chemistry were a wonderful combination, in addition to his ability to kindly mentor younger students, myself included. Ken always seemed to have an ingenious solution to difficult experimental problems and his research in the group is still legendary to this day. He also took me on my first long bike ride around the Twin Cities, all the way out to the airport, which I will always remember. During this time, I also greatly admired the older graduate students in the group, Van Vu and Andy Fielding, for their quiet leadership and willingness to hear my experimental difficulties and offer valuable advice. The other graduate students, Feifei Li, Anusree Mukherjee, Partha Das and Yan Feng, also helped me greatly that first year in the group.

As I became more comfortable in the lab, my fellow graduate students were the ones I would touch base with daily and receive advice from. Greg Rohde was the senior graduate student during most of my time in the group and one of my closest friends. His mixture of leadership and humility was something I still greatly admire. He was always willing to lend advice, whether it was on kinetics, crystallography or how to repair a flat bicycle tire. I will very much treasure our early morning bicycle rides and breakfast combinations, as well as hikes during our trips up to Duluth. Jen Bigelow was always the first one in the office in the mornings and was a great person to receive advice from in those calm early hours. Scott Kleespies and I went through the whole program together, from the obscene problem sets in our first year to thesis writing in our last year. I always admired Scott's working knowledge of all the lab equipment / instruments and his ability to find a solution to problems that would inevitably come up. Andy Jasniewski was always willing to help me, whether it was understanding various spectroscopic techniques, fishing EXAFS samples from the bottom of storage dewars, or helping me roll my first D&D character. His awesome sense of humor made group meetings much more lively and I will fondly remember our bike rides back to Uptown together. I had the pleasure of meeting Ang Zhou when he first joined the group and the even greater privilege of watching him grow into an incredibly skilled and successful scientist. And just as important, I will always remember our chats about science fiction novels, movies and trips out to the Minnesota Orchestra together. Waqas Rasheed and I first spoke over Skype while he was an undergraduate student in Pakistan. Since then, he has joined the department, our group and been a wonderful friend from whom I've enjoyed hearing the latest tech news and Pixar quotes.

The Biocave has always been an oasis of calm for me and was where I wrote the majority of this thesis. Dr. Lisa Engstrom was always willing to proofread any conference or grant abstracts I needed to write, and offered valuable advice and kind encouragement when I needed it. Some of my best memories in the Que group involved grabbing early morning coffee with Anna Komor, who along with Greg was a key member of our Friday morning Breakfast Club. Anna's insight into life both in and out of the lab was something I always valued and will come back to time and time again.

As my time in the lab grew, I had the privilege of interacting with more postdocs. Jai Prakash was my soluble iodosylbenzene partner-in-crime and a great mentor in synthetic chemistry. I was always amazed at the molecules he was able to make and the beautiful crystal structures he would show us during group meetings. Will Oloo was someone I could always bounce a research idea off of, which inevitably ended up in hour(s)-long conversations. His critical mind and willingness to discuss science was something that really helped me and my research over the past years. Caleb Allpress helped me make countless NRVS, EXAFS and Mössbauer samples and would gladly troubleshoot any problems I came into along the way. He has also been a valuable colleague to bounce idea off of, and he and Teresa have been wonderful hosts for our Dungeons & Dragons hangouts! Johannes Klein added a great burst of energy to our group and was always willing to wax philosophy or analyze new research articles in our field with me. Seesaw Ching has been a wonderful colleague to talk to about synthetic chemistry or spectroscopic techniques with, as well as being a great friend who values art, family and traveling. Appu Draksharapu has been a terrific colleague and especially helpful for running resonance Raman experiments and getting excited about iron-imido chemistry with me!

The newer graduate students – Saikat Banerjee, Subhasree Kal, Shuangning Xu, Pat Crossland, and Sheng Yuan - have been really fun to work with and get to know during my last year in the group. I look forward to hearing about their groundbreaking research in the future!

My friends outside of the Que lab were a huge source of encouragement and laughter. I would look forward to my weekly coffee hour with Will Isley from the Cramer group, where we would talk about anything and everything related to Brandon Sanderson fantasy novels, board games and of course, Star Wars. Members from the Tolman group - Dave Boyce, Gereon Yee, Ben Neisen, and Debanjan Dhar - were always there as either softball teammates or bitter rivals (depending on the year), and certainly always up for happy hour and jokes afterwards. REL Pressman was the one who picked me up from the airport when I first landed in Minneapolis and has been a constant friend of mine since middle school. I could always rely on him to help me out in a bind and I am very proud to see him succeed in his farming endeavors. And Louis Bergelson and Anton Kovalsky, of course, for Zelda adventures late into the weekend nights and supportive phone conversations. Finally, a big shout out to Robin Voreis who helped Nirja and I find our home in my second year of graduate school, and who has always been excited and enthusiastic to hear about my latest research!

I thank my family especially. My sister, Mans, for starting a pact with me during the beginning of my PhD program and supporting me throughout the whole process. My dad / Popa, with whom I've had had some ups and downs but have always known that he has supported and been proud of me. My grandmother / Nani, for her constant love and gardening advice. And of course, my mom for being the best support in every little and large aspect of my life and for loving me so much – you're the best.

Finally, I want to thank the most important person in the world to me, my partner Nirja. We started this journey together and you have been an endless source of support, inspiration and happiness for me. From giving me a ride home on rainy evenings to Friday night pizza / art revolutions, I will always remember how we started our family during my time in graduate school and will always cherish this time with you. I mentioned during my thesis defense that if I actually get this degree, it is just as much yours as it is mine, and I fully meant that. I thank you and love you.

Dedication

This thesis is dedicated to my partner, Nirj, my puppy, Kashi, and all of my family and friends.

“The great only appear great because we are on our knees. Let us rise!”
– James Larkin.

Abstract

Nonheme oxoiron(IV) intermediates are proposed to be involved in a number of important biological oxidation reactions, where all characterized examples thus far have a $S = 2$ ground spin state. In contrast, the majority of synthetic nonheme oxoiron(IV) complexes have a $S = 1$ ground spin state. In order to gain a deeper understanding of these important biological species, it is critical to expand the number of synthetic $S = 2$ nonheme oxoiron(IV) complexes and to study their reactivity with organic substrates.

This thesis explores a synthetic strategy to obtain $S = 2$ nonheme oxoiron(IV) complexes by utilizing weak-field equatorial quinoline donors, in contrast to the relatively strong-field pyridine donors that are often used. The resulting $S = 2$ nonheme oxoiron(IV) complexes demonstrate spectroscopic signatures similar to those of the enzymatic oxoiron(IV) intermediates and reproduce the reactivity observed by these nonheme iron enzymes. Thus, this research has given rise to the first electronic and functional models of the nonheme oxoiron(IV) intermediates found in the enzymes TauD, CytC3 and SyrB2.

In addition, the reactivity of known $S = 1$ nonheme oxoiron(IV) complexes were explored in the context of oxygen-atom exchange with H_2O, which is an important reaction in tracking metal-oxo intermediates proposed to be involved in catalytic substrate oxidation reactions. Finally, a six-coordinate $S = 1$ nonheme imidoiron(IV)

complex supported by a tetradentate ligand was synthesized and compared to its isoelectronic $S = 1$ nonheme oxoiron(IV) analogue.

Table of Contents

List of Tables

List of Figures and Schemes

Abbreviations

1Py-BnTPEN	*N*-benzyl-*N*-((4-methoxy-3,5-dimethylpyridin-2-yl)methyl)-*N*’,*N’*-bis(2-pyridylmethyl)ethylenediamine
3Py-BnTPEN	*N*-benzyl-*N,N’,N’*-tris((5-methylpyridin-2-yl)methyl)ethylenediamine
6MeTPA	6-methyl-2-pyridylmethyl)bis(2-pyridylmethyl)amine
6Me$_3$TPA	tris(6-methyl-2-pyridylmethyl)amine
Ad	adamantly
ArIO	2-(*tert*-butylsulfonyl)iodosylbenzene
BDE	bond dissociation energy
BnTPEN	*N*-benzyl-*N,N,N*-tris(2-pyridylmethyl)-1,2-diaminoethane
BQPA	bis(2-quinolylmethyl)(2-pyridylmethy1)amine
CHD	1,4-cyclohexadiene
DFT	density functional theory
DHA	9,10-dihydroanthracene
ESI-MS	electrospray-ionization mass spectrometry
EXAFS	extended x-ray absorption fine-structure
H$_3$buea	1,1,1-tris[(N-*tert*-butylureaylato)-*N*-ethyl]aminato
HAT	hydrogen-atom transfer
HOMO	highest occupied molecular orbital
KIE	kinetic isotope effect

MCD	magnetic circular dichroism
MeCN	acetonitrile
Me_3NTB	tris((N-methylbenzimidazol-2-yl)methyl)amine
$MePy_2TACN$	N-methyl-N′,N″-bis(2-pyridylmethyl)-1,4,7-triazacyclononane
Me_2Py_2TACN	1-di(2-pyridyl)methyl-4,7-dimethyl-1,4,7-triazacyclononane
MO	molecular orbital
MsINTs	mesityl-*N*-tosylimidoiodinane
N3S2	2,6-bis-(2-methylthiophenyliminomethyl)pyridine
N4Py	*N,N*-bis(2-pyridylmethyl)-*N*-bis(2-pyridyl)methylamine
NIR	near-infrared
NRVS	nuclear resonance vibrational spectroscopy
Ns	nosylate
OAE	oxygen-atom exchange
OAT	oxygen-atom transfer
OEC	oxygen-evolving complex
OTf	triflate
PhINNs	phenyl-*N*-nosylimidoiodinane
PhINTs	phenyl-*N*-tosylimidoiodinane
PhIO	iodosylbenzene
PyTACN	1-(2’-pyridylmethyl)-4,7-dimethyl-1,4,7-triazacyclononane

QBPA	2-quinolylmethyl)bis(2-pyridylmethyl)amine
RDS	rate-determining step
rRaman	resonance Raman
TAML	tetraazamacrocyclic ligand
TauD	taurine dioxygenase
^{t}Bu	*tertiary*-butyl
TFE	2,2,2-trifluoroethanol
TMC	1,4,8,11-tetramethyl-1,4,8,11-tetraazacyclotetradecane
TMC-Py	1-(2-pyridylmethyl)-4,8,11-trimethyl-1,4,8,11-tetraazacyclotetradecane
TMG$_2$dien	2,2-(2,2 -(methylazanediyl)bis(ethane-1,2-diyl))bis(1,1,3,3-tetramethylguanidine
TMG$_3$tren	1,1,1-tris(2-[N2-(1,1,3,3-tetramethylguanidino)]ethyl)amine
TPA	tris(2-pyridylmethyl)amine
TPA*	tris[(3,5-dimethyl-4-methoxy)pyridyl-2-methyl]amine
tpa^{Ph}	tris(5-phenylpyrrol-2-ylmethyl)amine
TQA	tris(2-quinolylmethyl)amine
Ts	tosylate
XANES	x-ray absorption near edge structure
ΔE_Q	quadrupole splitting
δ	isomer shift

Compound Abbreviations by Chapter

Chapter 1

1	$[\mathrm{Fe^{IV}(O)(OH_2)_5}]^{2+}$
2	$[\mathrm{Fe^{IV}(O)(TMG_3tren)}]^{2+}$
3	$[\mathrm{Fe^{IV}(O)(TMG_2dien)(X)}]^{2+/1+}$ (X = MeCN, Cl, N_3)
4	$[\mathrm{Fe^{IV}(O)(H_3buea)}]^{-1}$
5	$[\mathrm{Fe^{IV}(O)(tpa^{Ph})}]^{-1}$
6	$[\mathrm{(TPA^*)_2Fe^{III}Fe^{IV}(\mu\text{-}O)_2}]^{3+}$
7	$[\mathrm{(HO)(TPA^*)Fe^{III}\text{-}O\text{-}Fe^{IV}(O)(TPA^*)}]^{2+}$
8	$[\mathrm{(F)(TPA^*)Fe^{III}\text{-}O\text{-}Fe^{IV}(O)(TPA^*)}]^{2+}$
9	$[\mathrm{(MeO)(TPA^*)Fe^{III}\text{-}O\text{-}Fe^{IV}(O)(TPA^*)}]^{2+}$
10	$[\mathrm{(HO)(TPA^*)\ Fe^{IV}\text{-}O\text{-}Fe^{IV}(O)(TPA^*)}]^{3+}$
11	$[\mathrm{Fe^{IV}(O)(TPA^*)(MeCN)}]^{2+}$
12	$[\mathrm{Fe^{IV}(O)(6MeTPA)(MeCN)}]^{2+}$
13	$[\mathrm{Fe^{IV}(O)(QBPA)(MeCN)}]^{2+}$
14	$[\mathrm{Fe^{IV}(O)(TMC)(CH_3CN)}]^{2+}$
15	$[\mathrm{Fe^{IV}(O)(N4Py)}]^{2+}$
16	$[\mathrm{Fe^{IV}(NTs)(N4Py)}]^{2+}$

Chapter 2 & 3

1	$[\mathrm{Fe^{IV}(O)(TQA)(MeCN)}]^{2+}$
2	$[\mathrm{Fe^{IV}(O)(TQA)(Cl)}]^{1+}$
3	$[\mathrm{Fe^{IV}(O)(TQA)(Br)}]^{1+}$

Chapter 4

1	$[\mathrm{Fe^{IV}(O)(TMC)(CH_3CN)}]^{2+}$
2	$[\mathrm{Fe^{IV}(O)(TMC\text{-}Py)}]^{2+}$
3	$[\mathrm{Fe^{IV}(O)(N4Py)}]^{2+}$
4	$[\mathrm{Fe^{IV}(O)(BnTPEN)}]^{2+}$
5	$[\mathrm{Fe^{IV}(O)(1Py\text{-}BnTPEN)}]^{2+}$
6	$[\mathrm{Fe^{IV}(O)(3Py\text{-}BnTPEN)}]^{2+}$
7	$[\mathrm{Fe^{IV}(O)(PyTACN)(MeCN)}]^{2+}$
8	$[\mathrm{Fe^{IV}(O)(Me_2Py_2TACN)}]^{2+}$
9	$[\mathrm{Fe^{IV}(O)(MePy_2TACN)}]^{2+}$

Chapter 5

1	$[\mathrm{Fe^{IV}(NTs)(N4Py)}]^{2+}$
2	$[\mathrm{Fe^{IV}(NTs)(BnTPEN)}]^{2+}$
3	$[\mathrm{Fe^{IV}(NTs)(TPA^*)(MeCN)}]^{2+}$
4	$[\mathrm{Fe^{IV}(NNs)(N4Py)}]^{2+}$

Chapter 6

1	$[\mathrm{Fe^{IV}(O)(TQA)(MeCN)}]^{2+}$
2	$[\mathrm{Fe^{IV}(O)(TQA)(Cl)}]^{1+}$
3	$[\mathrm{Fe^{IV}(O)(TQA)(Br)}]^{1+}$

Chapter 1:
$S = 2$ Nonheme Oxoiron(IV) Species, Oxygen-atom Exchange and Nonheme Imidoiron(IV) Complexes

Parts of this chapter were published in:

1. Puri, M.; Que, L. Jr. Towards the Synthesis of More Reactive *S* = 2 Nonheme Oxoiron(IV) Complexes. *Acc. Chem. Res.*, **2015**, *48*, 2443 – 2452.

2. Biswas, A. N.; Puri, M.; Meier, K. K.; Oloo, W. N.; Rohde, G. T.; Bominaar, E. L.; Münck, E.; Que, L. Jr. Modeling TauD-J: A High-Spin Nonheme Oxoiron(IV) Complex with High Reactivity toward C-H Bonds. *J. Am. Chem. Soc.*, **2015**, *137*, 2428 – 2431.

3. Puri, M.; Biswas, A. N.; Fan, R.; Guo, Y.; Que, L. Jr. Modeling Non-heme Iron Halogenases: High-Spin Oxoiron(IV)-Halide Complexes that Halogenate C-H Bonds. *J. Am. Chem. Soc.* **2016**, *138*, 2484 – 2487.

4. Puri, M; Company, A.; Sabenya, G.; Costas, M.; Que, L. Jr. Oxygen-Atom Exchange Between H_2O and Nonheme Oxoiron(IV) Complexes: Ligand Dependence and Mechanism. *Inorg. Chem.* Manuscript Accepted.

1.1 Synthetic Strategies Towards *S* = 2 Nonheme Oxoiron(IV) Complexes

1.1.1 *S = 2 Nonheme Oxoiron(IV) Intermediates in Nature*

Nonheme iron enzymes carry out critical oxidative transformations in biology.[1] These enzymes activate dioxygen, with the aid of a 2-e^- sacrificial reductant, to generate a highly reactive oxoiron(IV) species, which is proposed to be the active intermediate in the oxidation of a number of important biomolecules. Oxoiron(IV) intermediates have been elegantly trapped and characterized by the efforts of Krebs and Bollinger in a number of different enzymes,[2] the first of which was taurine dioxygenase (TauD) in 2003.[3,4] The enzymatic oxoiron(IV) intermediate, TauD-***J***, has a *S* = 2 ground spin state with an isomer shift of 0.30 mm/s. The high-spin state of TauD-***J*** has been rationalized by the presence of weak-field ligands, such as histidines and carboxylates, which support the $Fe^{IV}(O)$ center. Since 2003, oxoiron(IV) intermediates in two more classes of nonheme iron enzymes have been trapped and characterized, all of which demonstrate an *S* = 2 ground state, with isomer shifts in the range of 0.22 mm/s – 0.30 mm/s.[2,5]

Also in 2003, the Que group reported the first structurally characterized synthetic oxoiron(IV) complex, $[Fe^{IV}(O)(TMC)(MeCN)]^{2+}$ (where TMC is 1,4,8,11-tetramethyl-1,4,8,11-tetraazacyclotetradecane and MeCN is acetonitrile).[6] However, unlike TauD-***J***, $[Fe^{IV}(O)(TMC)(MeCN)]^{2+}$ has a *S* = 1 ground spin state and its Mossbauer parameters are notably different, with an isomer shift of 0.17 mm/s. In the years since, over sixty additional synthetic oxoiron(IV) species have been reported, with more than 90% of them characterized as having a *S* = 1 ground state.[5] The initial investigations of these new *S* = 1 oxoiron(IV) complexes were discussed in a 2007 Accounts article.[7] At the time, the only reported *S* = 2 oxoiron(IV) complex was $[\mathrm{Fe^{IV}(O)(OH_2)_5}]^{2+}$ (**1**, Figure 1.1**),** characterized by Bakac,[8] where the oxoiron(IV) center was supported by weak-field aqua ligands. Complex **1** was found to be a powerful oxidant, capable of undergoing fast hydrogen-atom transfer (HAT) reactions with a range of organic substrates.[9] While the isomer shift of 0.38(2) mm s^{-1} found for **1** made it a close spectroscopic analogue to TauD-***J***, its short half-life of 7 seconds at 25 °C and the aqueous medium have limited further studies. Since then, a number of groups have attempted to address the discrepancy in electronic structure between enzymatic and synthetic oxoiron(IV) systems by synthesizing *S* = 2 oxoiron(IV) complexes supported by polydentate ligands. There are a number of different synthetic strategies that may be employed to stabilize the *S* = 2 ground state, illustrated by the high-spin oxoiron(IV) complexes in Figure 1.1.

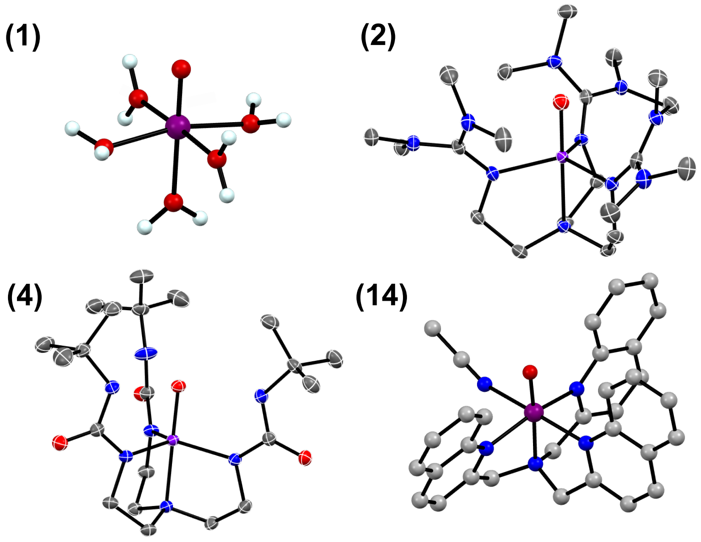

Figure 1.1. Structures of *S* = 2 oxoiron(IV) complexes **1** and **14**, based on DFT-derived coordinates from refs. 8 and 10, and of **2** and **4**, based on crystallographic data from refs. 11 and 12.

In considering the d-orbital splitting diagram for a pseudo-octahedral metal-oxo center, first detailed by Gray and Ballhausen,[13] it can be seen that the energy gap between the d_{x2-y2} and d_{xy} orbitals competes with the spin-pairing energy to determine whether an $S = 1$ intermediate spin state or $S = 2$ high spin state is formed (Figure 1.2, left). Therefore, the key to achieving an $S = 2$ spin state is to diminish the energy gap between the d_{xy} and d_{x2-y2} orbitals. There are a number of synthetic approaches to achieve this goal. In section 1.1.2, I detail the use of bulky tripodal ligands to enforce a trigonal bipyramidal geometry about the oxoiron(IV) center, thereby making the d_{xy} and d_{x2-y2} orbitals degenerate (Figure 1.2, right) and allowing for a $S = 2$ ground state. While in Sections1.1.3 and 1.1.4, I have highlighted different attempts to weaken the equatorial ligand field and decrease the energy of the d_{x2-y2} orbital in a pseudo-octahedral geometry, leading in some instances, to stabilization of the $S = 2$ ground state.

1.1.2 *Trigonal Bipyramidal S = 2 Nonheme Oxoiron(IV) Complexes*

The majority of reported synthetic nonheme oxoiron(IV) complexes have a $S = 1$ ground state, likely due to a combination of the relatively strong-field ligands employed, namely tertiary amines and pyridines, and the 6-coordinate pseudo-octahedral geometry these complexes adopt, leading to a pairing of electrons in the lowest-lying d_{xy} orbital (Figure 1.2, left). In contrast, the geometry of enzymatic $S = 2$ oxoiron(IV) species is still under debate, with both trigonal bipyramidal and pseudo-octahedral configurations being plausible. Theoretical calculations performed on TauD-***J*** by Neese supported the possibility of either geometry,[4] while the recent analysis of nuclear resonance vibrational spectroscopy (NRVS) data by Solomon favored a trigonal bipyramidal geometry for the oxoiron(IV) intermediate in the halogenase SyrB2.[14]

With this in mind, one synthetic strategy to diminish the energy gap between d_{xy} and d_{x2-y2} orbitals is to move away from the 6-coordinate pseudo-octahedral geometry adopted by the majority of oxoiron(IV) complexes and towards a C_3-symmetric trigonal bipyramidal geometry, where the d_{xy} and d_{x2-y2} orbitals become degenerate, guaranteeing population of four unpaired electrons and access to a $S = 2$ ground state (Figure 1.2, right).

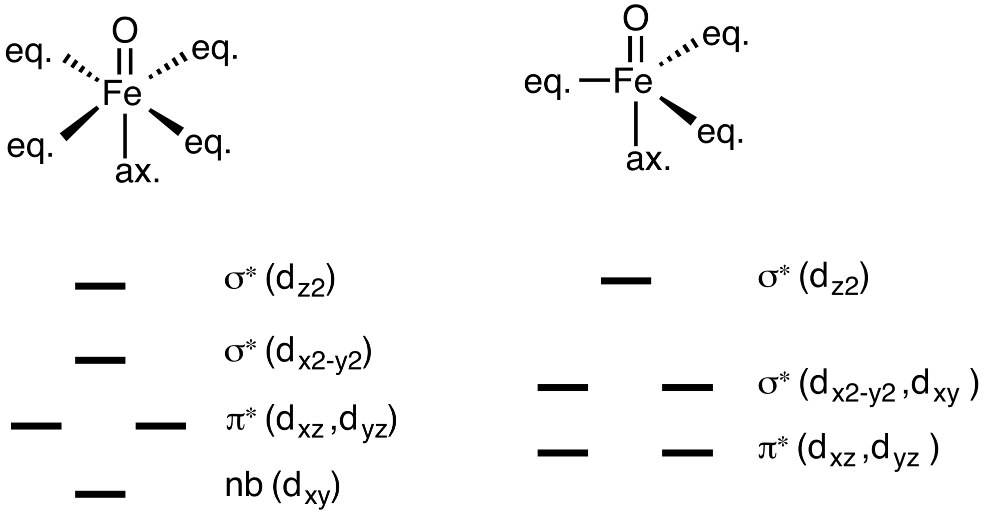

Figure 1.2. Splitting of d-orbitals associated with oxoiron(IV) complexes in a pseudo-octahedral (left) and trigonal bipyramidal (right) geometry.

The first example of a trigonal bipyramidal $S = 2$ oxoiron(IV) complex came from the Que group in 2009 where they utilized the sterically bulky TMG_3tren ligand to stabilize the oxoiron(IV) species, $[Fe^{IV}(O)(TMG_3tren)]^{2+}$ (where TMG_3tren is 1,1,1-tris(2-[N2-(1,1,3,3-tetramethylguanidino)]ethyl)amine) (**2,** Figures 1.1 and 1.3).[15] The benefits of the tripodal tetradentate ligand were twofold – first, the electron richness of the imine donors helped stabilize the high-valent Fe^{IV} oxidation state and second, the steric bulk of the six dimethylamine end caps enforced the C_3-symmetry while preventing formation of undesired (μ-oxo)diferric byproducts. Mössbauer spectroscopy of **2** revealed a quadrupole doublet with $\delta = 0.09$ mm s^{-1} and $\Delta E_Q = -0.29$ mm s^{-1}. While the isomer shift of **2** was notably smaller than that of the enzymatic intermediate, TauD-***J***, high-field Mössbauer experiments established **2** to have an $S = 2$ ground state (Table 1.1).

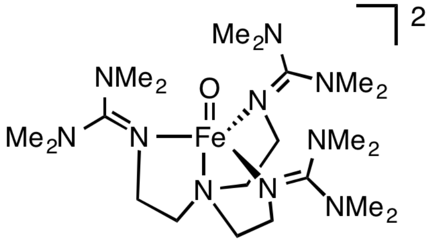

$[Fe^{IV}(O)(TMG_3tren)]^{2+}$ **(2)** *

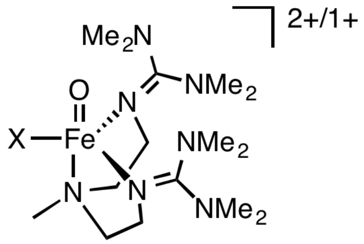

$[Fe^{IV}(O)(TMG_2dien)(X)]^{2+/1+}$ **(3)** *
X = NCMe, N_3, Cl

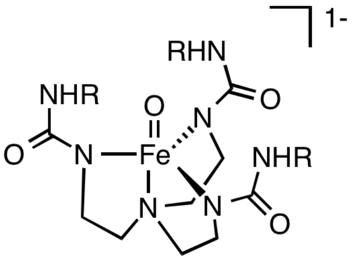

$[Fe^{IV}(O)(H_3buea)]^{1-}$ **(4)** *

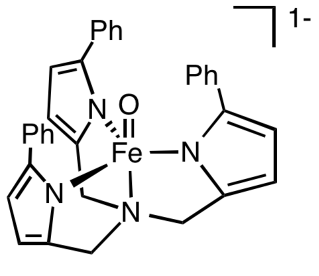

$[Fe^{IV}(O)(tpa^{Ph})]^{1-}$ **(5)** *

Figure 1.3. Synthetic trigonal bipyramidal $S = 2$ nonheme oxoiron(IV) complexes.

Compared to its $S = 1$ counterparts characterized at that time, species **2** was relatively unstable, with a $t_{1/2}$ of 30 seconds at 25 °C. Closer inspection of the self-decay of **2** revealed an intramolecular pathway through which the reactive $S = 2$ oxoiron(IV) center attacked one of the terminal methyl groups of the ligand to form an alkoxoiron(III) product.[11] This result demonstrated that the $Fe^{IV}=O$ unit of **2** was reactive enough to cleave a C–H bond of ~93 kcal mol^{-1} in strength within a few minutes at 25 °C. Indeed, upon perdeuteration of the methyl groups in TMG_3tren to form d_{36}-TMG_3tren, a large KIE of 24 was observed at 25 °C, and the increased stability of the $[Fe^{IV}(O)(d_{36}\text{-}TMG_3tren)]^{2+}$ isotopomer allowed its isolation and crystallization to afford the first structure of a synthetic high-spin oxoiron(IV) species (Figure 1.1).[11] Complex **2** was found to have a $Fe^{IV}=O$ distance of 1.661(2) Å and an $Fe^{IV}=O$ stretch of 843 cm^{-1}. These values were comparable to those reported for structurally characterized $S = 1$ oxoiron(IV) species,[5] consistent with the expectation that the $Fe^{IV}=O$ bond order should be independent of spin state.

The same steric constraints of the TMG_3tren ligand that enforce the C_3 symmetry is also responsible for the diminished reactivity between **2** and external organic substrates. Steric hindrance from the ligand is best illustrated by the difference in rates of oxidation of 1,4-cyclohexadiene (CHD) and 9,10-dihydroanthracene (DHA). While both have approximately the same C–H bond dissociation energy (BDE), the rate of DHA oxidation was 13 times slower than that with CHD,[15] consistent with greater steric hindrance from the approach of the bulkier DHA to the oxo moiety. In contrast, CHD and DHA were oxidized at comparable rates by other oxoiron(IV) species such as $[Fe^{IV}(O)(TMC)(MeCN)]^{2+}$.[16]

Table 1.1. Spectroscopic signatures of select *S* = 1 and *S* = 2 nonheme oxoiron(IV) species.

Complex	***S***	**Near-IR Bands (nm)**	**δ (mm/s)**	**ΔE_Q (mm/s)**	**D (cm^{-1})**	**Refs**
$[Fe^{IV}(O)(TMC)(MeCN)]^{2+}$	1	824	0.17	1.24	27	6,17
$[Fe^{IV}(O)(N4Py)]^{2+}$	1	695	-0.04	0.93	22	18
$[Fe^{IV}(O)(OH_2)_5]^{2+}$ (**1**)	2		0.38	0.33	9.7(7)	8
$[Fe^{IV}(O)(TMG_3tren)]^{2+}$ (**2**)	2	825	0.09	-0.29	5.0(5)	15
$[Fe^{IV}(O)(TMG_2dien)(X)]^{2+}$ (**3-X**) X = MeCN X = Cl X = N_3	 2 2 2	 724, 805 745, 803 827	 0.08 0.08 0.12	 0.58 0.41 -0.30	 4.5(5) 4.0(5) 4.6(5)	19
$[Fe^{IV}(O)(H_3buea)]^{-1}$ (**4**)	2	808	0.02	0.43	4.0(5)	12
$[Fe^{IV}(O)(tpa^{Ph})]^{-1}$ (**5**)	2	~900	0.09	0.51	4.3	20
$[Fe^{IV}(O)(TPA^*)(MeCN)]^{2+}$ (**11**)	1		0.01	0.95		21
$[(HO)(L)\,Fe^{IV}\text{-}O\text{-}Fe^{IV}(O)(L)]^{3+}$ L = TPA* (**10**)	1		-0.03	0.92		21
$[(TPA^*)_2Fe^{IV}{}_2(\mu\text{-}O)_2]^{4+}$	1		-0.03	2.04		22
$[(TPA^*)_2Fe^{III}Fe^{IV}(\mu\text{-}O)_2]^{3+}$ (**6**)	1		0.11	0.44		22
$[(HO)(L)Fe^{III}\text{-}O\text{-}Fe^{IV}(O)(L)]^{2+}$ L = TPA* (**7**)	2		0.09	-0.40		23
$[(F)(L)Fe^{III}\text{-}O\text{-}Fe^{IV}(O)(L)]^{2+}$ L = TPA* (**8**)	2		0.10	0.60		24
$[(H_2O)(L)\,Fe^{III}\text{-}O\text{-}Fe^{IV}(O)(L)]^{3+}$ L = $6Me_3TPA$	2		0.10	1.14		25,26
$[(H_2O)(L)\,Fe^{III}\text{-}O\text{-}Fe^{IV}(O)(L)]^{3+}$ L = 6MeTPA	2		0.08	0.5		27
$[Fe^{IV}(O)(TPA)(MeCN)]^{2+}$	1	724	0.01	0.92	28(2)	28
$[Fe^{IV}(O)(6MeTPA)(MeCN)]^{2+}$ (**12**)	1	770				29
$[Fe^{IV}(O)(QBPA)(MeCN)]^{2+}$ (**13**)	1	770				29

Fe^{IV}O Enzyme Intermediates						
Taurine dioxygenase (TauD-***J)***	2		0.30	-0.88	10.5	3
Prolyl 4-hydroxylase	2		0.30	-0.82	15.5	30
Halogenase CytC3	2		0.30, 0.22	-1.09, -0.70	8.1	31
Halogenase SyrB2	2		0.30, 0.23	1.09, 0.76		32
Tyrosine hydroxylase	2		0.25	1.27	12.5	33

In order to provide greater access to the Fe^{IV}=O unit, the Que group converted the tetradentate ligand, TMG_3tren, to the facial tridentate ligand, TMG_2dien, in which one of the TMG_3tren donor arms was replaced with a methyl group.[19] The corresponding oxoiron(IV) species $[Fe^{IV}(O)TMG_2dien(MeCN)]^{2+}$ (where TMG_2dien is 2,2 -(2,2 -(methylazanediyl)bis(ethane-1,2-diyl))bis(1,1,3,3-tetramethylguanidine) (Figure 1.3, **3-MeCN**) retained the $S = 2$ ground state of **2**, with similar Mössbauer parameters of $\delta = 0.08$ mm s^{-1} and $\Delta E_Q = 0.58$ mm s^{-1} (Table 1.1). However, the reactivity of **3-MeCN** was found to greatly surpass that of **2**, with a 630-fold increase in DHA oxidation rate. In addition, the MeCN ligand in **3-MeCN** could be replaced by Cl^- and N_3^- to form **3-Cl** and **3-N$_3$**, respectively. Notably, **3-Cl** exhibited a Fe^{IV}–Cl bond distance of 2.27 Å as measured by EXAFS, comparable to the 2.31-Å Fe^{IV}-Cl distance found for the SyrB2 intermediate.[32]

Using a parallel strategy, Borovik and coworkers reported the structural characterization of a different trigonal bipyramidal $S = 2$ oxoiron(IV) species, $[Fe^{IV}(O)(H_3buea)]^{1-}$ (where H_3buea is 1,1,1-tris[(N-tert-butylureaylato)-N-ethyl]aminato) (**4**, Figures 1.1 and 1.3).[12] Like TMG_3tren, H_3buea is a tripodal N4 ligand with bulky end caps, but the equatorial donors are anionic. The negatively charged ligand gave rise to an oxoiron(IV) complex with Mössbauer parameters $\delta = 0.02$ mm s^{-1} and $\Delta E_Q = 0.43$ mm s^{-1} (Table 1.1). Complex **4** has a Fe^{IV}=O bond length of 1.680(1) Å, slightly longer than the 1.661(2) Å length reported for **2 (**Figure 1.1) and an Fe^{IV}=O stretch of 799 cm^{-1} in its IR spectrum, 42 cm^{-1} weaker than that found for the shorter Fe^{IV}=O bond of **2**.[12] Perhaps the most interesting feature of the chemistry of **4** is the fact that it was generated by one-electron oxidation of its iron(III) congener $[\mathrm{Fe^{III}(O)(H_3buea)}]^{2-}$(**$4_{red}$**), which has also been structurally characterized.[34] The H_3buea ligand was designed to provide a hydrogen bond donor on each arm of the tripod to interact with the oxo ligand. These interactions were clearly observed for the oxo ligand of **4_{red}** but significantly diminished for the oxo ligand in **4**, reflecting the change in the nucleophilicity of the oxo ligand upon oxidation of the iron(III) center to iron(IV), as well as the shift of the iron(IV) center away from the plane of the urea H-bond donors in complex **4**.[12]

Similarly, Chang and coworkers utilized a tripodal tris(pyrrolide) ligand scaffold to support another trigonal bipyramidal $S = 2$ oxoiron(IV) center, $[\mathrm{Fe^{IV}(O)(tpa^{Ph})}]^-$ (where $\mathrm{tpa^{Ph}}$ is tris(5-phenylpyrrol-2-ylmethyl)amine) (**5**, Figure 1.3),[20] with a Mössbauer isomer shift of 0.09 mm/s like **2** (Table 1.1). Its reactivity with organic substrates reflected a sterically protected oxoiron(IV) center. Although **5** did not react with triphenylphosphine, it did oxidize the less bulky and more easily oxidized dimethylphenylphosphine to the corresponding phosphine oxide. Similarly, the oxoiron(IV) species was capable of oxidizing CHD but not the more bulky DHA.[20]

1.1.3 *Dinuclear Complexes with S = 2 Oxoiron(IV) Components*

While the trigonal bipyramidal oxoiron(IV) complexes **2 - 5** did indeed achieve an $S = 2$ ground state, their Mössbauer isomer shifts (~0.1 mm $\mathrm{s^{-1}}$) were notably smaller from those of TauD-***J*** and related enzyme intermediates (~ 0.3 mm $\mathrm{s^{-1}}$). Moreover, their intermolecular reactivity was limited by the steric constraints imposed by the ligand on access to the oxo moiety. For this reason, the Que group sought out alternate strategies to obtain $S = 2$ oxoiron(IV) complexes.

In the course of developing models for high-valent intermediates of methane monooxygenase and Class 1A ribonucleotide reductases,[35-37] the Que group discovered an interesting series of diiron complexes supported by the tetradentate ligand TPA* (tris [(3,5-dimethyl-4-methoxy)pyridyl-2-methyl]amine) (Figure 1.4). TPA* is an electron-rich derivative of TPA (tris(2- pyridylmethyl)amine), with electron donating substituents at the 3-, 4-, and 5-positions of all three pyridines to stabilize a highly reactive terminal oxoiron(IV) center. In this series of (L)Fe–O–Fe^{IV}(O)(L) complexes, the left-hand (L)Fe–O fragment can be construed as the sixth ligand to the right-hand Fe^{IV}(O)(L) unit. We found that the oxidation state of the left-hand fragment could be used to tune the spin state of the adjacent terminal oxoiron(IV) center, leading to the most reactive oxoiron(IV) complexes to date.

Starting with the $S = 3/2$ diamond-core complex $[Fe^{III}Fe^{IV}(\mu\text{-}O)_2(TPA^*)_2]^{3+}$ (**6**, Figure 1.4), Xue found that adding hydroxide, fluoride or methoxide opened up the diamond core to generate $S = ½$ derivatives with antiferromagnetically coupled ($S_a = 5/2$ Fe^{III}-X) / ($S_b = 2$ Fe^{IV}=O) species featuring a high-spin terminal oxoiron(IV) center (**7**, **8**, and **9**, respectively).[23,24,38-40] In the course of this investigation, we also obtained **10**, the one-electron oxidized derivative of **7**, which was characterized to have a ferromagnetically coupled ($S_a = 1$ Fe^{IV}-OH) / ($S_b = 1$ Fe^{IV}=O) center (Figure 1.4, Table 1.1). We speculate that the spin states of the terminal oxoiron(IV) units in **7** and **10** differ because of the nature of the adjacent (HO)(TPA*)Fe–O^- unit. The more reduced HO-

Fe^{III}-O^{-} unit of **7** should be a better π-donor than the corresponding HO-Fe^{IV}-O^{-} unit in **10**, leading to a decrease in the ligand field splitting of the Fe^{IV}=O unit in **7** that gives rise to its observed *S* = 2 spin state. Taken together, **7** - **10** comprise a unique set of structurally related complexes supported by the same tetradentate ligand but having a terminal oxoiron(IV) center in either an *S* = 1 or 2 spin state, which affect their HAT abilities.

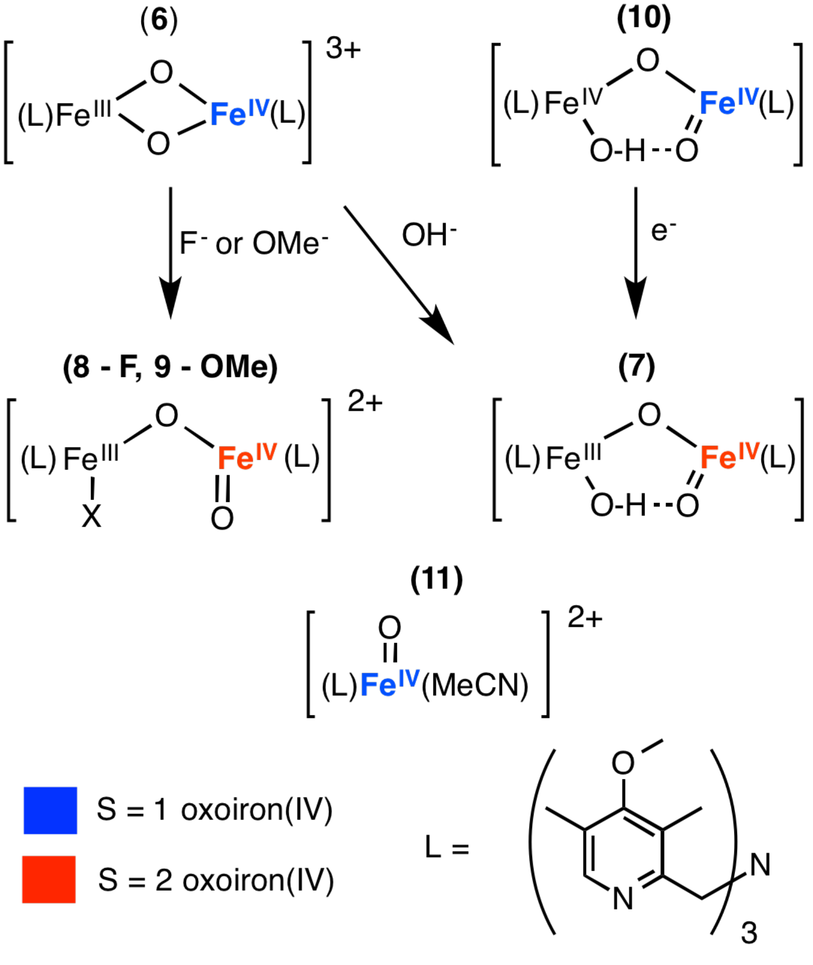

Figure 1.4. Generation of terminal *S* = 2 nonheme oxoiron(IV) centers in a diiron framework, where each iron center is supported by the electron-rich TPA ligand, TPA*.

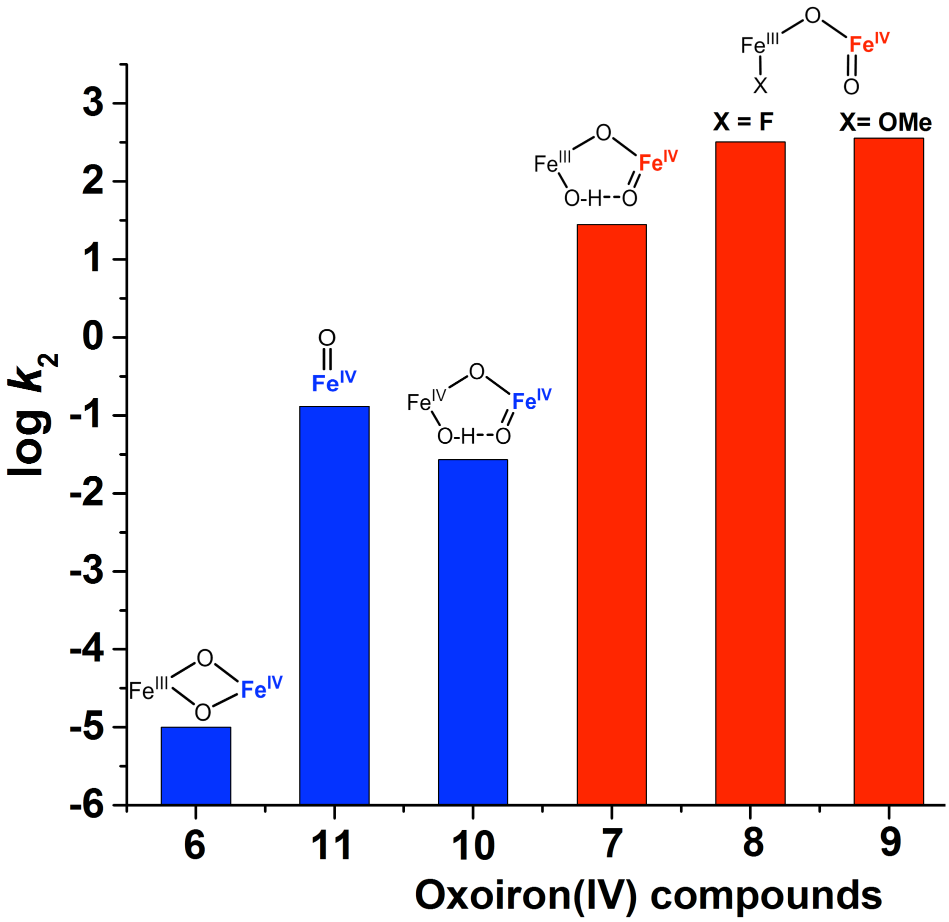

Figure 1.5. Second order rate constants for the reaction of nonheme oxoiron(IV) complexes with 9,10-dihydroanthracene (DHA) at -80 °C. Red bars indicate complexes with an $S = 2$ oxoiron(IV) center, while blue bars indicate complexes with an $S = 1$ oxoiron(IV) center. All iron centers are supported by the TPA* ligand.

Due to the thermal instability of **7** - **9**, their HAT reactivity had to be probed at -80 °C with DHA as the substrate (Figure 1.5). Notably, the three diiron complexes containing a terminal $S = 2$ oxoiron(IV) unit, **7** - **9**, demonstrated the fastest rates of DHA oxidation.[23] The 10-fold higher reactivity of **8** and **9** is attributed to the absence of the hydrogen bond between the Fe^{III}–OH and Fe^{IV}=O units in **7**.[39] Complex **7** in turn reacts 3000-fold faster than **10**, which has a terminal $S = 1$ oxoiron(IV) unit. Notably, these two complexes comprise the only pair of complexes where the oxoiron(IV) units are in nearly identical environments but have different spin states and provide the strongest experimental argument thus far in favor of the higher reactivity of the $S = 2$ oxoiron(IV) unit, as predicted by computational methods.[41-45] Complex **10** in turn was 1000-fold more reactive than the diamond core complex **6**, demonstrating that a terminal oxo unit is better at HAT than a bridging oxo unit. Overall, the series of five diiron complexes **6** – **10** shown in Figure 1.5 represents an impressive 34-million-fold range in HAT reactivity.[23]

1.1.4. ***Nonheme Oxoiron(IV) Complexes Supported by Sterically Hindered TPA Ligands***

Despite the success in generating $S = 2$ oxoiron(IV) species supported by electron-rich TPA ligands, these reactive centers were housed within a diiron core, making them less faithful analogs of mononuclear nonheme iron enzyme active sites. Furthermore, the thermal instability of the most reactive complexes required reactivity studies to be carried out only at -80 °C, a temperature too low for substrates with strong C–H bonds to be oxidized. The Que group thus focused on generating an $S = 2$ oxoiron(IV) complex within a mononuclear six-coordinate environment.

One strategy to diminish the energy gap between d_{xy} and d_{x2-y2} orbitals within a six-coordinate oxoiron(IV) environment is to weaken the equatorial ligand field and decrease the d_{x2-y2} orbital energy. For example, by replacing the relatively strong-field pyridine ligands that support many of synthetic oxoiron(IV) complexes with weaker-field donors, one could in principle attain an $S = 2$ ground state. Indeed the successful generation of the aqueous oxoiron(IV) complex **1**[8] serves to demonstrate the viability of this approach, but analogous attempts to employ carboxylate ligands have not yet led to stable $S = 2$ oxoiron(IV) complexes.[46-48]

The Que group applied a modified strategy by modulating the steric environment around the TPA pyridine nitrogen atoms to weaken the ligand field about the iron center. Such an approach was used in the 1990s for the tuning of the spin states of various Fe(TPA) complexes, where introduction of one or more α-substituents on the pyridine rings of TPA generated a steric interaction between the Fe center and the H-atoms of the α-substituent, preventing the formation of the short Fe-N_{Py} bonds necessary to adopt lower-spin configurations.[49] The steric effect with α-methyl substitution on pyridine rings is clearly illustrated in the ^{1}H NMR spectra of two $[Fe^{II}(L)(MeCN)_2](ClO_4)$ complexes. The spectrum of the L = TPA complex is consistent with a diamagnetic low-spin $S = 0$ species (Figure 1.6, top), while that of the L = 6Me$_3$TPA complex (where 6Me$_3$TPA is tris(6-methyl-2-pyridylmethyl)amine) instead reveals a paramagnetic high-spin $S = 2$ species (Figure 1.6, bottom). In fact, it was found that only a single methyl α-substituent was sufficient to trigger a spin state change in these (TPA)Fe^{II} family of compounds (Table 1.2).[49]

Table 1.2. Spin states of complexes supported by TPA ligands versus the extent of α-substitution on the pyridine rings.

Number of α-substituents	**0**	**1**	**3**	**Ref**
(L)Fe^{II}(MeCN)$_2$	0	0	2	49
(L)Fe^{III}(OOR)	1/2	1/2 & 5/2	5/2	49
(L)Fe^{III}(O)$_2$Fe^{IV}(L)	3/2 [1/2,1]	1/2 [5/2,2]	1/2 [5/2,2]	25-27,50
(L)Fe^{IV}(O)(MeCN)	1	1	2	10,28,29

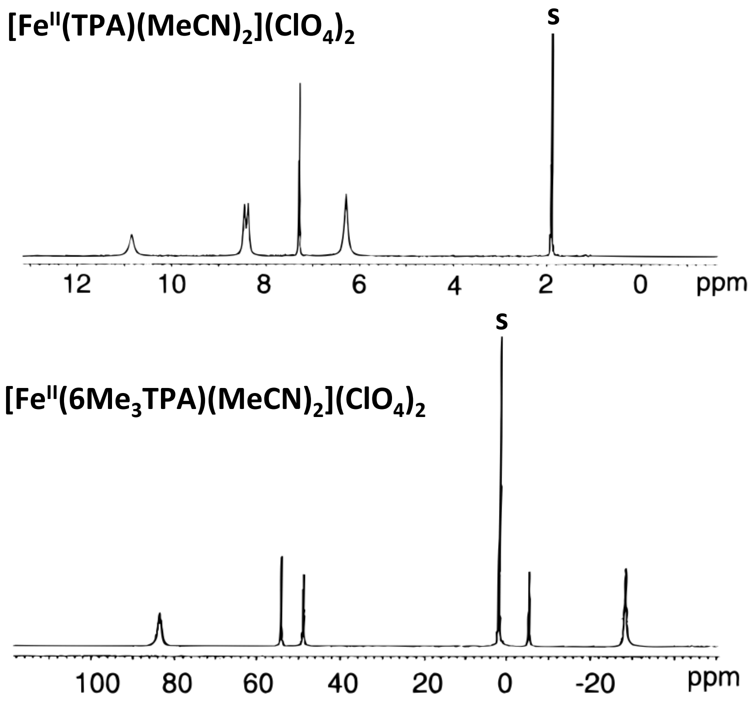

Figure 1.6. ^{1}H NMR spectrum of $S = 0$ [Fe^{II}(TPA)(MeCN)$_2$](ClO$_4$)$_2$ (top) and $S = 2$ [Fe^{II}(6Me$_3$TPA)(MeCN)$_2$](ClO$_4$)$_2$ (bottom) in CD$_3$CN. Reproduced with permission from ref 49. Copyright 1997 American Chemical Society.

The same strategies to enforce spin state changes within stable Fe^{II} coordination complexes extended to reactive Fe^{III}-peroxo intermediates as well. The alkylperoxoiron(III) intermediates, $[Fe^{III}(TPA)(OH_2)(OO^tBu)]^+$ and $[Fe^{III}(6Me_3TPA)(OH_2)(OO^tBu)]^+$ were distinguished in having an $S = 1/2$ Fe^{III} center for the former and an $S = 5/2$ Fe^{III} center for the latter. Interestingly, the complex with one α-substituent, $[Fe^{III}(6MeTPA)(OH_2)(OO^tBu)]^+$ (where 6MeTPA is (6-methyl-2-pyridylmethyl)bis(2-pyridylmethyl)amine) consisted of a mixture of low-spin Fe^{III} and high-spin Fe^{III} centers, hinting at the flexibility of this synthetic strategy at providing access to intermediate points prior to a complete spin state change (Table 1.2).[49]

Gratifyingly, this same synthetic strategy could be extended to oxodiiron(III/IV) systems. In 1995, a $[Fe^{III}Fe^{IV}(\mu\text{-}O)_2(TPA)_2]^{3+}$ diamond-core complex was identified and described as having valence-delocalized ($S_a = 1/2$ Fe^{III}) / ($S_b = 1$ Fe^{IV}) centers with a system spin of $S = 3/2$.[25,26] The corresponding complexes with 6MeTPA or $6Me_3TPA$ instead gave rise to valence-localized ($S_a = 5/2$ Fe^{III}) / ($S_b = 2$ Fe^{IV}) centers with a system spin of $S = ½$ due to antiferromagnetic coupling of the two iron components.[27,50] Thus, introduction of even one α-substituent was sufficient to trigger a change in the spin state of both Fe centers from low-spin to high-spin (Table 1.2). Further characterization of $[Fe^{III}Fe^{IV}(O)_2(6Me_3TPA)_2]^{3+}$ by resonance Raman spectroscopy revealed an $Fe^{IV}{=}O$ vibration at 840 cm^{-1},[50] with a frequency similar to those associated with $[Fe^{IV}(O)(TMC)(MeCN)]^{2+}$ ($S = 1$) and **2** ($S = 2$), suggesting that the $S = 2$ Fe^{IV} unit was in fact a terminal oxoiron(IV) center.[15,47] The diiron(III/IV) complexes of 6MeTPA and $6Me_3TPA$ showed for the first time that synthetic $S = 2$ oxoiron(IV) centers could be achieved, albeit within a diiron framework. While the reactivity of these complexes has not been investigated, they are closely related to the $S = ½$ diiron complexes supported by the electron-rich TPA* ligand, **7 – 9,** discussed in the preceding section, for which very high rates of oxidation of DHA have been reported (Figure 1.5).

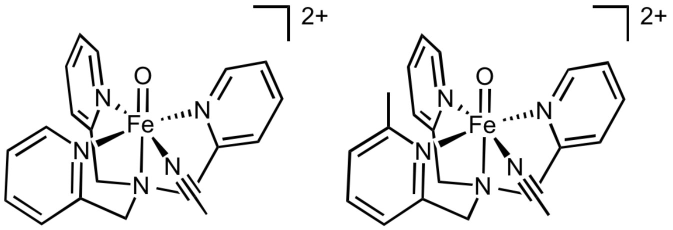

$[Fe^{IV}(O)(TPA)(MeCN)]^{2+}$ $[Fe^{IV}(O)(6MeTPA)(MeCN)]^{2+}$ **(12)**

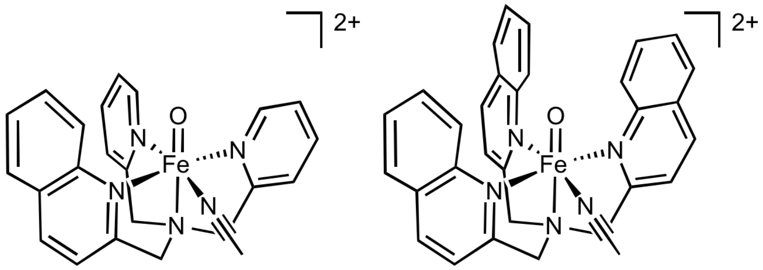

$[Fe^{IV}(O)(QBPA)(MeCN)]^{2+}$ **(13)** $[Fe^{IV}(O)(TQA)(MeCN)]^{2+}$ **(14)** *

Figure 1.7. Synthetic nonheme oxoiron(IV) complexes supported by TPA and derivatives, where those with an *S* = 2 ground state are marked with an asterisk (*).

With evidence that this synthetic strategy could stabilize a terminal *S* = 2 oxoiron(IV) center in a diiron framework, the Que group attempted to apply these ideas towards the generation of mononuclear *S* = 2 oxoiron(IV) species by modifying the parent *S* = 1 $[Fe^{IV}(O)(TPA)(MeCN)]^{2+}$ complex (Figure 1.7). In 2006, Paine and Que reported the characterization of oxoiron(IV) complexes of 6MeTPA and QBPA (where QBPA is (2-quinolylmethyl)bis(2-pyridylmethyl)amine) (**12** and **13**, respectively; Figure 1.7) obtained by reaction of peracetic acid with their iron(II) precursors.[29] The new species **12** and **13** exhibited respective near-IR absorption features of λ_{max} = 770 and 775 nm, which were red-shifted compared to that of $[Fe^{IV}(O)(TPA)(MeCN)]^{2+}$ (λ_{max} = 720 nm), indicating a weakening of the ligand field ($\Delta\nu \sim 900$ cm^{-1}) (Table 1.1). Importantly, these results indicated that the steric effect of a H-atom on a sp^3-hybridized α-carbon substituent (6MeTPA) was comparable to that on a sp^2-hybridized α-carbon substituent (QBPA).[29] However, in neither case did the ground spin state deviate from $S = 1$. Although DFT calculations from Ghosh predicted that a TPA ligand with three α-substituents should lead to a $S = 2$ oxoiron(IV) center (Figure 1.8),[51] attempts at that time to obtain oxoiron(IV) complexes of such ligands were not successful, suggesting that the right reaction conditions had not yet been found to stabilize species that are likely to be more reactive than the $S = 1$ complexes **12** and **13**. In this thesis, these critical conditions will be established and a new example of a $S = 2$ nonheme oxoiron(IV) complex, $[Fe^{IV}(O)(TQA)(MeCN)]^{2+}$, (TQA is tris(2-quinolylmethyl)amine) where the Fe^{IV} center is supported by the weak-field quinoline donors of the TQA ligand, will be presented (Figure 1.8).

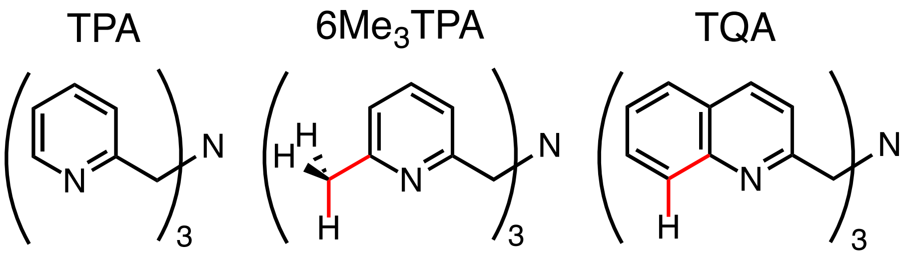

Figure 1.8. TPA ligand and derivatives with α-substituents.

1.2 Rebound Mechanism for C-H Bond Hydroxylation by *S* = 1 and *S* = 2 Nonheme Oxoiron(IV) Complexes

The reactivity of nonheme oxoiron(IV) complexes has been greatly influenced by seminal work on heme enzymes and their synthetic models, notably those related to the oxoiron(IV)-π-cation-radical species, compound I, found in the family of cytochrome P450 enzymes.[52] Groves has established a mechanism for the hydroxylation of C-H bonds by compound I, beginning with a rate-determining hydrogen-atom transfer step from the C-H bond bearing substrate to the oxoiron(IV)-π-cation-radical species, producing a one-electron reduced hydroxoiron(IV) species and a substrate radical. The radical may then recombine, or rebound, with the hydroxide ligand to give rise to the corresponding alcohol and a two-electron reduced ferric species (Figure 1.9).[52,53]

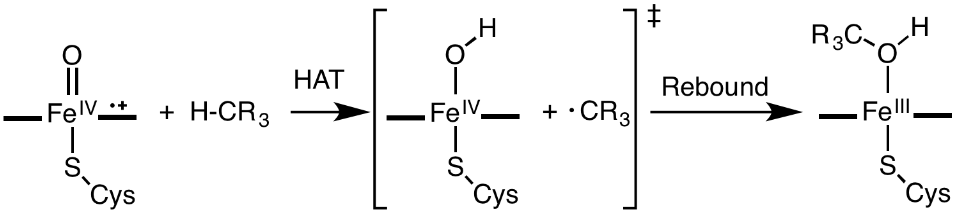

Figure 1.9. Proposed mechanism for C-H bond hydroxylation by high-valent oxoiron species, often called the rebound mechanism. Adapted from ref 54.

Experimental evidence for the initial rate-determining HAT step in this mechanism comes from observed non-classical H/D KIE values (KIE > 7), suggesting that C-H bond cleavage is the rate-determining step (RDS) and that this bond-breaking involves hydrogen-atom tunneling.[55] Since the subsequent rebound step in this mechanism occurs after the RDS, it is invisible to direct kinetic probes. However, the identity of products formed from the oxidation of special radical-clock substrates, such as norcarane and spiro[2,5]octane, has given insight into the nature of this post-RDS rebound step.[56] These substrates provide different products depending on if the oxidation process occurs through a concerted, cationic or radical-based mechanism, in addition to providing an approximate lifetime of the generated alkyl radical and ultimately a rate of radical rebound. Through these studies, it has been found that the radical lifetime in C-H bond hydroxylations with compound I species range between 16 ps and 52 ps, leading to an extremely rapid rate of rebound on the order of 10^{10} s^{-1}.[56] Further proof for a short radical lifetime and fast rebound comes from the highly retained stereochemistry of the oxidized substrates, with over 90% stereoretention in many cases.[57]

It is easy to assume that the mechanism of hydroxylation for compound I may be applied to the chemistry of nonheme oxoiron(IV) complexes. However, recently Nam and Shaik have presented experimental and theoretical evidence against the rebound mechanism in synthetic $S = 1$ nonheme oxoiron(IV) systems.[54,58] Nam and Shaik agree that initial HAT takes place, as evident from the large H/D KIEs observed in the oxidation of substrates by many nonheme oxoiron(IV) complexes. However, they then argue that the generated alkyl radical does not rebound but instead escapes from the solvent cage, allowing it to be trapped by a number of radical scavengers, such as O_2 or another equivalent of the oxoiron(IV) species, ultimately leading to hydroxylated products.[54,58]

Experimental evidence for this argument comes from analysis of both the iron and organic products found at the end of substrate oxidation reactions. Analyzing reactions between a wide range of substrates with the *S* = 1 oxoiron(IV) complexes, $[Fe^{IV}(O)(N4Py)]^{2+}$ and $[Fe^{IV}(O)(BnTPEN)]^{2+}$ (where N4Py is N,N-bis(2-pyridylmethyl)-N-bis(2-pyridyl)methylamine and BnTPEN is N-benzyl-N,N ,N -tris(2-pyridylmethyl)-1,2-diaminoethane), revealed the formation of 90% Fe^{III} decay products, rather than the expected Fe^{II} species.[54] It was confirmed that the Fe^{III} decay products do not arise from the comproportionation of Fe^{II} and $Fe^{IV}(O)$ intermediates, suggesting that these ferric decay species must be derived from the substrate oxidation reactions occurring through a non-rebound pathway. Additional evidence for escape of the substrate radical from the solvent cage comes from reactions carried out in the presence of a radical scavenger, $^{18}O_2$, where it was found all the oxygen-atoms of the alcohol and ketone products were derived from $^{18}O_2$, rather than the parent $Fe^{IV}(^{16}O)$ species.[54]

Others have argued against Nam and Shaik's proposal – Maiti and co-workers have provided ESI-MS evidence for a bound alcohol-ferrous species derived from the reaction of an electron-rich nonheme oxoiron(IV) complex with the substrates ethylbenzene and cumene, suggesting that the rebound mechanism may take place under certain conditions.[59] However, both of these studies are associated with *S* = 1 nonheme oxoiron(IV) complexes, while no work on the rebound mechanism of the more enzymatically relevant *S* = 2 nonheme oxoiron(IV) complexes has been presented in the literature.

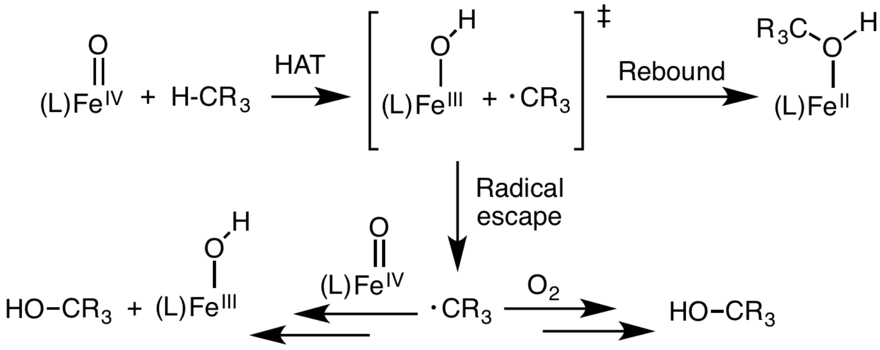

Figure 1.10. Proposed mode of hydroxylation by nonheme oxoiron(IV) complexes, where an alternative to the rebound mechanism is presented. Adapted from ref 54.

1.3 Oxygen-atom Exchange Reaction Between $H_2{}^{18}O$ and Nonheme Oxoiron(IV) Complexes

The reactivity of high-valent metal-oxo species is of immense interest to the bioinorganic community. One reaction that is shared across many metal-oxo systems is the oxygen-atom exchange (OAE) reaction with H_2O.[60-65] Importantly, this reaction has been utilized to indirectly establish the presence of high valent metal-oxo intermediates in catalytic substrate oxidation reactions, due to these metal-oxo intermediates being too reactive to trap and characterize.[61,62,64] In this indirect detection strategy, a reduced metal complex is reacted with an oxidant, $H_2{}^{18}O$ and a substrate simultaneously. Successful incorporation of the ^{18}O-atom into the final oxidized substrate suggests the initial generation of a metal-oxo species, rapid OAE with $H_2{}^{18}O$, and subsequent oxidation of the substrate, where the newly labeled metal-oxo intermediate incorporates its ^{18}O-atom into the substrate molecule.

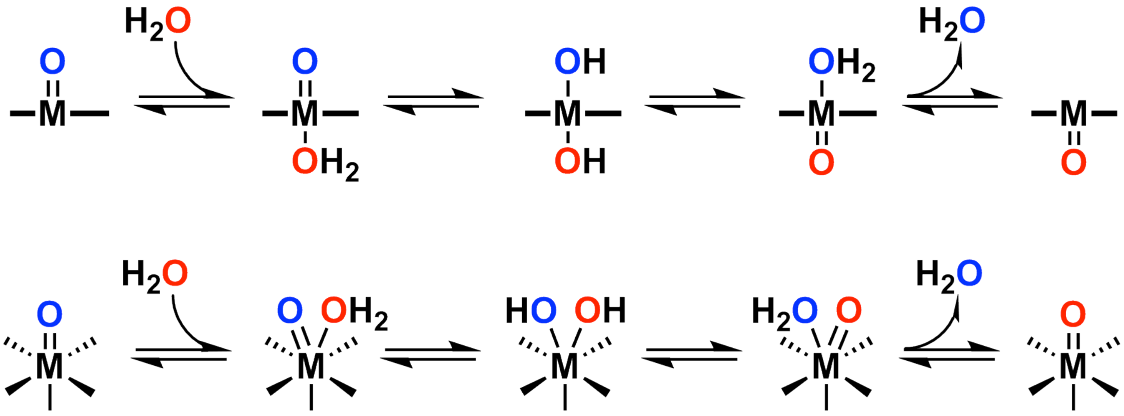

Figure 1.11. Proposed oxo-hydroxo tautomerization mechanism for OAE between $H_2{}^{18}O$ and metal-oxo species in heme systems (top) and nonheme systems (bottom).

Due to the importance of this reaction, the mechanism of OAE with $H_2{}^{18}O$ has been probed for different metal-oxo systems. In heme systems, Meunier and co-workers have proposed an oxo-hydroxo tautomerism mechanism,[61] in which $H_2{}^{18}O$ is proposed to bind *trans* to the oxo-ligand, forming an oxo-aqua metal species. Proton transfer between the aqua and oxo ligands then generates a bis-hydroxo intermediate species. Subsequent proton transfer between the two hydroxo ligands and release of $H_2{}^{16}O$ generates the labeled metal-oxo species (Figure 1.11, top). More recently, Seo *et al*. have proposed an analogous tautomerization to rationalize incorporation from $H_2{}^{18}O$ into nonheme oxoiron(IV) complexes via a bis-hydroxo intermediate species that derives from $H_2{}^{18}O$ binding *cis* to the oxo ligand (Figure 1.11, bottom).[64] This modification of the heme-based mechanism was necessitated by the fact that the two nonheme oxoiron(IV) complexes demonstrated to undergo OAE were supported by ligands lacking the plane of symmetry associated with a porphyrin ring (Figure 1.12).

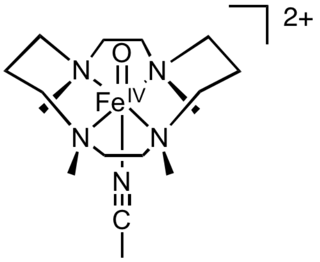

$[Fe^{IV}(O)(TMC)(CH_3CN)]^{2+}$ (**14**)

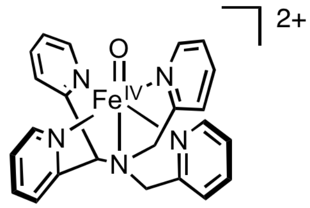

$[Fe^{IV}(O)(N4Py)]^{2+}$ (**15**)

Figure 1.12 Nonheme oxoiron(IV) complexes previously studied in the context of oxygen-atom exchange with $H_2{}^{18}O$.

Seo *et al.* provided direct kinetic evidence for OAE between $H_2{}^{18}O$ and two synthetic nonheme oxoiron(IV) species, $[Fe^{IV}(O)(TMC)(CH_3CN)](OTf)_2$ (**14**) (OTf = O_3SCF_3) and $[Fe^{IV}(O)(N4Py)](ClO_4)_2$ (**15**) using electrospray ionization mass spectrometry (ESI-MS).[64] While the study clearly demonstrates the ability of these complexes to exchange oxygen-atoms with $H_2{}^{18}O$, there were puzzling observations about this work. Notably, it was found that OAE between $H_2{}^{18}O$ and **14** and **15** in acetonitrile solution at 25 °C occurs at nearly identical rates ($k_2 = 7 \times 10^{-3}$ M^{-1} s^{-1} and $k_2 = 6 \times 10^{-3}$ M^{-1} s^{-1}, respectively) with identical Eyring activation parameters ($\Delta H^{\ddagger} = 17 \pm 3$ kJ mol^{-1} and $\Delta S^{\ddagger} = -238 \pm 33$ J K^{-1} mol), despite the fact that the two oxoiron(IV) centers are supported by two very different nonheme ligand frameworks, where TMC is a tetradentate macrocyclic ligand and N4Py is a pentadentate non-macrocyclic ligand (Figure 1.12). Very different conclusions concerning the effects of coordination environment on the rate of OAE with $H_2{}^{18}O$ have been presented in other metal-oxo systems. For example, Brudvig and Crabtree have investigated the kinetics of OAE between $H_2{}^{18}O$ and μ-oxo bridges in different di-μ-oxo-dimanganese complexes to model the Mn-oxo centers in the OEC.[65,66] Their results show an increase in the rates of OAE for a complex that features Mn centers with open coordination sites, 9.6 x 10^{-3} M^{-1} s^{-1} for $[(\text{mes-terpy})_2Mn_2^{III/IV}(\mu\text{-}O)_2(H_2O)_2](NO_3)_3$ (mes-terpy = 4'-mesityl-2,2':6',2"-terpyridine), compared to a complex with coordinatively saturated Mn centers, 2.3 x 10^{-3} M^{-1} s^{-1} for $[(\text{phen})_4Mn_2^{III/IV}(\mu\text{-}O)_2](ClO_4)_3$, both in acetonitrile solution at 20 °C. In addition, Bakac reported an OAE rate of 25 M^{-1} s^{-1} between $H_2{}^{18}O$ and the S = 2 oxoiron(IV) complex, $[Fe^{IV}(O)(H_2O)_5]^{2+}$, in 0.10 M aqueous $HClO_4$ solution at room temperature, which is over three orders of magnitude faster than the reported OAE rates for **14** and **15**, albeit in a different solvent. Based on these interesting differences, the effects of the ligand environment on the rate of OAE between $H_2{}^{18}O$ and nonheme oxoiron(IV) complexes warrants re-examination and further exploration.

1.4 Generation and Characterization of Nonheme Imidoiron(IV) Complexes

In surveying the range of complexes containing metal-ligand multiple bonds in coordination chemistry, it is noted that oxo (O^{-2}) and imido (NR^{-2}) ligands are isoelectronic, both bearing a formal -2 charge.[7,67] This provides an important basis for the comparison of two fundamental classes of synthetic bioinorganic compounds, metal-oxo and metal-imido species. While there are currently over sixty reported synthetic nonheme oxoiron(IV) complexes in the literature,[5] the chemistry of the analogous nonheme imidoiron(IV) species is still comparatively in its infancy.[67,68] Notably, of the seven isolated mononuclear nonheme imidoiron(IV) complexes reported to date, only one of them has a six-coordinate Fe^{IV} center, $[Fe^{IV}(NTs)(N4Py)]^{2+}$ (where Ts is tosylate) (**16**),[69] which is comparable to the coordination environment of the majority of synthetic nonheme oxoiron(IV) complexes (Figure 1.13).[5] While structural and spectroscopic comparisons between six-coordinate oxoiron(IV) and imidoiron(IV) analogues have been made,[69] there are only two reports on reactivity differences between these two functional units supported by the same ligand framework.[70,71] This is a shortcoming in the literature, as imidoiron(IV) species are believed to be important intermediates in group transfer and catalytic C-H bond amination reactions.[68,72-74] Therefore, there is a tremendous impetus for investigating the substrate reactivity and mechanisms of six-coordinate nonheme imidoiron(IV) species. In doing so, we may draw parallels to the abundant research already developed for the isoelectronic nonheme oxoiron(IV) system, ultimately increasing our insight into the unexplored but important realm of imidoiron(IV) chemistry.

It should be noted that the imidoiron(IV) chemistry described here is a small subsection of a larger group of imidoiron coordination complexes, where the examples are purposefully limited to mononuclear nonheme imidoiron species with Fe in the +4 oxidation state (or in a +3 oxidation state coupled to an oxidized iminyl radical). Readers are encouraged to explore other fascinating imidoiron complexes not described here, such as those found in dinuclear frameworks,[75] in different iron oxidation states (ranging from +2 to +5)[76-78] and examples of bisimidoiron(IV) complexes.[79,80]

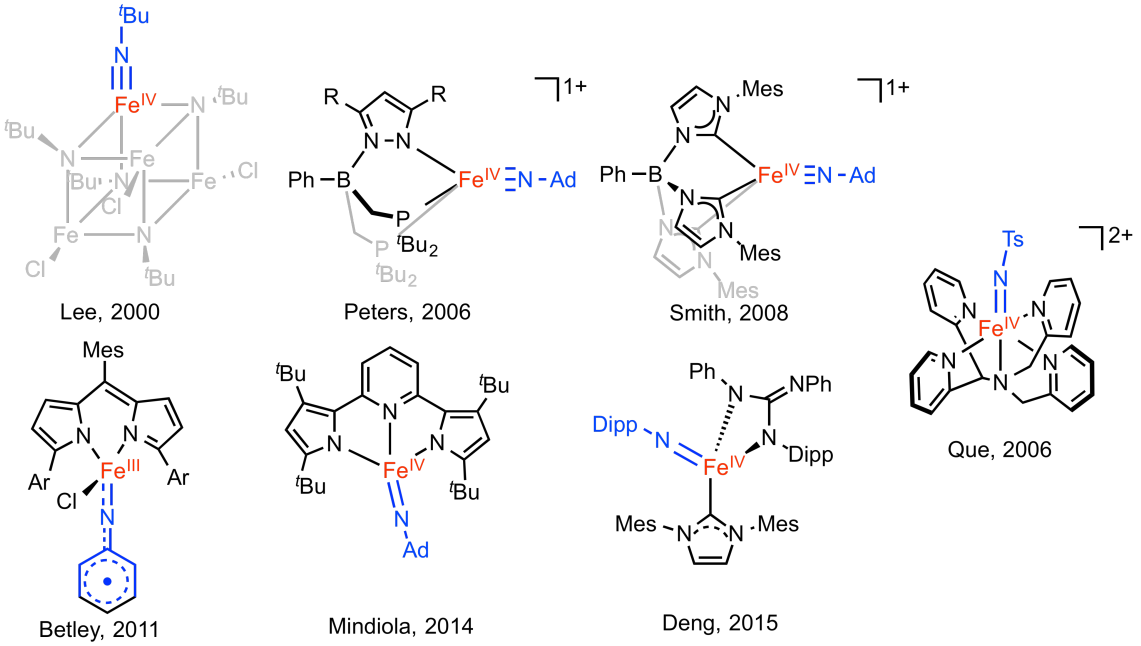
Lee, 2000 Peters, 2006 Smith, 2008 Que, 2006

Betley, 2011 Mindiola, 2014 Deng, 2015

Figure 1.13. Structures of select nonheme imidoiron(IV) complexes.

Sonny Lee first reported the isolation of an imidoiron(IV) species in 2000, when a $Fe^{III}_3Fe^{IV}(NR)_4$ cubane was synthesized containing a terminal Fe^{IV}=N^{t}Bu unit (^{t}Bu = *tertiary*-butyl) (Figure 1.13).[81] The cluster was found to be extremely stable at room temperature, allowing for single crystals to be grown and the Fe-N$_{imido}$ distance to be measured as 1.635(4) Å (Table 1.3). Unfortunately, the complex was obtained in very low yields (1 – 2%) and displayed no reactivity at room temperature with aniline, triphenylphosphine or styrene, precluding it from being a practical model for exploring the reactivity of imidoiron(IV) complexes.[81]

The second example of an isolated imidoiron(IV) species, a pseudo-tetrahedral $Fe^{IV}\equiv$NAd complex (Ad = adamantly) supported by the hybrid bis(phosphino)pyrazolylborate ligand, was reported by the Peters group in 2006 (Figure 1.13).[82] In this study, the authors have chosen to represent the Fe-N$_{imido}$ bond as a formal triple-bond, a consequence of the molecular orbital (MO) diagram derived from its pseudo-tetrahedral geometry (Figure 1.14). While Peters' imido species was obtained in much higher yields than Lee's $Fe^{III}_3Fe^{IV}(NR)_4$ cubane, it was also found to be much more reactive, with a half-life of only 50 minutes at -40 °C. In order to obtain x-ray quality crystals, additional methyl groups were appended to the 3 and 5 positions of the pyrazole ring, sufficiently increasing the lifetime for crystallization. The Fe-N_{imido} distance of the derivatized complex was nearly identical to Lee's complex, measuring to 1.634(4) Å, and confirming the shared presence of a Fe-N triple bond with a nearly-linear Fe-N-R bond angle (Table 1.3).[82] Despite being extensively characterized, Peters reported no reactivity data for substrate oxidation or NAd-group transfer, presumably due to the difficulties in carrying out extensive substrate reactivity and mechanistic studies with this species.

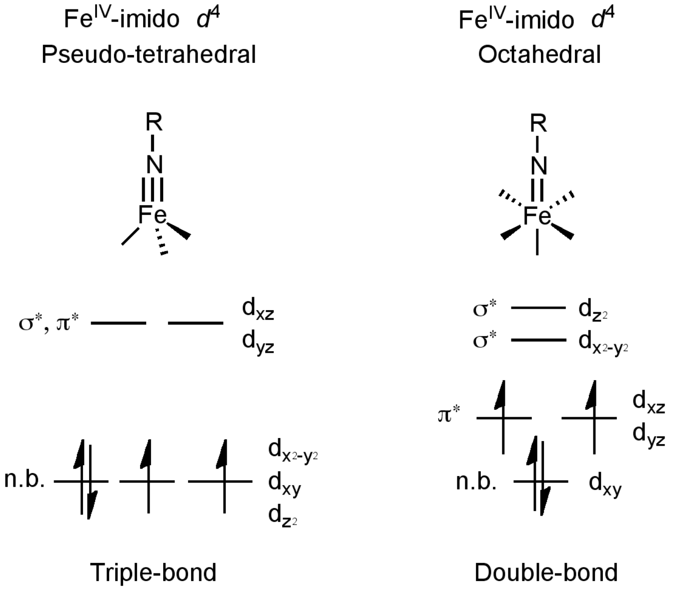

Figure 1.14. Molecular orbitals of pseudo-tetrahedral and octahedral nonheme imidoiron(IV) complexes. Adapted from references 67,83.

Table 1.3. Spectroscopic information on select nonheme imidoiron(IV) complexes.

Complex	Ox. state	Spin State	CN	Fe-N (Å)	δ (mm/s)	ΔE_Q (mm/s)	Ref
$Fe^{III}{}_3Fe^{IV}(NR)_4$ cubane	+4	N/A	4	1.635(4)	-0.17	0.38	81
$[Fe^{IV}(NAd)(PhBpz(PR_2)_2]^+$	+4	1	4	1.634(4)	-	-	82
$[Fe^{IV}(NAd)L^{carbene}Mes]^+$	+4	1	4	1.618(3)	-	-	84
$[Fe^{III}(pyrrol_2)(NC_6H_4\text{-}p\text{-}{}^tBu)]$	+3	2	4	1.768(2)	0.29	2.29	74
$[Fe^{IV}(NAd)(pyrr_2py)]$	+4	0	4	1.640(4)	-0.09	2.78	85
[Fe(NDipp)(IMes)(N(Dipp)C(NPh)(=NPh))]	+3 or +4	1 or 2	4	1.708(2)	0.17	1.31	80
$[Fe^{IV}(NTs)(N4Py)]^{2+}$ (**16**)	+4	1	6	1.73	0.02	0.98	69
$[Fe^{IV}(NTs)(BnTPEN)]^{2+}$	+4	1	6	-	0.06	0.99	86

The third example of a nonheme imidoiron(IV) complex was reported by the Smith group in 2008 and utilizes a related tris(carbene)borate ligand to stabilize a pseudo-tetrahedral $Fe^{IV}\equiv NAd$ species (Figure 1.13).[84] In this case however, the complex is much more stable than the Peters example, showing no signs of degradation even after being heated to 100 °C for many days. The crystal structure indicates a $Fe\text{-}N_{imido}$ distance of 1.618(3) Å, slightly shorter than the Peters or Lee structures (Table 1.3). Taking advantage of the thermal stability of this complex, Smith reported on the thermodynamics of HAT by analyzing the electron-transfer and proton-transfer steps individually. While Smith does not systematically report reactivity with a range of substrates, he notes briefly that the $Fe^{IV}\equiv NAd$ species reacts with DHA at 100 °C to form anthracene in 25 % yield.[84] Unfortunately, the use of these high temperatures and return of relatively low oxidation yields suggest that this complex, while appropriate for cursory mechanistic studies on HAT, is not well suited for broad substrate reactivity testing.

A breakthrough in the chemistry of nonheme imidoiron(IV) complexes came from the Betley group in 2011.[74] They reported the synthesis of a four-coordinate $[Fe^{III}(pyrrol_2)(NC_6H_4\text{-}p\text{-}{}^tBu)]$ species, formally an imidoiron(IV) complex but more accurately described as S = 5/2 imidoiron(III) center antiferromagnetically coupled to a bound S = ½ iminyl radical to form an overall $S = 2$ ground spin state molecule (Figure 1.13). This open-shell high-spin electronic configuration resulted in a significant elongation of the $Fe\text{-}N_{imido}$ bond compared to the previous closed-shell pseudo-tetrahedral imidoiron(IV) species, with a distance of 1.768(2) Å, as characterized by x-ray crystallography (Table 1.3). In addition, the isomer shift obtained from Mössbauer experiments is much larger at 0.29 mm/s, consistent with the assignment of an Fe^{III} oxidation state (Table 1.3).[74] Most importantly, this open-shell imidoiron(III)-iminyl-radical species is capable of elegant intermolecular and intramolecular C-H bond activation reactions,[74,87] as well as styrene azirdination.[88] Notably this complex was precedented in some respects by Chirik's imidioiron(III)-ligand-radical complex supported by a redox-active bis(imino)pyridine ligand.[89] However, the majority of synthetic nonheme oxoiron(IV) complexes do not adopt this open-shell electronic configuration, making it difficult to draw parallels between these two systems.

More recent examples of imidoiron(IV) complexes include an interesting $S = 0$ nonheme imidoiron(IV) species by Mindiola in 2014 where the four-coordinate imidoiron(IV) center is supported by a sterically bulky bis(pyrrolyl)pyridine ligand in what is best described as a *cis*-divacant octahedral geometry (Figure 1.13).[85] The bond distance is a bit longer than the Peters and Smith example at 1.640(4) Å and the Fe-N-R angle is more acute at 140.5(3)°. However, no reactivity with this low-spin nonheme imidoiron(IV) species has been presented.[85] In 2015, Deng reported the reaction between a three-coordinate bisimidoiron(IV) complex supported by an aminocarbene ligand framework and a heterocumulene, PhNCNPh, to yield a monoimidoiron(IV) species.[80] Similar to the Betley example, this complex has an elongated Fe-N_{imido} distance of 1.708(2) Å with an isomer shift of 0.17 mm/s, which may be described as an open-shell Fe^{III} center coordinated to an iminyl radical. Unlike the Betley system, no intermolecular or intramolecular reactivity was explored with this complex, although elegant reactivity studies were performed on the parent three-coordinate bisimidoiron(IV) species.[80]

The last example, **16**, reported by the Que group in 2006, is a tosylimidoiron(IV) complex supported by N4Py (Figure 1.13).[69] While published in the same year as the Peters example, **16** stands out from all the previous nonheme imidoiron(IV) species in a number of ways. First, **16** contains a six-coordinate Fe^{IV} center, in stark contrast to the four-coordinate geometries of all the previous examples. This change significantly affects the MO of **16,** where two electrons now populate π^* anti-bonding orbitals, suggesting the Fe-N bond be classified instead as a formal double-bond (Figure 1.14). **16** was also characterized by XAS to have a Fe-N_{imido} distance of 1.73 Å, significantly longer than the 1.618 – 1.635 Å range observed for the tetrahedral imidoiron(IV) complexes, and in line with its double-bond character.[69] In fact, this bond distance is comparable to the Betley example, where the imidoiron species has a formal Fe^{III} center.[74] This activated Fe-N bond sets **16** apart from its tetrahedral counterparts, and may allow for an increase in reactivity. Mostly importantly, **16** is a direct analogue of an extensively-characterized and well-studied oxoiron(IV) complex, $[Fe^{IV}(O)(N4Py)]^{2+}$, **15**,[18] greatly simplifying potential comparisons between these two functional units. Electronically, this is confirmed by DFT studies which suggests that **15** and **16** have an identical electronic configuration of $(3d_{xy})^2(3d_{xz})^1(3d_{yz})^1$, imparting a double-bond character, Fe=O and Fe=NR, to both species.[69] Another six-coordinate imidoiron(IV) complex supported by a very similar N5 ligand set, $[Fe^{IV}(NTs)(BnTPEN)]^{2+}$, has also been synthesized but has yet to be published. This molecule appears to show similar spectroscopic traits to complex **16**.[86]

The reactivity of complex **16** has been explored experimentally and computationally by Sastri and de Visser, where they find that **16** is more reactive than **15** in imido/oxo group/atom-transfer reactions with thioanisole, whereas the opposite is true for HAT reactions with substrates containing weak C-H bonds, such as xanthene, 1,4-cyclohexadiene, fluorine and benzyl alcohol.[70,71] This difference in rates is attributed to a long-range electron-transfer type mechanism for the oxidation of organic substrates by **16**, which has a much larger electron affinity than **15**, explaining the greater rate for **16** in thioanisole oxidation. However, this electron transfer mechanism results in slower rates in HAT reactions because it is the $[Fe^{III}(NTs)(N4Py)]^{+}$ species that actually abstracts the hydrogen-atom, which is a substantially less powerful oxidant compared to **15**. For this reason, **16** was only found to be capable of reacting with substrates containing weak C-H bonds (BDE < 80 kcal/mol).[70,71] It is not clear whether this is a function of the supporting ligand, N4Py, or a generalization for this class of compounds. For this reason, further study on the generation and reactivity of six-coordinate nonheme imidoiron(IV) are warranted.

1.5 Scope and Aim of Thesis

This thesis aims to cover a wide range of topics related to the chemistry of synthetic nonheme iron(IV) complexes. Chapter 2 illustrates how to systematically tune the spin state of a synthetic nonheme oxoiron(IV) complex from $S = 1$ to $S = 2$ by replacing the equatorial pyridine donors with weaker field quinoline donors. Using this strategy, the $S = 2$ ground spin state is stabilized in the complex $[Fe^{IV}(O)(TQA)(MeCN)]^{2+}$, where the three pyridine rings of TPA have been converted to quinoline rings. Variants of this $S = 2$ complex could be generated by replacing the labile acetonitrile ligand with halide ligands, Cl^{-1} and Br^{-1}, to produce $[Fe^{IV}(O)(TQA)(Cl)]^{+}$ and $[Fe^{IV}(O)(TQA)(Br)]^{+}$, respectively. These three $S = 2$ oxoiron(IV) complexes are characterized by a suite of spectroscopic methods including UV-visible, resonance Raman, Mössbauer and x-ray absorption spectroscopies, as well as ESI-MS. Density functional theory (DFT) calculations are also carried out, confirming the proposed structure of these complexes from their calculated spectroscopic signatures. Notably, these three $S = 2$ oxoiron(IV) reproduce the Mössbauer parameters of the oxoiron(IV) enzymatic intermediates in TauD, CytC3 and SyrB2, making them the closest electronic models of these important bioinorganic species to date. Chapter 3 examines the reactivity of these $S = 2$ oxoiron(IV) species in the context of HAT and OAT. The $S = 2$ complex $[Fe^{IV}(O)(TQA)(MeCN)]^{2+}$ is found to be the most reactive synthetic nonheme oxoiron(IV) to date, while the complexes $[Fe^{IV}(O)(TQA)(Cl)]^{+}$ and $[Fe^{IV}(O)(TQA)(Br)]^{+}$

are the first examples of synthetic nonheme oxoiron(IV)-halide complexes capable of halogenating C-H bonds.

Chapter 4 examines one particular reaction between oxoiron(IV) complexes and $H_2{}^{18}O$, in which they undergo an oxygen-atom exchange. These reactions are tracked by ESI-MS and mechanistic details are obtained regarding the exchange process for $S = 1$ nonheme oxoiron(IV) complexes supported by both tetradentate and pentadentate ligands. Lastly, in chapter 5 the chemistry of $S = 1$ nonheme oxoiron(IV) complexes are compared to analogous $S = 1$ nonheme imidoiron(IV) complexes, where for the first time the generation of a six-coordinate nonheme imidoiron(IV) complex supported by a tetradentate ligand is reported. Conclusions and perspectives for the future are then presented in chapter 6.

1.6 References

(1) Costas, M.; Mehn, M. P.; Jensen, M. P.; Que, L., Jr. *Chem. Rev.* **2004**, *104*, 939-986.

(2) Krebs, C.; Fujimori, D. G.; Walsh, C. T.; Bollinger, J. M., Jr. *Acc. Chem. Res.* **2007**, *40*, 484-492.

(3) Price, J. C.; Barr, E. W.; Tirupati, B.; Bollinger, J. M., Jr.; Krebs, C. *Biochemistry* **2003**, *42*, 7497-7508.

(4) Sinnecker, S.; Svensen, N.; Barr, E. W.; Ye, S.; Bollinger, J. M., Jr.; Neese, F.; Krebs, C. *J. Am. Chem. Soc.* **2007**, *129*, 6168-6179.

(5) McDonald, A. R.; Que, L., Jr. *Coord. Chem. Rev.* **2013**, *257*, 414-428.

(6) Rohde, J.-U.; In, J.-H.; Lim, M. H.; Brennessel, W. W.; Bukowski, M. R.; Stubna, A.; Münck, E.; Nam, W.; Que, L., Jr. *Science* **2003**, *299*, 1037-1039.

(7) Que, L., Jr. *Acc. Chem. Res.* **2007**, *40*, 493-500.

(8) Pestovsky, O.; Stoian, S.; Bominaar, E. L.; Shan, X.; Münck, E.; Que, L., Jr.; Bakac, A. *Angew. Chem. Int. Ed.* **2005**, *44*, 6871-6874.

(9) Pestovsky, O.; Bakac, A. *J. Am. Chem. Soc.* **2004**, *126*, 13757-13764.

(10) Biswas, A. N.; Puri, M.; Meier, K. K.; Oloo, W. N.; Rohde, G. T.; Bominaar, E. L.; Münck, E.; Que, L. *J. Am. Chem. Soc.* **2015**, *137*, 2428-2431.

(11) England, J.; Guo, Y.; Farquhar, E. R.; Young, V. G., Jr.; Münck, E.; Que, L., Jr. *J. Am. Chem. Soc.* **2010**, *132*, 8635-8644.

(12) Lacy, D. C.; Gupta, R.; Stone, K. L.; Greaves, J.; Ziller, J. W.; Hendrich, M. P.; Borovik, A. S. *J. Am. Chem. Soc.* **2010**, *132*, 12188-12190.

(13) Winkler, J. R.; Gray, H. B. *Struct. Bonding* **2012**, *142*, 17-28.

(14) Wong, S. D.; Srnec, M.; Matthews, M. L.; Liu, L. V.; Kwak, Y.; Park, K.; Bell, C. B., 3rd; Alp, E. E.; Zhao, J.; Yoda, Y.; Kitao, S.; Seto, M.; Krebs, C.; Bollinger, J. M., Jr.; Solomon, E. I. *Nature* **2013**, *499*, 320-323.

(15) England, J.; Martinho, M.; Farquhar, E. R.; Frisch, J. R.; Bominaar, E. L.; Münck, E.; Que, L., Jr. *Angew. Chem. Int. Ed.* **2009**, *48*, 3622-3626.

(16) Kleespies, S. T.; Oloo, W. N.; Mukherjee, A.; Que, L. *Inorg. Chem.* **2015**, *54*, 5053-5064.

(17) Ray, K.; England, J.; Fiedler, A. T.; Martinho, M.; Münck, E.; Que, L., Jr. *Angew. Chem. Int. Ed.* **2008**, *47*, 8068–8071.

(18) Kaizer, J.; Klinker, E. J.; Oh, N. Y.; Rohde, J.-U.; Song, W. J.; Stubna, A.; Kim, J.; Münck, E.; Nam, W.; Que, L., Jr. *J. Am. Chem. Soc.* **2004**, *126*, 472-473.

(19) England, J.; Guo, Y.; Van Heuvelen, K. M.; Cranswick, M. A.; Rohde, G. T.; Bominaar, E. L.; Münck, E.; Que, L., Jr. *J. Am. Chem. Soc.* **2011**, *133*, 11880–11883.

(20) Bigi, J. P.; Harman, W. H.; Lassalle-Kaiser, B.; Robles, D. M.; Stich, T. A.; Yano, J.; Britt, R. D.; Chang, C. J. *J. Am. Chem. Soc.* **2012**, *134*, 1536-1542.

(21) Xue, G.; Fiedler, A. T.; Martinho, M.; Münck, E.; Que, L., Jr. *Proc. Nat. Acad. Sci. USA* **2008**, *105*, 20615-20620.

(22) Xue, G.; Wang, D.; De Hont, R.; Fiedler, A. T.; Shan, X.; Münck, E.; Que, L., Jr. *Proc. Nat. Acad. Sci. USA* **2007**, *104*, 20713-20718.

(23) Xue, G.; De Hont, R.; Münck, E.; Que, L., Jr. *Nat. Chem.* **2010**, *2*, 400-405.

(24) De Hont, R. F.; Xue, G.; Hendrich, M. P.; Que, L., Jr.; Bominaar, E. L.; Münck, E. *Inorg. Chem.* **2010**, *49*, 8310-8322.

(25) Dong, Y.; Fujii, H.; Hendrich, M. P.; Leising, R. A.; Pan, G.; Randall, C. R.; Wilkinson, E. C.; Zang, Y.; Que, L., Jr.; Fox, B. G.; Kauffmann, K.; Münck, E. *J. Am. Chem. Soc.* **1995**, *117*, 2778-2792.

(26) Hsu, H.-F.; Dong, Y.; Shu, L.; Young, V. G., Jr.; Que, L., Jr. *J. Am. Chem. Soc.* **1999**, *121*, 5230-5237.

(27) Dong, Y.; Que, L., Jr.; Kauffmann, K.; Münck, E. *J. Am. Chem. Soc.* **1995**, *117*, 11377-11378.

(28) Lim, M. H.; Rohde, J.-U.; Stubna, A.; Bukowski, M. R.; Costas, M.; Ho, R. Y. N.; Münck, E.; Nam, W.; Que, L., Jr. *Proc. Natl. Acad. Sci. USA* **2003**, *100*, 3665-3670.

(29) Paine, T. K.; Costas, M.; Kaizer, J.; Que, L., Jr. *J. Biol. Inorg. Chem.* **2006**, *11*, 272-276.

(30) Hoffart, L. M.; Barr, E. W.; Guyer, R. B.; Bollinger, J. M., Jr.; Krebs, C. *Proc. Natl. Acad. Sci. USA* **2006**, *103*, 14738-14743.

(31) Galonić, D. P.; Barr, E. W.; Walsh, C. T.; Bollinger, J. M., Jr.; Krebs, C. *Nat. Chem. Biol.* **2007**, *3*, 113-116.

(32) Matthews, M. L.; Krest, C. M.; Barr, E. W.; Vaillancourt, F. H.; Walsh, C. T.; Green, M. T.; Krebs, C.; Bollinger, J. M., Jr. *Biochemistry* **2009**, *48*, 4331–4343.

(33) Eser, B. E.; Barr, E. W.; Frantom, P. A.; Saleh, L.; Bollinger, J. M.; Krebs, C.; Fitzpatrick, P. F. *J. Am. Chem. Soc.* **2007**, *129*, 11334-11335.

(34) MacBeth, C. E.; Golombek, A. P.; Young, V. G., Jr.; Yang, C.; Kuczera, K.; Hendrich, M. P.; Borovik, A. S. *Science* **2000**, *289*, 938-941.

(35) Shu, L.; Nesheim, J. C.; Kauffmann, K.; Münck, E.; Lipscomb, J. D.; Que, L., Jr. *Science* **1997**, *275*, 515-518.

(36) Banerjee, R.; Proshlyakov, Y.; Lipscomb, J. D.; Proshlyakov, D. A. *Nature* **2015**, *518*, 431-434.

(37) Dassama, L. M.; Silakov, A.; Krest, C. M.; Calixto, J. C.; Krebs, C.; Bollinger, J. M., Jr.; Green, M. T. *J. Am. Chem. Soc.* **2013**, *135*, 16758-16761.

(38) Xue, G.; Pokutsa, A.; Que, L., Jr. *J. Am. Chem. Soc.* **2011**, *133*, 16657–16667.

(39) Shanmugam, M.; Xue, G.; Que, L., Jr.; Hoffman, B. M. *Inorg. Chem.* **2012**, *51*, 10080-10082.

(40) Xue, G.; Geng, C.; Ye, S.; Fiedler, A. T.; Neese, F.; Que, L., Jr. *Inorg. Chem.* **2013**, *52*, 3976-3984.

(41) Decker, A.; Rohde, J.-U.; Klinker, E. J.; Wong, S. D.; Que, L., Jr.; Solomon, E. I. *J. Am. Chem. Soc.* **2007**, *129*, 15983-15996.

(42) Bernasconi, L.; Louwerse, M. J.; Baerends, E. J. *Eur. J. Inorg. Chem.* **2007**, 3023-3033.

(43) Geng, C.; Ye, S.; Neese, F. *Angew. Chem. Int. Ed.* **2010**, *49*, 5717-5720.

(44) Shaik, S.; Chen, H.; Janardanan, D. *Nat. Chem.* **2011**, *3*, 19-27.

(45) Usharani, D.; Janardanan, D.; Li, C.; Shaik, S. *Acc. Chem. Res.* **2013**, *46*, 471-482.

(46) Rohde, J.-U.; Stubna, A.; Bominaar, E. L.; Münck, E.; Nam, W.; Que, L., Jr. *Inorg. Chem.* **2006**, *45*, 6435-6445.

(47) Jackson, T. A.; Rohde, J.-U.; Seo, M. S.; Sastri, C. V.; DeHont, R.; Stubna, A.; Ohta, T.; Kitagawa, T.; Münck, E.; Nam, W.; Que, L., Jr. *J. Am. Chem. Soc.* **2008**, *130*, 12394-12407.

(48) McDonald, A. R.; Guo, Y.; Vu, V. V.; Bominaar, E. L.; Münck, E.; Que, L., Jr. *Chem. Sci.* **2012**, *3*, 1680-1693.

(49) Zang, Y.; Kim, J.; Dong, Y.; Wilkinson, E. C.; Appelman, E. H.; Que, L., Jr. *J. Am. Chem. Soc.* **1997**, *119*, 4197-4205.

(50) Zheng, H.; Yoo, S. J.; Münck, E.; Que, L., Jr. *J. Am. Chem. Soc.* **2000**, *122*, 3789-3790.

(51) Ghosh, A.; Tangen, E.; Ryeng, H.; Taylor, P. R. *Eur. J. Inorg. Chem.* **2004**, *2004*, 4555-4560.

(52) Groves, J. T. *J. Inorg. Biochem.* **2006**, *100*, 434-447.

(53) Groves, J. T. *J. Chem. Ed.* **1985**, *62*, 928-931.

(54) Cho, K.-B.; Wu, X.; Lee, Y.-M.; Kwon, Y. H.; Shaik, S.; Nam, W. *J. Am. Chem. Soc.* **2012**, *134*, 20222-20225.

(55) Groves, J. T.; McClusky, G. A.; White, R. E.; Coon, M. J. *Biochem. Biophys. Res. Comm.* **1978**, *81*, 154-160.

(56) Auclair, K.; Hu, Z.; Little, D. M.; Ortiz de Montellano, P. R.; Groves, J. T. *J. Am. Chem. Soc.* **2002**, *124*, 6020-6027.

(57) Fretz, H.; Woggon, W.-D.; Voges, R. *Helv. Chim. Acta.* **1989**, *72*, 391-400.

(58) Cho, K.-B.; Hirao, H.; Shaik, S.; Nam, W. *Chem. Soc. Rev.* **2016**.

(59) Rana, S.; Dey, A.; Maiti, D. *Chem. Comm.* **2015**, *51*, 14469-14472.

(60) Hashimoto, S.; Tatsuno, Y.; Kitagawa, T. *Proc. Natl. Acad. Sci. USA* **1986**, *83*, 2417-2421.

(61) Bernadou, J.; Fabiano, A.-S.; Robert, A.; Meunier, B. *J. Am. Chem. Soc.* **1994**, *116*, 9375-9376.

(62) Nam, W.; Valentine, J. S. *J. Am. Chem. Soc.* **1993**, *115*, 1772-1778.

(63) Lee, K. A.; Nam, W. *J. Am. Chem. Soc.* **1997**, *119*, 1916-1922.

(64) Seo, M. S.; In, J.-H.; Kim, S. O.; Oh, N. Y.; Hong, J.; Kim, J.; Que, L., Jr.; Nam, W. *Angew. Chem. Int. Ed.* **2004**, *43*, 2417-2420.

(65) Tagore, R.; Chen, H. Y.; Crabtree, R. H.; Brudvig, G. W. *J. Am. Chem. Soc.* **2006**, *128*, 9457-9465.

(66) Tagore, R.; Crabtree, R. H.; Brudvig, G. W. *Inorg. Chem.* **2007**, *46*, 2193-2203.

(67) Mehn, M. P.; Peters, J. C. *J. Inorg. Biochem.* **2006**, *100*, 634-643.

(68) Zhang, L.; Deng, L. *Chinese Sci. Bull.* **2012**, *57*, 2352-2360.

(69) Klinker, E. J.; Jackson, T. A.; Jensen, M. P.; Stubna, A.; Juhász, G.; Bominaar, E. L.; Münck, E.; Que, L., Jr. *Angew. Chem. Int. Ed.* **2006**, *45*, 7394-7397.

(70) Vardhaman, A. K.; Barman, P.; Kumar, S.; Sastri, C. V.; Kumar, D.; de Visser, S. P. *Angew. Chem.* **2013**, *125*, 12514-12518.

(71) Kumar, S.; Faponle, A. S.; Barman, P.; Vardhaman, A. K.; Sastri, C. V.; Kumar, D.; de Visser, S. P. *J. Am. Chem. Soc.* **2014**, *136*, 17102-17115.

(72) Jensen, M. P.; Mehn, M. P.; Que, L., Jr. *Angew. Chem. Int Ed.* **2003**, *42*, 4357-4360.

(73) Lucas, R. L.; Powell, D. R.; Borovik, A. S. *J. Am. Chem. Soc.* **2005**, *127*, 11596-11597.

(74) King, E. R.; Hennessy, E. T.; Betley, T. A. *J. Am. Chem. Soc.* **2011**, *133*, 4917-4923.

(75) Gouré, E.; Avenier, F.; Dubourdeaux, P.; Sénèque, O.; Albrieux, F.; Lebrun, C.; Clémancey, M.; Maldivi, P.; Latour, J.-M. *Angew. Chem. Int. Ed.* **2014**, *53*, 1580-1584.

(76) Brown, S. D.; Peters, J. C. *J. Am. Chem. Soc.* **2005**, *127*, 1913-1923.

(77) Brown, S. D.; Betley, T. A.; Peters, J. C. *J. Am. Chem. Soc.* **2003**, *125*, 322-323.

(78) Ni, C.; Fettinger, J. C.; Long, G. J.; Brynda, M.; Power, P. P. *Chem. Commun.* **2008**, 6045-6047.

(79) Zhang, H.; Ouyang, Z.; Liu, Y.; Zhang, Q.; Wang, L.; Deng, L. *Angew. Chem. Int. Ed.* **2014**, *53*, 8432-8436.

(80) Wang, L.; Hu, L.; Zhang, H.; Chen, H.; Deng, L. *J. Am. Chem. Soc.* **2015**, *137*, 14196-14207.

(81) Verma, A. K.; Nazif, T. N.; Achim, C.; Lee, S. C. *J. Am. Chem. Soc.* **2000**, *122*, 11013-11014.

(82) Thomas, C. M.; Mankad, N. P.; Peters, J. C. *J. Am. Chem. Soc.* **2006**, *128*, 4956-4957.

(83) Saouma, C. T.; Peters, J. C. *Coord. Chem. Rev.* **2011**, *255*, 920-937.

(84) Nieto, I.; Ding, F.; Bontchev, R. P.; Wang, H.; Smith, J. M. *J. Am. Chem. Soc.* **2008**, *130*, 2716-2717.

(85) Searles, K.; Fortier, S.; Khusniyarov, M. M.; Carroll, P. J.; Sutter, J.; Meyer, K.; Mindiola, D. J.; Caulton, K. G. *Angew. Chem. Int. Ed.* **2014**, *53*, 14139-14143.

(86) Klinker, E. J.: *High-valent iron compounds supported by pentadentate ligands*; ProQuest, 2007.

(87) Hennessy, E. T.; Betley, T. A. *Science* **2013**, *340*, 591-595.

(88) Hennessy, E. T.; Liu, R. Y.; Iovan, D. A.; Duncan, R. A.; Betley, T. A. *Chem. Sci.* **2014**, *5*, 1526-1532.

(89) Bart, S. C.; Lobkovsky, E.; Bill, E.; Chirik, P. J. *J. Am. Chem. Soc.* **2006**, *128*, 5302-5303.

Chapter 2:
Generation and Characterization of *S* = 2 Nonheme Oxoiron(IV) Complexes

Parts of this chapter were published in:

1. Puri, M.; Que, L. Jr. Towards the Synthesis of More Reactive *S* = 2 Nonheme Oxoiron(IV) Complexes. *Acc. Chem. Res.*, **2015**, *48*, 2443 – 2452.

2. Biswas, A. N.; Puri, M.; Meier, K. K.; Oloo, W. N.; Rohde, G. T.; Bominaar, E. L.; Münck, E.; Que, L. Jr. Modeling TauD-J: A High-Spin Nonheme Oxoiron(IV) Complex with High Reactivity toward C-H Bonds. *J. Am. Chem. Soc.*, **2015**, *137*, 2428 – 2431.

3. Puri, M.; Biswas, A. N.; Fan, R.; Guo, Y.; Que, L. Jr. Modeling Non-heme Iron Halogenases: High-Spin Oxoiron(IV)-Halide Complexes that Halogenate C-H Bonds. *J. Am. Chem. Soc.* **2016**, *138*, 2484 – 2487.

2.1 Introduction

$S = 2$ oxoiron(IV) species have been trapped and characterized as key intermediates in the dioxygen activation mechanisms of mononuclear nonheme iron enzymes.[1,2,3-5] Biochemists have found these $S = 2$ oxoiron(IV) species capable of undergoing an impressively diverse range of oxidative reactivity, including the hydroxylation of unactivated C-H bonds, desaturation of C-C bonds, electrophilic aromatic substitutions, as well as oxidative ligand transfer reactions in which C-H bonds are converted to C-halogen bonds.[3] For this reason, synthetic chemists have been very interested in modeling these oxoiron(IV) intermediates, leading to the characterization of over sixty oxoiron(IV) complexes in the past decade.[6-8] However, most of these complexes have a $S = 1$ ground states, with only a handful shown to possess a $S = 2$ ground state, as found for the enzymatic oxoiron(IV) intermediates.[9]

One successful strategy to obtain $S = 2$ oxoiron(IV) complexes has been to employ sterically bulky tripodal ligands that enforce trigonal bipyramidal geometry on the iron(IV) center, [10,11,12,13] but these complexes exhibit rather sluggish intermolecular reactivity, likely due to steric constraints. An alternative strategy to obtain $S = 2$ oxoiron(IV) complexes is to use a weaker field ligand environment than that provided by the tertiary amine/N-heterocycle combinations predominantly used by bioinorganic chemists thus far. Bakac and coworkers have shown that the $S = 2$ $[\mathrm{Fe}^{\mathrm{IV}}(\mathrm{O})(\mathrm{H_2O})_5]^{2+}$ ion, in which the oxoiron(IV) center is supported by weak-field aqua ligands, can be obtained in acidic aqueous solution and is in fact highly reactive towards the oxidation of organic substrates,[14] but its short lifetime ($t_{1/2} \sim 20$ s at 25 °C) has made its detailed characterization challenging.

We have thus sought to identify a ligand with weak-field donors that would allow the trapping of a sterically less hindered $S = 2$ nonheme oxoiron(IV) species with high reactivity and sufficient lifetime to allow thorough spectroscopic studies to be carried out. This goal was accomplished by tuning the ligand field strength of the popular tripodal ligand, TPA, through the systematic replacement of the relatively strong-field pyridine donors with weaker-field quinoline donors (Figure 2.1).[15-17] In doing so, we report the characterization of the $S = 2$ oxoiron(IV) complex, $[\mathrm{Fe^{IV}(O)(TQA)(MeCN)}]^{2+}$ (**1**), which is both a functional and electron model of the enzymatic intermediate ***J*** found in the nonheme iron enzyme, taurine dioxygenase (TauD).

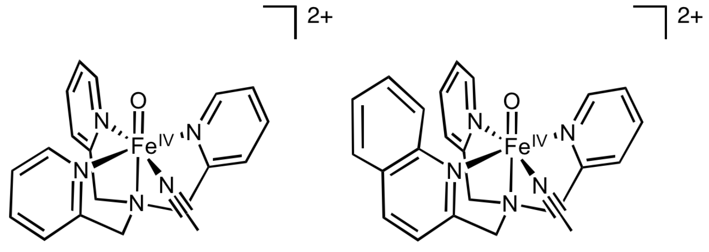

$[\mathrm{Fe^{IV}(O)(TPA)(MeCN)}]^{2+}$
$S = 1$

$[\mathrm{Fe^{IV}(O)(QBPA)(MeCN)}]^{2+}$
$S = 1$

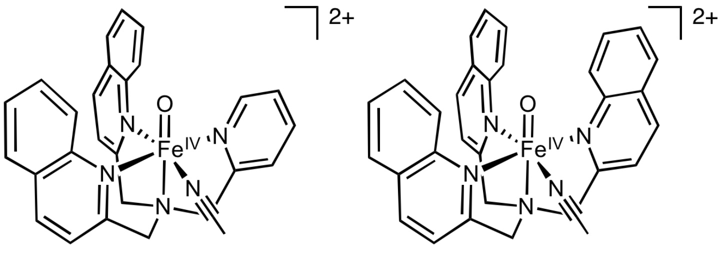

$[\mathrm{Fe^{IV}(O)(BQPA)(MeCN)}]^{2+}$
$S = 1$

$[\mathrm{Fe^{IV}(O)(TQA)(MeCN)}]^{2+}$ (**1**)
$S = 2$

Figure 2.1. A series of nonheme oxoiron(IV) complexes in which each pyridine of the TPA ligand is sequentially replaced by weaker-field quinoline rings.

Upon generating the *S* = 2 oxoiron(IV) complex, **1**, we attempted to apply this synthetic system to the modeling of other nonheme iron enzymes, notably the halogenase enzymes. Nonheme iron halogenases are an important subclass of the aKG-dependent family of nonheme iron enzymes that utilize O_2 to transform C-hydrogen bonds to C-halogen bonds in reactions central to the biosynthesis of natural products.[3] Two well-studied examples are the enzymes CytC3 and SyrB2, which are responsible for the synthesis of cytotrienin A/B and syringomycin E, known to have anti-tumor and biosurfactant properties, respectively.[18,19,20] The mechanism of dioxygen activation by nonheme iron halogenases is thought to be analogous to that of other aKG-dependent nonheme iron enzymes. The active oxidant is proposed to be a *S* = 2 oxoiron(IV)-halide species that abstracts a H-atom to form a hydroxoiron(III)-halide species and a substrate radical. In the next step, the incipient radical can undergo rebound with either the hydroxo or the halo ligand to afford respective R-OH or R-Cl products.

There has been some effort to obtain synthetic models for the oxoiron(IV)-halide intermediates of the halogenases. While these complexes serve as suitable spectroscopic models, no nonheme oxoiron(IV)-halide complex has yet been demonstrated to have the ability to transform C–H bonds into C–(Cl/Br) bonds. In this chapter, the synthesis and characterization of the *S* = 2 nonheme oxoiron(IV)-halide complexes, $[Fe^{IV}(O)(TQA)(Cl)]^+$ (**2**) and $[Fe^{IV}(O)(TQA)(Br)]^+$ (**3**), is reported. These species serve as both electronic and functional models for the enzymatic intermediates of nonheme iron halogenases.

2.2 Experimental Details

All reagents were purchased from Aldrich and used as received, unless noted otherwise. 2-(*tert*-butylsulfonyl)iodosylbenzene (2-(^{t}BuSO$_2$)C$_6$H$_4$IO) was synthesized through modification of a previous literature procedure (*Caution*: An injury was recently reported while attempting to synthesize this oxidant. This synthetic procedure should therefore be carried out with the appropriate safety precautions and protective equipment),[21,22] and the salt Fe(OTf)$_2$(CH$_3$CN)$_2$ [23] was prepared according to published procedures. The ligands TPA,[24] QBPA[17] and BQPA[17] were synthesized according to published procedures, as well as the corresponding [Fe^{II}(TPA)(MeCN)$_2$](OTf)$_2$,[25] [Fe^{II}(QBPA)(OTf)$_2$][26] and [Fe^{II}(BQPA)(OTf)$_2$] complexes.

All moisture and oxygen sensitive compounds were synthesized in a nitrogen-filled glove box. ^{1}H NMR spectra were recorded on a Bruker Avance III 500 MHz spectrometer at ambient temperature. ^{19}F NMR spectra were recorded on a Varian Inova 300 MHz spectrometer at -40 °C with trifluorotoluene as an internal standard (δ = -63.7 ppm). Elemental analysis for [Fe^{II}(TQA)(OTf)$_2$] (**1**) was performed by Atlantic Microlab (Norcross, GA). UV-vis spectra were recorded on a HP8453A diode array spectrometer equipped with a cryostat from Unisoku Scientific Instruments (Osaka, Japan). Mössbauer spectra were recorded with two spectrometers, using Janis Research Super-Varitemp dewars that allowed studies in applied magnetic fields up to 8.0T in the temperature range from 1.5 to 200K. Mössbauer spectral simulations were performed using the

WMOSS software package (SEE Co, Edina, MN). Isomer shifts are quoted relative to Fe metal at 298K.

DFT calculations were performed using Becke's three parameter hybrid (B3LYP) functional and basis set 6-311G provided by Gaussian'09 software package.[27] The initial structural model for **2** and **3** were constructed using the published DFT optimized structure of **1** by replacing the CH_3CN ligand with a Cl^- (for **2**) or a Br^- (for **3**) at the *cis* position to the oxo ligand.[28] The SCF procedure and geometry optimization were terminated upon reaching the default convergence criteria. The quadrupole splitting ΔE_Q was calculated using the property keyword of the Gaussian code and $Q(^{57}Fe) = 0.17$ barn. The ^{57}Fe isomer shift δ was evaluated from the DFT charge density at the Fe nucleus using the calibration given by Vrajmasu et al.[29]

X-ray Crystallography

A suitable crystal of the complex $[Fe^{II}(TQA)(OTf)_2]$ (approximate dimensions 0.30 x 0.20 x 0.20 mm^3) was placed onto the tip of a 0.1 mm diameter glass capillary and mounted on a Bruker APEX-II CCD diffractometer for a data collection at 173(2) K.[30] A preliminary set of cell constants was calculated from reflections harvested from three sets of 12 frames. These initial sets of frames were oriented such that orthogonal wedges of reciprocal space were surveyed. This produced initial orientation matrices determined from 201 reflections. The data collection was carried out using MoKα radiation (graphite monochromator) with a frame time of 30 seconds and a detector distance of 6.0 cm. A randomly oriented region of reciprocal space was surveyed to the extent of one sphere and to a resolution of 0.77 Å. Four major sections of frames were collected with 0.30º steps in ω at four different φ settings and a detector position of -28º in 2θ. The intensity data were corrected for absorption and decay (SADABS).[31] Final cell constants were calculated from the xyz centroids of 6852 strong reflections from the actual data collection after integration (SAINT).[32] The structure was solved using SHELXS-97[33] and refined using SHELXL-97.[33] The space group $P2_1/c$ was determined based on systematic absences and intensity statistics. A direct-methods solution was calculated which provided most non-hydrogen atoms from the E-map. Full-matrix least squares / difference Fourier cycles were performed which located the remaining non-hydrogen atoms. All non-hydrogen atoms were refined with anisotropic displacement parameters. All hydrogen atoms were placed in ideal positions and refined as riding atoms with relative isotropic displacement parameters. The final full matrix least squares refinement converged to $R1 = 0.0374$ and $wR2 = 0.0885$ (F^2, all data).

Synthesis of 2-(^{t}BuSO$_2$)C$_6$H$_4$IO (ArIO)

The synthesis of ArIO follows literature procedure up until the oxidation of 2-(*tert*-butylsulfonyl)iodobenzene to 2-(*tert*-butylsulfonyl)iodosylbenzene.[21] The previous procedure for this step involved the combination of acetic anhydride and aqueous hydrogen peroxide, which recently caused a severe explosion at Northwestern University.[22] For this reason, a new procedure was developed utilizing an alternate oxidant, Oxone, at low temperatures, to yield the desired product. As always, this reaction should only be performed by an experienced chemist with proper safety equipment.

2-(*tert*-butylsulfonyl)iodobenzene (4 g, 12.3 mmol) was added to a 200 mL round-bottom flask, submerged in a -20 °C cooling bath. A 3:1 mixture of CF_3COOH : $CHCl_3$ (50 mL) was then added to the solid, producing a clear solution. Over 30 seconds, Oxone (5.7 g, 1.5 eq, 18.5 mmol) was added to the reaction mixture, making the solution turbid. The reaction was tracked by TLC (Silica, 3:1 Hexanes:EtOAc). Upon consumption of the starting material, generally occurring within 10 – 30 minutes, the turbid solution was kept at -20 °C and placed under vacuum to remove both CF_3COOH and $CHCl_3$, leaving a yellow oil.

CH_2Cl_2 (50 mL) was added to the yellow oil to produce a cloudy slurry. This slurry was filtered, leaving a white solid and yellow filtrate. The solid was washed with CH_2Cl_2 (3 x 25 mL) and the filtrates were combined. The combined filtrate was placed under vacuum to leave a yellow oil, likely iodosylbenzene bis(trifluoroacetate). The oil was not further purified or characterized, and was instead used directly in the next step in the reaction.

The oil was immediately submerged in an ice bath and NaOH (3M) was added dropwise until the pH of the reaction mixture was highly basic (pH = 14). The addition of NaOH caused a yellow precipitate to form. The precipitate was filtered and washed with copious amounts of H_2O until the pH of the washings was neutral (pH = 7). During this washing process, the color of the solid changed from bright yellow color to a dull yellow color. Upon reaching pH 7, the solid was further washed with diethyl ether and then air dried to yield a yellow powder (Yield: 2.0 g, 50%). ^{1}H NMR is identical to what has been previously reported for this compound.

Synthesis of ArI^{18}O

ArI^{18}O was easily prepared by dissolving ArIO in CD_2Cl_2 or 2,2,2-trifluoroethanol and adding $H_2{}^{18}O$ (20 μL). The oxygen-atom exchange is rapid at room temperature (< 30 min) and can be monitored by ESI-MS. After complete oxygen-atom exchange, the organic solvent and $H_2{}^{18}O$ are removed under vacuum to leave solid ArI^{18}O as a light yellow solid.

Synthesis of tris(2-quinolylmethyl)amine (TQA)

The ligand was synthesized according to previously reported procedures,[17] up until purification of the obtained yellow oil. At this point, white crystalline product was obtained by washing the oil with acetone. The white crystals were filtered, washed with acetone and air dried to yield the desired product. (Yield: 1.2g, 55%). ^{1}H NMR is identical to what has been previously reported for this compound.

Synthesis of [Fe^{II}(TQA)(OTf)$_2$]

The preparation of **1** was carried out in a nitrogen-filled glove box. Equimolar amounts of TQA (0.50 g, 1.13 mmol) and $Fe(OTf)_2(CH_3CN)_2$ (0.50 g, 1.13 mmol) were dissolved in anhydrous acetonitrile (5 mL) and stirred for 3 hours, producing a yellow precipitate. Diethyl ether (15 mL) was then added to the reaction mixture and the solution was kept overnight at -40 °C. The yellow colored solid was then filtered off, washed with Et_2O and dried to give the title complex (**1**) (Yield, 0.67g, 75%). Single crystals suitable for X-ray diffraction study were obtained by slow diffusion of Et_2O into a concentrated solution of **1** in acetonitrile. ^{1}H-NMR (CD_3CN, 25 °C, all peaks appear as broad singlets): δ 50.6 (1H), 22.7 (1H), 1.69 (1H), 0.38 (1H), -3.4 (1H), -60.7 (1H). ^{19}F-NMR (CD_3CN, -40 °C): δ -79.8 ppm (broad singlet, 480 Hz peak full-width at half-maximum height (FWHM)). MS (+ESI): *m/z* 645.1 [$(M\text{-}OTf)^+$], 248.0 [$(M)^{2+}$]. UV/Vis (CH_3CN): l_{max} (ε) = 305 nm (13000), 375 nm (500). Anal calcd. for $C_{32}H_{24}F_6FeN_4O_6S_2.H_2O$: C, 47.30; H, 3.23; N, 6.90, S, 7.89. Found: C, 46.86; H, 3.14; N, 6.81; S, 7.87.

[$^{57}Fe^{II}(TQA)(OTf)_2$] was prepared in a similar manner using $^{57}Fe^{II}(OTf)_2.2CH_3CN$ as the metal source.

Generation of [$Fe^{IV}(O)(TQA)(CH_3CN)$]$(OTf)_2$ (1)

Under an atmosphere of nitrogen, 2-(^{t}BuSO$_2$)C$_6$H$_4$IO (ArIO, 2 equivalents, 0.003 mmol) was dissolved in 2,2,2-trifluoroethanol or CD_2Cl_2 and added to a 1.5 mL 1.0 mM acetonitrile solution of [$Fe^{II}(TQA)(OTf)_2$] at -40 °C. ^{19}F-NMR (CD_3CN, -40 °C): δ -79.9 ppm (broad singlet, 81 Hz FWHM). The same synthetic strategy was used to generate the related oxoiron(IV) complexes, [$Fe^{IV}(O)(TPA)(MeCN)$]$^{2+}$, [$Fe^{IV}(O)(QBPA)(MeCN)$]$^{2+}$, and [$Fe^{IV}(O)(BQPA)(MeCN)$]$^{2+}$ from the corresponding [$Fe^{II}(L)(OTf)_2$] starting compounds.

Generation of [$Fe^{IV}(O)(TQA)(Cl)$](OTf) (2)

Upon generation of **1** at -40 °C in acetonitrile, NBu_4Cl (1 - 2 equivalents, 0.0015 - 0.003 mmol) was dissolved in acetonitrile and added to the reaction mixture to immediately generate **2**.

Generation of [$Fe^{IV}(O)(TQA)(Br)$](OTf) (3)

Upon generation of **1** at -40 °C in acetonitrile, NBu_4Br (1 - 2 equivalents, 0.0015 – 0.003 mmol) was dissolved in acetonitrile and added to the reaction mixture to immediately generate **3**.

Generation of $[Fe^{IV}(^{18}O)(TQA)(X)](OTf)$

The ^{18}O-**1**, ^{18}O-**2** and ^{18}O-**3** isotopomers were generated analogously to **1**, **2** and **3**, substituting ArIO for $ArI^{18}O$.

2.3 Synthesis of TQA and [Fe^{II}(TQA)(OTf)$_2$]

The ligand, TQA, was synthesized in a one-pot procedure, as reported by Karlin and co-workers (Scheme 2.1). However, our procedure deviated in the purification of the crude ligand, where it was discovered that the desired compound could be obtained in pure form by washing the crude reaction mixture with acetone at room temperature.

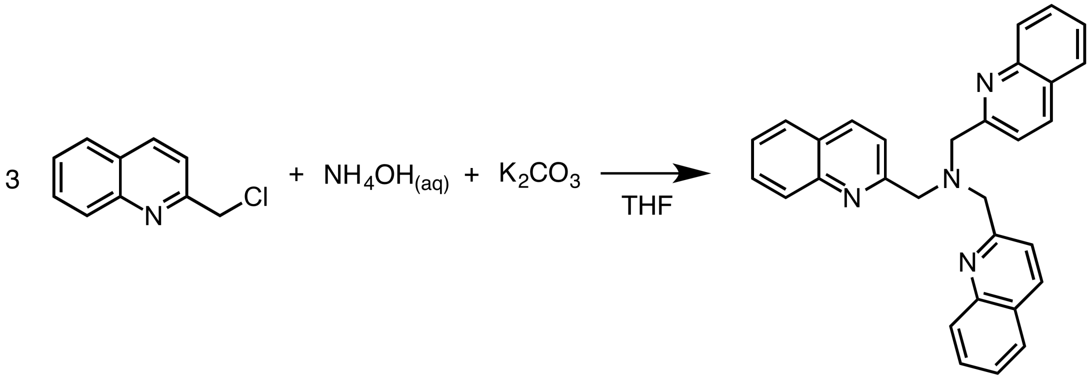

Scheme 2.1. One-pot synthesis of the ligand TQA.

The metallation of TQA with Fe^{II}(OTf)$_2$(CH$_3$CN)$_2$ in CH$_3$CN affords [Fe^{II}(TQA)(OTf)$_2$] (**1,** Scheme 2.2). Its crystal structure reveals a 6-coordinate iron(II) center (Figure 2.2 and Table 2.2), with Fe-N$_{quin}$ bonds lengths averaging 2.20 Å, consistent with a high-spin $S = 2$ iron(II) complex. ^{1}H NMR spectroscopy of [Fe^{II}(TQA)(OTf)$_2$] in CD$_3$CN reveals six broad peaks ranging from -60.7 ppm to 50.6 ppm, also consistent with the formation of a paramagnetic $S = 2$ iron(II) complex.

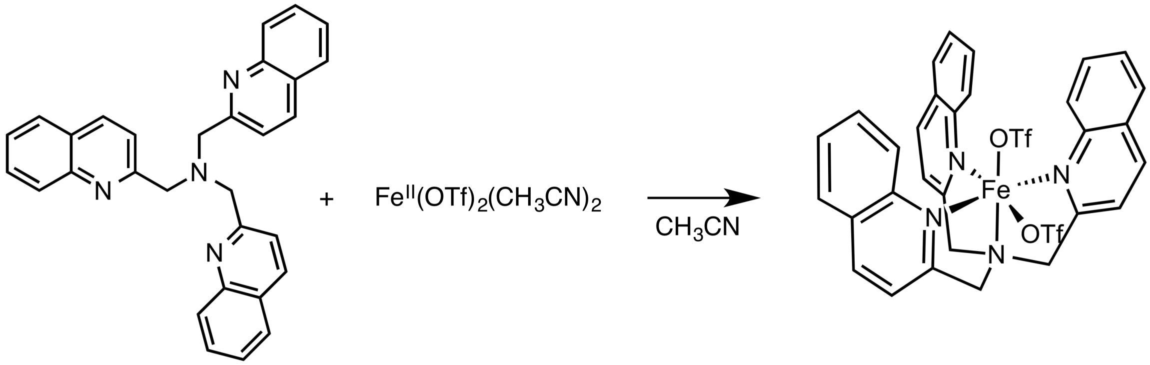

Scheme 2.2 Metallation of the TQA ligand with $Fe^{II}(OTf)_2(CH_3CN)_2$ in acetonitrile solution to yield $[Fe^{II}(TQA)(OTf)_2]$.

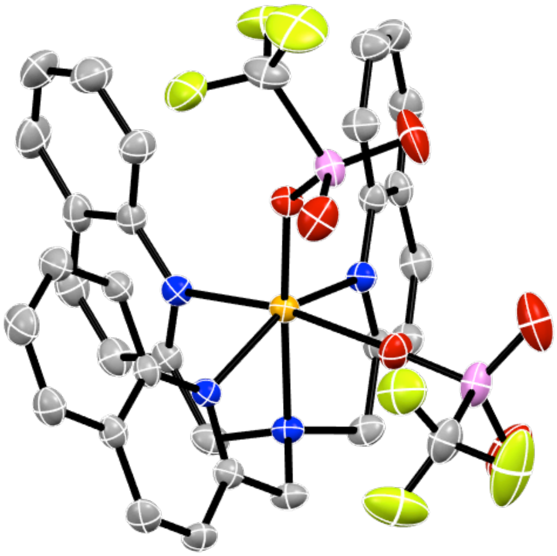

Figure 2.2 ORTEP plot of $[Fe^{II}(TQA)(OTf)_2]$ with thermal ellipsoids shown at 50% probability. All hydrogen-atoms have been removed for clarity.

Table 2.1. Crystal data and structure refinement for $[\mathrm{Fe^{II}(TQA)(OTf)_2}]$.

Identification code	13205_0m	
Empirical formula	$C_{32}\ H_{24}\ F_6\ Fe\ N_4\ O_6\ S_2$	
Formula weight	794.52	
Temperature	173(2) K	
Wavelength	0.71073 Å	
Crystal system	Monoclinic	
Space group	$P2_1/c$	
Unit cell dimensions	a = 11.0386(9) Å	α = 90°
	b = 14.1263(11) Å	β = 103.6530(10)°
	c = 21.5894(17) Å	γ = 90°
Volume	3271.4(4) $Å^3$	
Z	4	
Density (calculated)	1.613 Mg/m^3	
Absorption coefficient	0.675 mm^{-1}	
F(000)	1616	
Crystal color, morphology	yellow, block	
Crystal size	0.30 x 0.20 x 0.20 mm^3	
Theta range for data collection	1.74 to 27.50°	
Index ranges	$-14 \le h \le 14, -18 \le k \le 18, -28 \le l \le 28$	
Reflections collected	37911	
Independent reflections	7510 [*R*(int) = 0.0490]	
Observed reflections	5643	
Completeness to theta = 27.50°	99.8%	
Absorption correction	Multi-scan	
Max. and min. transmission	0.8768 and 0.8232	
Refinement method	Full-matrix least-squares on F^2	
Data / restraints / parameters	7510 / 0 / 460	
Goodness-of-fit on F^2	1.031	
Final *R* indices [I>2sigma(I)]	*R*1 = 0.0374, *wR*2 = 0.0794	
R indices (all data)	R1 = 0.0567, wR2 = 0.0885	

Largest diff. peak and hole	0.380 and -0.564 e.Å^{-3}

Table 2.2. Selected bond lengths [Å] and angles [°] for [Fe^{II}(TQA)(OTf)$_2$].

Bond lengths [Å]			
Fe(1)-N(1)	2.2155(17)	Fe(1)-O(1)	2.0450(14)
Fe(1)-N(2)	2.2308(17)	Fe(1)-O(4)	2.1965(15)
Fe(1)-N(3)	2.1954(17)		
Fe(1)-N(4)	2.1748(17)		
Bond angles [°]			
O(1)-Fe(1)-N(4)	172.98(6)	N(3)-Fe(1)-N(1)	153.99(6)
O(1)-Fe(1)-N(3)	100.64(6)	O(4)-Fe(1)-N(1)	93.24(6)
N(4)-Fe(1)-N(3)	75.52(6)	O(1)-Fe(1)-N(2)	106.13(6)
O(1)-Fe(1)-O(4)	86.16(6)	N(4)-Fe(1)-N(2)	80.02(7)
N(4)-Fe(1)-O(4)	87.80(6)	N(3)-Fe(1)-N(2)	91.12(6)
N(3)-Fe(1)-O(4)	87.79(6)	O(4)-Fe(1)-N(2)	167.65(6)
O(1)-Fe(1)-N(1)	105.36(6)	N(1)-Fe(1)-N(2)	82.40(6)
N(4)-Fe(1)-N(1)	78.55(6)		

2.4 Systematically Tuning the Spin State of a Nonheme Oxoiron(IV) Complex

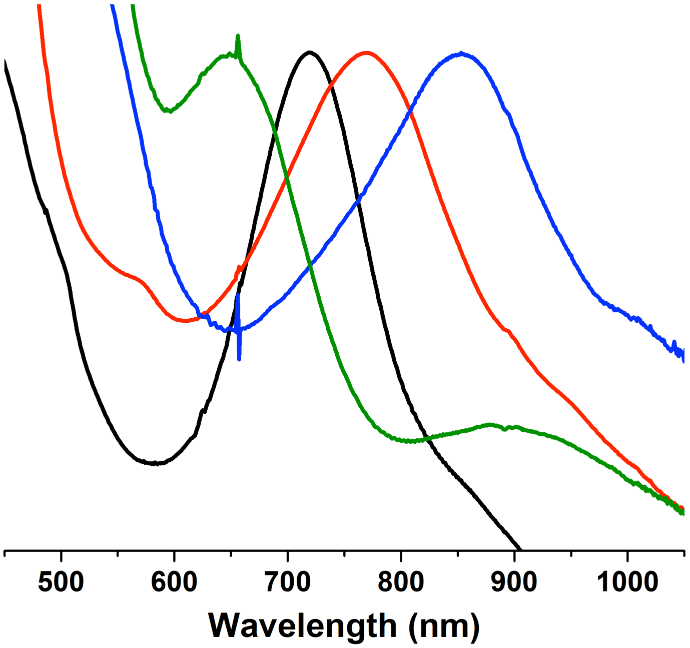

Figure 2.3. Overlaid UV-visible spectra of $[Fe^{IV}(O)(TPA)(MeCN)]^{2+}$ (black), $[Fe^{IV}(O)(QBPA)(MeCN)]^{2+}$ (red), $[Fe^{IV}(O)(BQPA)(MeCN)]^{2+}$ (blue) and **1** (green), where the λ_{max} of each complex has been normalized to clearly illustrate the distinct red-shift upon replacing pyridine rings with quinoline rings until the formation of the $S = 2$ complex **1**, which demonstrates a distinct set of UV-vis features.

One strategy to tune the spin state of $S = 1$ nonheme oxoiron(IV) complexes is to lower the energy of the d_{x2-y2} orbital by weakening the equatorial ligand field. This may be accomplished by systematically replacing the equatorial pyridine rings of the TPA ligand with weaker-field quinoline rings, where TPA is tris(2-pyridylmethyl)amine. Our starting point was the nonheme oxoiron(IV) complex $[Fe^{IV}(O)(TPA)(MeCN)]^{2+}$, which could be generated by the addition of the soluble oxygen-atom transfer agent, 2-

(^{t}BuSO$_2$)C$_6$H$_4$IO (ArIO), to the corresponding ferrous starting material, [Fe^{II}(TPA)(OTf)$_2$], at -40 °C in acetonitrile solution. This molecule was reported in 2003 and adopts an $S = 1$ ground spin state with a $\lambda_{max} = 720$ nm. Through magnetic circular dichroism (MCD) studies of other $S = 1$ nonheme oxoiron(IV) complexes,[34,35] the Solomon group has found that this near-infrared (NIR) absorption feature is associated with d-d electronic transitions, thus reflecting the strength of the ligand field.

By replacing one of the pyridine rings with a quinoline ring, the TPA ligand is converted into the QBPA ligand, where QBPA is 2-(quinolylmethyl)bis(2-pyridylmethyl)amine (Figure 2.1). The corresponding [Fe^{IV}(O)(QBPA)(MeCN)]$^{2+}$ complex was reported in 2006 and demonstrated a NIR absorption feature at 775 nm, which is red-shifted by 50 nm compared to that of [Fe^{IV}(O)(TPA)(MeCN)]$^{2+}$, indicating a weakening of the ligand field ($\Delta\nu \sim 900$ cm^{-1}) (Figure 2.3, Table 2.3).[16] However, based on the similar spectroscopic features, this weakening of the ligand field was not sufficient to enforce a spin state change from $S = 1$ to $S = 2$.

Replacing a second pyridine ring with a quinoline ring converts the QBPA ligand to BQPA, where BQPA is bis(2-quinolylmethyl)(2-pyridylmethy1)amine (Figure 2.1). The corresponding [Fe^{IV}(O)(BQPA)(MeCN)]$^{2+}$ complex is a reactive species with a NIR absorption feature at 850 nm, indicating an even further weakening of the ligand field based on the observed red-shift ($\Delta\nu \sim 1140$ cm^{-1}) in the d-d electronic transitions (Figure 2.3, Table 2.3). However, Mössbauer experiments reveal that the ground spin state remains $S = 1$, suggesting that the ligand field is not weak enough to support an $S = 2$ ground spin state.

Finally, replacing all three pyridine rings of the TPA ligand with quinoline rings forms the TQA ligand, where TQA is tris(2-quinolylmethyl)amine (Figure 2.1). Following an analogous procedure as the related nonheme oxoiron(IV) species, $[\mathrm{Fe^{IV}(O)(TQA)(MeCN)}]^{2+}$ (**1**) could be generated at -40 °C in acetonitrile solution.[28] In this case, the complex exhibits a λ_{max} = 650 nm and 900 nm, suggesting a dramatic change in the electronic nature of the nonheme oxoiron(IV) species, compared to the other nonheme oxoiron(IV) complexes in the series (Figure 2.3, Table 2.3). In fact, upon analysis by Mossbauer spectroscopy, complex **1** is found to have a $S = 2$ ground spin state, suggesting that the equatorial ligand-field has been weakened to such an extent that population of the d_{x2-y2} orbital is now more energetically favorable than pairing electrons in the d_{xy} orbital.

Table 2.3. Spectroscopic signatures of select $S = 1$ and $S = 2$ nonheme oxoiron(IV) species.

Compound	***S***	**λ_{max} (nm)**	**δ (mm/s)**	**ΔE_Q (mm/s)**	**D (cm^{-1})**	**$\nu(Fe={}^{16}O)$ (cm^{-1})**	**Ref**
$[\mathrm{Fe^{IV}(O)(TPA)(MeCN)}]^{2+}$	1	724	0.01	0.92	28 (2)	833 (-34)	25a,b
$[\mathrm{Fe^{IV}(O)(QBPA)(MeCN)}]^{2+}$	1	775	-	-		-	16
$[\mathrm{Fe^{IV}(O)(BQPA)(MeCN)}]^{2+}$	1	850	0.04	0.85		-	
1	2	650, 900	0.24	-1.05	17 (1)	838 (-35)	28
2	2	625, 875	0.22	0.96		827 (-35)	
3	2	625, 875	0.21	0.94		828 (-37)	
$[\mathrm{Fe^{IV}(O)(TMG_2dien)(MeCN)}]^{2+}$	2	380, 805	0.08	0.38	4.5 (5)	807 (-34)	11
$[\mathrm{Fe^{IV}(O)(TMG_2dien)(Cl)}]^{+}$	2	385, 803,825	0.08	0.41	4.0 (5)	810 (-35)	11
TauD-***J***	2	318	0.30	-0.90	10.5	821 (-34)	36a,b
$\mathrm{Fe^{IV}O}$ in SyrB2-Cl	2	318	0.23, 0.30	0.76, 1.09			20

$Fe^{IV}O$ in CytC3-Cl	2	318	0.22, 0.30	0.70, 1.09	8.1		18
$Fe^{IV}O$ in CytC3-Br	2		0.23, 0.31	0.81, 1.06			19

2.5 Characterization of *S* = 2 Nonheme Oxoiron(IV) Complexes

2.5.1 *UV-Visible-NIR spectroscopy*

As noted, treatment of $[Fe^{II}(TQA)(OTf)_2]$ with ArIO in acetonitrile solution at -40 °C leads to the formation of the highly reactive intermediate **1** that exhibits a near-UV shoulder at 400 nm and weak bands at 650 (ε_M 300) and 900 (ε_M 75) nm (Figure 2.3, Figure 2.4, black). The 400 nm shoulder has been tentatively assigned to an oxo-to-Fe charge transfer band, while the bands at 650 nm and 900 nm are likely to be d-d transitions, based on previous studies on $S = 1$ nonheme oxoiron(IV) complexes and the $S = 2$ nonheme oxoiron(IV) complex $[Fe^{IV}(O)(TMG_3tren)]^{2+}$.[34,35,37] Complex **1** demonstrates a $t_{1/2}$ at -40 °C of 15 minutes, hinting at the high reactivity of this molecule.

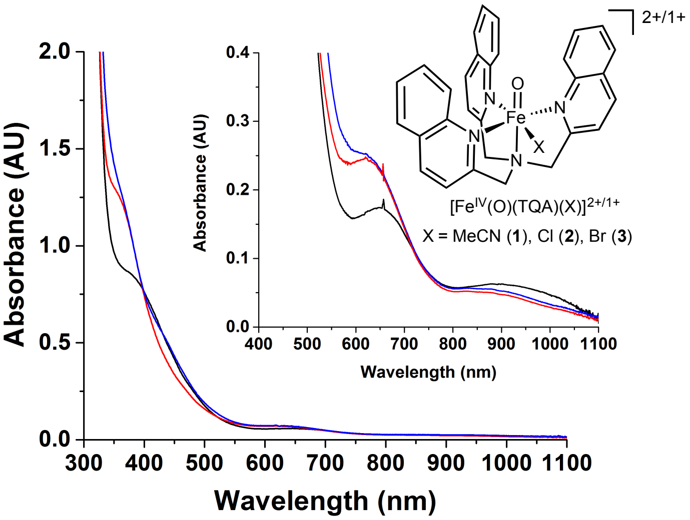

Figure 2.4. UV-visible spectrum of a 0.25 mM solution of **1** (black), **2** (red) and **3** (blue) in acetonitrile at -40 °C, with a 1.0 mM solution of **1** (black), **2** (red) and **3** (blue) focused on the near-IR region shown in the inset.

Addition of 1 equiv. NBu_4X (X = Cl or Br) to **1** in acetonitrile at -40 °C initiates ligand exchange to afford new oxoiron(IV) complexes, $[Fe^{IV}(O)(TQA)(Cl)]^+$ (**2**) and $[Fe^{IV}(O)(TQA)(Br)]^+$ (**3**), respectively (Figure 2.4). UV-vis titration experiments (Figure 2.5) show that 1 equiv. halide is sufficient to generate these new species fully.

The electronic spectra of **2** and **3** display weak bands at 625 nm ($\varepsilon = 460\ M^{-1}\ cm^{-1}$) and 875 nm ($\varepsilon = 110\ M^{-1}\ cm^{-1}$), which are both blue-shifted relative to the corresponding features of **1** (Figure 2.4). Similarly, a small blue shift is observed upon replacement of the solvent ligand in the $S = 2$ $[Fe^{IV}(O)(TMG_2dien)(MeCN)]^{2+}$ complex with chloride.[11] In contrast, $S = 1$ $[Fe^{IV}(O)(L)(MeCN)]^{2+}$ complexes with L = TPA[38] or PyTACN[39] (where PyTACN is 1,4-dimethyl-7-(2 -pyridylmethyl)-1,4,7-triazacyclonane) exhibit near-IR features that are red shifted by 50-80 nm upon halide addition (Table 2.4), which can be rationalized by the fact that chloride and bromide anions are weaker-field ligands than acetonitrile. An explanation for the observed blue shift from **1** to **2** and **3** will require a better understanding of the electronic spectra of this new family of $S = 2$ oxoiron(IV) complexes. In addition, the intense near-UV feature at 400 nm also blue-shifts upon formation of **2** and **3** and gains in intensity. Finally, **2** and **3** have a half-life of approximately 5 minutes at -40 °C, decaying three-fold faster than **1**.

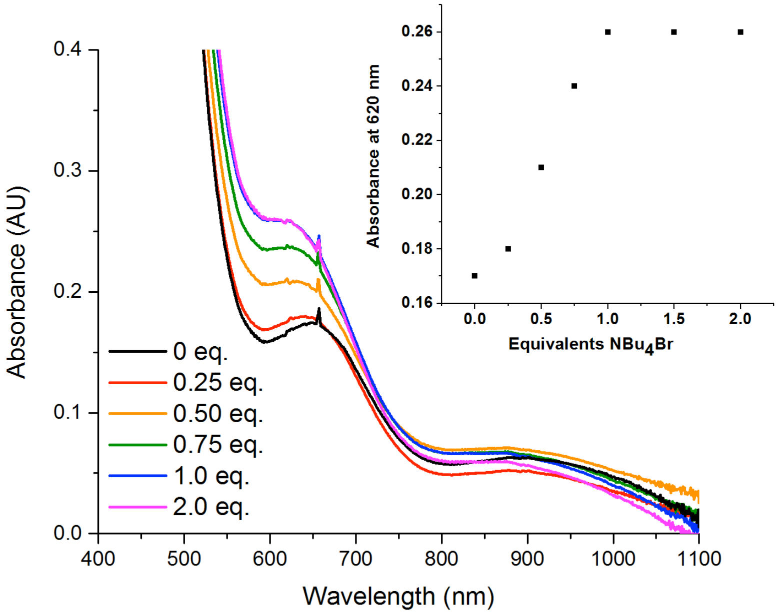

Figure 2.5. Overlaid UV-visible spectra of the addition of NBu_4Br (varying equivalents) to solutions of **1** in acetonitrile at -40 °C to form **3**. Inset is a plot of the absorbance at 620 nm versus equivalents of NBu_4Br, revealing 1 equivalent of NBu_4Br is sufficient to generate **3** in full yield.

2.5.2 *Electrospray ionization mass spectrometry*

Electrospray ionization mass spectrometric (ESI-MS) analysis of **1** supports its formulation as $[Fe^{IV}(O)(TQA)]^{2+}$, with a peak observed at m/z 256.1 (Figure 2.6). However the isotope distribution pattern suggests contamination with $[Fe^{III}(OH)(TQA)]^{2+}$ (m/z 256.6), due to the instability of **1** (Figure 2.6). Indeed the dominant feature in its ESIMS spectrum is a peak at m/z 662 that corresponds to $[Fe^{III}(OH)(TQA)(O_3SCF_3)]^+$ (Figure 2.7). Also present is a peak at m/z 676 that corresponds to $\{[Fe^{III}(OH)(TQA)(OTf)] + O - 2H\}^+$, indicating the oxidation of one TQA CH_2 group to a carbonyl. This ligand oxidation is further probed in the self-decay of complex **1** (*vide infra*, chapter 3).

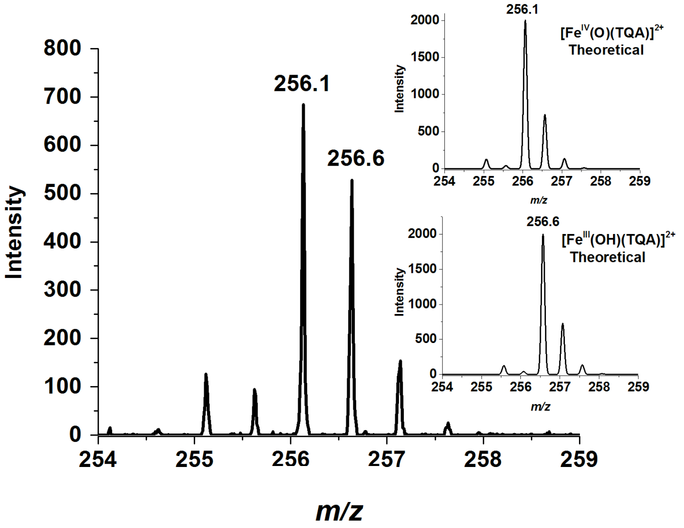

Figure 2.6 Highlight of the ESI-MS of **1** near 256 *m/z*, corresponding to a mixture of molecular ions [Fe^{IV}(O)(TQA)]$^{2+}$ and [Fe^{III}(OH)(TQA)]$^{2+}$. The theoretical isotope distribution patterns for both molecular ions are shown in the inset.

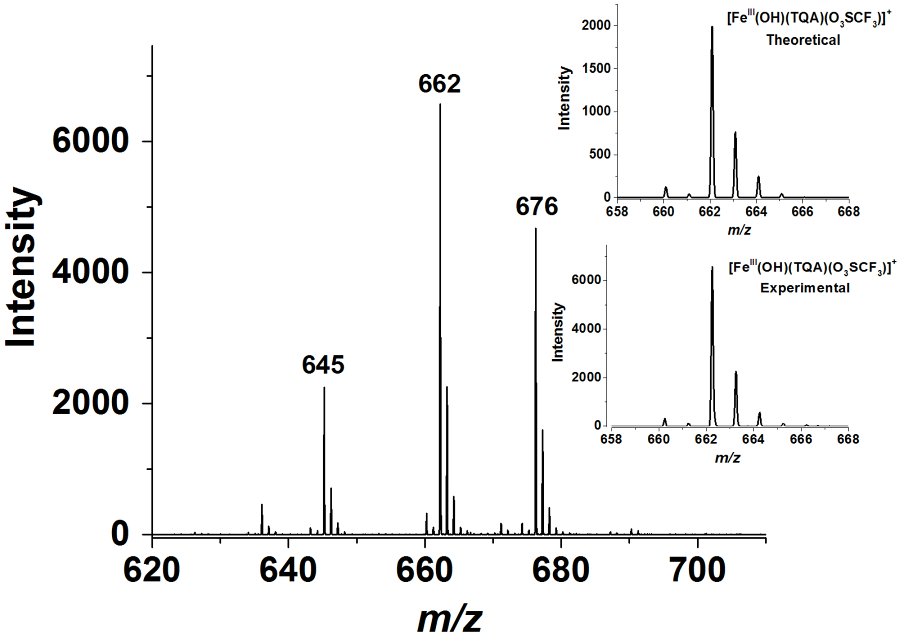

Figure 2.7 ESI- MS of **1**; the peak at *m/z* = 645 corresponds to the molecular ion [Fe^{II}(TQA)(O$_3$SCF$_3$)]$^+$, the peak at *m/z* = 662 to [Fe^{III}(OH)(TQA)(O$_3$SCF$_3$)]$^+$, and the peak at *m/z* = 676 to [Fe^{III}(OH)(*TQA)(O$_3$SCF$_3$)]$^+$, where a –CH$_2$ group on the TQA ligand has been oxidized to a carbonyl. The theoretical and exp. isotope distribution for [Fe^{III}(OH)(TQA)(O$_3$SCF$_3$)]$^+$ are shown in the inset.

No signals for the corresponding nonheme oxoiron(IV)-halide complexes of **2** and **3** could be observed and only signals for $[\mathrm{Fe^{III}(OH)(TQA)(Cl)}]^+$ and $[\mathrm{Fe^{III}(OH)(TQA)(Br)}]^+$ were visible (Figure 2.8). This may be rationalized by the three-fold shorter lifetime of complexes **2** and **3** compared to complex **1**.

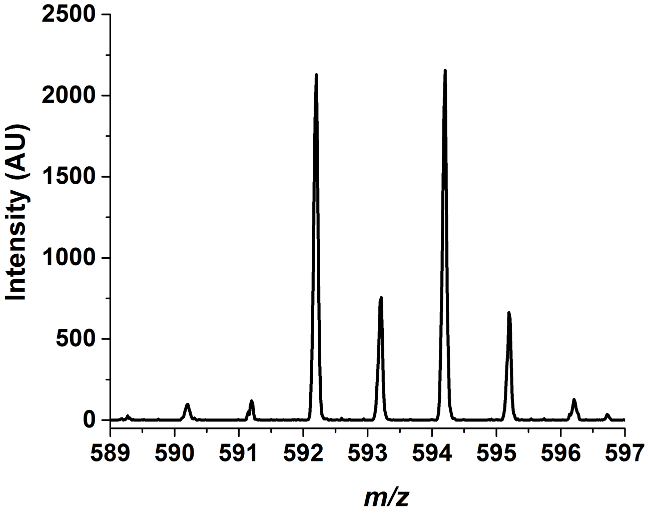

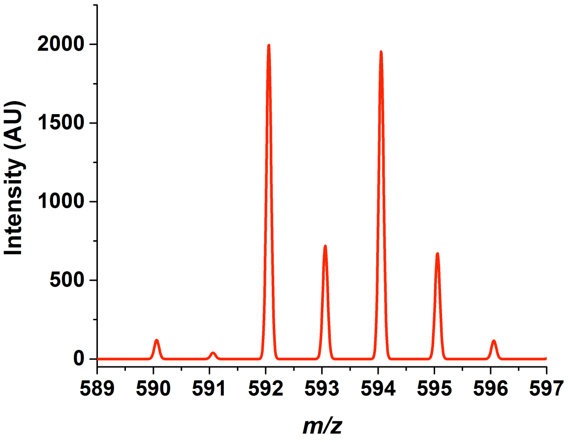

Figure 2.8. Top: Highlight of the experimental ESI-MS of **3** near 592 *m/z*, corresponding to the $[\mathrm{Fe^{III}(OH)(Br)(TQA)}]^+$ ion. **Bottom**: Theoretical isotope distribution pattern for $[\mathrm{Fe^{III}(OH)(Br)(TQA)}]^+$.

2.5.3 *Resonance Raman Spectroscopy*

Vibrational evidence for the Fe^{IV}=O unit in complexes **1** – **3** was provided by resonance Raman spectroscopy. Initial attempts at probing the oxo-to-Fe^{IV} charge transfer band in the UV region with 413.1 nm excitation of a frozen solution of **1** did not lead to any vibrational signals, likely due to decomposition of the oxoiron(IV) complex from the high energy of the laser source. However, excitation of **1** with a lower-energy laser with λ_{exc} = 514.5 nm led to the successful observation of a resonance-enhanced Raman vibration at 838 cm^{-1}, which shifts to 803 cm^{-1} upon ^{18}O-labeling of **1**, as expected for the ν(Fe=O) mode (Figure 2.9, Table 2.3). Notably this value is similar to the Fe=O stretching frequencies found for $S = 1$ nonheme oxoiron(IV) complexes $[Fe^{IV}(O)(N4Py)]^{2+}$ and $[Fe^{IV}(O)(TMC)(MeCN)]^{2+}$ (824 cm^{-1} and 839 cm^{-1}, respectively),[7] consistent with the notion that the Fe^{IV}=O vibrational frequency should be independent of the oxoiron(IV) spin state.

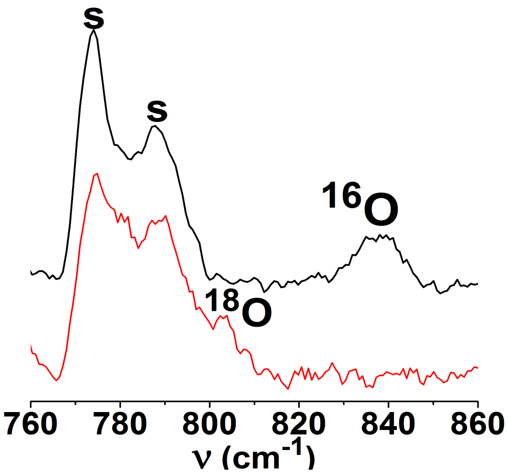

Figure 2.9. Resonance Raman spectra (λ_{ex} = 514.5 nm, 60 mW power) of $[^{16}O]$-**1** (top, black) and $[^{18}O]$-**1** (bottom, red) in frozen CH_3CN solution.

Upon replacement of the bound MeCN ligand with the halide anions, Cl^{-1} and Br^{-1}, the ν(Fe=O) mode shifted from 838 cm-1 to 827 cm^{-1} and 828 cm^{-1}, respectively, representing a downshift of ~10 cm^{-1} relative to that of **1** (Table 2.3, Figures 2.10 and 2.11, respectively). ^{18}O-labeling of **2** and **3** elicits respective downshifts of 35 and 37 cm^{-1}, consistent with the 36-cm^{-1} shift calculated for an Fe=O vibration by Hooke's law (Figures 2.10 and 2.11). These ν(Fe=O) values are remarkably close to the frequencies predicted by DFT calculations for the Fe^{IV}(O)Cl and Fe^{IV}(O)Br intermediates of the nonheme iron halogenase enzyme, SyrB2 (824 cm^{-1} and 825 cm^{-1}).[40]

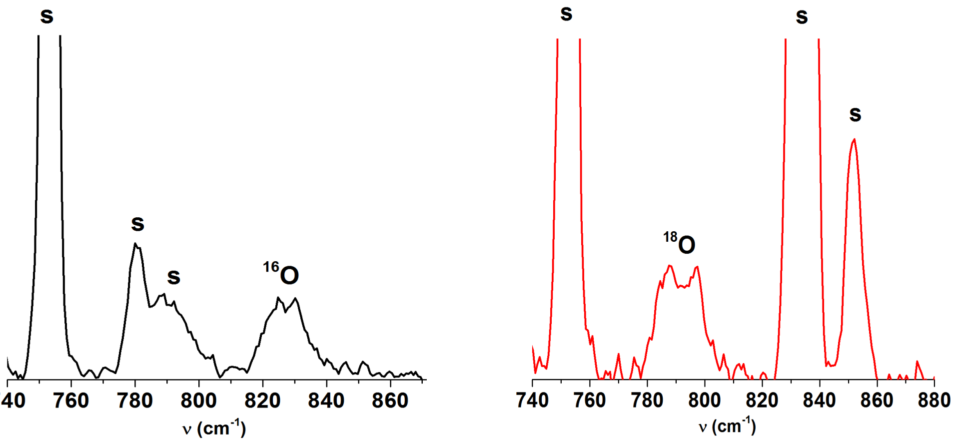

Figure 2.10. (Left) Resonance Raman spectrum (λ_{max} = 514.5 nm, 60 mW power) of [^{16}O]**2** in frozen CH_3CN solution, revealing a non-solvent peak at 827 cm^{-1}. "S" denotes solvent peaks. (**Right**) Resonance Raman spectrum (λ_{max} = 514.5 nm, 60 mW power) of [^{18}O]**2** in frozen CD_3CN solution, revealing a non-solvent peak at 792 cm^{-1}. The solvent was switched from CH_3CN to CD_3CN to prevent overlap with solvent peaks.

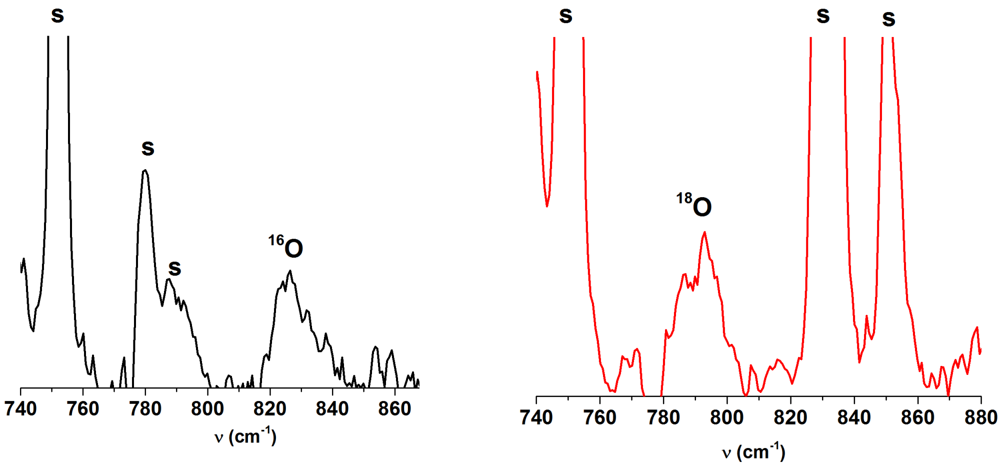

Figure 2.11. (Left) Resonance Raman spectrum (λ_{max} = 514.5 nm, 60 mW power) of [^{16}O]**3** in frozen CH_3CN solution, revealing a non-solvent peak at 828 cm^{-1}. "S" denotes solvent peaks. **(Right)** Resonance Raman spectrum (λ_{max} = 514.5 nm, 60 mW power) of [^{18}O]**3** in frozen CD_3CN solution, revealing a non-solvent peak at 791 cm^{-1}. The solvent was switched from CH_3CN to CD_3CN to prevent overlap with solvent peaks.

2.5.4 *X-Ray Absorption Spectroscopy*

The short lifetimes of the $S = 2$ nonheme oxoiron(IV) complexes **1** – **3** have prevented the growth of single crystals and structure analysis by X-ray diffraction methods. Therefore, structural information was instead obtained from X-ray absorption spectroscopy (XAS) experiments. The X-ray absorption near edge structure (XANES) of complex **1** reveals an edge-energy of 7124.4 eV, which is ~2 eV higher than the starting [Fe^{II}(TQA)(OTf)$_2$] compound, consistent with the assignment of the +4 oxidation state (Table 2.4). The XANES also revealed a pre-edge energy for **1** of 26.5 units, much larger than the pre-edge area of 5.1 for the starting [Fe^{II}(TQA)(OTf)$_2$] compound, suggesting the environment for **1** significantly deviates from centrosymmetry, likely due to the short Fe^{IV}=O bond (Table 2.4). Furthermore, XANES on a fully-decayed sample of **1** also revealed a small pre-edge area of 5.0, confirming that complex **1** is responsible for producing the large pre-edge area (Table 2.4).

Table 2.4 XANES data on the *S* = 2 oxoiron(IV) complexes **1** – **3**.

Compound	Edge Energy (eV)	Pre-edge Energy (eV)	Total Pre-edge Area
$[Fe^{II}(TQA)(OTf)_2]$	7122.2	7112.4, 7114.4	5.1
1	7124.4	7114.0, 7115.3, 7118.2	26.5
1 decay	7123.4	7112.4 7114.4	5.0
2	7123.2	7113.3, 7115.1	26
3	7123.2	7113.6, 7115.4	25

Analysis of the extended x-ray absorption fine-structure (EXAFS) for **1** reveals an oxygen scatterer at 1.65 Å, which is consistent with the Fe^{IV}=O unit. A shell of nitrogen scatterers at 2.18 Å is also observed, likely assigned to the Fe-N_{quin} bonds (Figure 2.12a, Table 2.5). However, the EXAFS data also illustrates a scatter at 1.93 Å that could not be identified, which may be fit to either a nitrogen or an oxygen scatterer.

Since EXAFS is an averaging technique and complex **1** is only generated in 70% yield, the short 1.93 Å scatterer may be due to the 30% decay products present in the reaction mixture. To test this hypothesis, complex **1** was allowed to fully decay and EXAFS experiments were then run on the decayed sample. The decayed sample revealed a prominent scatterer at 1.9 Å (Figure 2.12b, Table 2.5), suggesting that this impurity is likely to be present in the EXAFS spectrum of **1**, as well as those for **2** and **3**.

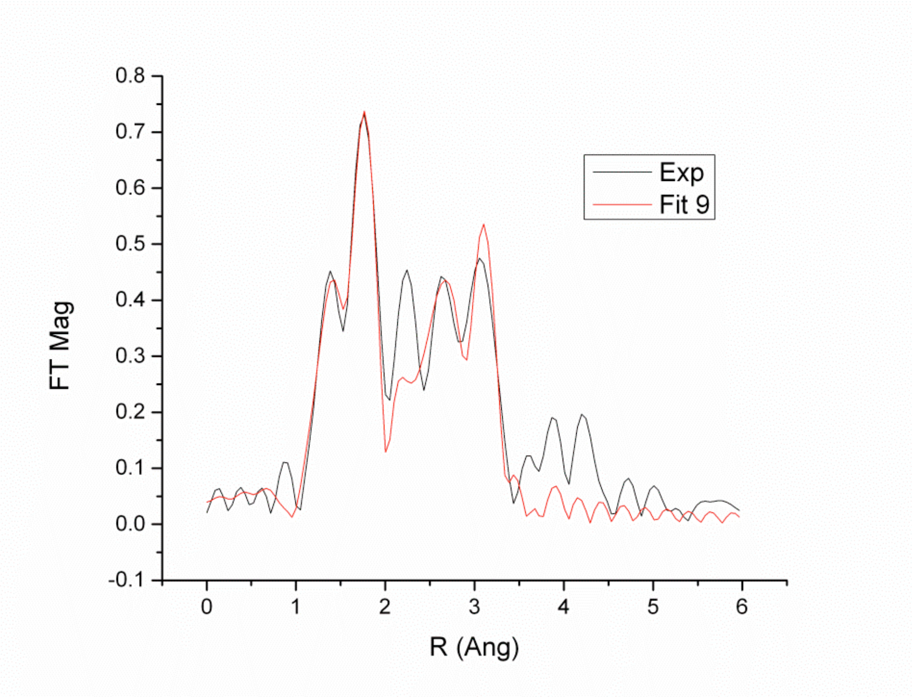

Figure 2.12a. EXAFS data for complex **1**, where the black is the experimental data and the red are the results from the EXAFS fitting.

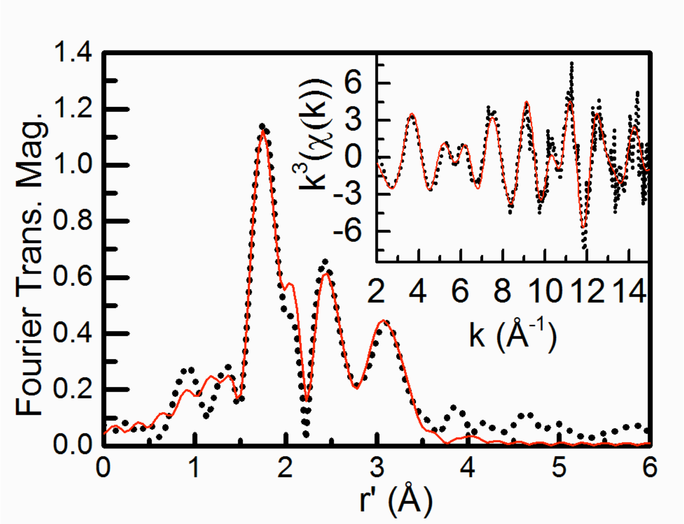

Figure 2.12b. EXAFS data for the fully decayed complex **1**, where the black is the experimental data and the red are the results from the EXAFS fitting.

Table 2.5 EXAFS fitting to unfiltered EXAFS data for **1** and **1** decay using Feff phase and amp. parameters (Å).

Complex	Fe-N			Fe-O			Fe-C								
#	**N**	**R**	**σ^2**	**N**	**R**	**σ^2**	**N**	**R**	**σ^2**	**N**	**R**	**σ^2**	**E_0**	**F**	**F'**
1 (MeCN)	**1 4.3**	**1.934 2.182**	**6.6 5.9**	**0.7**	**1.647**	**6.7**	**6 6 6**	**2.997 3.265 3.517**	**3.2 4.0 2.8**				**0.32**	**238**	**501**
1 decay	**4**	**2.150**	**1.6**	**2**	**1.886**	**8.0**	**6 4 6**	**2.924 3.250 3.487**	**2.3 5.1 1.3**				**-9.25**	**286**	**437**

k range = 2-15 Å^{-1}, resolution = 0.12 Å, back transform range ~, σ^2 = mean-squared deviation in units of 10^{-3} Å ^{2}. Scale Factor S_0^2 = 0.9. Goodness-of-fit = F calculated as

$$F = \sqrt{\sum k^6(\chi_{\exp} - \chi_{calc})^2} \ . \ F' = \sqrt{\sum k^6(\chi_{\exp} - \chi_{calc})^2 / \sum k^6 \chi_{\exp}{}^2} \ .$$

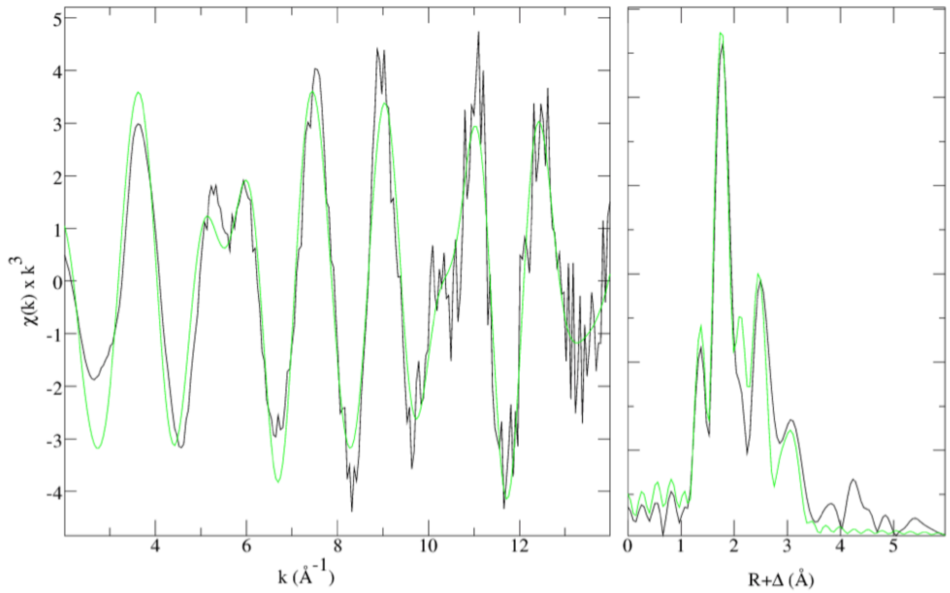

Figure 2.13. Left: EXAFS experimental data (black line) and the fitting results (green line) for complex **2**. **Right**: Fourier transform of the experimental data (black line) and the fitting results (green line). Transform is from 2-14 k.

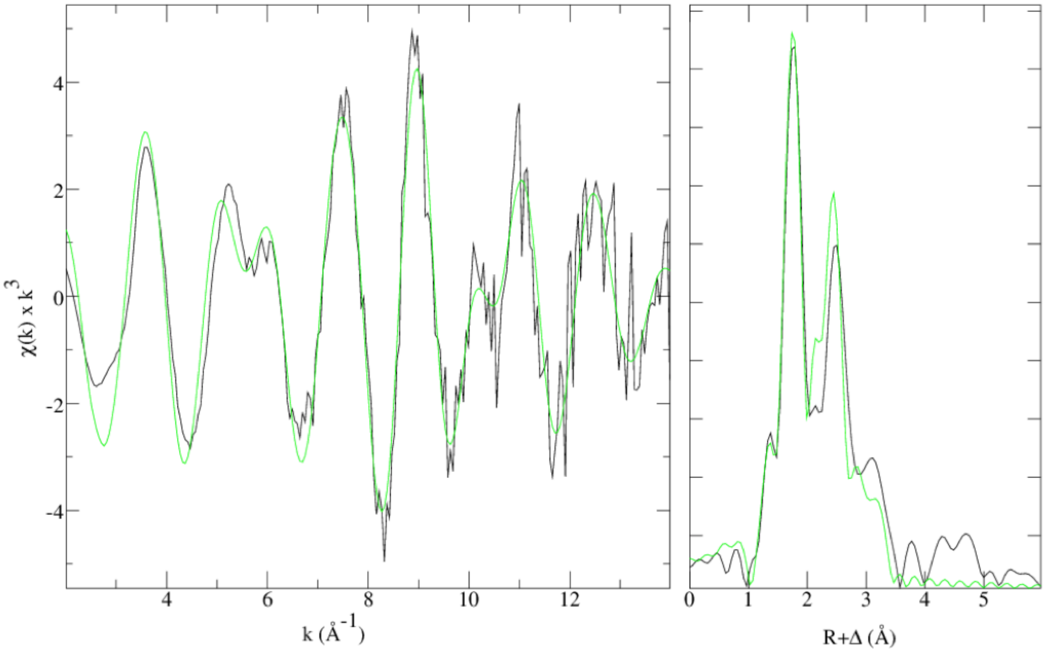

Figure 2.14. Left: EXAFS experimental data (black line) and the fitting results (green line) for complex **3**. **Right:** Fourier transform of the experimental data (black line) and the fitting results (green line). Transform is from 2-14 k.

Table 2.6. EXAFS fitting to unfiltered EXAFS data for **2** and **3** using Feff phase and amp. parameters (Å).

Complex	Fe-N			Fe-O			Fe-C			Fe-X					
#	N	R	σ^2	N	R	σ^2	N	R	σ^2	N	R	σ^2	E_0	F	F'
2(Cl)	**4** **2**	**2.15** **1.93**	**3.2** **4.2**	**0.6**	**1.66**	**7.4**	**6**	**2.96**	**3.4**	**1**	**2.33**	**7.3**	**-7.18**	**151**	**380**
3(Br)	**4** **2**	**2.17** **1.91**	**3.7** **8.6**	**0.6**	**1.64**	**10.3**	**6**	**2.96**	**3.1**	**1**	**2.50**	**10.2**	**-5.25**	**121**	**373**

k range = 2-14 $Å^{-1}$, resolution = 0.13 Å, σ^2 = mean-squared deviation in units of 10^{-3} $Å^2$. Scale Factor S_0^2 = 0.9. Goodness-of-fit = F calculated as $F = \sqrt{\sum k^6(\chi_{\exp} - \chi_{calc})^2}$.

$F' = \sqrt{\sum k^6(\chi_{\exp} - \chi_{calc})^2 / \sum k^6 \chi_{\exp}^{\ 2}}$.

Similarly, XAS experiments were carried out on complexes **2** and **3** (Table 2.4). Notably, the edge energies were found to be 1 eV lower than that found for **1**. The same observation was made when comparing the *S* = 1 complexes, $[Fe^{IV}(O)(TPA)(MeCN)]^{2+}$

and its halide-substituted analogues, $[Fe^{IV}(O)(TPA)(Cl)]^+$ and $[Fe^{IV}(O)(TPA)(Br)]^+$, suggesting that the decrease in edge energy is likely associated with halide binding to the Fe^{IV} center.[38] From the EXAFS data, **2** and **3** also reveal a short scatterer at 1.66 Å and 1.64 Å, respectively, consistent with the Fe^{IV}=O unit (Figure 2.13 and 2.14, Table 2.6). As expected, the decay product is visible with a scatterer at 1.9 Å in both spectra. Complexes **2** and **3** also demonstrate a scatterer at 2.33 Å and 2.50 Å, corresponding to the Fe^{IV}-Cl and Fe^{IV}-Br bonds. These distances are consistent with the EXAFS-derived distances of 2.31 Å and 2.43 Å measured for the oxoiron(IV)-halide intermediates of SyrB2-Cl and CytC3-Br, respectively.[40] In addition, these distances nicely match the DFT-calculated distances of 2.36 Å and 2.51 Å for the Fe^{IV}-Cl and Fe^{IV}-Br bonds of **2** and **3**, respectively (*vide infra*).

2.5.5 *Mössbauer Spectroscopy*

The zero field spectrum of **1** exhibits a quadrupole doublet (~70% of Fe) with $\Delta E_Q = -1.05$ mm/s and isomer shift $\delta = 0.24$ mm/s (Table 2.3, Figure 2.15). The remainder of the Fe is composed of 18% mononuclear high-spin Fe(III) that presumably corresponds to the $[Fe^{III}(OH)(L)]^{2+}$ species observed in the ESI-MS spectrum (Figure 2.7) and 12% high-spin diferric complex ($\delta = 0.45$ mm/s, $\Delta E_Q = +1.90$ mm/s). Notably, **1** is the first synthetic high-spin oxoiron(IV) complex to have an isomer shift that falls within the range of values found for the enzymatic oxoiron(IV) intermediates (0.22–0.30 mm s^{-1}, Table 2.3). Furthermore, among synthetic oxoiron(IV) complexes characterized thus far, the magnetic hyperfine parameters deduced for **14** from the analysis of high-field

Mössbauer data (Figure 2.15)[28] most closely resemble those found for TauD-***J*** [36] and the corresponding intermediate for prolyl 4-hydroxylase,[41] making complex **1** the closest electronic model for these high-spin oxoiron(IV) enzyme intermediates to date.[28]

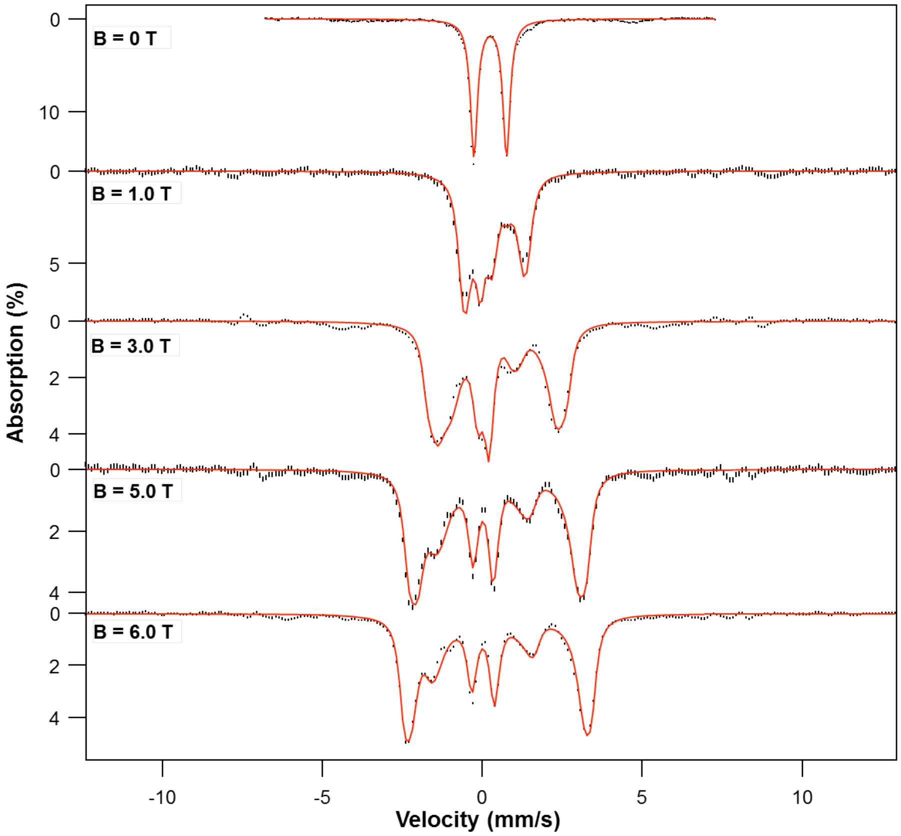

Figure 2.15. 4.2 K Mössbauer spectra of **1**, recorded in parallel applied magnetic fields of 0 T, 1 T, 3 T, 5 T, and 6 T. The black dashed curves are difference spectra obtained after subtraction of 12% diiron(III) and ~18% mononuclear high-spin iron(III) contaminants. The red curves are simulations of **1** prepared using the $S = 2$ spin Hamiltonian.

The Mössbauer analysis of **2** and **3** at 4.2 K shows quadrupole doublets for the oxoiron(IV) centers, respectively representing 65% and 70% of the iron in the samples, with parameters similar to those of **1**[28] (Table 2.3, Figures 2.16 and 2.17). Monoferric and diferric byproducts make up the balance of the iron in the samples, which became more evident in the high-field spectra (Figure 2.16 and 2.17, bottom). Complexes **2** and **3** exhibit isomer shifts of 0.22 and 0.21 mm/s, quite close to those determined for **1** with an isomer shift of 0.24 mm/s.[28] Mössbauer spectra were also collected for a fully decayed sample of complex **3** in the absence and presence of substrate, toluene and cyclohexane, revealing only monoferric and diferric products (Figure 2.18).

As noted earlier, the isomer shifts of **1**, **2**, and **3** are in fact quite close to those determined for nonheme enzyme intermediates with $S = 2$ oxoiron(IV) centers, which range from 0.22 to 0.30 mm/s (Table 2.4). Other synthetic $S = 2$ oxoiron(IV) centers have isomer shifts out of this range, namely 0.38 mm/s for the $[Fe^{IV}(O)(OH_2)_5]^{2+}$ ion characterized by Bakac[14] and 0.10 mm/s and below for oxoiron(IV) complexes with tripodal N-rich ligands that enforce trigonal bipyramidal geometry described by the Borovik, Chang and Que groups (Table 2.4).[12,13,10] Interestingly, the oxoiron(IV)-halide intermediates of CytC3 and SyrB2 each exhibit two quadrupole doublets with distinct isomer shifts, one at 0.30 mm/s that matches that of the prototypical TauD-***J*** enzyme intermediate and the other at 0.23 mm/s, approaching the values for **2** and **3** (Table 2.4). As has been pointed out, TQA is the only polydentate ligand thus far that serves as a good electronic mimic for the iron coordination environments of TauD, CytC3, and SyrB2.[9]

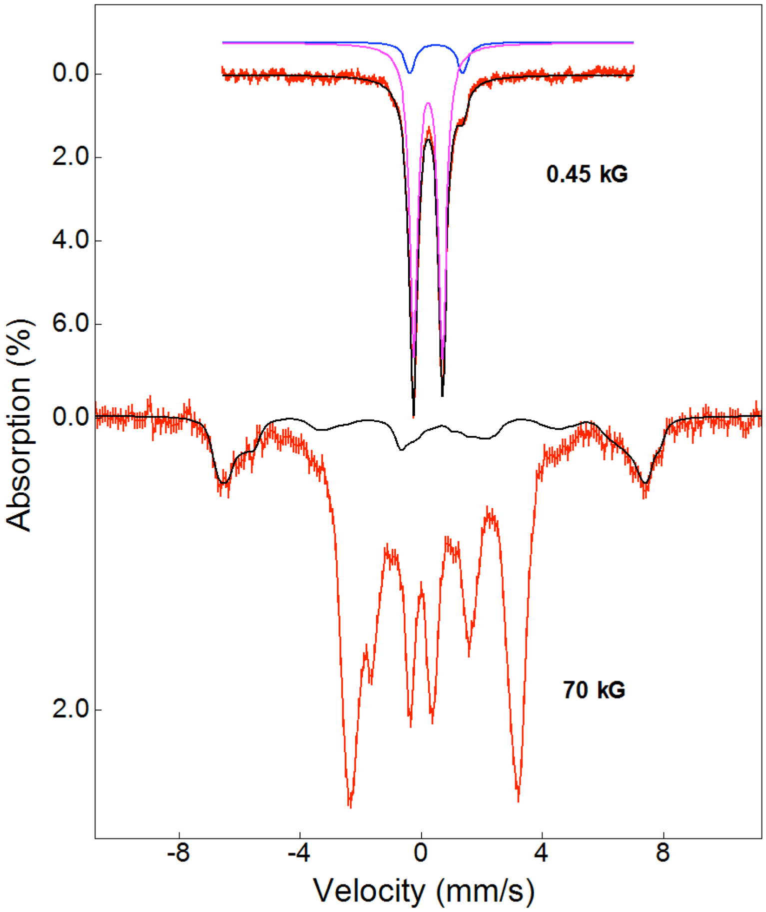

Figure 2.16. 4.2 K Mössbauer spectra of the sample containing **2** under different applied magnetic fields as indicated in the figure. Top: the low field spectrum (red) and the spectral simulation (black) containing $Fe^{IV}=O$ species with δ = 0.22 mm/s, ΔE_Q = 0.96 mm/s representing 70% of the total iron (magenta) and diferric decay product with δ = 0.5 mm/s, ΔE_Q = 1.75 mm/s representing 10% of the total iron (blue); Bottom: the high field spectrum (red) and the spectral simulation (black) of mononuclear high-spin ferric species representing 18% of the total iron.

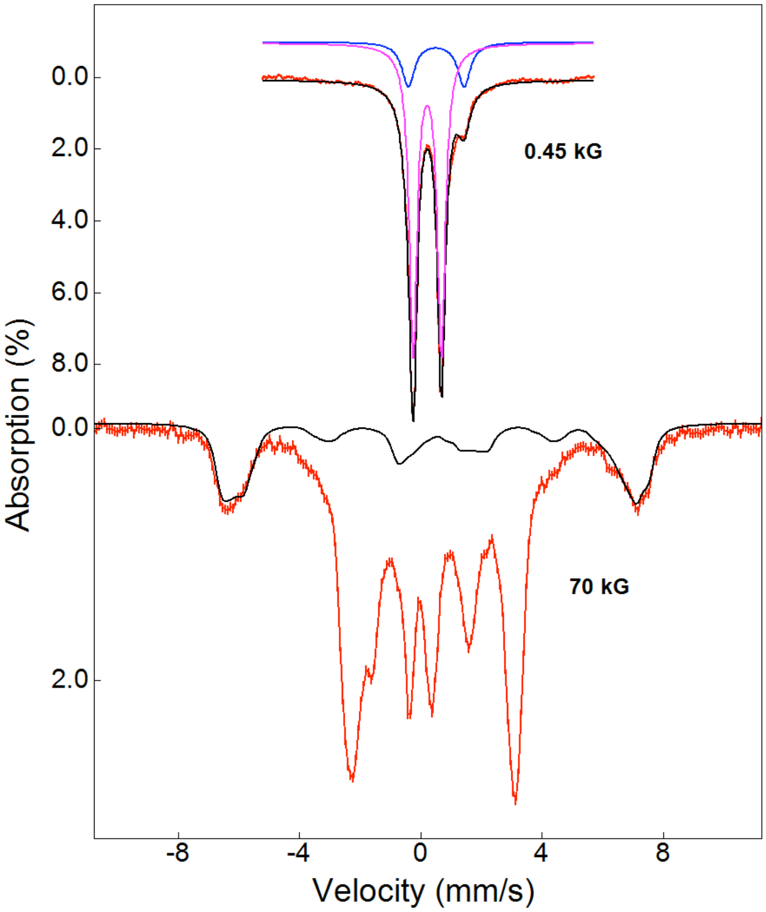

Figure 2.17. 4.2 K Mössbauer spectra of the sample containing **3** under different applied magnetic fields as indicated in the figure. Top: the low field spectrum (red) and the spectral simulation (black) containing $Fe^{IV}=O$ species with $\delta = 0.21$ mm/s, $\Delta E_Q = 0.94$ mm/s representing 65% of the total iron (magenta) and diferric decay product with $\delta = 0.5$ mm/s, $\Delta E_Q = 1.85$ mm/s representing 12% of the total iron (blue); Bottom: the high field spectrum (red) and the spectral simulation (black) of mononuclear high-spin ferric species representing 22% of the total iron.

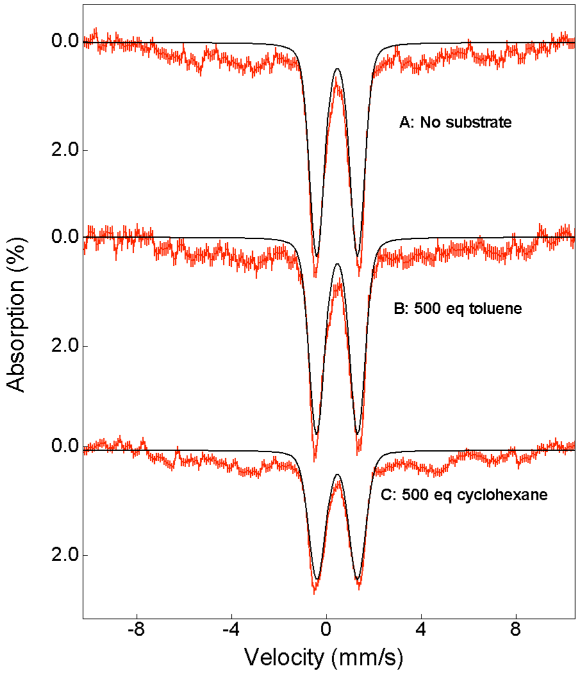

Figure 2.18. Mössbauer spectra of samples containing fully-decayed Fe^{IV}=O species, **3**, with and without the presence of substrates as indicated in the figure. Red vertical bars: experimental data; Black solid lines: spectral simulations using a quadrupole doublet with $\delta = 0.45$ mm/s, $\Delta E_Q \sim 1.70$ mm/s. This quadrupole doublet, representing ~ 56% of the total iron in the sample, is typical diferric species. The rest of the absorption observed as broad baseline is mononuclear high-spin ferric species. All of the spectra were recorded under 0.45 kG (parallel) magnetic field and 4.2 K.

2.5.6 *DFT Calculations*

Unfortunately, the lack of x-ray crystallographic data makes the absolute structure of **1** difficult to determine. Indeed, there are three possible structures for complex **1** including $[Fe^{IV}(O)(TQA)]^{2+}$ in which the oxoiron(IV) center adopts a 5-coordinate trigonal bipyramidal geometry, $[Fe^{IV}(O)(TQA)(OTf)]^{+}$ in which the oxoiron(IV) center adopts a 6-coordinate pseudo-octahedral geometry with triflate bound in the sixth-coordination site, and $[Fe^{IV}(O)(TQA)(MeCN)]^{2+}$ in which the oxoiron(IV) center also adopts a 6-coordinate pseudo-octahedral geometry with acetonitrile bound in the sixth-coordination site (Figure 2.19).

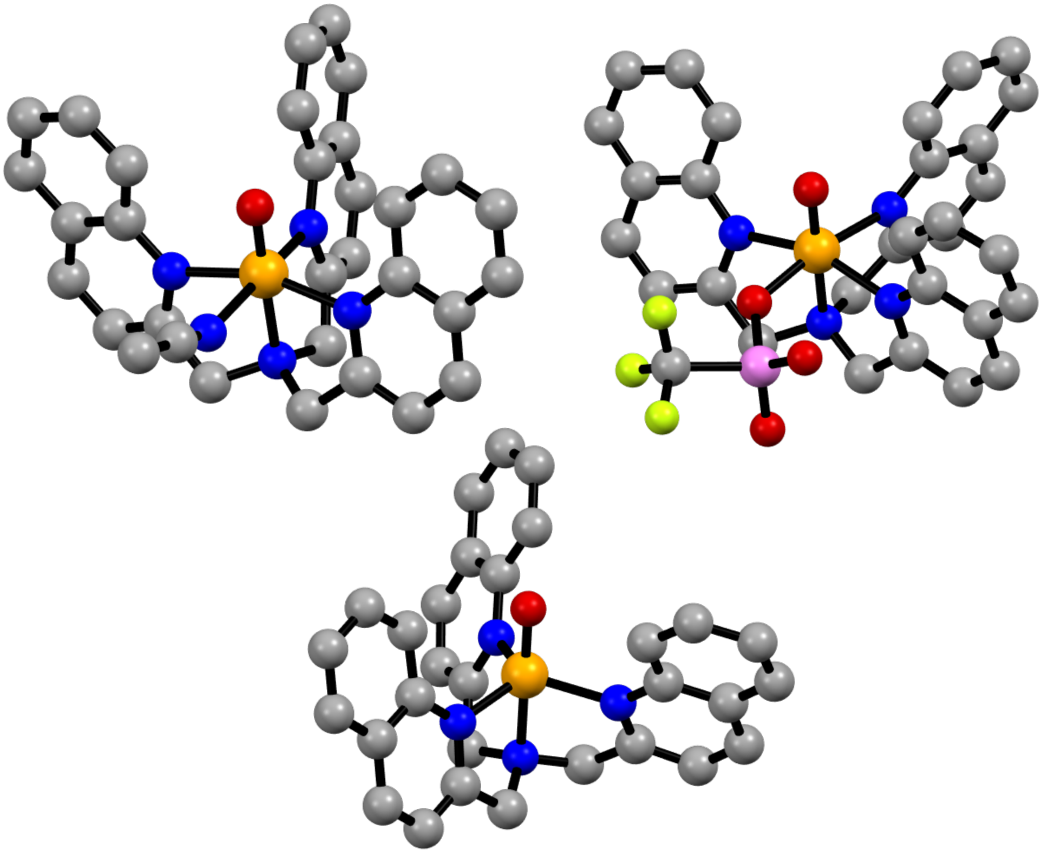

Figure 2.19. Three possible structure of the S = 2 oxoiron(IV) complex **1** from geometry optimized DFT calculations, with 5-coordinate $[Fe^{IV}(O)(TQA)]^{2+}$ (bottom middle), 6-coordinate $[Fe^{IV}(O)(TQA)(MeCN)]^{2+}$ (top left), and 6-coordinate $[Fe^{IV}(O)(TQA)(OTf)]^{+}$ (top right).

Based on DFT calculations, the five-coordinate $[Fe^{IV}(O)(TQA)]^{2+}$ structure may be ruled out, as it gives rise to a calculated isomer shift of $\delta = 0.15$ mm s^{-1}, which is inconsistent with the experimental value of $\delta = 0.24$ mm s^{-1}. However, the two six-coordinate structures, $[Fe^{IV}(O)(TQA)(OTf)]^{+}$ and $[Fe^{IV}(O)(TQA)(MeCN)]^{2+}$ both gave rise to calculated isomer shifts of $\delta = 0.24$ mm s^{-1}, consistent with the experimental data.

In order to distinguish between the two, ^{19}F NMR experiments were carried out on **1** (*vide infra*), suggesting **1** consists mostly of the $[Fe^{IV}(O)(TQA)(NCMe)]^{2+}$ species in solution.

DFT calculations on **2** and **3** were also performed to obtain geometry-optimized structures (Figure 2.20) that give rise to calculated Mössbauer isomer shifts that match the experimental values. These afford Fe^{IV}=O distances of 1.64 Å for both **2** and **3** and respective Fe^{IV}–Cl and Fe^{IV}–Br distances of 2.36 and 2.51 Å, which agrees with the experimental EXAFS-derived Fe^{IV}-Cl and Fe^{IV}-Br distances of 2.33 Å and 2.50 Å.

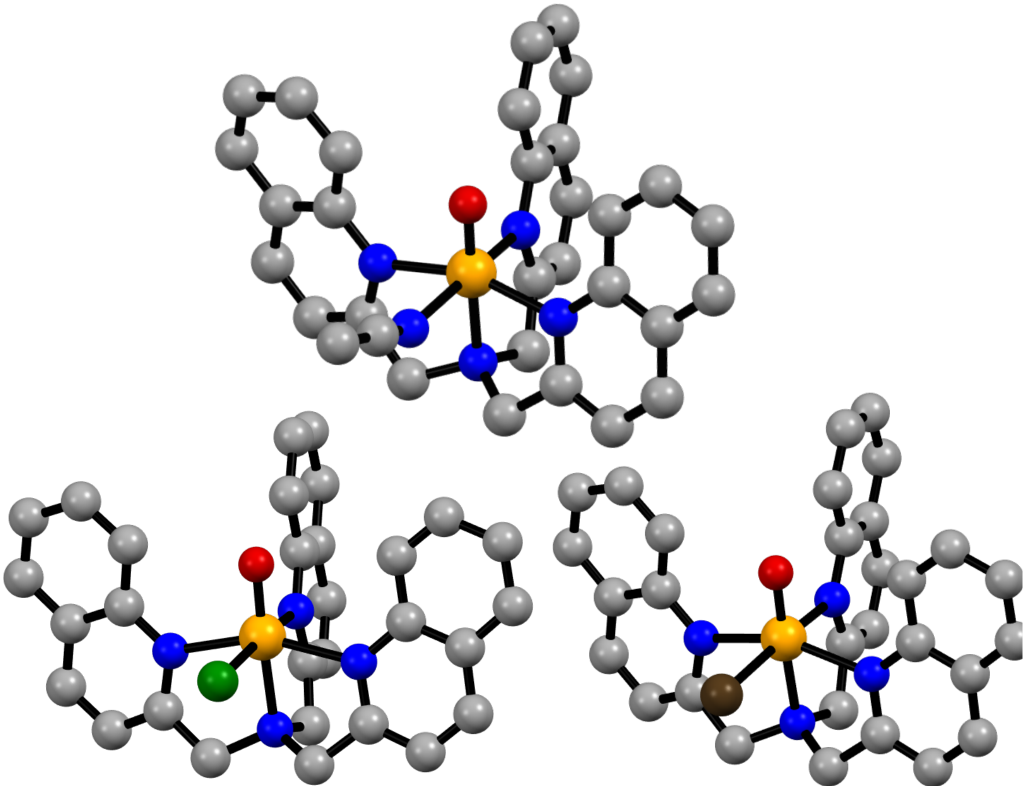

Figure 2.20. Geometry optimized DFT structures of *S* = 2 oxoiron(IV) complexes **1** (top middle), **2** (bottom left), and **3** (bottom right).

2.5.7 ^{19}F NMR Spectroscopy

To distinguish between the two six-coordinate formulations of complex **1**, a ^{19}F-NMR study was performed at -40 °C, revealing only one peak at -80 ppm, where free triflate is also observed (Figure 2.21). Its peak area represents all of the triflate in the sample. Its 80-Hz line width is 5-fold broader than that found for free triflate (Figure 2.22). When judged against the data accumulated in Table 2.7, we surmise that only a small fraction of the triflate binds to the $Fe^{IV}(O)$ unit and is in rapid equilibrium with unbound triflate, making $[Fe^{IV}(O)(TQA)(OTf)]^+$ a minor component of **1** in acetonitrile solution. Thus, taking the ^{19}F-NMR and DFT results together, we conclude that **1** is best formulated as $[Fe^{IV}(O)(TQA)(NCMe)]^{2+}$.

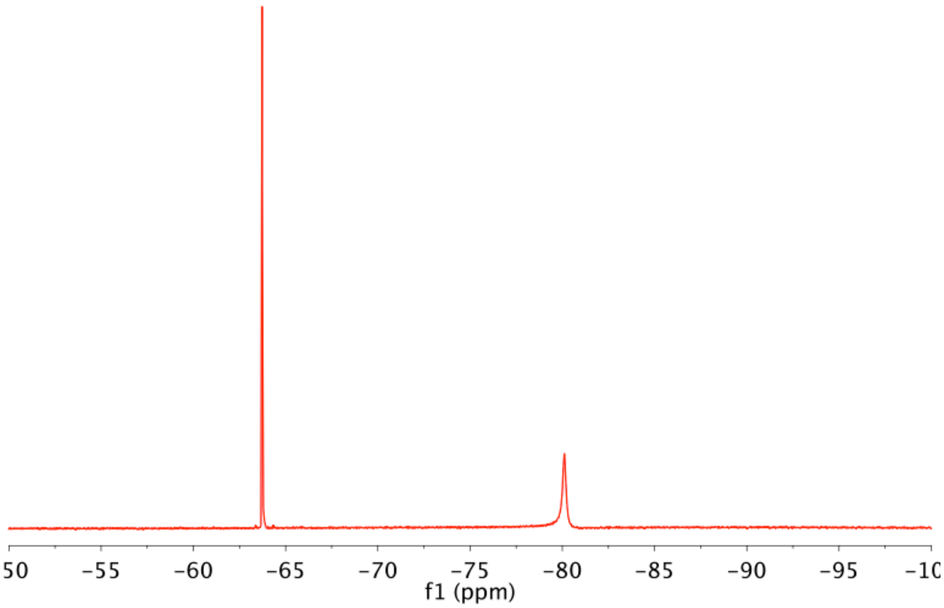

Figure 2.21. ^{19}F NMR spectrum of **1** in CD_3CN at -40 °C with trifluorotoluene as an internal standard (δ = -63.7 ppm), displaying a single peak at -79.9 ppm with a line width at half-maximum of 81 Hz.

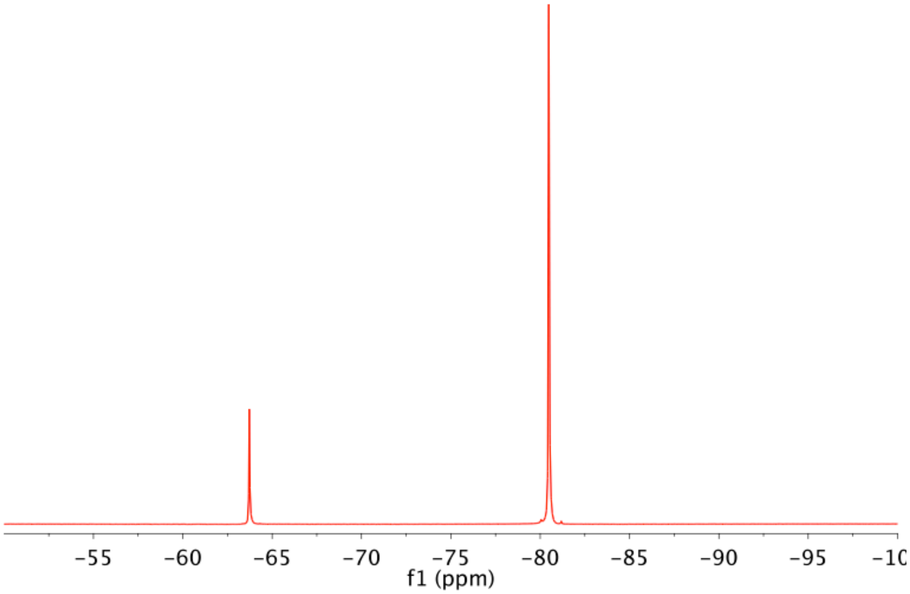

Figure 2.22. ^{19}F NMR spectrum of NBu_4OTf in CD_3CN at -40 °C with trifluorotoluene as an internal standard (δ = -63.7 ppm), displaying a single peak at -80.3 ppm with a line width at half-maximum of 15 Hz.

Table 2.7. Summary of ^{19}F NMR data for species related to **1.**

Complex	**^{19}F NMR shift (ppm)**	**Peak full width at half maximum height (FWHM) (Hz)**	**Peak FWHM of $PhCF_3$ standard (Hz)**	**Integration vs. $PhCF_3$ standard**
$[Fe^{II}(TQA)(OTf)_2]$	-79.8	480	14	1.9
1	-79.9	81	17	1.9
1 decayed	-79.6	57	15	1.7
$[Fe^{II}(TPA)(NCMe)_2](OTf)_2$	-80.2	36	17	1.9
$[Fe^{IV}(O)(TPA)(NCMe)](OTf)_2$	-80.1	27	17	1.7
Bu_4NOTf	-80.3	15	15	1.0

2.6 Discussion

We have been successful in synthetically tuning the spin state of the *S* = 1 oxoiron(IV) complex $[Fe^{IV}(O)(TPA)(MeCN)]^{2+}$ by systematically replacing the equatorial pyridine rings of the TPA ligand with quinoline rings. Upon replacement of one or two pyridine rings, the ligand field appears to weaken, as illustrated by the red-shift of the near-IR d-d electronic transitions in the corresponding complexes $[Fe^{IV}(O)(QBPA)(MeCN)]^{2+}$ and $[Fe^{IV}(O)(BQPA)(MeCN)]^{2+}$ (Figure 2.3). However, in both of these nonheme oxoiron(IV) species the ground spin state remains *S* = 1, suggesting that the ligand field has not been weakened enough to stabilize the *S* = 2 ground spin state. Finally, upon replacing all three pyridine rings of the TPA ligand with quinoline rings, a new absorption feature appears at 650 nm, suggesting a change in the electronic configuration of the nonheme oxoiron(IV) complex. Indeed, Mössbauer spectroscopy confirms that replacement of all three pyridine rings for quinoline rings results in the *S* = 2 oxoiron(IV) complex **1**.

Notably, we can measure the shift in the near-IR electronic absorption band of these nonheme oxoiron(IV) complexes to quantify the weakening of the ligand field and estimate the energy gap between the *S* = 1 and *S* = 2 spin states. Upon replacing one pyridine ring for a quinoline ring and converting $[Fe^{IV}(O)(TPA)(MeCN)]^{2+}$ to $[Fe^{IV}(O)(QBPA)(MeCN)]^{2+}$, the near-IR band shifts by 900 cm^{-1}, approximately 3 kcal/mol. Similarly, upon replacing two pyridines rings for quinoline rings and converting $[Fe^{IV}(O)(QBPA)(MeCN)]^{2+}$ to $[Fe^{IV}(O)(BQPA)(MeCN)]^{2+}$, the NIR band shifts by an additional 1140 cm^{-1}, or approximately 4 kcal/mol. Therefore, it appears that replacement of each pyridine ring for a quinoline ring weakens the ligand field by 3 - 4 kcal/mol. From this, one can estimate that the energetic cost to replace all three pyridines rings with quinoline rings and induce a spin state change from *S* = 1 $[Fe^{IV}(O)(TPA)(MeCN)]^{2+}$ to *S* = 2 complex **1** is likely between 9 – 12 kcal/mol, if the 3 – 4 kcal/mol weakening of the ligand field per quinoline ring substitution remains constant. Computational support for this experimental estimation of the Fe^{IV} spin state transition barrier would be welcomed.

Through the synthesis of complexes **1** – **3**, we have successfully generated a family of *S* = 2 nonheme oxoiron(IV) complexes with a pseudo-octahedral geometry. The electronic environments of these complexes are notably different from trigonal bipyramidal *S* = 2 nonheme oxoiron(IV) complexes and remarkably similar to the nonheme oxoiron(IV) intermediates found in the enzymes TauD-J, CytC3 and SyrB2. Indeed, complexes **1** – **3** are currently the only oxoiron(IV) complexes with Mössbauer isomer shifts that fall within the range observed for enzymatic nonheme oxoiron(IV) species (0.22–0.30 mm s^{-1}, Table 2.3).

This resemblance leads us to ask why **1 - 3**, of all the synthetic oxoiron(IV) complexes characterized, should have an isomer shift most similar to those of the enzyme intermediates, given that its donor set does not match the 2-His-1-carboxylate combination associated the enzymatic intermediates of TauD, CytC3, or SyrB2. All other *S* = 2 nonheme oxoiron(IV) complexes with *N*-donor sets have isomer shifts of 0.12 mm s^{-1} or smaller, while that of $[Fe^{IV}(O)(OH_2)_5]^{2+}$ [14,28] at 0.38 mm s^{-1} is above the range for enzyme intermediates. As the isomer shift reflects the donation of electron density from the ligands into the iron 4s orbital, TQA must represent a good electronic approximation of the donor set found in the enzyme active sites. Additional examples of $S = 2$ oxoiron(IV) complexes with isomer shifts falling into this range would obviously help to clarify what factors govern the isomer shifts, and hence the electronic environments, of nonheme oxoiron(IV) enzyme intermediates.

2.7 Acknowledgements

The work described in this chapter could not have been accomplished without the help and collaboration of a number of extremely talented scientists. Dr. Achintesh N. Biswas first discovered and generated the $S = 2$ nonheme oxoiron(IV) complex **1**. He also prepared the necessary Mössbauer samples of **1**, which were analyzed by Dr. Katlyn K. Meier and Professor Eckard Münck at Carnegie Mellon University. Mössbauer experiments on **2** and **3** were carried out by Professor Yisong Alex Guo and Ruixi Fan. Dr. Gregory T. Rohde carried out the X-ray crystallography measurements on $[Fe^{II}(TQA)(OTf)_2]$, as well as the initial EXAFS experiments on **1**. Ang Zhou carried out subsequent EXAFS experiments on complexes **2** and **3**. ^{19}F NMR experiments were carried out with the help of Dr. Williamson N. Oloo and Ang Zhou. DFT calculations on **1** were carried out by Professor Emile L. Bominaar and Dr. Katlyn K. Meier, while those on **2** and **3** were carried out by Professor Yisong Guo and Ruixi Fan, all at Carnegie Mellon University.

2.8 References

(1) Costas, M.; Mehn, M. P.; Jensen, M. P.; Que, L., Jr. *Chem. Rev.* **2004**, *104*, 939-986.

(2) Solomon, E. I.; Brunold, T. C.; Davis, M. I.; Kemsley, J. N.; Lee, S.-K.; Lehnert, N.; Neese, F.; Skulan, A. J.; Yang, Y.-S.; Zhou, J. *Chem. Rev.* **2000**, *100*, 235-349.

(3) Krebs, C.; Fujimori, D. G.; Walsh, C. T.; Bollinger, J. M., Jr. *Acc. Chem. Res.* **2007**, *40*, 484-492.

(4) Price, J. C.; Barr, E. W.; Glass, T. E.; Krebs, C.; Bollinger, J. M., Jr. *J. Am. Chem. Soc.* **2003**, *125*, 13008-13009.

(5) Sinnecker, S.; Svensen, N.; Barr, E. W.; Ye, S.; Bollinger, J. M., Jr.; Neese, F.; Krebs, C. *J. Am. Chem. Soc.* **2007**, *129*, 6168-6179.

(6) Que, L., Jr. *Acc. Chem. Res.* **2007**, *40*, 493-500.

(7) McDonald, A. R.; Que, L., Jr. *Coord. Chem. Rev.* **2013**, *257*, 414-428.

(8) Ray, K.; Pfaff, F. F.; Wang, B.; Nam, W. *J. Am. Chem. Soc.* **2014**, *136*, 13942 - 13958.

(9) Puri, M.; Que, L. *Acc. Chem. Res.* **2015**, *48*, 2443-2452.

(10) England, J.; Martinho, M.; Farquhar, E. R.; Frisch, J. R.; Bominaar, E. L.; Münck, E.; Que, L., Jr. *Angew. Chem. Int. Ed.* **2009**, *48*, 3622-3626.

(11) England, J.; Guo, Y.; Van Heuvelen, K. M.; Cranswick, M. A.; Rohde, G. T.; Bominaar, E. L.; Münck, E.; Que, L., Jr. *J. Am. Chem. Soc.* **2011**, *133*, 11880–11883.

(12) Lacy, D. C.; Gupta, R.; Stone, K. L.; Greaves, J.; Ziller, J. W.; Hendrich, M. P.; Borovik, A. S. *J. Am. Chem. Soc.* **2010**, *132*, 12188-12190.

(13) Bigi, J. P.; Harman, W. H.; Lassalle-Kaiser, B.; Robles, D. M.; Stich, T. A.; Yano, J.; Britt, R. D.; Chang, C. J. *J. Am. Chem. Soc.* **2012**, *134*, 1536-1542.

(14) Pestovsky, O.; Stoian, S.; Bominaar, E. L.; Shan, X.; Münck, E.; Que, L., Jr.; Bakac, A. *Angew. Chem. Int. Ed.* **2005**, *44*, 6871-6874.

(15) Zang, Y.; Kim, J.; Dong, Y.; Wilkinson, E. C.; Appelman, E. H.; Que, L., Jr. *J. Am. Chem. Soc.* **1997**, *119*, 4197-4205.

(16) Paine, T. K.; Costas, M.; Kaizer, J.; Que, L., Jr. *J. Biol. Inorg. Chem.* **2006**, *11*, 272-276.

(17) Wei, N.; Murthy, N. N.; Chen, Q.; Zubieta, J.; Karlin, K. D. *Inorg. Chem.* **1994**, *33*, 1953-1965.

(18) Galonić, D. P.; Barr, E. W.; Walsh, C. T.; Bollinger, J. M., Jr.; Krebs, C. *Nat. Chem. Biol.* **2007**, *3*, 113-116.

(19) Galonić Fujimori, D.; Barr, E. W.; Matthews, M. L.; Koch, G. M.; Yonce, J. R.; Walsh, C. T.; Bollinger, J. M., Jr.; Krebs, C.; Riggs-Gelasco, P. J. *J. Am. Chem. Soc.* **2007**, *129*, 13408-13409.

(20) Matthews, M. L.; Krest, C. M.; Barr, E. W.; Vaillancourt, F. H.; Walsh, C. T.; Green, M. T.; Krebs, C.; Bollinger, J. M., Jr. *Biochemistry* **2009**, *48*, 4331–4343.

(21) Macikenas, D.; Skrzypczak-Jankun, E.; Protasiewicz, J. D. *J. Am. Chem. Soc.* **1999**, *121*, 7164-7165.

(22) Macikenas, D.; Skrzypczak-Jankun, E.; Protasiewicz, J. D. *J. Am. Chem. Soc.* **2011**, *133*, 4151-4151.

(23) Hagen, K. S. *Inorg. Chem.* **2000**, *39*, 5867-5869.

(24) Gafford, B. G.; O'Rear, C.; Zhang, J. H.; O'Connor, C. J.; Holwerda, R. A. *Inorg. Chem.* **1989**, *28*, 1720-1726.

(25) a) Lim, M. H.; Rohde, J.-U.; Stubna, A.; Bukowski, M. R.; Costas, M.; Ho, R. Y. N.; Münck, E.; Nam, W.; Que, L., Jr. *Proc. Natl. Acad. Sci. USA* **2003**, *100*, 3665-3670.

b) Frisch, J. R., *Spectroscopic and crystallographic characterization of peroxo- and oxoiron complexes*. ProQuest: 2010.

(26) Chen, K.; Que, L., Jr. *J. Am. Chem. Soc.* **2001**, *123*, 6327-6337.

(27) M. J. Frisch, G. W. T., H. B. Schlegel, G. E. Scuseria, M. A. Robb, J. R. Cheeseman, G. Scalmani, V. Barone, B. Mennucci, G. A. Petersson, H. Nakatsuji, M. Caricato, X. Li, H. P. Hratchian, A. F. Izmaylov, J. Bloino, G. Zheng, J. L. Sonnenberg, M. Hada, M. Ehara, K. Toyota, R. Fukuda, J. Hasegawa, M. Ishida, T. Nakajima, Y. Honda, O. Kitao, H. Nakai, T. Vreven, J. A. Montgomery, Jr., J. E. Peralta, F. Ogliaro, M. Bearpark, J. J. Heyd, E. Brothers, ; K. N. Kudin, V. N. S., R. Kobayashi, J. Normand,

K. Raghavachari, A. Rendell, J. C. Burant, S. S. Iyengar, J. Tomasi, M. Cossi, N. Rega, J. M. Millam, M. Klene, J. E. Knox, J. B. Cross, V. Bakken, C. Adamo, J. Jaramillo, R. Gomperts, R. E. Stratmann, O. Yazyev, A. J. Austin, R. Cammi, C. Pomelli, J. W. Ochterski, R. L. Martin, K. Morokuma, V. G. Zakrzewski, G. A. Voth, P. Salvador, J. J. Dannenberg, S. Dapprich, A. D. Daniels, O. Farkas, J. B. Foresman, J. V. Ortiz, J. Cioslowski, and D. J. Fox: Gaussian-09. Gaussian, Inc.: Wallingford CT, 2009.

(28) Biswas, A. N.; Puri, M.; Meier, K. K.; Oloo, W. N.; Rohde, G. T.; Bominaar, E. L.; Münck, E.; Que, L. *J. Am. Chem. Soc.* **2015**, *137*, 2428-2431.

(29) Vrajmasu, V.; Münck, E.; Bominaar, E. L. *Inorg. Chem.* **2003**, *42*, 5974-5988.

(30) APEX2 v2012-4.3 ed.; Bruker Analytical X-ray Systems: Madison, WI, 2012.

(31) Blessing, R. *Acta Cryst.* **1995**, *A51*, 33-38.

(32) SAINT+. V8.18c ed.; Bruker Analytical X-Ray Systems: Madison, WI, 2011.

(33) SHELXTL. V2008/2 ed.; Bruker Analytical X-Ray Systems: Madison, WI, 2008.

(34) Decker, A.; Rohde, J.-U.; Que, L., Jr.; Solomon, E. I. *J. Am. Chem. Soc.* **2004**, *126*, 5378-5379.

(35) Decker, A.; Rohde, J.-U.; Klinker, E. J.; Wong, S. D.; Que, L., Jr.; Solomon, E. I. *J. Am. Chem. Soc.* **2007**, *129*, 15983-15996.

(36) a) Price, J. C.; Barr, E. W.; Tirupati, B.; Bollinger, J. M., Jr.; Krebs, C. *Biochemistry* **2003**, *42*, 7497-7508. b) Proshlyakov, D. A.; Henshaw, T. F.; Monterosso, G.; Ryle, M. J.; Hausinger, R. P. *J. Am. Chem. Soc.* **2004**, *126*, 1022 - 1023.

(37) Wong, S. D.; Bell, C. B., III; Liu, L. V.; Kwak, Y.; England, J.; Zhao, J.; Que, L., Jr.; Solomon, E. I. *Angew. Chem. Int. Ed.* **2011**, *50*, 3215 –3218.

(38) Rohde, J.-U.; Stubna, A.; Bominaar, E. L.; Münck, E.; Nam, W.; Que, L., Jr. *Inorg. Chem.* **2006**, *45*, 6435-6445.

(39) Planas, O.; Clemancey, M.; Latour, J.-M.; Company, A.; Costas, M. *Chem. Comm.* **2014**, *50*, 10887-10890.

(40) Wong, S. D.; Srnec, M.; Matthews, M. L.; Liu, L. V.; Kwak, Y.; Park, K.; Bell, C. B., 3rd; Alp, E. E.; Zhao, J.; Yoda, Y.; Kitao, S.; Seto, M.; Krebs, C.; Bollinger, J. M., Jr.; Solomon, E. I. *Nature* **2013**, *499*, 320-323.

(41) Hoffart, L. M.; Barr, E. W.; Guyer, R. B.; Bollinger, J. M., Jr.; Krebs, C. *Proc. Natl. Acad. Sci. USA* **2006**, *103*, 14738-14743.

2.9 Appendix

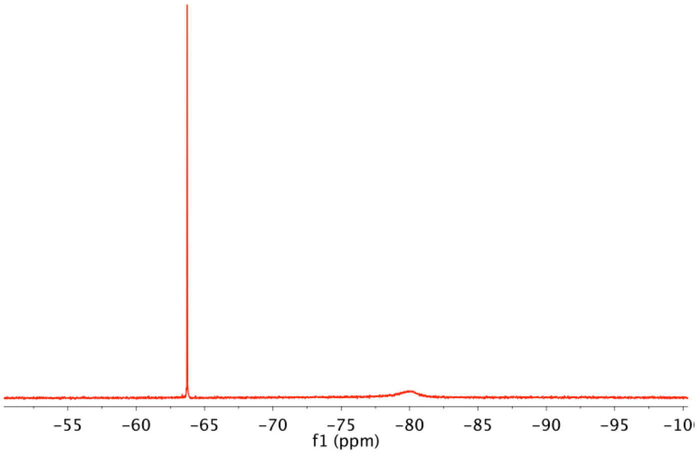

Figure 2.23. ^{19}F NMR spectrum of [Fe^{II}(TQA)(OTf)$_2$] in CD$_3$CN at -40 °C with trifluorotoluene as an internal standard (δ = -63.7 ppm), displaying a single peak at -79.8 ppm with a line width at half-maximum of 480 Hz.

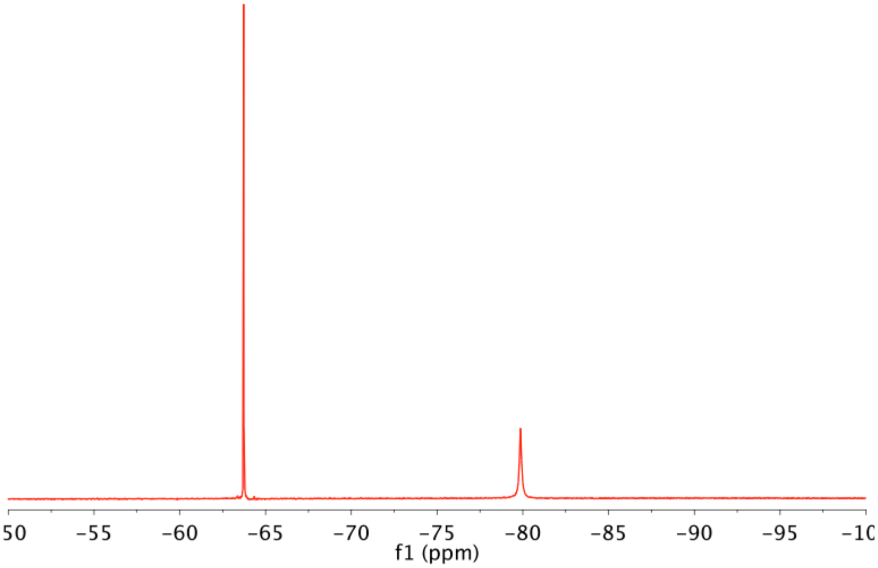

Figure 2.24. ^{19}F NMR spectrum upon complete decay of **1** in CD$_3$CN at -40 °C with trifluorotoluene as an internal standard (δ = -63.7 ppm), displaying a single peak at -79.6 ppm with a line width at half-maximum of 57 Hz.

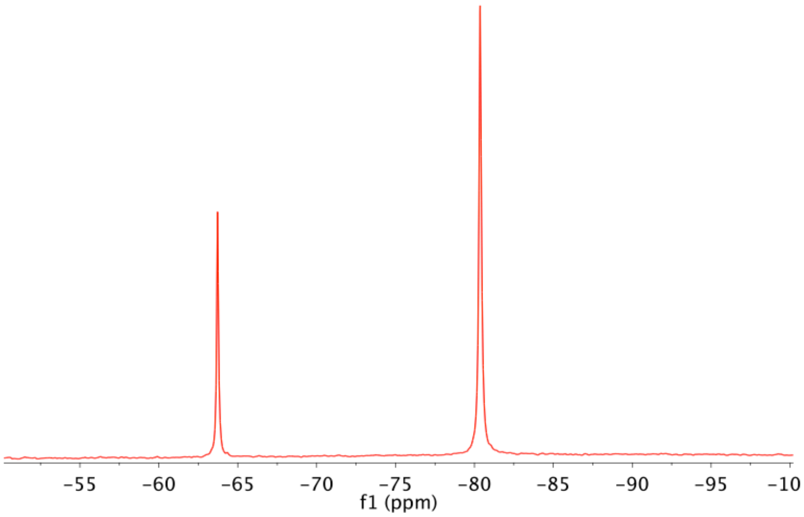

Figure 2.25. ^{19}F NMR spectrum of [Fe^{II}(TPA)(NCMe)$_2$](OTf)$_2$ in CD$_3$CN at -40 °C with trifluorotoluene as an internal standard (δ = -63.7 ppm), displaying a single peak at -80.2 ppm with a line width at half-maximum of 36 Hz.

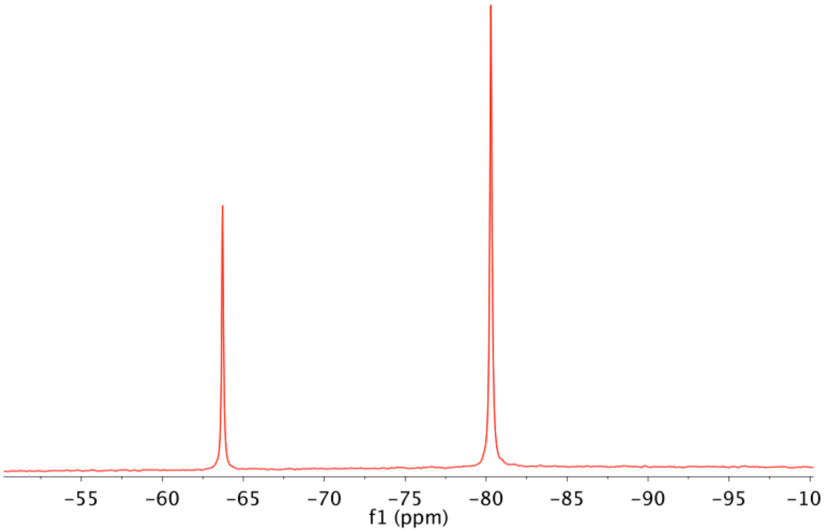

Figure 2.26. ^{19}F NMR spectrum of [Fe^{IV}(O)(TPA)(NCMe)](OTf)$_2$ in CD$_3$CN at -40 °C with trifluorotoluene as an internal standard (δ = -63.7 ppm), displaying a single peak at -80.1 ppm with a line width at half-maximum of 27 Hz.

Chapter 3:
Reactivity of *S* = 2 Nonheme Oxoiron(IV) Complexes

Parts of this chapter were published in:

1. Puri, M.; Que, L. Jr. Towards the Synthesis of More Reactive *S* = 2 Nonheme Oxoiron(IV) Complexes. *Acc. Chem. Res.*, **2015**, *48*, 2443 – 2452.

2. Biswas, A. N.; Puri, M.; Meier, K. K.; Oloo, W. N.; Rohde, G. T.; Bominaar, E. L.; Münck, E.; Que, L. Jr. Modeling TauD-J: A High-Spin Nonheme Oxoiron(IV) Complex with High Reactivity toward C-H Bonds. *J. Am. Chem. Soc.*, **2015**, *137*, 2428 – 2431.

3. Puri, M.; Biswas, A. N.; Fan, R.; Guo, Y.; Que, L. Jr. Modeling Non-heme Iron Halogenases: High-Spin Oxoiron(IV)-Halide Complexes that Halogenate C-H Bonds. *J. Am. Chem. Soc.* **2016**, *138*, 2484 – 2487.

3.1 Introduction

Nonheme oxoiron(IV) intermediates have been shown capable of carrying out a diverse range of oxidative transformations in nature, including the hydroxylation of C-H bonds, desaturation of C-C bonds, electrophilic aromatic substitutions, as well as oxidative ligand transfer reactions in which C-H bonds are converted to C-halogen bonds.[1] For this reason, chemists have attempted to synthesize nonheme oxoiron(IV) complexes that demonstrate comparable reactivity in the laboratory. Indeed, over the past thirteen years, a number of $S = 1$ oxoiron(IV) complexes have been shown to carry out impressive hydrogen-atom transfer (HAT), oxygen-atom transfer (OAT), and electron-transfer (ET) reactions.[2] $S = 2$ oxoiron(IV) complexes, while still in their infancy, have also demonstrated some HAT and OAT reactivity,[3,4,5] but this reactivity is often limited by the bulky tripodal ligands used to stabilize trigonal bipyramidal S = 2 nonheme oxoiron(IV) complexes.

Many interesting questions have arisen from these reactivity studies with nonheme oxoiron(IV) complexes – namely, what are the factors that govern reactivity? Is it possible to have $S = 1$ and $S = 2$ nonheme oxoiron(IV) complexes that demonstrate comparable reactivity? Why did nature evolve all the nonheme oxoiron(IV) intermediates to have a $S = 2$ ground spin state? The quintet ($S = 2$) species is predicted by density functional theory (DFT) calculations to be more reactive in HAT than the corresponding triplet ($S = 1$) species.[6-9] In particular, Shaik has emphasized the role of exchange to stabilize the high-spin hydroxoiron(III) transition state in HAT by high-spin nonheme oxoiron(IV) complexes.[6] However, direct experimental proof for these claims are still lacking. In fact, the most reactive $S = 1$ nonheme oxoiron(IV) complex has been shown to be more reactive than the majority of $S = 2$ nonheme oxoiron(IV) complexes.

Another interesting question that has arisen from the reactivity of nonheme oxoiron(IV) complexes is whether or not C-H bond activation follows a rebound mechanism, initially proposed by Groves for high-valent heme oxoiron species.[10] This mechanism would involve initial abstraction of a hydrogen-atom by the oxoiron(IV) species, producing a hydroxoiron(III) intermediate and an organic radical (Figure 3.1). The radical may then recombine with the bound hydroxide ligand to generate the corresponding hydroxylated product. Initial reports by Nam suggest that $S = 1$ nonheme oxoiron(IV) complexes do not follow a rebound mechanism, with the generated organic radical instead migrating out of the solvent cage to intercept a second equivalent of the nonheme oxoiron(IV) species or a radical trapping agent, such as O_2 or $BrCCl_3$.[11] However, Maiti and co-workers recently reported ESI-MS evidence in support of the rebound mechanism in a different $S = 1$ nonheme oxoiron(IV) complex.[12] Importantly, these differing reports only examine $S = 1$ nonheme oxoiron(IV) complexes, while the rebound mechanism for $S = 2$ nonheme oxoiron(IV) complexes has been entirely unexplored.

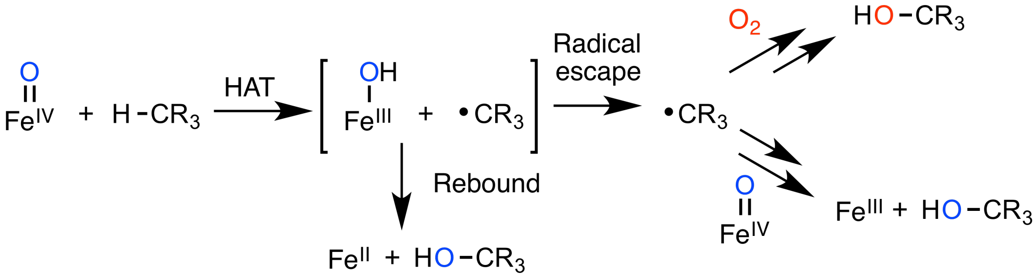

Figure 3.1. Generalized mechanism for radical rebound in HAT reactions with nonheme oxoiron(IV) complexes, as well as potential radical interception pathways.

In addition to oxygen-rebound, nonheme iron halogenase enzymes have been shown capable of halogen-rebound, where these enzymes transform C-hydrogen bonds to C-halogen bonds in reactions central to the biosynthesis of natural products.[1] The mechanism of dioxygen activation by nonheme iron halogenases is thought to be analogous to that of other aKG-dependent nonheme iron enzymes. The active oxidant derived is proposed to be a $S = 2$ oxoiron(IV)-halide species that abstracts a H-atom to form a hydroxoiron(III)-halide species and a substrate radical. In the next step, the incipient radical can undergo rebound with either the hydroxo or the halo ligand to afford respective R-OH or R-Cl products. In an elegant mechanistic study, Matthews et al. showed that substrate positioning controls the chemoselectivity of halogenation over hydroxylation in SyrB2,[13] which was subsequently corroborated by recent HYSCORE experiments on SyrB2-substrate-NO complexes.[14]

There has been some effort to obtain synthetic models for the oxoiron(IV)-halide intermediates of the halogenases. However, no oxoiron(IV)-halide complex has yet been demonstrated to have the ability to transform C–H bonds into C–(Cl/Br) bonds. For this reason, no insights into halogen-rebound rates for these complexes have been obtained.

3.2 Experimental Details

All reagents were purchased from Aldrich and used as received, unless noted otherwise. The substrates used in kinetic experiments were purified using standard methods.[15] 2-(*tert*-butylsulfonyl)iodosylbenzene (2-(^{t}BuSO$_2$)C$_6$H$_4$IO) was synthesized through modification of a previous literature procedure (*Caution*: An injury was recently reported while attempting to synthesize this oxidant. This synthetic procedure should therefore be carried out with the appropriate safety precautions and protective equipment),[16,17] and the salt $Fe(OTf)_2(CH_3CN)_2$ [18] was prepared according to published procedures. UV-vis spectra were recorded on a HP8453A diode array spectrometer equipped with a cryostat from Unisoku Scientific Instruments (Osaka, Japan).

Synthesis of TQA-*d_6*: This procedure was adapted from the previously reported synthesis of TPA*-d_6.[19] The ligand TQA (160 mg, 0.36 mmol) was mixed with CD_3CN (4.0 mL), forming an insoluble white slurry. NaH (105 mg, 4.4 mmol) was slowly added to the mixture. The flask was then placed under Ar and heated to 50 °C, turning the solution bright neon green/blue after 15 minutes. After stirring over 2 days at 50 °C, the flask was cooled to room temperature and D_2O (2.0 mL) was slowly added, initially turning the mixture dark pink and then dark brown. The flask was placed under vacuum, leaving a dark residue. The residue was re-dissolved in methylene chloride (20 mL) and H_2O (20 mL) was added to the solution, forming two layers. The organic layer was separated from the aqueous layer, and the aqueous layer was washed twice with additional methylene chloride (20 mL). The combined organic layers were placed under vacuum, leaving a brown oil. TLC indicated a mixture of many products – however, the desired TQA-d_6 ligand could be cleanly separated from the byproducts by treating the brown oil with acetone to leave a white powder, which was then washed 3x with acetone (10 mg, < 10% yield).

Note: This synthetic method has not been optimized and needs further work.

$[Fe^{II}(TQA\text{-}d_6)(OTf)_2]$ was synthesized analogously to $[Fe^{II}(TQA\text{-}h_6)(OTf)_2]$, and $[Fe^{IV}(O)(TQA\text{-}d_6)(MeCN)](OTf)_2$ was generated analogously to $[Fe^{IV}(O)(TQA)(MeCN)](OTf)_2$.

Oxidation kinetics with 1:

Kinetic measurements of substrate oxidations with **1** were performed at -40 °C under a N_2 atmosphere. The substrates were first added to a 2.0 mL 1.0 mM acetonitrile solutions of $[Fe^{II}(TQA)(OTf)_2]$, followed by 2 equivalents of 2-(^{t}BuSO$_2$)C$_6$H$_4$IO (ArIO). The decay of the 650 nm UV-Vis band associated with **1** was then monitored over time (Figure 3.5). Fitting the decay of **1** to a single-exponential function yielded a pseudo-first order rate constant, k_{obs}. Second-order rate constants, k_2 ($M^{-1}s^{-1}$), were determined from the slope of a plot of k_{obs} (s^{-1}) against substrate concentration (Figures 3.14 – 3.22).

To isolate and identify the organic products upon completion of the reaction, the reaction mixtures were warmed to room temperature, filtered through a plug of silica and eluted with chloroform or ethyl acetate. The filtered solutions were then analyzed by GC with naphthalene as the quantification standard. Alternatively, the mixtures may also be worked up according to published methods involving treatment of the reaction solution with dilute acid.[23]

Halogenation kinetics with 2 and 3: Kinetic measurements of substrate oxidations were performed at -40 °C under a nitrogen atmosphere. Complex **1** was first generated by the addition of 2 equivalents of 2-(^{t}BuSO$_2$)C$_6$H$_4$IO to a CD_3CN solution of

$[Fe^{II}(TQA)(OTf)]_2$. Complexes **2** or **3** was then formed through the addition of 1 – 2 equivalents of NBu_4Cl or NBu_4Br, respectively. Finally, 500 equivalents of the organic substrate was added to the reaction mixture last. In the case of cyclohexane, some freezing of the substrate was observed upon addition to the reaction mixture at -40 °C. The decay of the 620 nm UV-Vis band, associated with **2** and **3**, was monitored over time. Fitting the decay of **2** or **3** to a single-exponential function yielded a pseudo-first order rate constant, k_{obs}. Second-order rate constants, k_2 ($M^{-1}s^{-1}$), were determined from the slope of a plot of k_{obs} (s^{-1}) against substrate concentration.

Halogenation Experiments Under O_2: Substrate oxidation experiments carried out in the presence of O_2 were performed as stated above except a balloon O_2 was first bubbled into the solution of $[Fe^{II}(TQA)(OTf)_2]$ for 60 seconds prior to cooling to -40 °C and injection of 2-(^{t}BuSO$_2$)C_6H_4IO to generate complex **1**.

Substrate Oxidation Product Analysis: To identify and quantify the organic products formed upon completion of the reaction, the reaction mixtures were warmed to room temperature and an internal standard, 1,1,2,2-tetrachloroethane, was added to the reaction mixture. The peaks associated with the products were identified (Figure 3.23 – 3.27) and integrated relative to the 1,1,2,2-tetrachloroethane standard by ^{1}H NMR spectroscopy. To ensure accurate integration values, the relaxation delay in the ^{1}H NMR experiment was set to 20 seconds.

Intermolecular Competition KIE Experiments: Intermolecular competition KIE experiments were performed by generating complex **3** in acetonitrile solutions at -40 °C and adding 500 equivalents of a premixed solution of 10 : 1 toluene-d_8 : toluene-h_8. Upon complete decay of **3**, the reaction mixture was warmed to room temperature and the reaction mixture was treated with dilute H_2SO_4 and extracted with $CHCl_3$ to isolate the organic products, according to our previously reported procedure.[20] The organic solution was then analyzed by GC/MS to determine the ratio of benzyl bromide-d_7 and benzyl bromide-h_7 (Figure 3.12).

3.3 Self-decay of the *S* = 2 Nonheme Oxoiron(IV) Complex 1

The ESI-MS spectrum of complex **1** suggests the formation of a ferric decay product in which two methylene protons of the ligand have been oxidized to a ketone (Chapter 2). In fact, upon complete decay of **1**, this peak at 676 m/z is the only prominent peak in the spectrum (Figure 3.2).

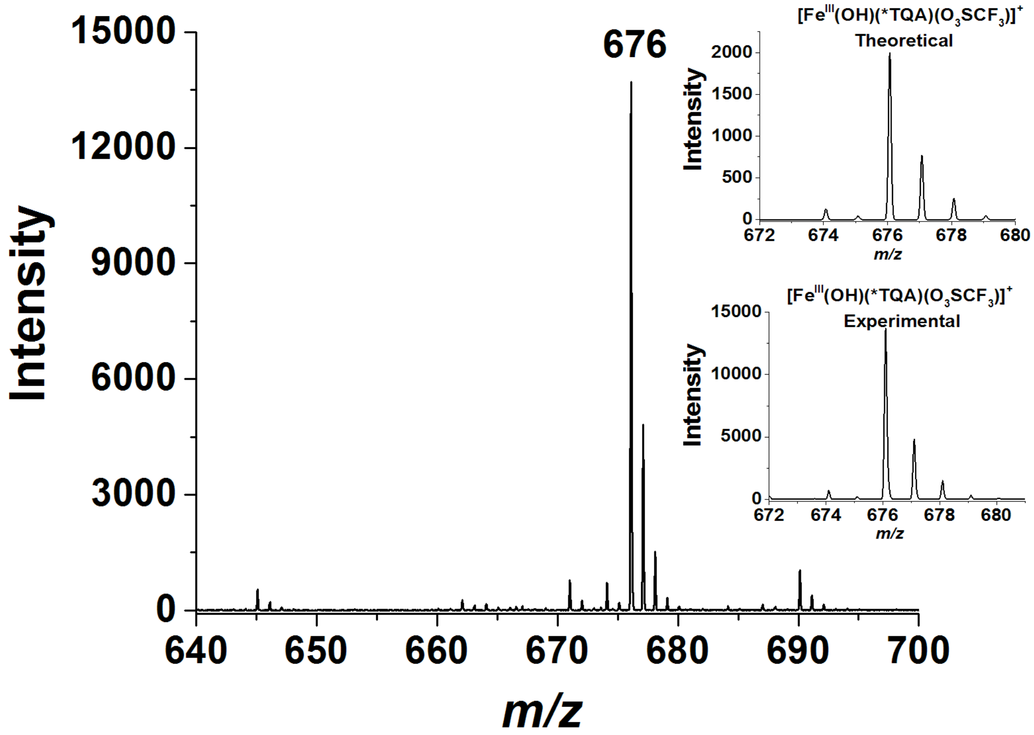

Figure 3.2. Electrospray ionization mass spectrum (ESI-MS) of **1** upon complete decay; the single peak at m/z 676 corresponds to the molecular ion $[Fe^{III}(OH)(*TQA)(O_3SCF_3)]^+$, where a $–CH_2$ group on the TQA ligand has been oxidized to a carbonyl. The theoretical and experimental isotope distribution patterns for the $[Fe^{III}(OH)(*TQA)(O_3SCF_3)]^+$ molecular ion are shown in the inset.

In order to support the hypothesis that oxidation of the TQA ligand is a self-decay pathway for complex **1**, a KIE experiment was performed by comparing the rates of self-decay of **1**-h_6 and **1**-d_6. The ligand, TQA-h_6, was converted to TQA-d_6 by treatment with NaH in a CD_3CN / D_2O mixture. The corresponding [Fe^{II}(TQA-d_6)($OTf)_2$] complex was synthesized analogously to [Fe^{II}(TQA-h_6)($OTf)_2$], and **1**-d_6 generated analogously to **1**-h_6 by treatment with 2 equivalents ArIO in acetonitrile at -40 °C.

Upon analyzing the kinetics of self-decay, **1**-d_6 demonstrates a $t_{1/2}$ of 3000 seconds, whereas the parent **1**-h_6 complex decays with a $t_{1/2}$ of 1200 seconds, giving rise to a H / D KIE of 2.5. This kinetic data gives direct evidence that the C-H / C-D bonds of the ligand are being cleaved in the rate-determining step. While it is currently unclear what the mechanism of oxidation is, whether it be intermolecular or intramolecular, this ligand oxidation represents one of the decay pathways of the $S = 2$ nonheme oxoiron(IV) complex **1**.

This type of self-decay pathway is well precedented for nonheme oxoiron(IV) complexes supported by related tripodal ligands. For example, nonheme oxodiiron(III/IV) complexes supported by the electron-rich ligand, TPA*, can only be stabilized if TPA*-d_6 is used in place of TPA*-h_6, suggesting that deuteration of the methylene protons is critical for stabilizing reactive intermediates from ligand oxidation decay pathways.

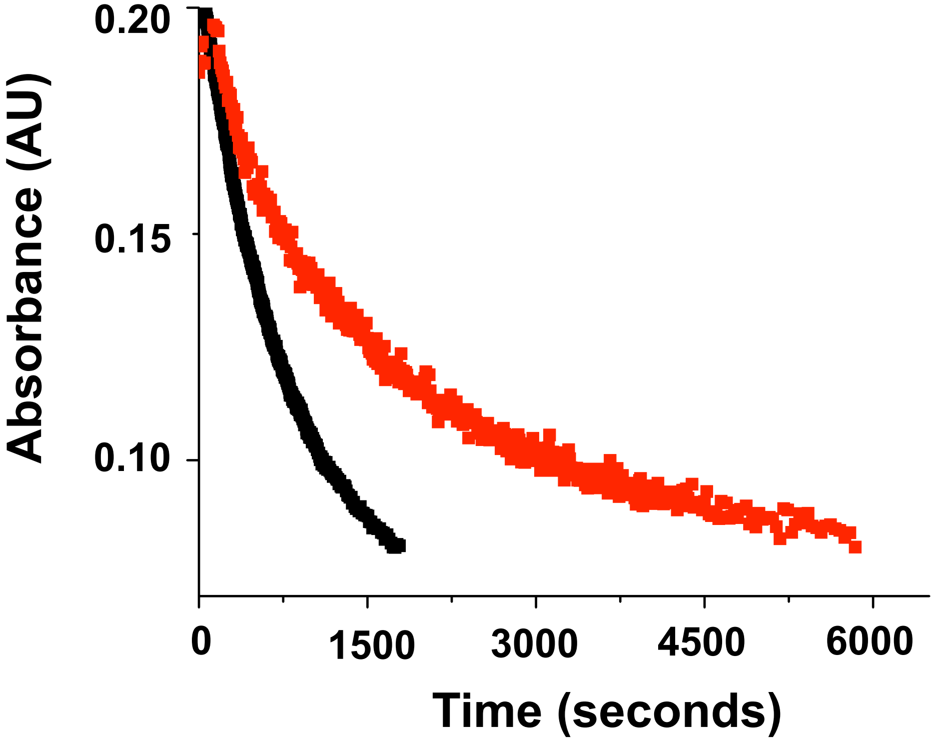

Figure 3.3. Plot of absorbance at 650 nm versus time for **1**-d_6 (red) and **1**-h_6 (black), yielding a H / D KIE of 2.5.

3.4 Hydrogen-atom Transfer (HAT) and Oxygen-atom Transfer (OAT) Reactivity of 1

3.4.*1 Cleavage of C-H bonds at -40 °C*

In addition to ligand oxidation, we evaluated the ability of **1** to oxidize hydrocarbons (Table 3.1). Oxidation of cyclohexane and cyclooctane by **1** under nitrogen afforded cyclohexanone and cyclooctanone in respective yields of 35% and 40%. As these products represent 4-e$^-$ oxidations, their yields correspond essentially to quantitative conversion of the oxidizing equivalents from **1** present in the solution.

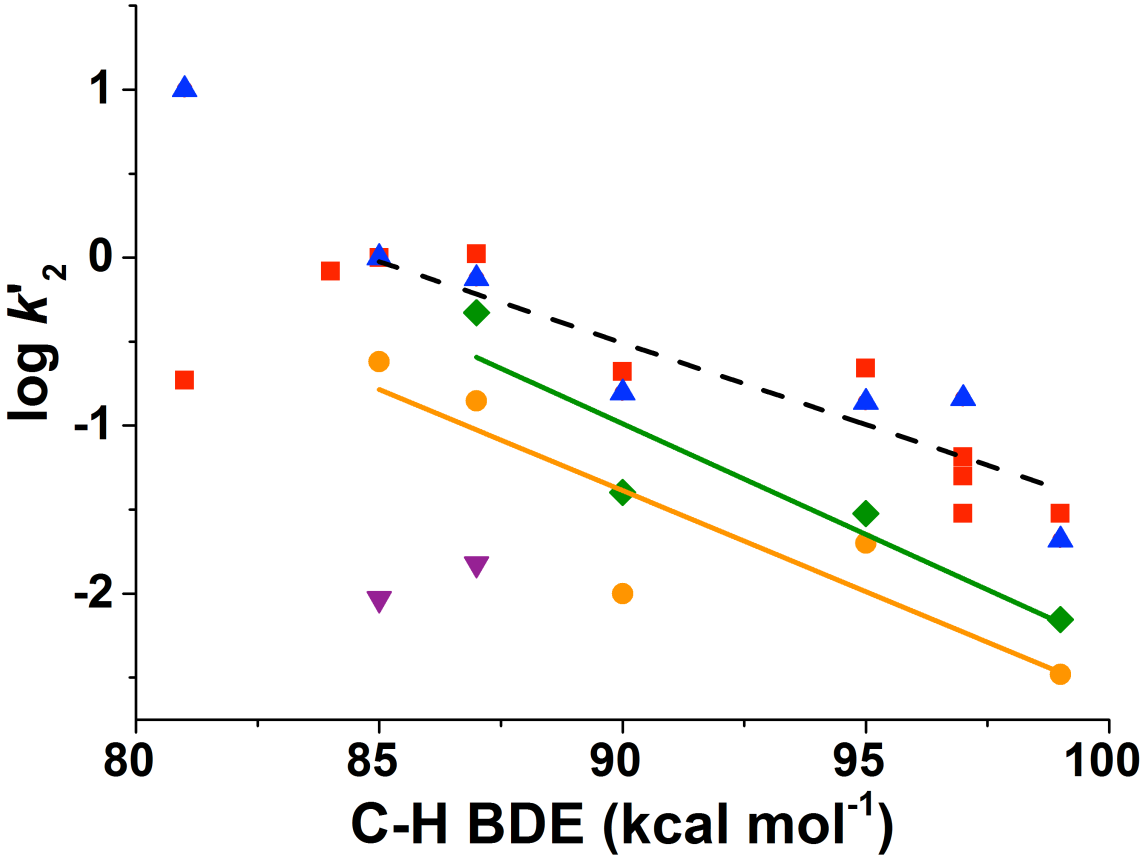

Figure 3.4. Plot of log k_2' values for the reactions of various substrates with **1** (red squares), $[Fe^{IV}(O)(Me_3NTB)(MeCN)]^{2+}$ (blue triangles), $[Fe^{IV}(O)(BQPA)(MeCN)]^{2+}$ (green diamonds), and $[Fe^{IV}(O)(QBPA)(MeCN)]^{2+}$ (purple triangles) at -40 °C, as well as $[Fe^{IV}(O)(TPA)(MeCN)]^{2+}$ (orange circles) at 25 °C, versus their C–H bond dissociation energies ($k_2' = k_2/n$ where n = the number of equivalent substrate C-H bonds).

Second order rate constants were measured for the reaction of **1** with substrates having different C–H bond strengths (Table 3.1). Figure 3 shows a plot of log k_2' values ($k_2' = k_2$/number of equivalent target C–H bonds) as a function of bond dissociation energy ($D_{C–H}$), for which a linear correlation is seen, as previously found for other high-valent oxoiron centers (Figure 3.4, black dashed line).[21,22] However, this linear relationship does not appear to hold in oxidative reactions between **1** and bulky substrates, such as diphenylmethane and triphenylmethane, where the rate of oxidation is lower than anticipated, possibly due to steric hindrance between the substrate and quinoline rings of **1**.

Complex **1** exhibits C–H/D kinetic isotope effects (KIE) of 28 and 25 for toluene and cyclohexane oxidation, respectively, showing that C–H bond cleavage is the rate determining step. The nonclassical KIE values are suggestive of hydrogen tunneling effects.[21,22] Notably, these values are larger than the KIE of ligand oxidation, measured at 2.5. This may suggest a difference in mechanism between these oxidative reactions.

Comparison of the HAT reactivity of **1** and other high-valent nonheme iron-oxo complexes (Table 3.2) shows that **1** is much more reactive at cleaving C–H bonds than other well-characterized S = 2 oxoiron(IV) complexes reported thus far.[4,23,24,25] In fact, **1** exhibits the highest cyclohexane oxidation rate (k_2 = 0.37 $M^{-1}s^{-1}$ at -40 °C) found to date for this class of complexes. Notably the closely related S = 1 $[Fe^{IV}(O)(TPA)(NCMe)]^{2+}$ complex does not react at all with cyclohexane at -40 °C. Even without correcting for the temperature difference, the cyclohexane oxidation rate we find for **1** at -40 °C is 3-4 orders of magnitude higher than k_2 values at 25 °C for S = 1 $[Fe^{IV}(O)(N4Py)]^{2+}$ and $[Fe^{IV}(O)(BnTPEN)]^{2+}$ [22] and an order of magnitude higher than that for a recently reported nonheme oxoiron(V) complex.[26]

However, the S = 1 complex $[Fe^{IV}(O)(Me_3NTB)(MeCN)]^{2+}$ (where Me_3NTB is tris((N-methylbenzimidazol-2-yl)methyl)amine) (**3**) has comparable reactivity to **1**, with k_2(cyclohexane) = 0.23 $M^{-1}s^{-1}$ at -40 °C.[21] Indeed, the HAT data points for $[Fe^{IV}(O)(Me_3NTB)(MeCN)]^{2+}$ (Figure 3.4, blue triangles)[21] fall on the same trend line as those for **1** (Figure 3.4, black dashed line). This surprising resemblance suggests that two nonheme oxoiron(IV) complexes, despite having different ground spin states, can achieve comparably high HAT reactivity. On the basis of DFT calculations, Nam and Shaik rationalized the high HAT reactivity of $[Fe^{IV}(O)(Me_3NTB)(MeCN)]^{2+}$ by invoking a highly reactive close-lying $S = 2$ excited state.[21]

In addition, the rates of substrate oxidation with **1** were compared to unpublished results on related $S = 1$ complexes, $[Fe^{IV}(O)(TPA)(MeCN)]^{2+}$, $[Fe^{IV}(O)(QBPA)(MeCN)]^{2+}$, and $[Fe^{IV}(O)(BQPA)(MeCN)]^{2+}$, obtained by Dr. Jale Ocal and Dr. Joan Serrano-Plana. As noted earlier, the reactions with $[Fe^{IV}(O)(TPA)(MeCN)]^{2+}$ were too slow to monitor at -40 °C, so Dr. Ocal instead carried them out at 25 °C (Figure 3.4, orange circles). Despite the 65 °C lower temperature, complex **1** is still nearly an order of magnitude faster in cyclohexane oxidation than $[Fe^{IV}(O)(TPA)(MeCN)]^{2+}$. In contrast, Dr. Serrano-Plana found the rates of oxidation with $[Fe^{IV}(O)(BQPA)(MeCN)]^{2+}$ (Figure 3.4, green diamonds) to be comparable to $[Fe^{IV}(O)(Me_3NTB)(MeCN)]^{2+}$ and complex **1** at -40 °C, giving rise to a second example of a $S = 1$ oxoiron(IV) complex that demonstrates reactivity close to the $S = 2$ oxoiron(IV) complex **1**. Finally, the slopes observed in this plot are similar amongst all the complexes examined, suggesting a shared mechanism for C-H bond cleavage and a similar transition-state for reaction between these substrates and the oxoiron(IV) intermediates, despite the difference in ground spin state. An interesting data point involves the oxidation of toluene, which is lower than expected based on the slope of the line for complex **1**, $[Fe^{IV}(O)(Me_3NTB)(MeCN)]^{2+}$, $[Fe^{IV}(O)(BQPA)(MeCN)]^{2+}$, and $[Fe^{IV}(O)(TPA)(MeCN)]^{2+}$. This systematic deviation may imply an incorrect BDE value associated with toluene or a difference in mechanism compared to the other substrates. However, a drastically different mechanism for toluene oxidation is unlikely given the reported KIE of 28 for complex **1**, which is consistent with a HAT-type mechanism.[27]

Table 3.1. Summary of oxidation data for complex **1.**

Substrate	**$D_{C\text{-}H}$ kcal/mol**	**k_2 ($M^{-1}s^{-1}$)**	**k_2' ($M^{-1}s^{-1}$)**	**Products (equiv/Fe [a])**	**KIE**
Triphenylmethane	81	0.19	0.19		
Diphenylmethane	83	1.7	0.8		
Cumene	85	1	1		
Ethylbenzene	87	2.1	1.1	Acetophenone (0.35)	
Toluene	90	0.64	2.1×10^{-1}		28
Cyclooctane	95	3.5	2.2×10^{-1}	Cyclooctanone (0.40)	
Cyclopentane	97	0.32	3.0×10^{-2}		
2,3-dimethyl-butane	97	0.13	6.5×10^{-2}		
tert-butyl methyl ether	97	1.5×10^{-1}	5.0×10^{-2}		
Butane	98	-	-	2-butanone (0.30) 2-butanol (0.08)	-
Cyclohexane	99	0.37	3.0×10^{-2}	Cyclohexanone (0.35)	25
cis-cyclooctene		3.3		Epoxycyclooctane (0.55)	
1-octene		5.3		1,2-epoxyoctane (0.35) 1-octen-3-one (0.15)	
cis-2-heptene		-		*cis*-epoxide (0.28) *trans*-epoxide (0.02)	
trans-2-heptene		-		*trans*-epoxide (0.36)	
Cyclohexene		-		2-cyclohexen-1-one (0.07) 2-cyclohexen-1-ol (0.36)	
Styrene		0.67		Styrene oxide (1.8)	

[a] Fe corresponds to the amount of $[Fe^{II}(TQA)(OTf)_2]$ used to generate **1**.

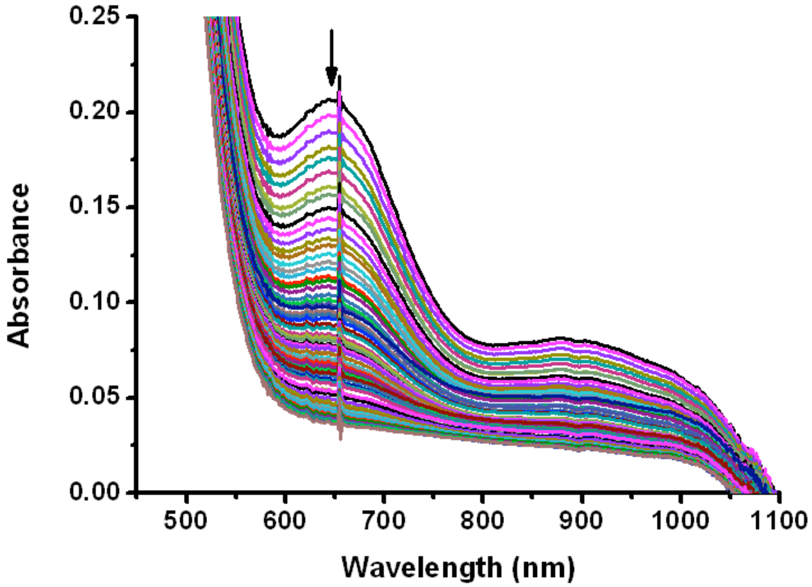

Figure 3.5. Spectral changes observed over time in the reaction of **1** (1.0 mM) and toluene (50 mM) in CH_3CN at -40 °C.

3.4.2 *Cleavage of C-H Bonds at -80 °C*

While S = 2 nonheme oxoiron(IV) complexes with a trigonal bipyramidal geometry have shown a limited degree of reactivity, nonheme oxodiiron(III/IV) species containing a terminal S = 2 oxoiron(IV) center have been shown to be potent oxidants, cleaving C-H bonds at temperatures as low as -80 °C.[19]

To be able to place the HAT reactivity of complex **1** with those the S = 2 oxoiron(IV) units in nonheme oxodiiron(III/IV) species, we measured the DHA oxidation rate of **1** at -80 °C in a 1 : 3 mixture of CD_3CN : acetone-d_6, allowing us to obtain a k_2 value of 200 $M^{-1}s^{-1}$ (Figure 3.6). This comparison shows that **1** is almost as reactive with DHA as the S = 2 oxoiron(IV) units in nonheme oxodiiron(III/IV) species (Figure 3.7).[19]

This is an important point, as it suggests that the high reactivity of these species is independent of whether the *S* = 2 $Fe^{IV}(O)$ unit is in a mononuclear or a dinuclear framework. These results further support our idea that the $(X)(TPA^*)Fe^{III}–O^-$ unit in these dinuclear systems can be construed simply as a 6th ligand for the *S* = 2 oxoiron(IV) center. In addition, the *S* = 2 nonheme oxoiron(IV) complexes in the plot (red bars) all shown higher reactivity that the related *S* = 1 nonheme oxoiron(IV) complexes (blue bars). However, as previously noted, this relationship does not seem to hold when the ligand framework is changed from pyridine donors to benzimidazole donors, where the *S* = 1 nonheme oxoiron(IV) complex $[Fe^{IV}(O)(Me_3NTB)(MeCN)]^{2+}$ has been shown to be just as reactive as the *S* = 2 oxoiron(IV) complex **1**.[21]

Interestingly, while we were able to measure the rate of DHA oxidation by **1** at -80 °C, similar attempts to oxidize 1,4-cyclohexadiene (CHD) were unsuccessful due to the reaction rate being too fast to accurately monitor. Thus, despite both substrates having a similar BDE of 77 kcal/mol, the reaction between **1** and DHA is qualitatively slower than that with CHD, perhaps due to steric hindrance between the TQA ligand of **1** and the bulky DHA substrate. This is supported by the observation that DHA oxidation with $[Fe^{IV}(O)(Me_3NTB)(MeCN)]^{2+}$ at -80 °C is also too fast to monitor, suggesting **1** reacts slower than $[Fe^{IV}(O)(Me_3NTB)(MeCN)]^{2+}$ when the substrate is sterically bulky. Similarly, the reactions between diphenylmethane and triphenylmethane and complex **1** at -40 °C do not follow the linear dependence of C-H BDE, likely due to steric hindrance between the substrate and oxoiron(IV) complex (Figure 3.4).

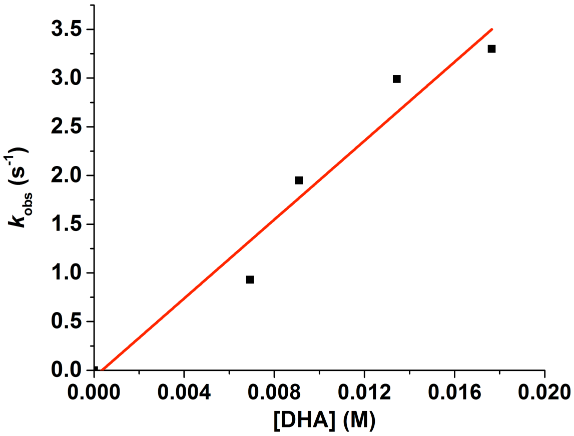

Figure 3.6. Plot of the pseudo-first-order rate constants, k_{obs} (s^{-1}), versus DHA concentration for the reaction of **1** (1.0 mM) with DHA in a 3:1 mixture of acetone-d_6: acetonitrile-d_3 at -80 °C.

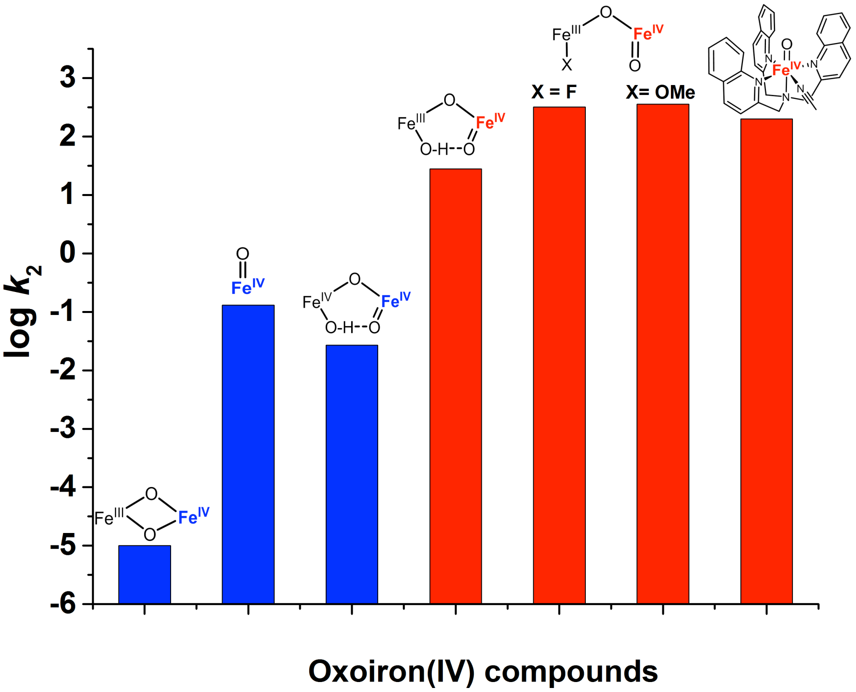

Figure 3.7. Second order rate constants for the reaction of oxoiron(IV) complexes with 9,10-dihydroanthracene (DHA) at -80 °C. Red bars indicate complexes with an S = 2 oxoiron(IV) center, while blue bars indicate complexes with an S = 1 oxoiron(IV) center.

All iron centers are supported by the TPA* ligand, except complex **1**, which is supported by the TQA ligand.

Table 3.2. Comparison of HAT and OAT rates of select *S* = 1 and *S* =2 nonheme oxoiron(IV) complexes.

$[Fe^{IV}(O)(L)(MeCN)]^{2+}$	**CHD/ DHA 77 kcal/mol**	**Tri phenyl methane 81 kcal/mol**	**Cumene 85 kcal/mol**	**Ethyl benzene 87 kcal/mol**	**Toluene 90 kcal/mol**	**Cyclo octane 95 kcal/mol**	**Cyclo hexane 99 kcal/mol**	**Thio ani sole**	**Ref**
1	200 DHA (-80)	0.19 (-40)	1 (-40)	2.1 (-40)	0.64 (-40)	3.5 (-40)	0.37 (-40)		5, 27
2					0.05 (-40)				28
3					0.07 (-40)				28
$[Fe^{IV}(O)(Me_3NTB)(MeCN)]^{2+}$	940 CHD (-40) --- 3100 DHA (-40)	10 (-40)	1 (-40)	1.5 (-40)	0.47 (-40)	2.2 (-40)	0.25 (-40)	2.1 x 10^{4} (-40)	21
$[Fe^{IV}(O)(BQPA)(MeCN)]^{2+}$				0.94 (-40)	0.12 (-40)	0.52 (-40)	0.09 (-40)		29
$[Fe^{IV}(O)(QBPA)(MeCN)]^{2+}$		1.6 x 10^{-4} (-40)	9.3 x 10^{-3} (-40)	3.1 x 10^{-2} (-40)				2.4 x 10^{-2} (-40)	29, 30
$[Fe^{IV}(O)(TPA)(MeCN)]^{2+}$		7.0 x 10^{-5} (-40)	0.24 (25)	0.27 (25)	0.03 (25)	0.16 (25)	0.04 (25)	9.7 x 10^{-4} (-40)	30, 31
$[Fe^{IV}(O)(TPA^*)(MeCN)]^{2+}$	0.13 DHA (-80)								19
$[(HO)(L)Fe^{IV}\text{-}O\text{-}Fe^{IV}(O)(L)]^{3+}$ L = TPA*	0.027 DHA (-80)								19
$[(HO)(L)Fe^{III}\text{-}O\text{-}Fe^{IV}(O)(L)]^{2+}$ L = TPA*	28 DHA (-80)								19
$[(F)(L)Fe^{III}\text{-}O\text{-}Fe^{IV}(O)(L)]^{2+}$ L = TPA*	322 DHA (-80)								19

$[(MeO)(L)Fe^{III}\text{-}O\text{-}Fe^{IV}(O)(L)]^{2+}$ **L = TPA***	360 DHA (-80)								19
$[Fe^{IV}(O)(TMG_3tren)]^{2+}$	1.2 CHD (-30) --- 0.090 DHA (-30)								23
$[Fe^{IV}(O)(TMG_2dien)(MeCN)]^{2+}$	18 CHD (-30) --- 57 DHA (-30)								4
$[Fe^{IV}(O)(tpa^{Ph})]^{-}$	1.4 CHD (-40)								25
$[Fe^{IV}(O)(N4Py)]^{2+}$	0.07 CHD (-40)						0.000055 (25)		22
$[Fe^{IV}(O)(BnTPEN)]^{2+}$	0.96 CHD (-40)						0.00039 (25)		22
$[Fe^{V}(O)(TAML)]^{-}$							0.023 (25)		26

3.4.3 *OAT Reactions with Olefins*

Complex **1** is also capable of oxidizing olefins to their corresponding epoxides (Table 3.1). Although commonly associated with oxoiron(IV) porphyrin cation radical complexes,[32] olefin epoxidation has only been reported for three nonheme oxoiron(IV) complexes, in reactions limited to only one or two types of olefins. Banse reported the epoxidation of cyclooctene and *cis*-stilbene in <20% yield by a $[Fe^{IV}(O)(N5)]$ complex.[33] Rybak-Akimova found that a complex supported by a pyridine containing tetraazamacrocycle afforded 80% yield of cyclooctene oxide with a k_2 of 0.45 $M^{-1}s^{-1}$ at 0 °C,[34] while Nam obtained 60% yield of styrene oxide from $[Fe^{IV}(O)(N3S2)]^{2+}$ (where N3S2 is 2,6-bis-(2-methylthiophenyliminomethyl)pyridine) with a $k_2 = 0.03$ $M^{-1}s^{-1}$ at 25 °C.[35] Although Que and co-workers initially reported the epoxidation of *cis*-cyclooctene by $[Fe^{IV}(O)(TPA)(NCMe)]^{2+}$,[36] subsequent studies with rigorous exclusion of O_2 showed no epoxide formation from cyclooctene and cyclohexene.[37] In contrast, **1** reacted with *cis*-cyclooctene at -40 °C to form epoxide in 80% yield relative to the amount of **1** present in solution. The k_2 value for cyclooctene epoxidation was determined to be 3.3 $M^{-1}s^{-1}$ (Table 3.1), a value that is orders of magnitude faster than those for the $S = 1$ oxoiron(IV) complexes mentioned above (given the higher temperatures at which the latter results were obtained). These comparisons suggest a significantly higher reactivity of the $S = 2$ complex **1** towards C=C bonds than found for its $S = 1$ nonheme counterparts. However, due to the paucity of rate data for such reactions, additional examples are needed to draw firm conclusions on the role of spin state on the rates of epoxidation.

The reactions of **1** with other olefins were investigated. Epoxidation of *cis*- and *trans*-2-heptene exhibited a high degree of stereoretention, 87% for the *cis* isomer and >99% for the *trans* isomer, indicating that substrate-based radical intermediates if formed must be short-lived. Interestingly, 1-octene was oxidized by **1** with a k_2 value of 5.3 $M^{-1}s^{-1}$; however in this case, both the epoxide and 1-octen-3-one were observed in respective yields of 35% and 15% relative to $[Fe^{II}(TQA)(OTf)_2]$, representing 90% of the oxidizing equivalents available from **1**. On the other hand, cyclohexene oxidation by **1** afforded only allylic oxidation products. These results show that **1** can mediate the oxidation of both C–H and C=C bonds at comparable rates. Indeed the k_2 values for cyclooctene and cyclooctane oxidation by **1** are identical, indicating that **1** attacks the cyclooctene C=C bond only 16-fold faster than the 95-kcal/mol C–H bond of cyclooctane, which was confirmed by a competitive oxidation of equimolar amounts of the two substrates that afforded 35% cyclooctene oxide and 15% cyclooctanone. These results represent the first instance for which the rates of C=C and C–H bond attack by a nonheme oxoiron(IV) complex can be compared directly, which emphasizes the uniqueness of complex **1** within the nonheme iron-oxo family.[27]

Complex **1** was also capable of oxidizing styrene to give the corresponding epoxide in nearly quantitative yield relative to the oxidant, with 2 equivalents of ArIO yielding 1.8 equivalents of styrene oxide, implying catalytic activity. This catalytic behavior may be derived from the lack of allylic C-H bonds in the substrate, the presence of which may introduce an alternative oxidation pathway involving HAT. By eliminating potential HAT reactions in styrene, complex **1** is forced to undergo OAT, which likely allows the system to maintain a Fe^{II} / Fe^{IV} cycle and undergo catalysis. The rate of styrene oxidation was measured at 0.67 $M^{-1}s^{-1}$, which is approximately five-fold slower than the oxidation of *cis*-cyclooctene and 1-octene. In addition, a Hammet plot was carried out with *para*-substituted styrene substrates, revealing a ρ value of -1.9 (Figure 3.8), which suggests an electrophilic oxidation mechanism. This is nearly identical to the ρ value of -2.0 measured by Nam and co-workers for the oxidation of styrene derivatives by $Fe^{IV}(O)(N3S2)]^{2+}$.[35] Notably, the bulkier olefin, *cis*-stilbene, was found not to react with complex **1**, likely due to steric hindrance between the TQA ligand of **1** and the substrate. Steric hindrance is also observed in HAT reactions with complex **1** and bulky substrates such as diphenylmethane and triphenylmethane (Figure 3.4)

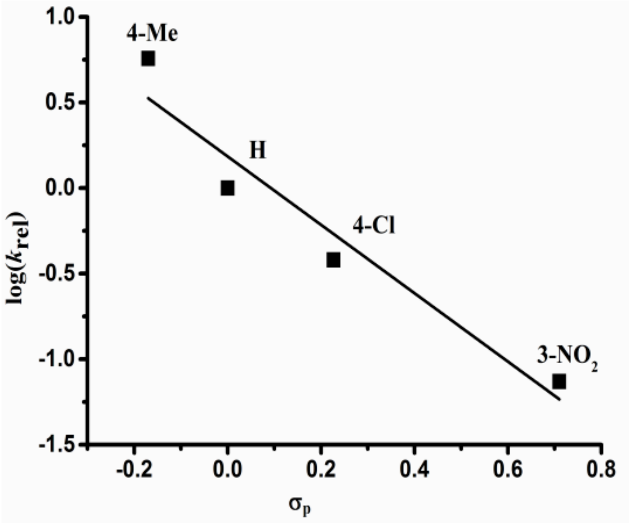

Figure 3.8. Hammett plot for the oxidation of styrene and *para*-substituted styrene with **1** (1.0 mM) in CH_3CN at -40 °C, where σ^+ values were used on the x-axis to give a slope, or ρ value, or -1.9.

3.5 Evaluating Complex 1 for Oxygen-Rebound

In order to determine if rebound is occurring in the hydroxylation of C-H bonds by the *S* = 2 nonheme oxoiron(IV) complex **1**, reactions with **1**-^{18}O and cyclohexane were carried out. However, it was soon discovered that the sole product of cyclohexane oxidation, cyclohexanone, rapidly undergoes oxygen-atom exchange with residual amounts of $H_2{}^{16}O$ in the presence of the decay products of **1**, causing loss of the ^{18}O-labeling in cyclohexanone and making the experiments irreproducible. For this reason, we sought out an organic substrate that could not over-oxidize to a ketone, thereby preventing oxygen-atom exchange with adventitious water in solution. Triphenylmethane oxidation leads solely to the alcohol product, triphenylmethanol, making it an ideal candidate for these rebound studies.

Formation of **1**-^{18}O could be accomplished by reaction of $[Fe^{II}(TQA)(OTf)]_2$ with ArI^{18}O in acetonitrile at -40 °C. Ar^{18}O is synthesized upon dissolving ArIO in CD_2Cl_2 or

2,2,2-trifluoroethanol and adding $H_2{}^{18}O$ to the resulting solution, causing the rapid oxygen-atom exchange between ArIO and $H_2{}^{18}O$. This procedure could be monitored by ESI-MS, as shown in Figure 3.8. Here the ESI-MS of ArIO illustrates the presence of 55% ^{18}O-ArIO and 45% ^{16}O-ArIO, likely due to residual $H_2{}^{16}O$ in the acetonitrile solvent during generation of ^{18}O-ArIO.

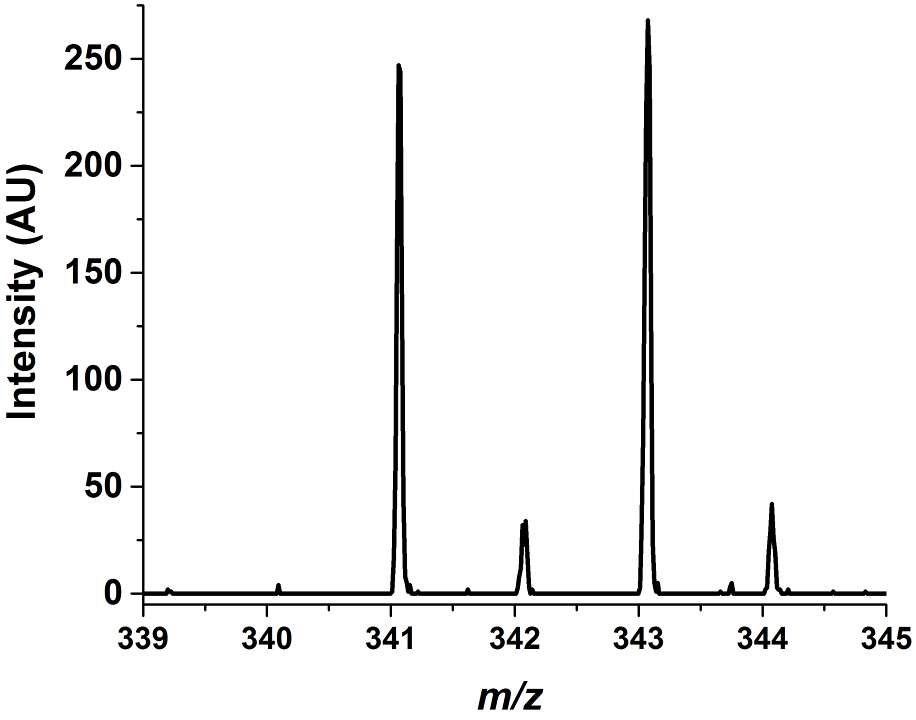

Figure 3.9. ESI-MS of ArIO in TFE, indicating a mixture of 55% ^{18}O-ArIO and 45% ^{16}O-ArIO.

Under an N_2 atmosphere, the reaction between **1** and triphenylmethane yielded triphenylmethanol with an isotopomer ratio of 59% ^{18}O and 41% ^{16}O, within a +/- 5% error of the labeling observed for $ArI^{18}O$ (Figure 3.10). This result is significant, as it suggests the labeling originating from the oxidant remains intact upon incorporation into the oxidized product. This suggests that the substrate oxidation mechanism of **1** indeed follows a rebound mechanism.

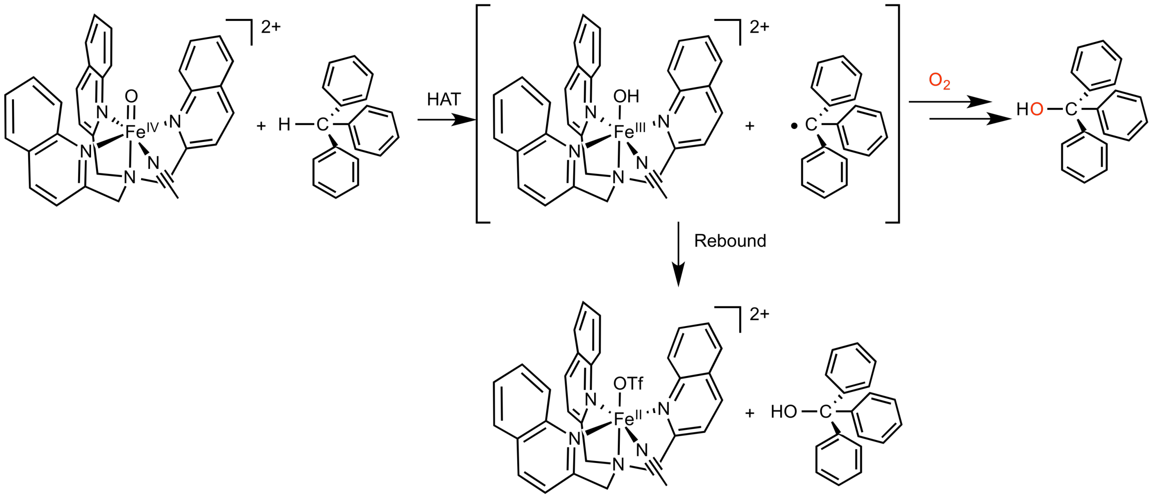

Figure 3.10. Proposed C-H bond hydroxylation mechanisms for complex **1**.

However, in the presence of $^{16}O_2$, the same reaction yielded triphenylmethanol with an isotopomer ratio of 30% ^{18}O and 70% ^{16}O, suggesting that half of the ^{18}O-labeling has decreased due to reaction with $^{16}O_2$ (Figure 3.10). This implies that the rate of rebound is comparable to the rate of radical interception by $^{16}O_2$, unlike for heme systems where the rate of rebound is significantly faster.[38]

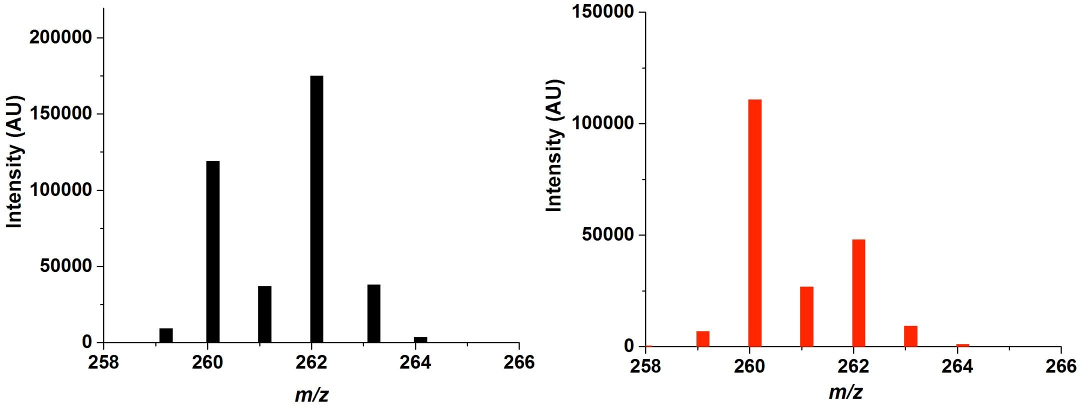

Figure 3.11. Mass spectra of triphenylmethanol produced by the reaction of **1** and triphenylmethane under Ar (left, black) and $^{16}O_2$ (right, red) in acetonitrile at -40 C.

Table 3.3. Summary of oxygen-rebound data for select *S* = 1 and *S* = 2 nonheme oxoiron(IV) complexes.

$(L)Fe^{IV}(O)$	**Spin State**	**Product analyzed**	**% ^{18}O-product (under Ar)**	**% ^{18}O-product (under $^{16}O_2$)**	**% Rebound (under $^{16}O_2$)**	**Ref**
TQA	2	Triphenylmethanol	59	30	50%	This work
PyTACN	1	Triphenylmethanol	90	78	87%	39
BnTPEN	1	Cyclohexanol	100	23	23%	11

Comparison of these rebound results with *S* = 1 nonheme oxoiron(IV) complexes reveal a similar behavior, where rebound proceeds under a N_2 atmosphere and is found to be competitive with radical interception in the presence of radical scavengers, such as $^{16}O_2$. This suggests two things – first, the rate of rebound is slower in nonheme systems than heme systems, and second that there does not appear to be an intrinsic difference in the rate of rebound between *S* = 1 and *S* = 2 nonheme oxoiron(IV) complexes.

3.6 Evaluating Complexes 2 and 3 For Halogen Rebound

Halogen rebound was tested for the *S* = 2 nonheme oxoiron(IV)-halide complexes, **2** and **3**. As noted earlier, the reaction between **1** and cyclohexane produces 35% cyclohexanone as the oxidation product, a 4-electron oxidation that is consistent with the 70% yield of **1** in acetonitrile solution at -40 °C.[27] In extending our reactivity study to **2** and **3**, we found that their reactions with cyclohexane at -40 °C afforded halocyclohexanes, cyclohexanol and cyclohexanone as products, as identified by ^{1}H NMR spectroscopy (Figures 3.23 - 3.27).[28] The halogenated products were obtained at 3- to 6-fold higher yields than the oxygenated products (Table 3.4). With toluene as substrate, more comparable yields of halogenated and oxygenated products were observed. These results represent the first examples of substrate halogenation by a bona fide synthetic *S* = 2 Fe^{IV}(O)X complex, thereby mimicking the reactivity of the oxoiron(IV)-halide intermediates of SyrB2 and CytC3.[28]

Table 3.4. Products from the reactions of **1**, **2** and **3** with cyclohexane and toluene in CD_3CN solution at -40 °C.[a]

Reaction products	**Cyclohexane**			**Toluene**		
	1 [b]	**2**	**3**	**1**	**2**	**3**
R–X	-	35%	41%	2% [c]	25%	33%
R–OH	-	7%	3%	27%	13%	7%
R=O	35%	3%	4%	15%	19%	22%

[a] Reactions of 0.5 M substrate with 1 mM **1**, **2**, or **3** were carried out under anaerobic

conditions. The product yields are relative to $Fe(TQA)(OTf)_2$ and reflect the average of three runs. Complexes **2** and **3** were obtained by treatment of **1** with 1 equiv. NBu_4Cl/Br; **1** in turn was generated from the reaction of $[Fe^{II}(TQA)(OTf)_2]$ and 2 equiv. ArIO (dissolved in CD_2Cl_2) in CD_3CN at -40 °C. [b] Results from ref 14. [c] The small amount of benzyl chloride observed in the reaction of **1** with toluene likely derives from benzyl radical interception by the CD_2Cl_2 used to dissolve ArIO. Parallel experiments with 2,2,2-trifluoroethanol in place of CD_2Cl_2 showed no halogenated product.

To gain more insight into the halogenation reactions, kinetic studies were carried out on **2** and **3**. For cyclohexane oxidation, **2** and **3** decayed at rates comparable to self-decay, so second order rate constants could not be determined accurately. On the other hand, toluene was oxidized at significantly faster rates due to its weaker aliphatic C–H bonds. Kinetic measurements showed that **2** and **3** reacted with toluene at rates approximately 10-fold smaller than **1** (Figure 3.11, Figures 3.28 and 3.29), reflecting the trend in decreased substrate C–H bond cleaving rates observed for the oxoiron(IV) intermediates of the halogenases SyrB2 and CytC3 versus TauD-***J***.[13] Interestingly, this reactivity trend is opposite to that for the $S = 1$ $[Fe^{IV}(O)(PyTACN)(X)]^+$ complexes, where the halo variants are 2-3 fold faster at oxidizing 9,10-dihydroanthracene (DHA) than the parent MeCN complex.[39] With these results in mind, there are three important mechanistic points to clarify about the observed halogenation of cyclohexane and toluene: a) the nature of the species that cleaves the substrate C–H bond, b) whether the classic rebound mechanism applies to **2** and **3**, and c) the chemoselectivity between hydroxylation and halogenation.

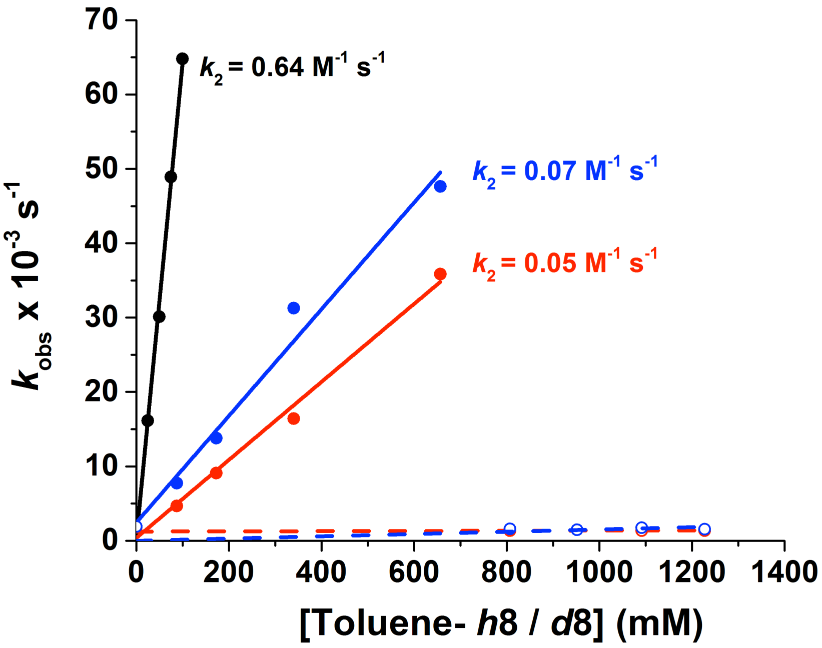

Figure 3.12. Plot of pseudo-first order rate constants (k_{obs}) versus toluene-h_8/d_8 concentration for **1** (black), **2** (red), and **3** (blue). Solid lines indicate reactions with toluene-h_8 and dashed lines indicate reactions with toluene-d_8.

To ascertain that the Fe=O unit in **2** and **3** was responsible for the halogenation, we have measured the kinetic isotope effect for C–H bond cleavage with toluene as the substrate. As shown in Figure 2, the oxidation of toluene-h_8 by **2** and **3** is significantly faster than that of toluene-d_8, which occurs at a rate comparable to that of self-decay (Figure 3.11, dashed blue and red lines). These results show that C–H bond cleavage by the oxoiron(IV) species **2** and **3** must be the rate-determining step, with a KIE well above the classical limit of 7. Other nonheme oxoiron(IV) complexes have been found to exhibit large nonclassical KIE, implicating a significant contribution from a tunneling mechanism for H-atom abstraction.[21,22] A more accurate estimate of the KIE could be obtained from the benzyl bromide-h_7/d_7 product ratio for the intermolecular competitive halogenation of toluene-h_8 and toluene-d_8 by **3**. A value of 20 was obtained (Figure 3.12), which is comparable to the KIE of 25 reported for the oxidation of toluene by **1**.[27] The observed large KIE also excludes the possibility of free radical bromination of toluene, for which a much smaller KIE value of 4.9 has been reported in such a reaction with toluene-α-d_2;[40] furthermore, the yield of R–Br did not increase with the addition of excess bromide ion and in fact decreased by 30% with 5-20 equiv. of added bromide ion (Table 3.5). Even more importantly, the toluene KIE value we measured for **3** is essentially identical to that reported by Matthews *et al.* for oxidation of the C4-protio and C4-deuterio native substrate in SyrB2.[13] Taken together, these data support the notion that the initial C–H bond cleavage step occurs via H-atom abstraction by the oxoiron(IV)-halide complexes **2** and **3**.

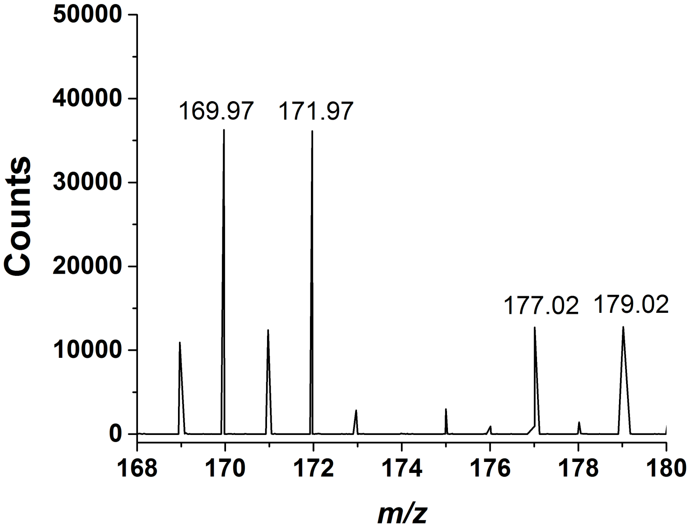

Figure 3.13. Mass-spectrum of the reaction between **3** and 500 equivalents of a 10 : 1 mixture of toluene-d_8 : toluene-h_8 in CH_3CN at -40 °C, displaying the peaks for benzyl bromide-h_7 $\{C_7H_7Br\}^+$ (169.97 m/z, 171.97 m/z) and benzyl bromide-d_7 $\{C_7D_7Br\}^+$ (177.02 m/z, 179.02 m/z), giving an approximate H/D ratio of 2, giving rise to a KIE of 20.

Table 3.5. Product distribution for the reaction of **3** with cyclohexane in CD_3CN at -40 °C with varying eq. of NBu_4Br.

	0 eq	**1 eq**	**2 eq**	**5 eq**	**10 eq**	**20 eq**
R–X	0%	41%	36%	30%	26%	25%
R–OH	0%	3%	0%	0%	0%	0%
R=O	35%	4%	3%	0%	0%	0%

H-atom abstraction from the substrate should initially convert **2** and **3** into hydroxoiron(III)-halide species together with an organic radical within a solvent cage (Figure 3.13). If the P450 paradigm applies to this chemistry,[10] the alkyl radical would then react with the incipient $Fe^{III}(OH)X$ species in a rapid rebound step to yield hydroxylated or halogenated products. Alternatively, the radical may be longer lived than found in heme systems and react with other species in solution,[11] such as residual $Fe^{IV}(O)X$ or radical traps such as O_2. The latter mechanistic outcome has been demonstrated experimentally by Nam in studies of several $S = 1$ nonheme oxoiron(IV) complexes.[11]

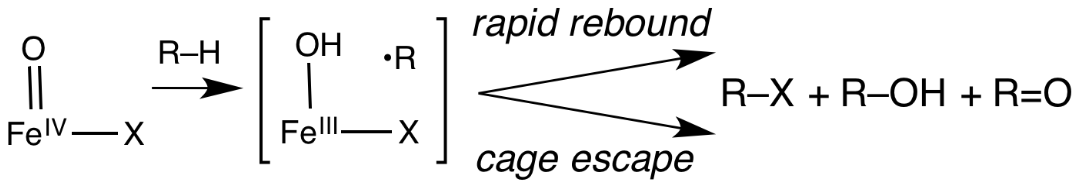

Figure 3.14. Proposed mechanisms for substrate hydroxylation and halogenation by **2** and **3**.

To assess the lifetime of the nascent substrate alkyl radical produced in the reactions of **2** and **3**, O_2 was introduced into the reaction mixture to act as a radical trap (Figure 3.13). In reactions of **2** and **3** with either cyclohexane or toluene, the introduction of O_2 resulted in no halogenation and exclusive formation of oxygenated products (Table 3.6). These results show that C–X bond formation with the alkyl radical occurs at a slower rate than that for its interception by O_2, strongly suggesting that these complexes do not follow the classic heme-based rebound mechanism.[10,38] In fact, it is possible to estimate the rate constant for radical recombination, based on the concentration of O_2 in acetonitrile, which has been measured to be 8 mM at 25 °C,[41a] and the rate of O_2 interception by a cyclohexyl radical, which has been measured to be 8×10^{9} $M^{-1}s^{-1}$ at 25 °C in the gas phase,[41b] giving rise to an estimated rate constant of $\sim 10^{7}$ s^{-1}. This value is certainly an approximate as our reactions were carried out at -40 °C instead of 25 °C, and the estimated second-order rate constant relates to the gas phase and not the solution phase. Regardless, this value may still be compared to heme systems, where the rate constant for radical combination has been measured as 10^{10} s^{-1}, suggesting that our nonheme oxoiron(IV) complexes undergo rebound slower than their counterparts in heme systems.

Consistent with this interpretation, Mössbauer experiments performed on frozen solutions of **3** after reaction with toluene and cyclohexane reveal only Fe^{III} decay products (Figure 3.30), which is inconsistent with a rapid rebound scenario. These observations concur with recent results of Nam who has raised questions about the applicability of the heme paradigm to high-valent nonheme metal-oxo species.[11]

However, both these results are at odds with a recent report by Maiti providing ESI-MS evidence for oxygen rebound in the reactions of an electron-rich *S* = 1 oxoiron(IV) complex.[12] In addition, the results for **2** and **3** appear to differ from complex **1**, where the rate of oxygen-rebound was noted to be comparable to the rate of radical escape and O_2 interception. Clearly, more effort is required to clarify what factors control the rate of rebound in synthetic nonheme iron systems.

Table 3.6. Product yields (versus $Fe(TQA)(OTf)_2$) for the reactions of **2** and **3** with substrates in CD_3CN at -40 °C under N_2 and O_2.

Oxidation products	**Cyclohexane**		**Toluene**	
	N_2	**O_2**	**N_2**	**O_2**
R–Cl	35%	0%	25%	0%
R–OH	7%	22%	13%	9%
R=O	3%	39%	19%	73%
R–Br	41%	0%	33%	0%
R–OH	3%	8%	7%	8%
R=O	4%	24%	22%	58%

Lastly, our results also shed some light on the chemoselectivity of C–X bond formation. Table 2 shows that **2** and **3** favor formation of the halogenated product over oxygenated products in the oxidation of cyclohexane, but comparable amounts of the two types of products are obtained in the oxidation of toluene. These results suggest an inherent chemoselectivity that influences which product is formed. Ligand transfer preference may be influenced by electronic factors such as the oxidizability of the ligand where Cl^- and Br^- have lower oxidation potentials (1.36 V, 1.07 V, respectively) versus OH^- (2.02 V).[42] Steric factors may also play a role, given that the quinoline donors may partially shield the oxo/hydroxo ligand from attack by the nascent alkyl radical, which would be consistent with the greater halogenation yield observed for the sterically bulkier cyclohexane substrate. Additional work is required to assess the relative contributions of electronic and steric factors in determining the chemoselectivity observed in our synthetic models. On the other hand, the chemoselectivity of C–H bond functionalization in SyrB2 has been shown to be controlled by the positioning of the organic substrate within the active site relative to the nascent oxoiron(IV)-halide oxidant.[13]

3.7 Discussion

The reactivity of the $S = 2$ nonheme oxoiron(IV) complexes, **1** – **3**, has been explored. In the absence of external substrates, complex **1** undergoes ligand oxidation as a route of self-decay, giving rise to a KIE of 2.5 when the methylene protons of the ligand TQA-h_6 are deuterated to TQA-d_6. This self-decay pathway can be retarded by the introduction of an organic substrate with susceptible C-H bonds. Complex **1** was found capable of oxidizing a wide variety of hydrocarbons with C-H bond dissociation energies up to 99 kcal/mol.[27] Notably, the C-H/D KIE for the oxidation of toluene and cyclohexane was found to be 25 and 28,[27] respectively, suggesting both that C-H bond cleavage is the RDS in these oxidation reactions and that hydrogen-atom tunneling may be involved in the mechanism. The KIE of 25 – 28 for substrate oxidation is much larger than the KIE of 2.5 for ligand oxidation, suggesting a possible difference in the mechanism of oxidation in these two sets of reactions.

Complex **1** demonstrates the fastest rates of cyclohexane oxidation of any nonheme oxoiron(IV) complex to date. However, it is only 1.5x faster than the $S = 1$ nonheme oxoiron(IV) complex, $[\mathrm{Fe^{IV}(O)(Me_3NTB)(MeCN)}]^{2+}$, suggesting that the ground spin state may not dictate reactivity.[21] Instead, Mayer has argued that the HAT reactivity of an oxoiron(IV) complex is related to the strength of the O–H bond formed in the reaction, which in turn depends on the $\mathrm{Fe^{IV/III}}$ potential and the $\mathrm{p}K_a$ of the $\mathrm{Fe^{III}}$–OH moiety,[43] but these properties have proven difficult to measure. Indeed only Borovik has thus far been able to determine such thermodynamic properties for an oxoiron(IV) complex.[44] Regardless, complex **1** is a extremely potent oxidant, with the rate constant of $0.37\ \mathrm{s^{-1}}$ at -40 °C for oxidizing 1 M cyclohexane by **1** comparing favorably with the $13\ \mathrm{s^{-1}}$ rate constant for taurine oxidation by TauD-***J*** at 5 °C, after correction for the 45° temperature difference.[45]

We have also presented evidence for oxygen-rebound with complex **1**, the first evidence for rebound in $S = 2$ nonheme oxoiron(IV) systems. In the absence of radical scavengers, **1** demonstrates oxygen-rebound in the oxidation of triphenylmethane to triphenylmethanol, where the labeling of the oxygen-atom of **1** remains intact in the triphenylmethanol product. In the presence of a radical scavenger, such as $^{16}O_2$, the ^{18}O-labeling is cut in half, suggesting that that rate of rebound is comparable to the rate of radical interception by $^{16}O_2$, which is overall slower than rebound rates in heme systems.

In investigating the reactivity of **2** and **3**, we have discovered the first example of C-H bond halogenation by nonheme oxoiron(IV)-halide complexes with chemoselectivity for halogenation over hydroxylation in cyclohexane oxidation. The origin of this selectivity is currently not clear and may be attributed to electronic or steric effects. Similar to our oxygen-rebound studies with complex **1**, our investigation into halogen-rebound with the $S = 2$ nonheme oxoiron(IV)-halide complexes **2** and **3** also suggest that C–X bond formation is not as rapid as C–O bond formation in heme-mediated C–H bond oxidations.[28] However, since oxygen rebound still proceeds under an atmosphere of $^{16}O_2$ while halogen rebound does not, it suggests that the rates of halogen-rebound and oxygen-rebound in complexes **1** – **3** may be different. These results raise the intriguing question of whether the classic oxygen rebound mechanism applies to the high-valent metal centers in mononuclear nonheme iron oxygenases. To the best of our knowledge, no unequivocal stereochemical evidence is currently available requiring fast rebound to occur in the mechanisms of these enzymes.

3.8 Acknowledgements

Dr. Achintesh Biswas explored the reactivity of complex **1** with hydrocarbons and olefins, while Dr. Joan Serrano-Plana and Dr. Jale Ocal explored the reactivity of $[Fe^{IV}(O)(BQPA)(MeCN)]^{2+}$ and $[Fe^{IV}(O)(TPA)(MeCN)]^{2+}$, respectively. Dr. Williamson Oloo helped perform the rebound experiments with complex **1**. Sean Murray and Joe Dalluge are thanked for their technical assistance with the GCMS.

3.9 References

(1) Krebs, C.; Fujimori, D. G.; Walsh, C. T.; Bollinger, J. M., Jr. *Acc. Chem. Res.* **2007**, *40*, 484-492.

(2) Kleespies, S. T.; Oloo, W. N.; Mukherjee, A.; Que, L. *Inorg. Chem.* **2015**, *54*, 5053-5064.

(3) Pestovsky, O.; Bakac, A. *Inorg. Chem* **2006**, *45*, 814-820.

(4) England, J.; Guo, Y.; Van Heuvelen, K. M.; Cranswick, M. A.; Rohde, G. T.; Bominaar, E. L.; Münck, E.; Que, L., Jr. *J. Am. Chem. Soc.* **2011**, *133*, 11880–11883.

(5) Puri, M.; Que, L. *Acc. Chem. Res.* **2015**, *48*, 2443-2452.

(6) Shaik, S.; Hirao, H.; Kumar, D. *Acc. Chem. Res.* **2007**, *40*, 532–542.

(7) Decker, A.; Rohde, J.-U.; Klinker, E. J.; Wong, S. D.; Que, L., Jr.; Solomon, E. I. *J. Am. Chem. Soc.* **2007**, *129*, 15983-15996.

(8) Carine Michel, E. J. B. *Inorg. Chem.* **2009**, *48*, 3628-3638.

(9) Geng, C.; Ye, S.; Neese, F. *Angew. Chem., Int. Ed.* **2010**, *49*, 5717-5720.

(10) Groves, J. T. *J. Chem. Ed.* **1985**, *62*, 928-931.

(11) (a) Cho, K.-B.; Wu, X.; Lee, Y.-M.; Kwon, Y. H.; Shaik, S.; Nam, W. *J. Am. Chem. Soc.* **2012**, *134*, 20222-20225. (b) Cho, K.-B.; Hirao, H.; Shaik, S.; Nam, W. *Chem. Soc. Rev.* **2016**, *45*, 1197 - 1210.

(12) Rana, S.; Dey, A.; Maiti, D. *Chem. Comm.* **2015**, *51*, 14469-14472.

(13) Matthews, M. L.; Neumann, C. S.; Miles, L. A.; Grove, T. L.; Booker, S. J.; Krebs, C.; Walsh, C. T.; Bollinger, J. M., Jr. *Proc. Nat. Acad. Sci. USA* **2009**, *106*, 17723-17728.

(14) Martinie, R. J.; Livada, J.; Chang, W.-c.; Green, M. T.; Krebs, C.; Bollinger, J. M.; Silakov, A. *J. Am. Chem. Soc.* **2015**, *137*, 6912-6919.

(15) Armarego, W. L. F.; Perrin, D. D.: *Purification of Laboratory Chemicals*; Butterworth-Heinemann: Oxford, 1997.

(16) Macikenas, D.; Skrzypczak-Jankun, E.; Protasiewicz, J. D. *J. Am. Chem. Soc.* **1999**, *121*, 7164-7165.

(17) Macikenas, D.; Skrzypczak-Jankun, E.; Protasiewicz, J. D. *J. Am. Chem. Soc.* **2011**, *133*, 4151-4151.

(18) Hagen, K. S. *Inorg. Chem.* **2000**, *39*, 5867-5869.

(19) a) Xue, G.; Fiedler, A. T.; Martinho, M.; Münck, E.; Que, L., Jr. *Proc. Nat. Acad. Sci. USA* **2008**, *105*, 20615-20620. b) Xue, G.; De Hont, R.; Münck, E.; Que, L., Jr. *Nat. Chem.* **2010**, *2*, 400 - 405. c) Xue, G.; Pokutsa, A.; Que, L., Jr. *J. Am. Chem. Soc.* **2011**, *133*, 16657-16667.

(20) Chen, K.; Costas, M.; Kim, J.; Tipton, A. K.; Que, L., Jr. *J. Am. Chem. Soc.* **2002**, *124*, 3026-3035.

(21) Seo, M. S.; Kim, N. H.; Cho, K.-B.; So, J. E.; Park, S. K.; Clémancey, M.; Garcia-Serres, R.; Latour, J.-M.; Shaik, S.; Nam, W. *Chem. Sci.* **2011**, *2*, 1039-1045.

(22) Kaizer, J.; Klinker, E. J.; Oh, N. Y.; Rohde, J.-U.; Song, W. J.; Stubna, A.; Kim, J.; Münck, E.; Nam, W.; Que, L., Jr. *J. Am. Chem. Soc.* **2004**, *126*, 472-473.

(23) England, J.; Martinho, M.; Farquhar, E. R.; Frisch, J. R.; Bominaar, E. L.; Münck, E.; Que, L., Jr. *Angew. Chem. Int. Ed.* **2009**, *48*, 3622-3626.

(24) Lacy, D. C.; Gupta, R.; Stone, K. L.; Greaves, J.; Ziller, J. W.; Hendrich, M. P.; Borovik, A. S. *J. Am. Chem. Soc.* **2010**, *132*, 12188-12190.

(25) Bigi, J. P.; Harman, W. H.; Lassalle-Kaiser, B.; Robles, D. M.; Stich, T. A.; Yano, J.; Britt, R. D.; Chang, C. J. *J. Am. Chem. Soc.* **2012**, *134*, 1536-1542.

(26) Ghosh; M.; Sing, K. K.; Panda, C.; Weitz, A.; Hendrich, M. P.; Collins, T. J.; Dhar, B. B.; Gupta, S. S. *J. Am. Chem. Soc.* **2014**, *136*, 9524 - 9527.

(27) Biswas, A. N.; Puri, M.; Meier, K. K.; Oloo, W. N.; Rohde, G. T.; Bominaar, E. L.; Münck, E.; Que, L. *J. Am. Chem. Soc.* **2015**, *137*, 2428-2431.

(28) Puri, M.; Biswas, A. N.; Fan, R.; Guo, Y.; Que, L. *J. Am. Chem. Soc.* **2016**, *138*, 2484 - 2487.

(29) Serrano-Plana, J. *Personal Communication.*

(30) Paine, T. K.; Costas, M.; Kaizer, J.; Que, L. *J. Biol. Inorg. Chem.* **2006**, *11*, 272 - 276.

(31) Ocal, J. *Personal Communication.*

(32) a) Meunier, B. *Chem. Rev.* **1992**, *92*, 1411 - 1456. b) Groves, J. T.; Nemo, T. E. *J. Am. Chem. Soc.* **1983**, *105*, 5786 - 5791.

(33) Balland, V.; Charlot, M.-F.; Banse, F.; Girerd, J.-J.; Mattioli, T. A.; Bill, E.; Bartoli, J.-F.; Battioni, P.; Mansuy, D. *Eur. J. Inorg. Chem.* **2004**, 301-308.

(34) Ye, W.; Ho, D. M.; Friedle, S.; Palluccio, T. D.; Rybak-Akimova, E. V. *Inorg. Chem.* **2012**, *51*, 5006-5021.

(35) Annaraj, J.; Kim, S.; Seo, M. S.; Lee, Y.-M.; Kim, Y.; Kim, S.-J.; Choi, Y. S.; Nam, W. *Inorg. Chim. Acta* **2009**, *362*, 1031-1034.

(36) Lim, M. H.; Rohde, J.-U.; Stubna, A.; Bukowski, M. R.; Costas, M.; Ho, R. Y. N.; Münck, E.; Nam, W.; Que, L., Jr. *Proc. Natl. Acad. Sci. USA* **2003**, *100*, 3665-3670.

(37) a) Mas-Balleste, R.; Que, L., Jr. *J. Am. Chem. Soc.* **2007**, *129*, 15964 - 15972. b) Oloo, W. N.; Feng, Y.; Iyer, S.; Parmelee, S.; Xue, G.; Que, L., Jr. *New. J. Chem.* **2013**, *37*, 3411.

(38) a) Groves, J. T.; McClusky, G. A.; White, R. E.; Coon, M. J. *Biochem. Biophys. Res. Comm.* **1978**, *81*, 154-160. b) Auclair, K.; Hu, Z.; Little, D. M.; Ortiz de Montellano, P. R.; Groves, J. T. *J. Am. Chem. Soc.* **2002**, *124*, 6020 - 6027.

(39) Planas, O.; Clemancey, M.; Latour, J.-M.; Company, A.; Costas, M. *Chem. Comm.* **2014**, *50*, 10887-10890.

(40) Wiberg, K. B. *Chem. Rev.* **1955**, *55*, 713-743.

(41) a) Achord, J. M.; Hussey, C. L. *Anal. Chem.* **1980**, *52*, 601 - 602. b) Wu, D.; Bayes, K. D. *Int. J. Chem. Kinet.* **1986**, *18,* 547.

(42) *CRC Handbook of Chemistry and Physics*, 77th ed .; D. R., Ed.; CRC Press: Boca Raton, FL, 1996; pp 8 - 20.

(43) Saouma, C. T.; Mayer, J. M. *Chem. Sci.* **2014**, *5*, 21-31.

(44) Usharani, D.; Lacy, D. C.; Borovik, A. S.; Shaik, S. *J. Am. Chem. Soc.* **2013**, *135*, 17090-17104.

(45) Price, J. C.; Barr, E. W.; Glass, T. E.; Krebs, C.; Bollinger, J. M., Jr. *J. Am. Chem. Soc.* **2003**, *125*, 13008-13009.

3.10 Appendix

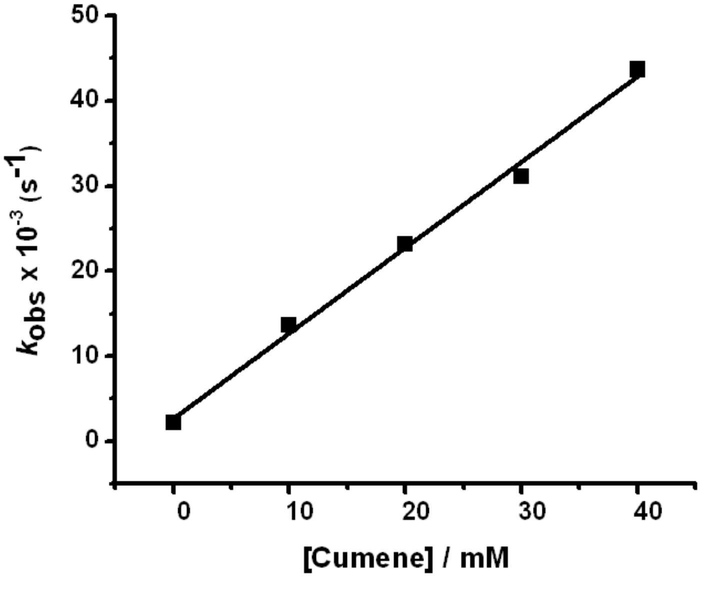

Figure 3.15. Plot of the pseudo-first-order rate constants, k_{obs} (s^{-1}), against substrate concentration to determine second-order rate constants, k_2 ($M^{-1}s^{-1}$), for the reaction of **1** with cumene (■, black solid line) in CH_3CN at -40 °C.

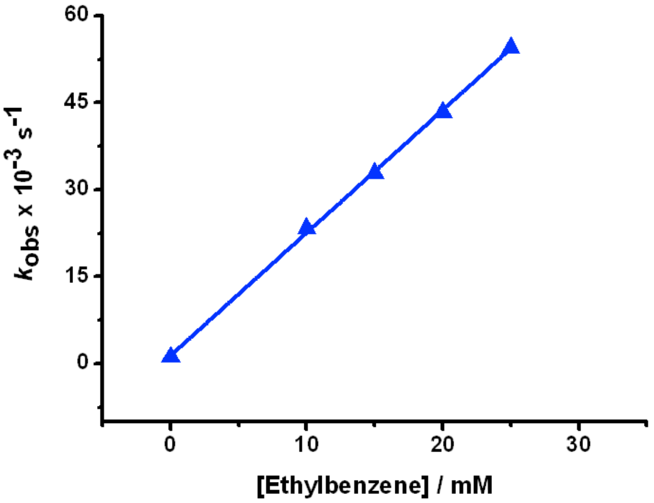

Figure 3.16. Plot of the pseudo-first-order rate constants, k_{obs} (s^{-1}), against substrate concentration to determine second-order rate constants, k_2 ($M^{-1}s^{-1}$), for the reaction of **1** with ethylbenzene (▲, blue solid line) in CH_3CN at -40 °C.

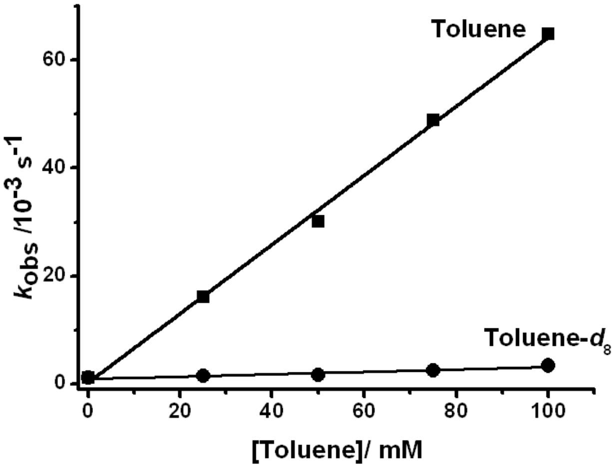

Figure 3.17. Plot of the pseudo-first-order rate constants, k_{obs} (s^{-1}) against substrate concentrations to determine second-order rate constants, k_2 (M^{-1} s^{-1}) and C-H kinetic isotope effect (KIE) value for the reaction of **1** (1.0 mM) with toluene (■, black solid line) and toluene-d8 (●, black solid line) in CH_3CN at -40 °C.

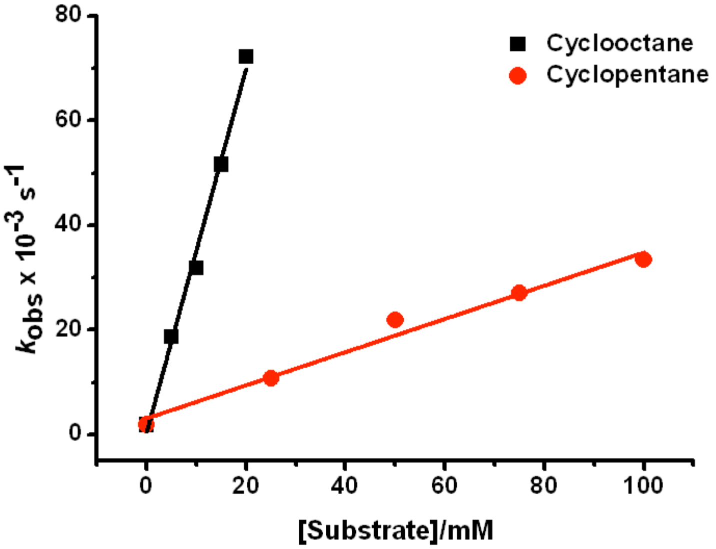

Figure 3.18. Plot of the pseudo-first-order rate constants, k_{obs} (s^{-1}) against substrate concentration to determine second-order rate constants, k_2 (M^{-1} s^{-1}) for the reaction of **1** (1.0 mM) with cyclooctane (■, black solid line) and cyclopentane (●, red solid line) in CH_3CN at -40 °C.

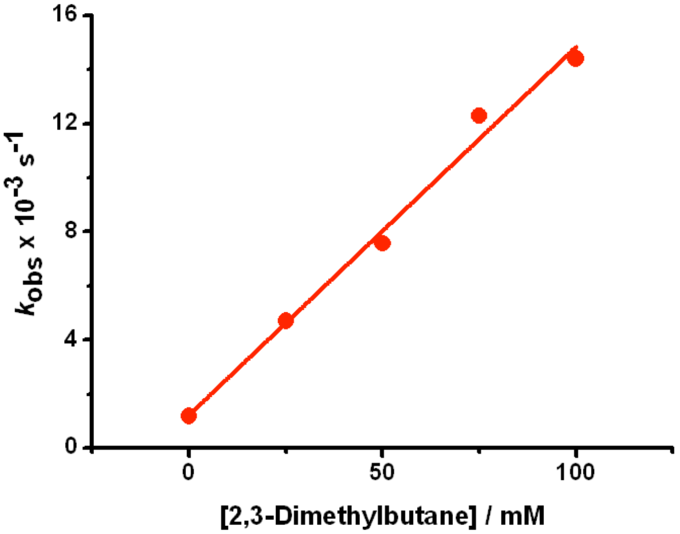

Figure 3.19. Plot of the pseudo-first-order rate constants, k_{obs} (s^{-1}) against substrate concentration to determine second-order rate constants, k_2 (M^{-1} s^{-1}) for the reaction of **1** (1.0 mM) with 2,3-dimethylbutane (●, red solid line) in CH_3CN at -40 °C.

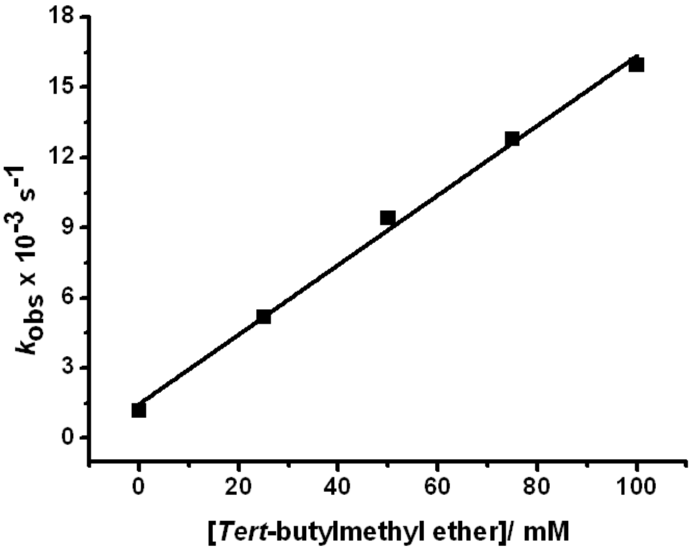

Figure 3.20. Plot of the pseudo-first-order rate constants, k_{obs} (s^{-1}) against substrate concentration to determine second-order rate constants, k_2 (M^{-1} s^{-1}) for the reaction of **1** (1.0 mM) with *tert*-butylmethyl ether (■, black solid line) in CH_3CN at -40 °C.

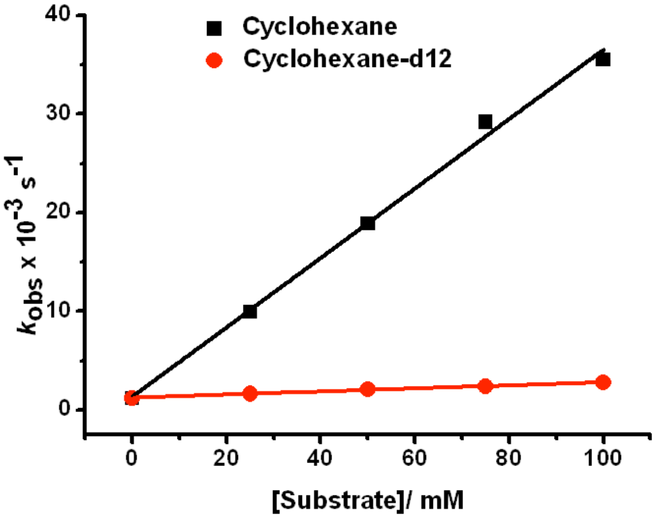

Figure 3.21. Plot of the pseudo-first-order rate constants, k_{obs} (s^{-1}) against substrate concentrations to determine second-order rate constants, k_2 (M^{-1} s^{-1}) and C-H kinetic isotope effect (KIE) value for the reaction of **1** (1.0 mM) with cyclohexane (■, black solid line) and cyclohexane-d12 (●, red solid line) in CH_3CN at -40 °C.

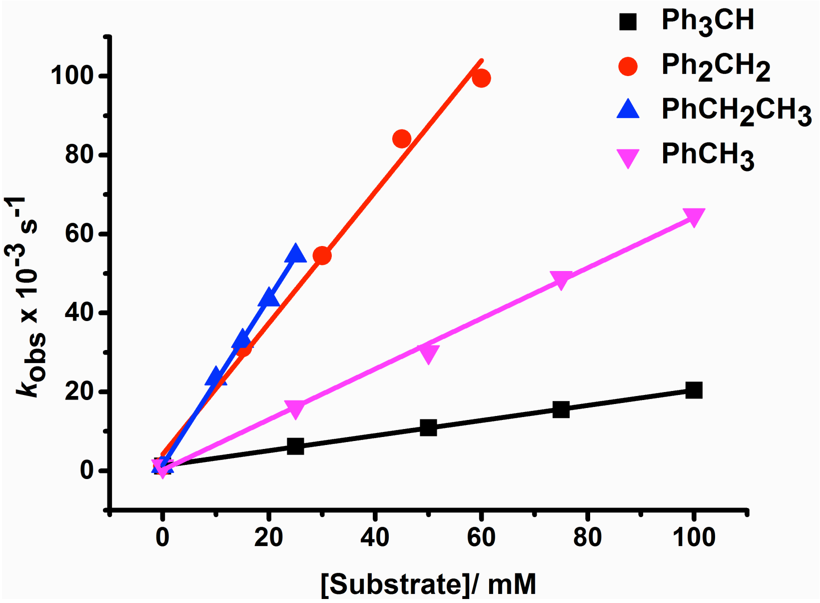

Figure 3.22. Plot of the pseudo-first-order rate constants, k_{obs} (s^{-1}) against substrate concentrations to determine second-order rate constants, k_2 (M^{-1} s^{-1}) for the reaction of **1** (1.0 mM) with triphenylmethane (■, black solid line), diphenylmethane (●, red solid line), toluene (pink solid line) and ethylbenzene (▲, blue solid line) in CH_3CN at -40 °C.

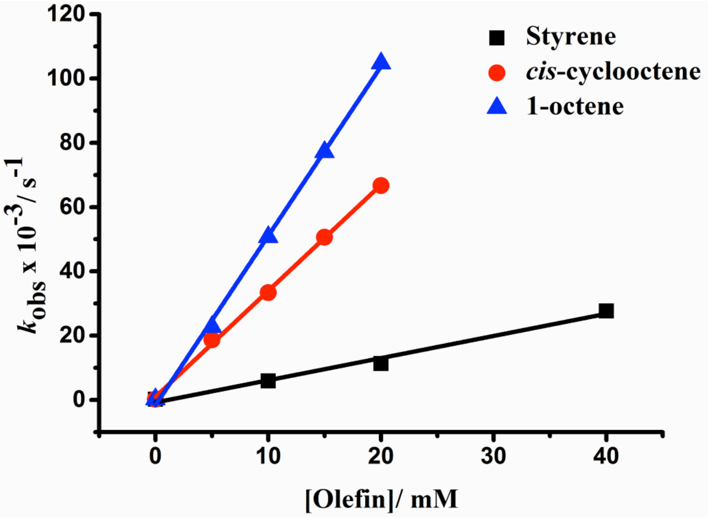

Figure 3.23. Plot of the pseudo-first-order rate constants, k_{obs} (s^{-1}) against substrate concentrations to determine second-order rate constants, k_2 (M^{-1} s^{-1}) for the reaction of **1** (1.0 mM) with styrene (■, black solid line), 1-octene (▲, blue solid line) and *cis*-cyclooctene (●, red solid line) in CH_3CN at -40 °C.

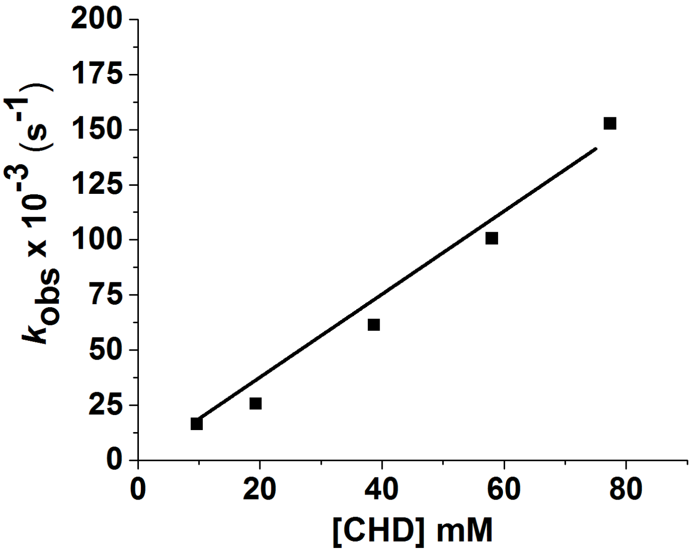

Figure 3.24. Plot of the pseudo-first-order rate constants, k_{obs} (s^{-1}) against substrate concentration to determine second-order rate constants, k_2 (M^{-1} s^{-1}) for the reaction of $[Fe^{IV}(O)(TPA)(NCMe)]^{2+}$ (1.0 mM) with 1,4-cyclohexadiene (■, black solid line) in CH_3CN at -40 °C. $[Fe^{IV}(O)(TPA)(NCMe)]^{2+}$ was generated at -40 °C by treating $[Fe^{II}(TPA)(NCMe)_2](OTf)_2$ with two equivalents of 2-(^{t}BuSO$_2$)C$_6$H$_4$IO.[2]

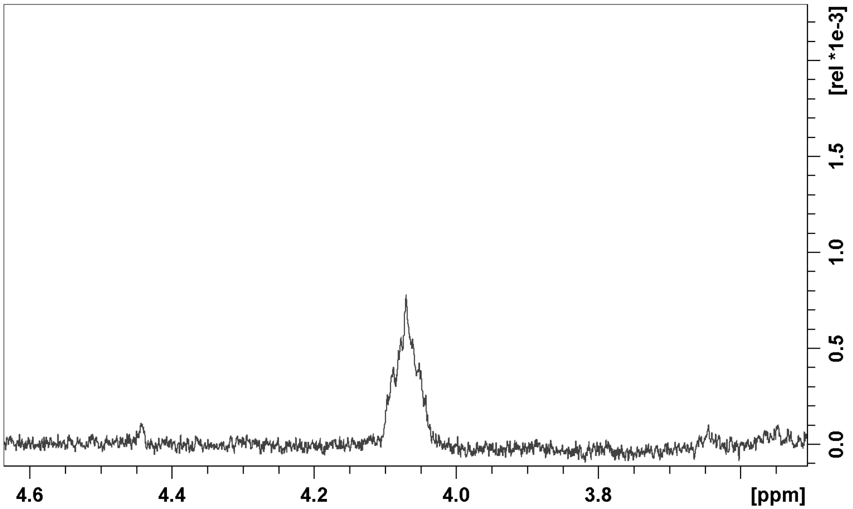

Figure 3.25. ^{1}H NMR spectrum of the reaction between **2** and cyclohexane in CD_3CN at -40 °C, displaying the Cl-$\mathit{H}C_6H_{10}$ proton of chlorocyclohexane (4.07 ppm).

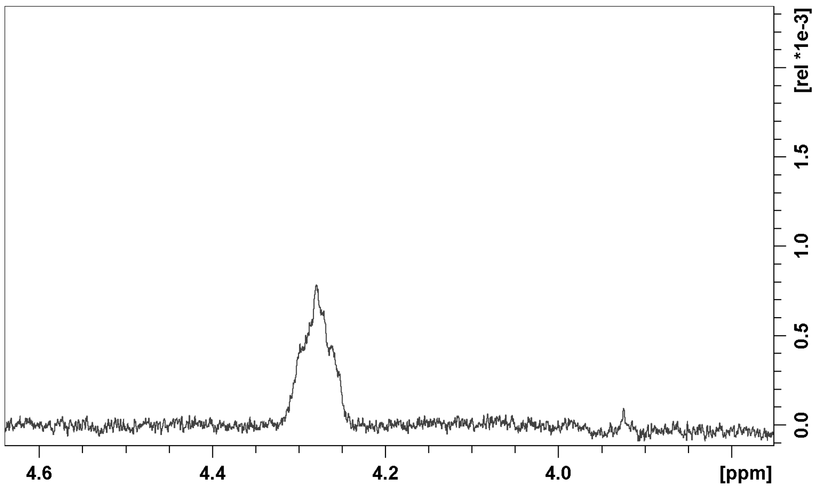

Figure 3.26. ^{1}H NMR spectrum of the reaction between **3** and cyclohexane in CD_3CN at -40 °C, displaying the Br-HC_6H_{10} proton peak of bromocyclohexane (4.27 ppm).

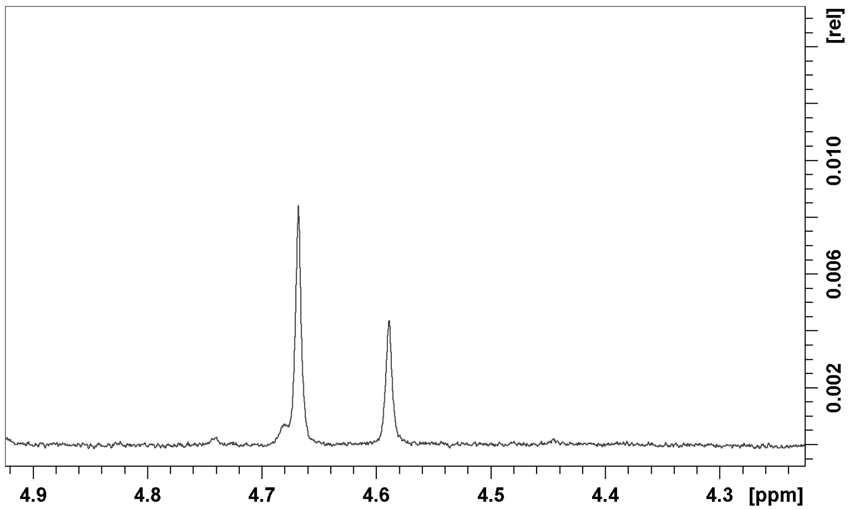

Figure 3.27. ^{1}H NMR spectrum of the reaction between **2** and toluene in CD_3CN at -40 °C, displaying the benzylic proton peaks of benzyl chloride (4.67 ppm) and benzyl alcohol (4.58 ppm).

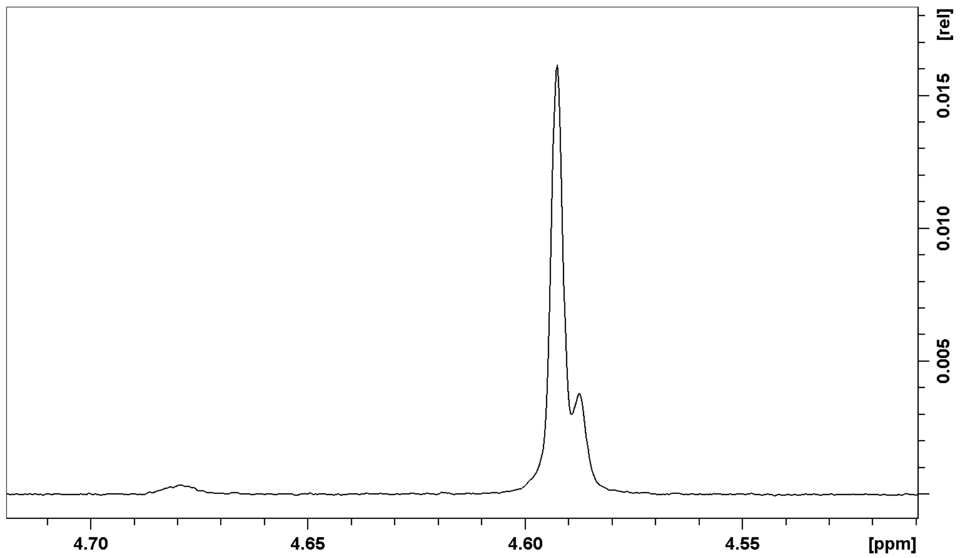

Figure 3.28: ^{1}H NMR spectrum of the reaction between **3** and toluene in CD_3CN at -40 °C, displaying the benzylic proton peaks of benzyl bromide (4.59 ppm) and benzyl alcohol (4.58 ppm). Due to the overlap between products, the ^{1}H NMR data was fit to deconvolute the data (see Figure 3.27).

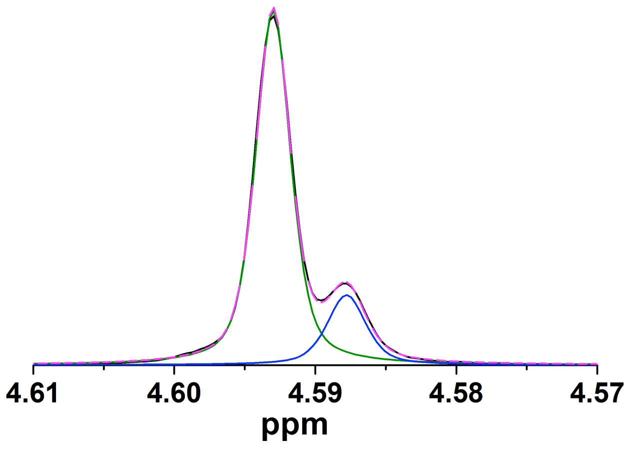

Figure 3.29: Fitting of the ^{1}H NMR spectrum of the reaction between **3** and toluene in CD_3CN at -40 °C, displaying the raw data in black, the benzyl bromide fit in green, the benzyl alcohol fit in blue and the overall fit in dashed pink. The fit indicates a ratio of ~80% benzyl bromide and ~20% benzyl alcohol. Fit done using 50% Gaussian and 50% Lorentzian curves with the Fityk software.

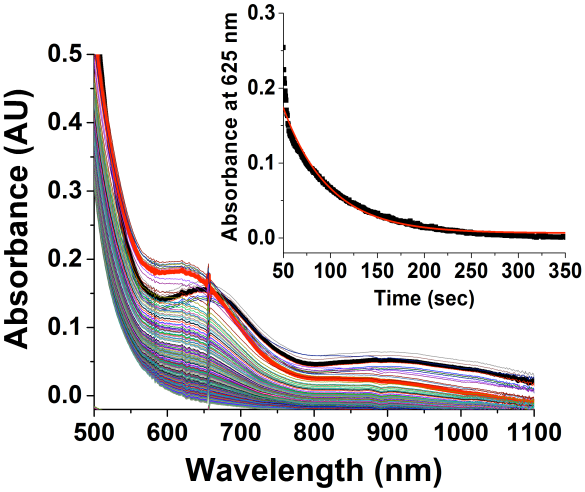

Figure 3.30. UV-visible spectra of the decay of a 1 mM solution of **2** (bold red line) in the presence of 400 equivalents toluene (0.60 mmol) in acetonitrile at -40 ºC. The spectrum of the initially generated complex **1** is shown in the bold black line. **Inset:** Plot of the absorbance at 625 nm versus time, where the black line is the raw data and the red line is the fit to a single exponential function.

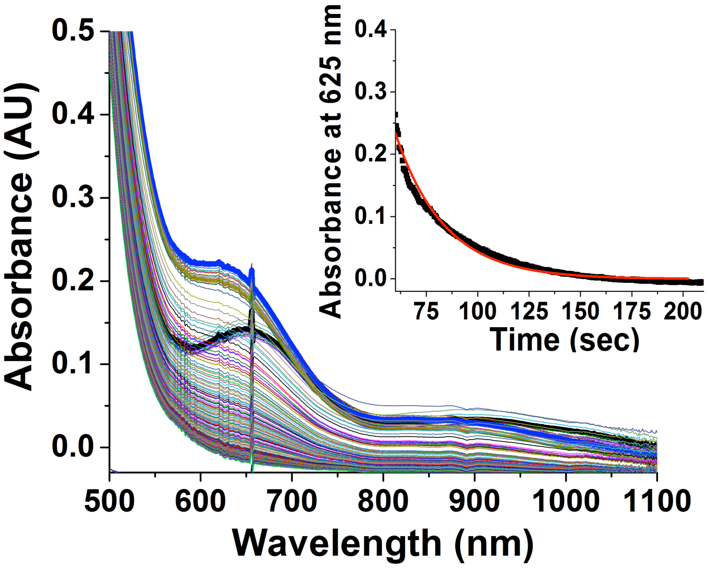

Figure 3.31. UV-visible spectra of the decay of a 1 mM solution of **3** (bold blue line) in the presence of 400 equivalents toluene (0.60 mmol) in acetonitrile at -40 ºC. The spectrum of the initially generated complex **1** is shown in the bold black line. **Inset:** Plot of the absorbance at 625 nm versus time, where the black line is the raw data and the red line is the fit to a single exponential function.

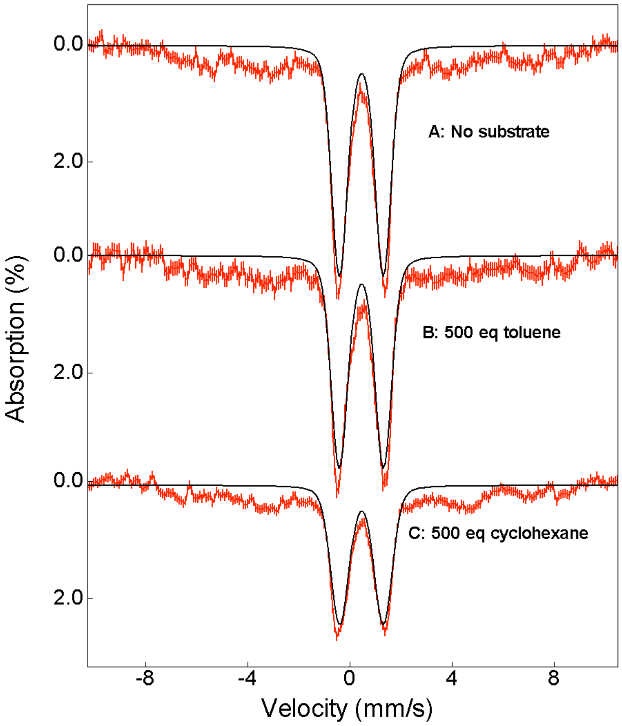

Figure 3.32. Mössbauer spectra of samples containing fully-decayed $Fe^{IV}=O$ species, **3**, with and without the presence of substrates as indicated in the figure. Red vertical bars: experimental data; Black solid lines: spectral simulations using a quadrupole doublet with $\delta = 0.45$ mm/s, $\Delta E_Q \sim 1.70$ mm/s. This quadrupole doublet, representing ~ 56% of the total iron in the sample, is typical diferric species. The rest of the absorption observed as broad baseline is mononuclear high-spin ferric species. All of the spectra were recorded under 0.45 kG (parallel) magnetic field and 4.2 K.

Chapter 4:
Oxygen-Atom Exchange (OAE) Between H_2O and Nonheme Oxoiron(IV) Complexes: Ligand Dependence and Mechanism

Parts of this chapter were published in:

1. Puri, M; Company, A.; Sabenya, G.; Costas, M.; Que, L. Jr. Oxygen-Atom Exchange Between H_2O and Nonheme Oxoiron(IV) Complexes: Ligand Dependence and Mechanism. *Inorg. Chem.* Manuscript Accepted.

4.1 Introduction

High-valent metal-oxo species are thought to play a critical role in fundamental biological reactions concerning dioxygen. Heme and nonheme iron enzymes, both capable of reducing dioxygen to water, have been proposed to generate high-valent oxoiron(IV/V) intermediates to carry out powerful oxidative transformations.[1-4,5] The reverse reaction, the oxidation of water to dioxygen, occurs in nature in Photosystem II at the oxygen-evolving complex (OEC), which has been characterized by X-ray crystallography as having a heterobimetallic Mn_4Ca cluster with oxo-ligands bridging the metal centers.[6]

The reactivity of these metal-oxo species has been of immense interest to the bioinorganic community. One reaction that is shared across many metal-oxo systems is the oxygen-atom exchange (OAE) reaction with H_2O.[7-13,14] Importantly, this reaction is used in catalytic substrate oxidation reactions to indirectly establish the presence of high-valent metal-oxo intermediates. [8,10,12,13,14-26] Due to the importance of this reaction, the mechanism of OAE with $H_2{}^{18}O$ has been probed for different metal-oxo systems. In heme systems, Meunier and co-workers have proposed an oxo-hydroxo tautomerism mechanism, (Scheme 4.1, top),[8] while Seo *et al.* have proposed an analogous tautomerization for nonheme oxoiron(IV) systems in which $H_2{}^{18}O$ initially binds *cis* to the oxo-ligand (Scheme 4.1, bottom).[12]

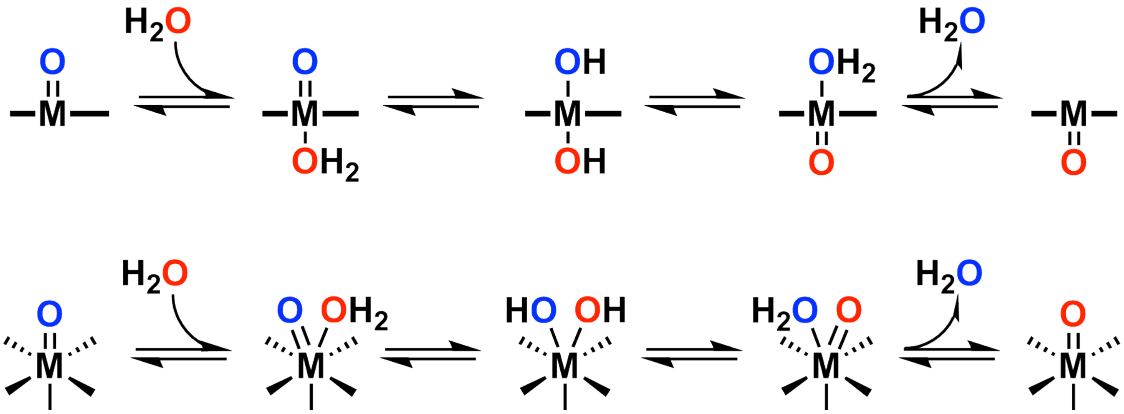

Scheme 4.1. Proposed oxo-hydroxo tautomerization mechanism for OAE between $H_2{}^{18}O$ and metal-oxo species in heme systems (top) and nonheme systems (bottom).[12]

Seo *et al*. previously studied the OAE between $H_2{}^{18}O$ and two synthetic nonheme oxoiron(IV) complexes, $[Fe^{IV}(O)(TMC)(CH_3CN)](OTf)_2$ (**1**) and $[Fe^{IV}(O)(N4Py)](ClO_4)_2$ (**3**), by tracking the extent of the reaction with ESI-MS.[12] In this study, it was found that OAE between $H_2{}^{18}O$ and **1** and **3** in acetonitrile solution at 25 °C occurs at comparable rates ($k_2 = 7 \times 10^{-3}$ M^{-1} s^{-1} and $k_2 = 6 \times 10^{-3}$ M^{-1} s^{-1}, respectively) and identical Eyring activation parameters ($\Delta H^{\ddagger} = 17 \pm 3$ kJ mol^{-1} and $\Delta S^{\ddagger} = -238 \pm 33$ J K^{-1} mol), even though the two oxoiron(IV) centers are supported by two different nonheme ligand frameworks, where TMC is a tetradentate macrocyclic ligand and N4Py is a pentadentate non-macrocyclic ligand. This is in contrast to OAE reactions investigated by Brudvig and Crabtree, where they find faster rates of OAE between $H_2{}^{18}O$ and di-μ-oxo-dimanganese complexes for oxomanganese centers that have open coordination sites versus those that are coordinatively saturated.[27,28] Similarly, for a $S = 2$ nonheme oxoiron(IV) system supported by monodentate aqua ligands, $[Fe^{IV}(O)(H_2O)_5]^{2+}$, Bakac reported an OAE rate of 25 M^{-1} s^{-1} in 0.10 M aqueous $HClO_4$ solution at room temperature, over four orders of magnitude faster than the reported OAE rates for **1** and **3**, albeit in a different solvent.[29] It is for these reasons that the effects of the ligand environment on the rate of OAE between $H_2{}^{18}O$ and nonheme oxoiron(IV) complexes are further explored in this chapter.

In an effort to address these questions and better understand how ligand architecture affects the rate of OAE in synthetic nonheme oxoiron(IV) systems, we have undertaken a comprehensive kinetic and mechanistic study of OAE between $H_2{}^{18}O$ and complexes **1** – **9** (Scheme 4.2). Our findings include the first direct experimental evidence for rate determining O–H bond cleavage in the OAE reaction between $H_2{}^{18}O$ and nonheme oxoiron(IV) complexes.

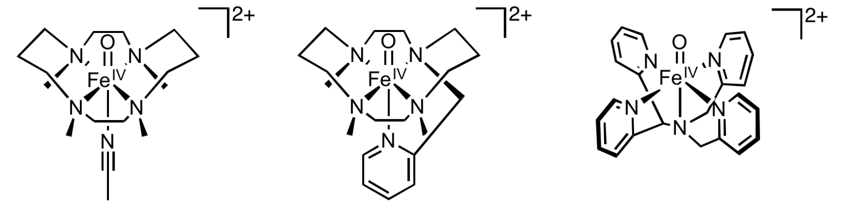

$[Fe^{IV}(O)(TMC)(MeCN)]^{2+}$ (**1**) $[Fe^{IV}(O)(TMC\text{-}Py)]^{2+}$ (**2**) $[Fe^{IV}(O)(N4Py)]^{2+}$ (**3**)

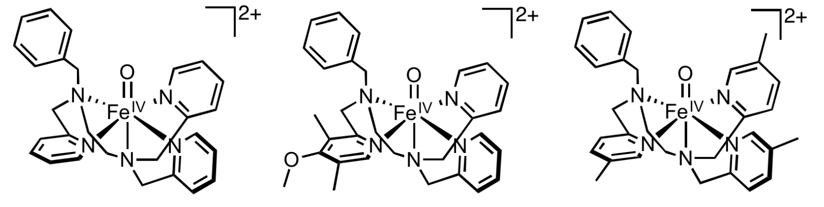

$[Fe^{IV}(O)(BnTPEN)]^{2+}$ (**4**) $[Fe^{IV}(O)(1Py\text{-}BnTPEN)]^{2+}$ (**5**) $[Fe^{IV}(O)(3Py\text{-}BnTPEN)]^{2+}$ (**6**)

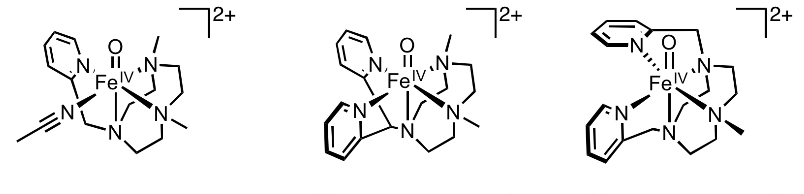

$[Fe^{IV}(O)(PyTACN)(CH_3CN)]^{2+}$ (**7**) $[Fe^{IV}(O)(Me_2Py_2TACN)]^{2+}$ (**8**) $[Fe^{IV}(O)(MePy_2TACN)]^{2+}$ (**9**)

Scheme 4.2. Synthetic nonheme oxoiron(IV) complexes studied in the context of OAE with $H_2{}^{18}O$.

4.2 Experimental Details

List of compounds:

[Fe^{II}(TMC)(OTf)](OTf) (**1a**)[30]

[Fe^{II}(TMC-Py)(OTf)](OTf) (**2a**)[31]

[Fe^{II}(N4Py)(CH_3CN)](ClO_4)$_2$ (**3a**)[32]

[Fe^{II}(BnTPEN)(OTf)](OTf) (**4a**)[33]

[Fe^{II}(1Py-BnTPEN)(OTf)](OTf) (**5a**)

[Fe^{II}(3Py-BnTPEN)(OTf)](OTf) (**6a**)

[Fe^{II}(PyTACN)(OTf)$_2$] (**7a**)[43]

[Fe^{II}(Me_2Py_2TACN)(CH_3CN)](OTf)$_2$ (**8a**)[34]

[Fe^{II}($MePy_2$TACN)(CH_3CN)](OTf)$_2$ (**9a**)[35]

[Fe^{IV}(O)(TMC)(CH_3CN)](OTf)$_2$ (**1**)[30]

[Fe^{IV}(O)(TMC-Py)](OTf)$_2$ (**2**)[31]

[Fe^{IV}(O)(N4Py)](ClO_4)$_2$ (**3**)[33]

[Fe^{IV}(O)(BnTPEN)](OTf)$_2$ (**4**)[33]

[Fe^{IV}(O)(1Py-BnTPEN)](OTf)$_2$ (**5**)

[Fe^{IV}(O)(3Py-BnTPEN)](OTf)$_2$ (**6**)

[Fe^{IV}(O)(PyTACN)(MeCN)](OTf)$_2$ (**7**)[43]

[Fe^{IV}(O)(Me_2Py_2TACN)](OTf)$_2$ (**8**)[36]

[Fe^{IV}(O)($MePy_2$TACN)](OTf)$_2$ (**9**)[35]

Materials and Instrumentation

All reagents were purchased from Aldrich and used as received, unless noted otherwise. Anhydrous acetonitrile (99.8 %) was purchased from Aldrich. $H_2{}^{18}O$ was purchased from Isoflex (now NucMedCor) with 98% ^{18}O-enrichment and 99.99% purity. $H_2{}^{16}O$ was treated with a Millipore Milli-Q water system prior to use. **1a**,[30] **2a**,[31] **3a**,[32] **4a**,[33] **7a**,[43] **8a**,[34] and **9a**[35] were synthesized according to reported procedures, while the synthesis for **5a** and **6a** is reported below. Iodosylbenzene (PhIO) and ^{18}O-iodosylbenzene ($PhI^{18}O$) was synthesized according to reported procedures.[37,38]

^1H NMR spectra were recorded on a Varian Inova 300 MHz and 500 MHz spectrometer at ambient temperature. Elemental analysis for $[Fe^{II}(1Py\text{-}BnTPEN)(OTf)](OTf)$ (**5a**) and $[Fe^{II}(3Py\text{-}BnTPEN)(OTf)](OTf)$ (**6a**) was performed by Atlantic Microlab (Norcross, GA). All electrochemical experiments were performed using a Cypress system CS1200 analyzer. The cyclic voltammetric (CV) measurements were carried out in acetonitrile, containing Fe^{II} complexes (1 mM) and tetrabutylammonium hexafluorophosphate ($TBAPF_6$, 0.1 M) as the supporting electrolyte, using a glassy carbon working electrode, a Ag / $AgNO_3$ (0.05 M) reference electrode, and a platinum auxiliary electrode. All potentials are reported versus the Fc^+ / Fc (Fc = ferrocene) couple. Electrospray ionization mass spectrometry experiments were carried out on a Bruker BioTOF II mass spectrometer using a spray chamber voltage of 4000 V and a gas carrier temperature of 200 °C.

General procedure for the generation of Fe^{IV}(O) complexes - 1, 2, 3, 4, 5, 6, 8, and **9**: [Fe^{II}(L)]$^{2+}$ (0.006 mmol) was dissolved in anhydrous CH_3CN (6.0 mL) and allowed to mix with solid iodosylbenzene (PhIO, 0.018 mmol, 3.0 eq) for 1 hour at room temperature. The resulting solution was then placed in the -40 °C freezer for 15 minutes and subsequently filtered with a 0.2 μm Acrodisk syringe filter to remove unreactive iodosylbenzene.

In contrast, complex **7** was generated with peracetic acid according to previously published procedures.[43]

1Py-BnTPEN (*N*-benzyl-*N*-(3,5-dimethyl-4-methoxy-2-pyridylmethyl)-*N'*,*N'*-bis(2-pyridylmethyl)-1,2-diaminoethane) Ligand.

The compounds *N,N*-bis(2-pyridylmethyl)-1,2-diaminoethane and *N*-Benzyl-*N',N'*-bis(2-pyridylmethyl)-1,2-diaminoethane were synthesized according to published procedures.[39,40]

N-Benzyl-*N',N'*-bis(2-pyridylmethyl)-1,2-diaminoethane (2.0 g, 6.0 mmol) was dissolved in CH_3CN (25 mL) and added to a 250 mL round-bottom flask. In a separate flask, 2-chloro-4-methoxy-3,5-dimethylpyridine hydrochloride (2.0 g, 9.0 mmol) was dissolved in CH_3CN (25 mL) and diisopropylethylamine (1.57 mL, 9.0 mmol) was very carefully added dropwise to this stirring solution. Upon complete addition, the mixture of 2-chloro-4-methoxy-3,5-dimethylpyridine hydrochloride and diisopropylethylamine was added to the flask containing *N*-Benzyl-*N',N'*-bis(2-pyridylmethyl)-1,2-diaminoethane.

Additional diisopropylethylamine (1.57 mL, 9.0 mmol) was added to this reaction mixture, along with sodium iodide (45 mg, 0.3 mmol). The solution was heated to reflux for 72 hours. Progress of the reaction was monitored by TLC (basic alumina, $R_f = 0.4$, ethyl acetate : hexanes : triethylamine 8:5:1) and ^{1}H NMR spectroscopy.

Upon disappearance of the starting *N*-Benzyl-*N',N'*-bis(2-pyridylmethyl)-1,2-diaminoethane, the flask was brought to room temperature and the solvent remove *en vacuo*, leaving behind a dark-brown oil. The oil was subsequently dissolved in water (200 mL) and the organic products extracted with EtOAc (5 x 100 mL). The organic layer was washed with brine, dried over $MgSO_4$ and filtered. The resulting filtrate was removed *en vacuo* leaving behind a dark yellow oil, which was further purified by flash column chromatography (basic alumina, $R_f = 0.4$, ethyl acetate : hexanes : triethylamine 8:5:1) to give a yellow oil as the desired product (600 mg, 21% yield). ^{1}H NMR (300 MHz, CD_2Cl_2): δ, ppm = 8.44 (m, 2H, α-Py), 8.06 (s, 1H, α-Py), 7.59 (dt, 2H, β-Py), 7.36 (d, 2H, β-Py), 7.25 to 7.18 (m, 5H, Ph), 7.11 (m, 2H, γ-Py), 3.67 (m, 8H, $-CH_2Py$), 3.51 (s, 3H, $O-CH_3$), 2.66 (m, 4H, $-CH_2CH_2-$), 2.17 (s, 3H, $-CH_3$), 2.14 (s, 3H, $-CH_3$).

[Fe^{II}(1Py-BnTPEN)(OTf)](OTf) (**5a**). Under an inert atmosphere, the 1Py-BnTPEN ligand (0.30 g, 0.62 mmol) was dissolved in dichloromethane (2.8 mL) and added dropwise to a stirring slurry of $Fe(OTf)_2 \cdot 2CH_3CN$ in dichloromethane (1.0 mL). During this addition, the color changed from light yellow to dark orange and finally to dark red. The mixture was allowed to stir overnight at room temperature. The next day, the solution had turned to a dark brown color. Et_2O (20 mL) was added to the reaction mixture and placed in the -40 °C freezer, resulting the formation of a brown oil. The Et_2O

solution was filtered and the oil placed under vacuum to leave a brown solid (100 mg, 37%). Anal. Calcd. for Fe^{II}(3Py-BnTPEN)$(OTf)_2 \bullet 2H_2O$ $C_{32}H_{39}F_6FeN_5O_9S_2$: C, 44.09; H, 4.51; N, 8.03; S, 7.36. Found: C, 44.72; H, 4.42; N, 8.09; S, 7.48.

3Py-BnTPEN (*N*-benzyl-*N,N',N'* -tris(5-methyl-2-pyridylmethyl)-1,2-diaminoethane) Ligand. 5-Methyl-2-pyridylmethyl chloride hydrochloride (3.02 g, 16.9 mmol) was dissolved in water and neutralized with an equimolar amount of 3 M NaOH. The neutralized compound was added to a solution of *N*-benzylethylenediamine (0.85 g, 5.6 mmol) in CH_2Cl_2 (10 mL). Additional NaOH (20 mmol) was added over 1 day and the solution was left to stir for 48 hours. The solution was extracted with CH_2Cl_2 (3 x 30 mL) and the organics were combined, dried over Na_2SO_4, and concentrated to yield an orange oil. The oil was purified by flash column chromatography (basic alumina, 5% MeOH/ethyl acetate) to give 5-Me_3-BnTPEN as a cream colored solid (1.8 g, 68% yield). ^1H NMR (300 MHz, CD_2Cl_2): δ, ppm = 8.32 (s, 3H, α-Py), 7.44 (d, 3H, β-Py), 7.40 (d, 3H, γ- Py), 7.38 to 7.22 (m, 5H, Ph), 3.70 (s, 4H, -CH_2Py), 3.67 (s, 2H, -CH_2Py), 3.58 (s, 2H, - CH_2Ph), 2.68 (m, 4H, -CH_2CH_2-), 2.20 (s, 9H, -CH_3).

[Fe^{II}(3Py-BnTPEN)(OTf)](OTf) (6a). A solution of 3Py-BnTPEN (747 mg, 1.6 mmol) in CH_2Cl_2 (4 mL) was added to a stirring suspension of $Fe(OTf)_2 \cdot 2CH_3CN$ (700 mg, 1.6 mmol) in CH_2Cl_2 (1 mL). The solution was left to stir overnight before the solvent was removed *in vacuo*, leaving a red colored solid. The solid was stirred in ether (10 mL) to leave a yellow powder, which was recrystallized from CH_2Cl_2/ether (1.0 g, 76%). Anal.

Calcd. For Fe^{II}(3Py- BnTPEN)$(OTf)_2$, $C_{32}H_{35}F_6FeN_5O_6S_2$: C, 46.90; H, 4.30; N, 8.50; S, 7.80. Found: C, 46.82; H, 4.48; N, 8.50; S, 7.68.

ESI-MS Studies – $H_2{}^{18}O$ Concentration Dependence

The procedure for monitoring the kinetics of OAE between $[Fe^{IV}(^{16}O)(L)]^{2+}$ and $H_2{}^{18}O$ by ESI-MS has been adapted from Tagore *et al* and Seo *et al*.[27,12] In a typical experiment, three reactions were carried out in parallel, with all reaction conditions held constant except for the volume of $H_2{}^{18}O$ introduced. This was done in an effort to minimize experimental variations and accurately determine the effects of $H_2{}^{18}O$ concentration on OAE rates.

1 mM solution of $[Fe^{IV}(^{16}O)(L)]^{2+}$ was generated and added to three separate vials (1.5 mL each), labeled A , B, and C. Additional CH_3CN was added to dilute the $[Fe^{IV}(^{16}O)(L)]^{2+}$ solution in vials A, B, and C (1.25 mL, 1.0 mL and 0.5 mL, respectively).

A stock solution of 1.11 M $H_2{}^{18}O$ was then prepared by dissolving $H_2{}^{18}O$ (40 μL) in CH_3CN (2.0 mL). To begin the reaction, the vials A, B and C were placed in a temperature-controlled bath set at the desired temperature (Figure 4.3). The $H_2{}^{18}O$ stock solution was then added to the vials A, B, and C (0.25 mL, 0.5 mL and 1.0 mL, respectively, corresponding to 5 μL, 10 μL, and 20 μL of $H_2{}^{18}O$, with each vial having a final volume of 3.0 mL) and the reaction progress in each vial was monitored by ESI-MS on a Bruker BioTOF II mass spectrometer using a spray chamber voltage of 4000 V and a gas carrier temperature of 200 °C.

Injection of the reaction mixtures into the ESI-MS was accomplished by inserting a capillary tube through the rubber-septum capping each of the vials. The capillary tube was then inserted into the ESI-MS outlet and the other end of the capillary tube was submerged into the acetonitrile solution containing the $[Fe^{IV}(^{16}O)(L)]^{2+}$ complex and $H_2{}^{18}O$. A syringe of air was then used to slightly pressurize the vial, causing the solution to transfer through the capillary tube into the ESI-MS. Each time-point was recorded during a span of 10-seconds, during which time the accumulated spectra were averaged to give one overall spectrum.

ESI-MS Studies – $H_2{}^{16}O$ / $D_2{}^{16}O$ KIE Experiments

$[Fe^{IV}(^{18}O)(L)]^{2+}$ was generated in one of two ways.

Method #1 for generation of $[Fe^{IV}(^{18}O)(L)]^{2+}$

$[Fe^{II}(L)]^{2+}$ (0.006 mmol) was dissolved in anhydrous CH_3CN (6.0 mL) and allowed to mix with solid ^{18}O-iodosylbenzene ($Ph^{18}O$, 0.018 mmol, 3.0 eq) for 1 hour at room temperature. The turbid solution was then placed in the -40 °C freezer for 15 minutes and subsequently filtered with a 0.2 μm Acrodisk syringe filter to remove unreactive iodosylbenzene.

Method #2 for generation of $[Fe^{IV}(^{18}O)(L)]^{2+}$

A 1 mM solution of $[Fe^{IV}(^{16}O)(L)]^{2+}$ was generated as detailed above. $H_2{}^{18}O$ (10 μL, 0.56 mmol) was added to the solution at room temperature and the reaction was monitored by ESI-MS until the $[Fe^{IV}(^{18}O)(L)]^{2+}$ isotopomer was fully formed (usually in 90% yield due to residual $H_2{}^{16}O$ in the acetonitrile solution).

Upon formation of a 1 mM solution of $[Fe^{IV}(^{18}O)(L)]^{2+}$, the solution was split into two vials (1.5 mL each), labeled H and D. Two separate stock solutions of 1.85 M $H_2{}^{16}O$ and 1.85 M $D_2{}^{16}O$ were then prepared by dissolving $H_2{}^{16}O$ (100 μL) and $D_2{}^{16}O$ (100 μL) in CH_3CN (3.0 mL). To begin the reaction, the vials H and D were placed in a temperature-controlled bath (see image below). The $H_2{}^{16}O$ stock solution was then added to vial H (1.5 mL corresponding to 50 μL of $H_2{}^{16}O$) and the $D_2{}^{16}O$ stock solution was added to vial D (1.5 mL corresponding to 50 μL of $D_2{}^{16}O$) and the reaction progress in each vial was monitored by ESI-MS on a Bruker BioTOF II mass spectrometer using a spray chamber voltage of 4000 V and a gas carrier temperature of 200 °C.

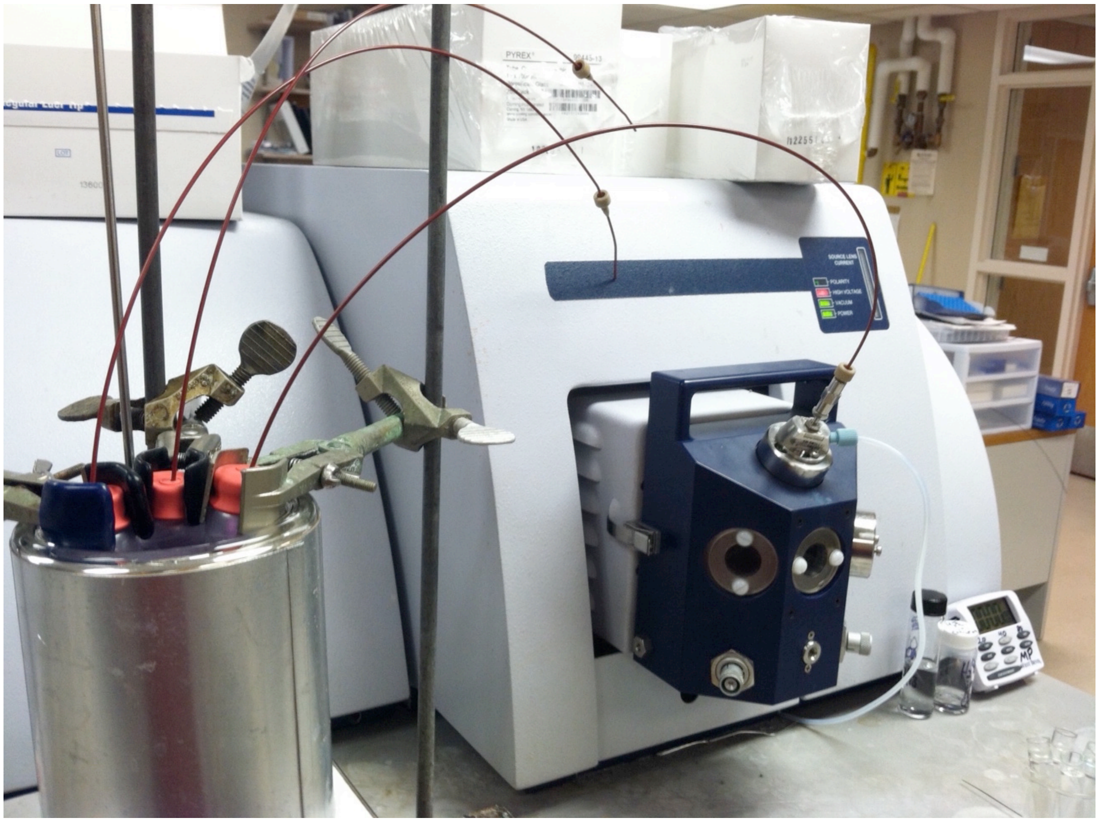

(Experimental setup for monitoring the kinetics of OAE between $H_2{}^{18}O$ and oxoiron(IV) complexes using ESI-MS.)

ESI-MS Studies – Data Analysis

Pseudo-first order rate constant (k_{obs}) for the OAE between $H_2{}^{18}O$ and $[Fe^{IV}({}^{16}O)(L)]^{2+}$ is determined by plotting the percentage of ${}^{18}O$-incorporation against time and fitting the resulting data to a single-exponential function.

The percentage of ${}^{18}O$-incorporation is determined by measuring the relative percentage of $[Fe^{IV}({}^{18}O)(L)]^{2+}$ in solution at each time point, which can be extrapolated from the intensity of the parent $[Fe^{IV}({}^{16}O)(L)]^{2+}$ peak (N) and the corresponding $[Fe^{IV}({}^{18}O)(L)]^{2+}$ peak (N+2). In order to account for the contribution from naturally occurring isotopes in the molecules, the following correction factors were applied to the intensity of the N and N+2 peaks:

The variables listed below are defined as follows:

I_0^N = Intensity of the parent peak (N) prior to OAE

I_0^{N+2} = Intensity of the N+2 peak prior to OAE

I_0^{N-2} = Intensity of the N-2 peak prior to OAE

I_t^N = Intensity of the parent peak (N) during OAE at time (t)

I_t^{N+2} = Intensity of the N+2 peak during OAE at time (t)

In the starting $[Fe^{IV}(^{16}O)(L)]^{2+}$ complex, the percentage of natural isotopic abundance N+2 contribution can be described as a variable B:

$$\mathbf{B = I_0^{N+2} / (I_0^N + I_0^{N+2})}$$

In the starting $[Fe^{IV}(^{16}O)(L)]^{2+}$ complex, the percentage of natural isotopic abundance N-2 contribution can be described as variable C:

$$\mathbf{C = I_0^{N-2} / (I_0^N + I_0^{N-2})}$$

The percentage of $[Fe^{IV}(^{18}O)(L)]^{2+}$ in solution at any time may be described as variable D:

$$\mathbf{D = \%\ [Fe^{IV}(^{18}O)(L)]^{2+}}$$

The percentage of $[Fe^{IV}(^{16}O)(L)]^{2+}$ in solution at any time may be described as 1-D:

$$\mathbf{1 - D = \%\ [Fe^{IV}(^{16}O)(L)]^{2+}}$$

The parent peak (N) at any given time can be described as a sum of the % of $[Fe^{IV}(^{16}O)(L)]^{2+}$ (1-D) and the % of the N-2 contribution of $[Fe^{IV}(^{18}O)(L)]^{2+}$ [(D)(C)].

$$\mathbf{I_t^N = [(1-D) + (D)(C)]}$$

The N+2 peak at any given time can be described as a sum of the % $[Fe^{IV}(^{18}O)(L)]^{2+}$ (D) and the % of the N+2 contribution of $[Fe^{IV}(^{16}O)(L)]^{2+}$ [(1-D)(B)].

$$\mathbf{I_t^{N+2} = [(1-D)B + D]}$$

The ratio of the I_t^N / I_t^{N+2} can then be described as follows:

$$\mathbf{I_t^N / I_t^{N+2} = [(1-D) + (D)(C)] / [(1-D)B + D]}$$

The equation may be rearranged to isolate the % $[Fe^{IV}(^{18}O)(L)]^{2+}$ (D):

$$\mathbf{D = [(I_t^N / I_t^{N+2})(B) - 1] / [(I_t^N / I_t^{N+2})(B) + C - (I_t^N / I_t^{N+2}) - 1]}$$

Therefore --

$$\mathbf{\%\ [Fe^{IV}(^{18}O)(L)]^{2+} = [(I_t^N / I_t^{N+2})(B) - 1] / [(I_t^N / I_t^{N+2})(B) + C - (I_t^N / I_t^{N+2}) - 1]}$$

From this equation, one can accurately determine the percentage of ^{18}O-incorporation from the percentage of $[Fe^{IV}(^{18}O)(L)]^{2+}$ in solution, while taking into account the contributions from naturally occurring isotopes.

4.3 Factors Influencing the ^{18}O Incorporation Percentage in OAE Reactions

Our first objective was to understand what factors affect the percent incorporation of the ^{18}O atom into oxoiron(IV) complexes during the OAE with $H_2{}^{18}O$. A puzzling aspect of the Seo *et al*. report is that OAE between $H_2{}^{18}O$ and **1** or **3** resulted in ^{18}O-atom incorporation of only 30 – 50%.[12] This percentage appeared to be quite different from what would be predicted for a system in equilibrium having a large $[H_2{}^{18}O] / [H_2{}^{16}O]$ ratio.

To probe this phenomenon, we conducted an experiment in which $H_2{}^{18}O$ and $H_2{}^{16}O$ were injected in a particular sequence into an acetonitrile solution of

$[Fe^{IV}(O)(BnTPEN)](OTf)_2$ (**4**) (Figure 4.1). Exchange of the oxo group was monitored by tracking the percentage of ^{18}O-incorporation in the molecular mass peak, $\{Fe^{IV}(O)(BnTPEN)(OTf)\}^+$, by ESI-MS. In this experiment, $H_2{}^{18}O$ (5 μL) was initially injected into a 3.0 mL 0.5-mM solution of **4** in MeCN at 5 °C, causing rapid ^{18}O-atom incorporation (Figure 4.1, Point A). The ^{18}O incorporation percentage plateaued after 500 seconds. At this point, $H_2{}^{16}O$ (5 μL) was injected into the solution (Point B), causing an immediate decrease in ^{18}O-atom incorporation. At 2220 seconds, an additional $H_2{}^{16}O$ (5 μL) was injected into the solution, causing a further decrease in ^{18}O-atom incorporation (Point C). At 3100 seconds, a final addition of $H_2{}^{16}O$ (5 μL) was injected into the solution (Point D). Afterwards, at 4350 seconds, $H_2{}^{18}O$ (10 μL) was injected back into the solution (Point E), causing a rise in the ^{18}O-atom incorporation. At the end of the reaction, a total of 15 μL $H_2{}^{18}O$ and 15 μL $H_2{}^{16}O$ had been injected into the solution, resulting in a total ^{18}O-atom incorporation of approximately 50%. These results suggest two things: first, OAE occurs rapidly in **4** and achieves an equilibrium that reflects the ratio of $[H_2{}^{18}O]$ and $[H_2{}^{16}O]$ in solution. Second, the low ^{18}O-atom incorporation reported for complexes **1** and **3** in the Seo *et al*. study may be due to the presence of $H_2{}^{16}O$ in the solvent prior to the introduction of $H_2{}^{18}O$.[12] Indeed, varying the $H_2{}^{18}O$ / $H_2{}^{16}O$ ratio in OAE experiments with complex **1** show the same influence on the percentage ^{18}O-atom incorporation as for complex **4** (Figure 4.8 Appendix). In our hands a typical OAE experiment between $H_2{}^{18}O$ and nonheme oxoiron(IV) complexes, including **1** and **3**, resulted in approximately 80-90% ^{18}O-atom incorporation, with the 10-20% loss attributed to residual $H_2{}^{16}O$ in the acetonitrile solvent (Figure 4.9 and 4.10 Appendix).

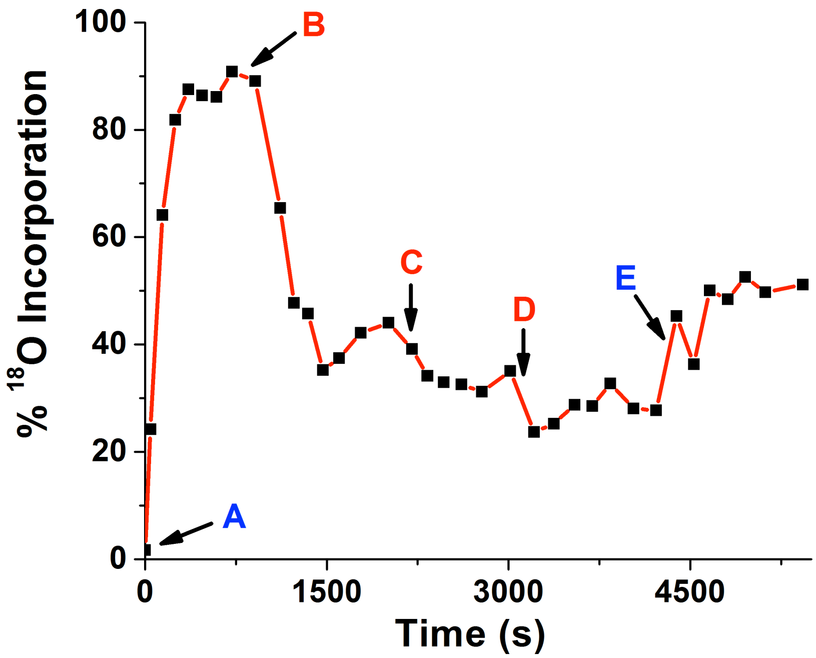

Figure 4.1. Percentage of ^{18}O-incorporation into the Fe^{IV}=O unit monitored by ESI-MS upon addition of $H_2{}^{18}O$ (blue points, A and E) and $H_2{}^{16}O$ (red points, B, C, and D) to a 3-mL MeCN solution of **4** (0.5 mM) at 5 °C.

4.4 Axial Ligand Effects on OAE: TMC vs. TMC-Py

Our second objective was to understand how the supporting ligand influences the rate and mechanism of OAE between $H_2{}^{18}O$ and nonheme oxoiron(IV) complexes. As mentioned, the OAE between $H_2{}^{18}O$ and **1** is well documented, with the rate of OAE previously measured as $k_2 = 7 \times 10^{-3}\ M^{-1}\ s^{-1}$ at 298 K.[12] We repeated these experiments and found a linear [$H_2{}^{18}O$] dependence with a $k_2 = 6 \times 10^{-3}\ M^{-1}\ s^{-1}$ at 298 K (red filled squares, Figure 4.2), in close agreement with the previously reported k_2 (red open squares, Figure 4.2). In contrast, we found that OAE between $H_2{}^{18}O$ and $[Fe^{IV}(O)(TMC\text{-}Py)](OTf)_2$ (where TMC-Py is 1-(2-pyridylmethyl)-4,8,11-trimethyl-1,4,8,11-tetraazacyclotetradecane) (**2**)[31] did not occur at any appreciable rate at room temperature.

Complex **2** is related to **1** in having a pyridine group in place of one of the H-atoms of a methyl group on the TMC ligand. The previously reported crystal structure of **2** shows the tethered pyridine moiety bound *trans* to the oxoiron(IV) center, replacing the MeCN ligand in **1**.[31]

The observed inability of complex **2** to undergo OAE with $H_2{}^{18}O$ indirectly lends insight into the mechanism of OAE between complex **1** and $H_2{}^{18}O$. Our results may be rationalized in one of two ways. The first is within the context of the *cis*-binding mechanism suggested by Seo *et al.*[12] (Scheme 1, bottom) where $H_2{}^{18}O$ is proposed to bind *cis* to the oxo ligand and then tautomerize to form a $Fe^{IV}({}^{16}OH)({}^{18}OH)$ intermediate. Such a species would require the iron(IV) center to move away from the N4 plane of the TMC macrocycle towards the oxo ligand in order to accommodate the additional aqua ligand, requiring the bond to the axial MeCN ligand to weaken and allowing it to dissociate. The proposed $Fe^{IV}({}^{16}OH)({}^{18}OH)$ adduct would be structurally somewhat analogous to the side-on bound peroxo complex, $[Fe^{III}(\eta^2\text{-}O_2)(TMC)]^+$, where the Fe^{III} center is crystallographically shown to lie above the N4 plane of TMC ligand with no ligand *trans* to the peroxo moiety.[41] However, in the case of **2**, the tethering of the axial pyridine ligand to the TMC macrocycle likely increases the entropic barrier for the dissociation of the axial ligand and could limit the ability of the iron center to move further away from the TMC N4 plane, thereby preventing coordination of $H_2{}^{18}O$ to the $Fe^{IV}O$ unit and subsequent OAE.

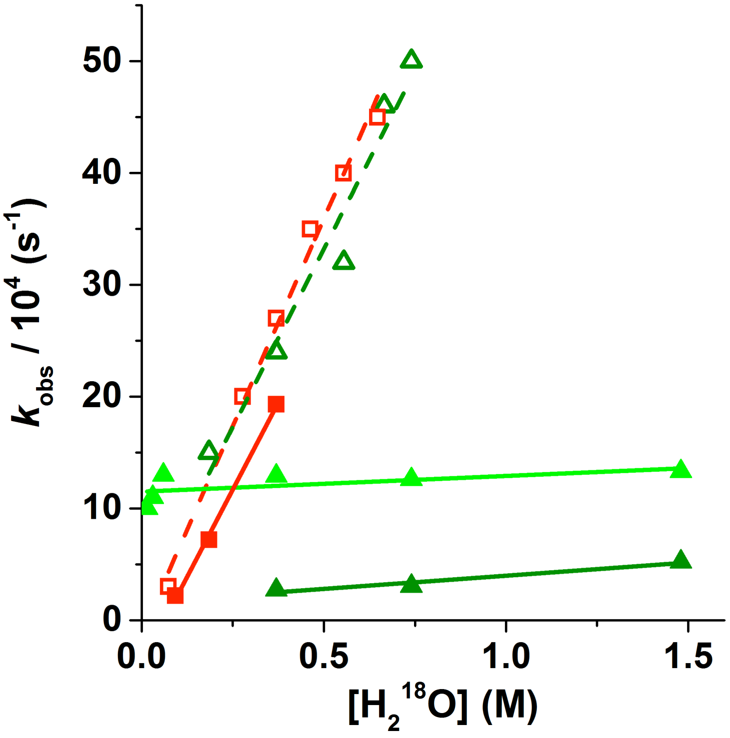

Figure 4.2. Plot of the $H_2^{18}O$ concentration dependence on the rate of OAE for **1** (2 mM open red squares, 0.5 mM filled red squares) and **3** (2 mM, open and filled green triangles) in MeCN solution at 25 °C (for all data points except the light green triangles, which were measured at 40 °C). Results previously reported in ref 12 are shown in open shapes, while new results are shown in filled shapes. The data points for **3** are all within experimental error for each temperature shown (25 °C and 40 °C).

Alternatively, we have considered whether the oxo-hydroxo tautomerism proposed by Bernardou and Meunier for OAE in heme complexes involving the binding of $H_2^{18}O$ *trans* to the oxo atom may be applied to OAE with **1** (Scheme 4.1, top). Indeed, the just reported crystal structure of a *syn* isomer of **1**, $[Fe^{IV}(O_{syn})(TMC)]^{2+}$ ($\mathbf{1}_{syn}$),[42] raises the possibility that OAE may entail the conversion of **1** to $\mathbf{1}_{syn}$ and then back again to **1.** In this mechanism, $H_2^{18}O$ would displace the axial MeCN ligand and bind *trans* to the oxo ligand followed by isomerization to generate the ^{18}O-labeled $\mathbf{1}_{syn}$. In a second exchange, $H_2{}^{18}O$ would bind *trans* to the oxo ligand of $\mathbf{1}_{syn}$ and ^{18}O-labeled **1** would be obtained after isomerization. The intermediate formation of $\mathbf{1}_{syn}$ could in principle be established by ^{1}H-NMR as it exhibits a spectrum distinct from that of **1,**[42] but the ^{1}H-NMR spectrum of **1** remained unchanged upon addition of $H_2{}^{18}O$, despite mass spectral evidence for label incorporation. This result suggests that either the *trans*-binding mechanism does not apply to the OAE reactions with **1** or the putative ^{18}O-$\mathbf{1}_{syn}$ species is only formed transiently and rapidly undergoes the second OAE step with $H_2{}^{18}O$ to yield ^{18}O-**1**, as observed by ESI-MS and ^{1}H NMR spectroscopy. A *trans*-binding mechanism would rationalize the lack of exchange with complex **2**, as the *trans* coordination site is occupied by the tethered pyridine ligand and would prevent binding of $H_2{}^{18}O$ and ultimately OAE. Based on our experimental results, both mechanisms, involving *cis* or *trans* binding of $H_2{}^{18}O$ to the Fe^{IV} center, remain a possibility and cannot be distinguished for OAE with **1**.

Table 1. Kinetic data for OAE between $H_2{}^{18}O$ and nonheme oxoiron(IV) complexes**.**

$[Fe^{IV}(O)(L)]^{2+}$	**$\Delta H^{\ddagger}$ (kJ mol^{-1})**	**$\Delta S^{\ddagger}$ (J K^{-1}- mol^{-1})**	**$\Delta G^{\ddagger}$ (kJ mol^{-1}) 298 K**	***k_2* * (x 10^{-3} M^{-1}s^{-1})**	***k_{obs}* w/ 0.28 M $H_2{}^{18}O$ (x 10^{-3} s^{-1}) ***
1 (ref 12)	17 ± 3	-240 ± 34	88	7	1.9
2 **(**)**	No ^{18}O-exchange observed				
3 (ref 12)	17 ± 3	-240 ± 34	88	6	1.7
3 **(**)**	43 ± 10	-160 ± 33	92		0.3
4 **(**)**	5 ± 1	-250 ± 10	79		75
5 **(**)**	12 ± 3	-240 ± 11	82		25
6 **(**)**	20 ± 5	-210 ± 19	82		23
7 (***)	34 ± 5 (linear regime) 26 ± 3 (saturation regime)	-161 ± 38 (linear regime) -194 ± 10 (saturation regime)	82 (linear regime) 84 (saturation regime)	28(3) (295 K)	7.8 (295 K)
8 **(**)**	22 ± 1	-220 ± 10	88		0.7 (323 K)
9 **(**)**	89 ± 10	-10 ± 30	92	12(1) (323 K)	3 (323 K)
L = TPA (ref 19)				8(2) (295 K)	2.2 (295 K)

* Data obtained at 298 K unless otherwise noted. In order to compare relative rates of OAE between oxoiron(IV) complexes that display a $[H_2{}^{18}O]$ dependence and those that do not display $[H_2{}^{18}O]$ dependence, a single $[H_2{}^{18}O]$ value was chosen that falls within

the saturation regime for all complexes with non-linear [$H_2^{18}O$] dependence (0.278 M), namely **3**, **4**, **5**, **6**, and **8**. In addition, Eyring plots were utilized to calculate k_{obs} values at 298K for **4**, **5**, and **6.** See Figure 4.14 Appendix for exact [$H_2^{18}O$] values used in experiments for determining the Eyring activation parameters.

** Data obtained in this work.

*** Combined data from ref 43 and data from this work.

4.5 OAE with BnTPEN-Based Nonheme Oxoiron(IV) Complexes

The main goal of this study is to extend the OAE investigation beyond complexes **1** and **3**, the first two nonheme oxoiron(IV) complexes reported to undergo OAE with $H_2^{18}O$ more than 10 years ago.[12] We thus explored the OAE reaction between $H_2^{18}O$ and **4**. Similar to **3**, the oxoiron(IV) center of **4** is supported by a non-macrocyclic N5 ligand. However, the OAE behavior of **4** differed in two ways from that reported for **1** and **3**: a) the exchange was too rapid to obtain accurate kinetic data at 25 °C, so experiments were carried out at -38 °C and b) a linear dependence on [$H_2^{18}O$] was not observed for **4** (Figure 4.11 Appendix).[12] These significant differences prompted us to look for mechanistic insights into the OAE reaction between $H_2^{18}O$ and nonheme oxoiron(IV) complexes supported by these ligands.

Examination of the [$H_2^{18}O$] dependence of the rate of OAE with **4** showed no linear dependence at $H_2^{18}O$ concentrations between 0.05 M and 0.4 M at -38 °C (Figure 4.11 Appendix), which is in contrast to the linear dependence previously reported in the [$H_2^{18}O$] range of 0.2 M to 0.75 M for a structurally related nonheme oxoiron(IV) complex, **3**, at 25 °C (green open triangles, Figure 4.2).[12] Interestingly, upon repeating the reported OAE experiments between $H_2^{18}O$ and **3**, we were unable to reproduce the observed linear [$H_2^{18}O$] dependence. Instead, similar to **4**, the rates of OAE with **3** were found to be constant at [$H_2{}^{18}O$] values between 0.4 M and 1.5 M at 25 °C (dark green filled triangles, Figure 4.2). In fact, this trend holds when OAE reactions between **3** and $H_2{}^{18}O$ are carried out at 40 °C, with a constant OAE rate observed between the wider $H_2{}^{18}O$ concentration range of 0.09 M to 1.5 M (light green filled triangles, Figure 4.2).

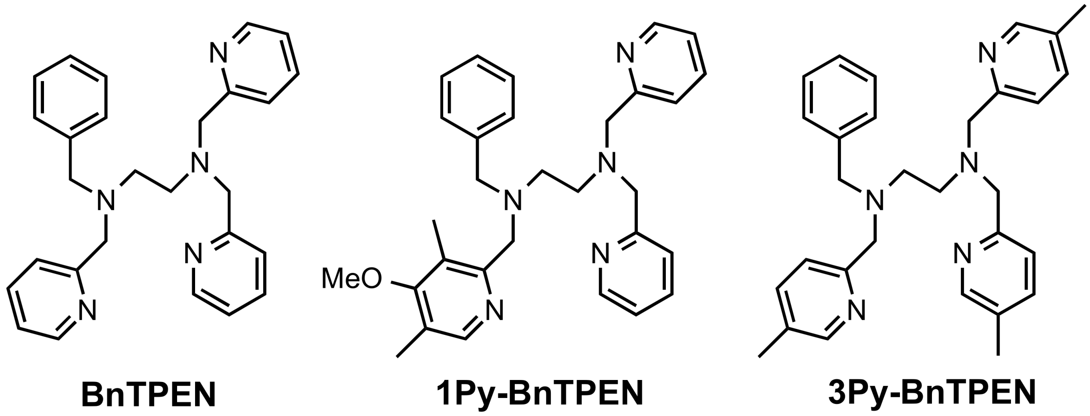

Scheme 4.3. Variants of the BnTPEN ligand.

The observed differences in [$H_2{}^{18}O$] dependence between **1** and complexes **3** and **4** reveal important mechanistic disparities. Because of the observed linear [$H_2{}^{18}O$] dependence on the OAE rate, $H_2{}^{18}O$ must be directly involved in the RDS of OAE for **1**, an oxoiron(IV) complex supported by a tetradentate ligand. In contrast, the fact that the OAE rate observed for the two oxoiron(IV) complexes supported by pentadentate ligands, **3** and **4**, was independent of [$H_2{}^{18}O$] suggests that $H_2{}^{18}O$ binding is not directly involved in the RDS.

To gain further insights into the RDS for **4**, electronic variants of the BnTPEN ligand[33] were synthesized (Scheme 4.3). The first ligand variant, 1Py-BnTPEN (where 1Py-BnTPEN is *N*-benzyl-*N*-((4-methoxy-3,5-dimethylpyridin-2-yl)methyl)-*N*',*N'*-bis(2-pyridylmethyl)ethylenediamine), differs from the parent ligand through the replacement of one pyridine ring for a more electron-rich 4-methoxy-3,5-dimethylpyridine ring, while the second ligand variant, 3Py-BnTPEN (where 3Py-BnTPEN is *N*-benzyl-*N,N',N'*-tris((5-methylpyridin-2-yl)methyl)ethylenediamine), differs from the parent ligand through the replacement of all three pyridine rings for more electron-rich 5-methylpyridine rings. The Fe^{II} complexes, $[Fe^{II}$(1Py-BnTPEN)(OTf)](OTf) (**5b**) and $[Fe^{II}$(3Py-BnTPEN)(OTf)](OTf) (**6b**) were synthesized analogously to $[Fe^{II}$(BnTPEN)(OTf)](OTf) (**4b**). In order to understand how the electronics of these new ligands affect the electron density at the Fe center, cyclic voltammetry (CV) experiments were performed on **4b** – **6b** to obtain $Fe^{III/II}$ reduction potentials (versus $Fc^{+/0}$, Figure 4.11 Appendix). The parent complex, **4b**, displays the highest reduction potential, $E_{1/2} = 0.58$ V, suggesting it has the most Lewis acidic Fe center, while **5b** and **6b** display lower reduction potentials, $E_{1/2} = 0.54$ V and 0.53 V, respectively, consistent with having more electron-rich Fe centers.[14]

The corresponding oxoiron(IV) complexes, $[Fe^{IV}(O)$(1Py-BnTPEN)$]^{2+}$ (**5**) and $[Fe^{IV}(O)$(3Py-BnTPEN)$]^{2+}$ (**6**), were generated analogously to **4** by treatment of the Fe^{II} precursors with excess iodosylbenzene (PhIO) in an acetonitrile solution at room temperature.[33] OAE experiments were then carried out with $H_2{}^{18}O$ and monitored by ESI-MS, with all three complexes demonstrating non-linear $[H_2{}^{18}O]$ dependence on the rate of OAE across a range of temperatures (Figure 4.12 Appendix). Eyring activation parameters were carried out and in order to limit experimental variations, the oxoiron(IV) solutions for complexes **4**, **5**, and **6** were combined into a single vial and their rates of OAE with $H_2{}^{18}O$ were tracked simultaneously. This strategy is made possible by the sufficient spread of the parent ion peaks in the mass spectrum (Figure 4.13 Appendix). Due to the fast rate of OAE, it was necessary to carry these reactions out at low temperatures, between -40 °C and -10 °C. Results for the OAE reaction carried out at -30 °C are detailed in Figure 4.3. As shown, the rate of OAE between $H_2{}^{18}O$ and **4** is the fastest, $k_{obs} = 38 \times 10^{-3}\ s^{-1}$, while OAE for the more electron-rich $Fe^{IV}(O)$ variants **5** and **6** is slower, with $k_{obs} = 6.0 \times 10^{-3}\ s^{-1}$ and $2.4 \times 10^{-3}\ s^{-1}$, respectively. The difference in rates is reflected in the difference in $Fe^{III/II}$ reduction potentials, where **4** shows the fastest rate of OAE and the highest $Fe^{III/II}$ reduction potential, while **5** and **6** are similar in both rates of OAE and $Fe^{III/II}$ reduction potentials. It could be argued that the iron center with the higher potential is more Lewis acidic and should thus have more acidic aqua ligands upon $H_2{}^{18}O$ binding to the oxoiron(IV) unit, ultimately promoting the rate of tautomerization involved in OAE (*vide infra*).

Results of the Eyring activation parameters for the OAE with these three complexes are listed in Table 4.1 and illustrated in Figure 4.14 Appendix. As the oxoiron(IV) center becomes more electron rich, going from **4** to **5** and **6**, the enthalpy of activation, $\Delta H^{\ddagger}$, increases, which is ultimately reflected in an increase in Gibbs activation energy, $\Delta G^{\ddagger}$, and a decrease in the rate of OAE. Interestingly, the entropies of activation, $\Delta S^{\ddagger}$, for the OAE reaction with these three complexes are extremely large and negative, ranging between -210 and -248 $J\ K^{-1}\ mol^{-1}$, and are indicative of an associative mechanism with a highly ordered transition state. Some of us have previously analyzed the OAE reaction between $H_2{}^{18}O$ and $[Fe^{IV}(O)(PyTACN)(MeCN)](OTf)_2$ (**7**) (where PyTACN is 1-(2'-pyridylmethyl)-4,7-dimethyl-1,4,7-triazacyclononane) through DFT calculations and have found that exogenous $H_2{}^{18}O$ molecules play a key role in the exchange mechanism, particularly by participating in hydrogen bonding with the aqua, hydroxo, and oxo ligands coordinated to the Fe center, ultimate aiding in the tautomerization steps of the mechanism.[43] In fact, removing these exogenous $H_2{}^{18}O$ molecules in the calculations resulted in an increase in energy of 20 kcal/mol, emphasizing their importance. Hydrogen bonding with these exogenous $H_2{}^{18}O$ molecules may rationalize a highly ordered transition state that would give rise to the highly negative $\Delta S^{\ddagger}$ values.

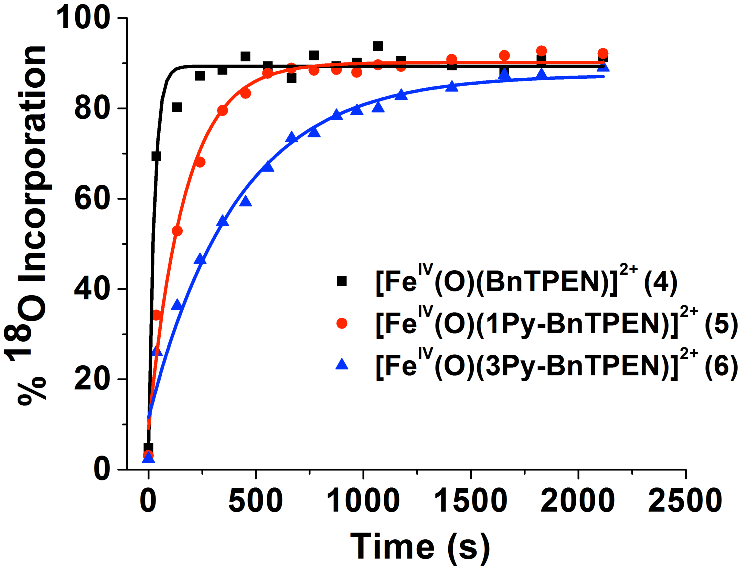

Figure 4.3. Plots of percent ^{18}O-atom incorporation against time for the OAE reactions between $H_2{}^{18}O$ (0.28 M) and a combined mixture of **4** (black squares), **5** (red circles), and **6** (blue triangles) (each at 0.5 mM) in MeCN solution at -30 °C. Single exponential fits are shown as solid lines.

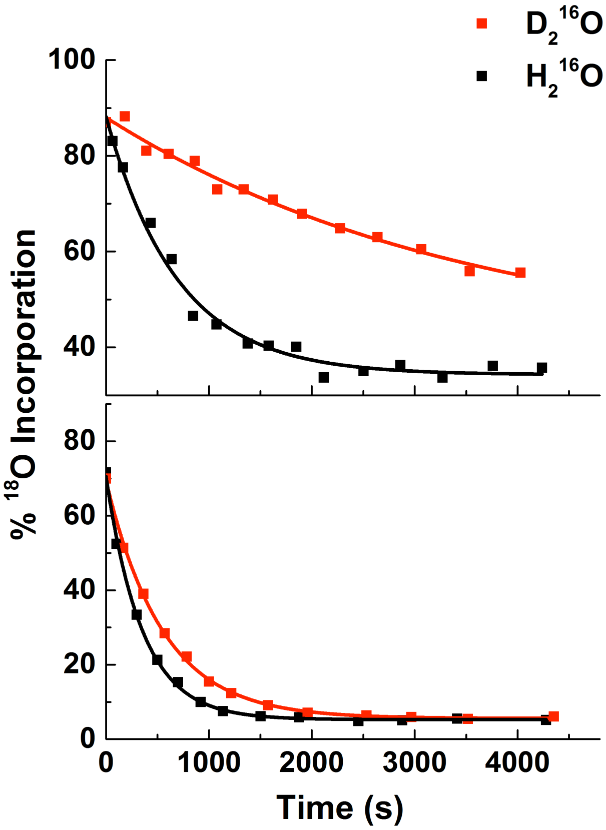

Figure 4.4. Top: Experiments between ^{18}O-labeled **6** (0.5 mM, generated from reaction of ^{16}O-labeled **6** and 0.19 M $H_2{}^{18}O$) and $H_2{}^{16}O$ (black, 0.56 M) or $D_2{}^{16}O$ (red, 0.56 M) at -25 °C, resulting in a KIE = 5.1. **Bottom**: Experiments between ^{18}O-labeled **1** (0.5 mM, generated from reaction of [Fe^{II}(TMC)(OTf)](OTf) and PhI^{18}O) and $H_2{}^{16}O$ (black, 0.37 M) or $D_2{}^{16}O$ (red, 0.37 M) at 30 °C, resulting in a KIE = 1.6. Single exponential fits are shown as solid lines.

To gain more insight into the nature of the transition state, kinetic isotope effect (KIE) experiments were carried out to probe the role of protons on the rate of the reaction. The H_2O/D_2O KIE experiment was performed by initially treating **6** with $H_2{}^{18}O$ to generate the **6**(^{18}O) isotopomer in ~90% yield. At this point, the solution was split into two separate vials. $H_2{}^{16}O$ was added to one reaction vial, while $D_2{}^{16}O$ was added to the other reaction vial, both regenerating the **6**(^{16}O) isotopomer. The different rates of exchange with $H_2{}^{16}O/D_2{}^{16}O$ presented in Figure 4.4 (top) correspond to a H/D KIE of approximately 5.1, indicating a large degree of O–H/O–D bond cleavage in the RDS for **6**. For comparison, the same KIE experiment was carried out with **1** and it afforded a much smaller H/D KIE of approximately 1.6 (Figure 4.4, bottom). In this case, $PhI^{18}O$ was used to generate the **1**(^{18}O) isotopomer from its Fe^{II} precursor, instead of $H_2{}^{18}O$ exchange with **1**(^{16}O).

Table 2. Observed H_2O/D_2O KIE values for OAE reactions between select nonheme oxoiron(IV) complexes and $H_2{}^{18}O$.

Complex	**H_2O / D_2O KIE**	**[H_2O] or [D_2O]**	**Temp.**	**[H_2O] Dependence Regime**
1	1.6	0.37 M	30 °C	Linear
6	5.1	0.56 M	-25 °C	Saturation
7	1.8	0.42 M	22 °C	Linear
7	1.6	0.42 M	0 °C	Saturation
7	1.7	0.74 M	0 °C	Saturation
7	1.5	1.57 M	0 °C	Saturation
8	5.7	0.37 M	45 °C	Saturation
9	1.3	0.37 M	30 °C	Linear

4.6 OAE with PyTACN-Based Nonheme Oxoiron(IV) Complexes

As reflected in the differences in [$H_2{}^{18}O$] dependence and H/D KIE values, there appears to be a different RDS for OAE reactions between $H_2{}^{18}O$ and oxoiron(IV) complexes supported by tetradentate ligands (such as TMC) and those supported by pentadentate ligands (such as BnTPEN and N4Py). However, the different structural frameworks among these supporting ligands hinder this comparison, as TMC is a macrocyclic ligand, while N4Py and BnTPEN are non-macrocyclic ligands. In an effort to make a comparison between oxoiron(IV) complexes with similar ligand frameworks, we have compared the rate of OAE between $H_2{}^{18}O$ and **7**, previously reported by some of us,[43] with two oxoiron(IV) complexes supported by pentadentate variants of the PyTACN ligand, $[Fe^{IV}(O)(Me_2Py_2TACN)]^{2+}$ (where Me_2Py_2TACN is 1-di(2-pyridyl)methyl-4,7-dimethyl-1,4,7-triazacyclononane) (**8**)[36] and $[Fe^{IV}(O)(MePy_2TACN)]^{2+}$ (where $MePy_2TACN$ is N-methyl-N′,N″-bis(2-pyridylmethyl)-1,4,7-triazacyclononane) (**9**).[35] In this comparison, the PyTACN ligand architecture is consistent for all three complexes, with the addition of one pyridine ring for the pentadentate variants Me_2Py_2TACN and $MePy_2TACN$. A small difference in this comparison is the oxidant used to generate the oxoiron(IV) species. Costas and co-workers employed peracetic acid to generate **7**, whereas we have used PhIO to generate **8** and **9**.

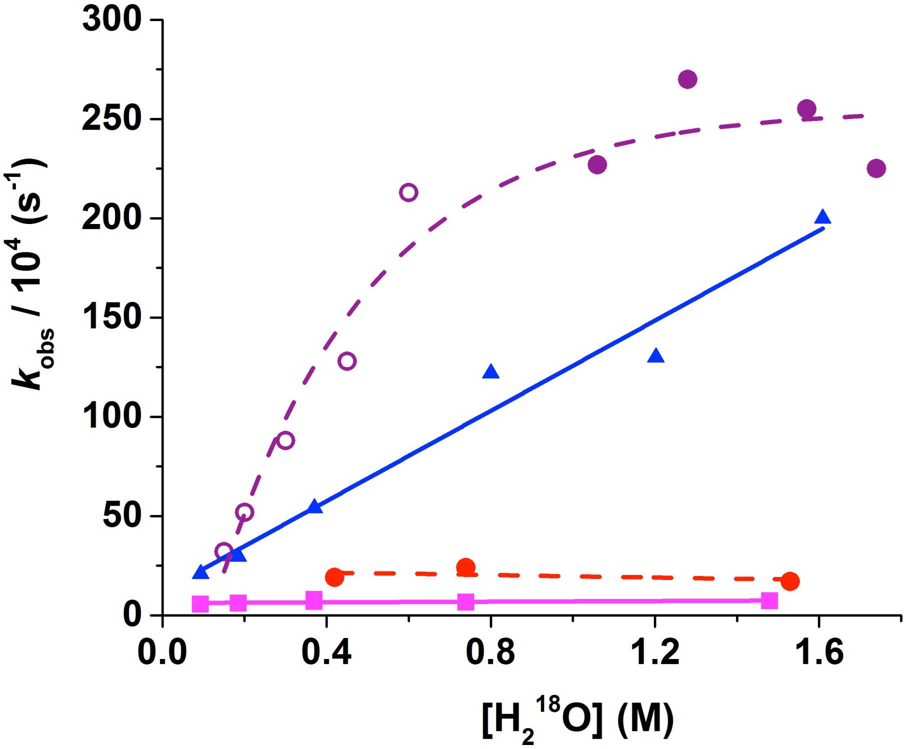

Figure 4.5. Plots of $H_2{}^{18}O$ concentration dependence for **7** (open and filled purple circles at 22 °C, filled red circles at 0 °C), **8** (0.5 mM, filled pink squares at 50 °C) and **9** (0.5 mM, filled blue triangles at 50 °C) in a MeCN solution.

Previously it was reported that **7** exhibited a linear [$H_2{}^{18}O$] dependence on the rate of OAE, with a k_2 value of 28 x 10^{-3} M^{-1} s^{-1} (open purple circles, Figure 4.5 and Table 4.1) at 22 °C.[43] Based on this linear [$H_2{}^{18}O$] dependence, the RDS is proposed to be a bimolecular association between $H_2{}^{18}O$ and **7**. This hypothesis has been supported by the generation of the oxoiron(IV)-halide complexes [Fe^{IV}(O)(Cl)(PyTACN)]$^+$ (**7-Cl**) and [Fe^{IV}(O)(Br)(PyTACN)]$^+$ (**7-Br**), where the halide ligands occupy the *cis*-coordination site thought to be necessary for OAE. No OAE is observed for **7-Cl** or **7-Br**, suggesting that the presence of these anionic ligands significantly inhibit binding of $H_2{}^{18}O$ *cis* to the oxo ligand and ultimately OAE.[44] In this study we have extended the range of [$H_2{}^{18}O$] examined for the OAE between **7** and $H_2{}^{18}O$ at 22 °C beyond 0.6 M (Figure 4.5, filled purple circles) and observed saturation behavior at these higher $H_2{}^{18}O$ concentrations. Importantly, we have also found that the [$H_2{}^{18}O$] dependence on the rate of OAE with complex **7** appears to change with temperature, where a gradual saturation is observed at 22 °C, while a very rapid saturation is observed at 0 °C (Figure 4.5, filled red circles).

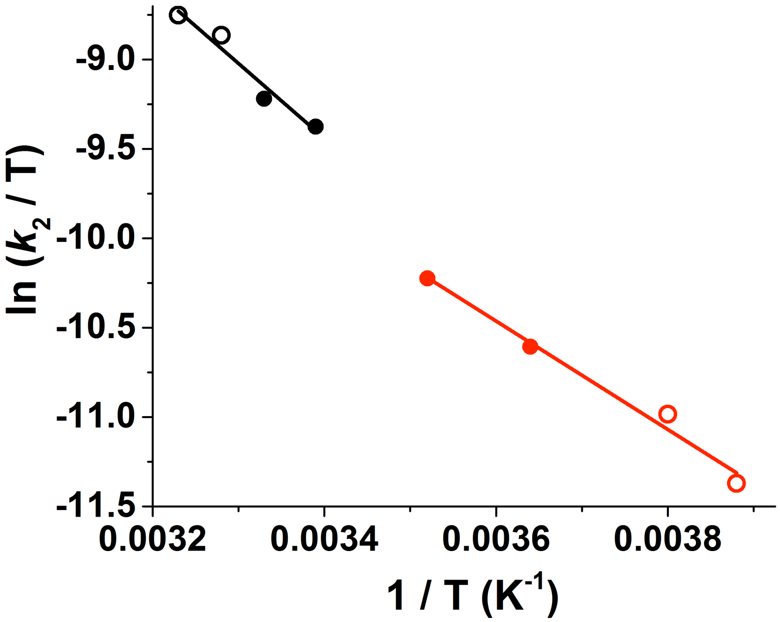

Figure 4.6. Eyring plot for complex **7** measured with 0.2 M $H_2{}^{18}O$. Points in black are associated with measurements in the linear regime, while points in red are associated with measurements in the saturation regime. Open circles are associated with data collected in this report, while those with filled circles were collected in ref 43.

New H/D KIE experiments with **7** at 0 °C using 1.57 M, 0.74 M and 0.42 M [H_2O]/[D_2O] (Figure 4.5, filled red circles) reveal values of 1.5, 1.7 and 1.6, respectively (Table 4.2, Figures 4.15 – 4.17 Appendix), suggesting that the KIE observed is independent of $H_2{}^{18}O$ concentration within the saturation regime. Furthermore, H/D KIE experiments with **7** at 22 °C using 0.42 M $[H_2O]/[D_2O]$, which falls within the linear regime (Figure 4.5, purple circles), reveals a value of 1.8 (Figure 4.18 Appendix), identical within experimental error to those obtained in the saturation regime (Table 4.2). Eyring parameters determined in the linear $[H_2{}^{18}O]$ dependence regime between 310 and 295 K (the limited temperature range is due to the fact that decomposition of **7** is observed at higher temperatures), reveal a $\Delta H^{\ddagger} = 34(5)$ kJ mol^{-1} and $\Delta S^{\ddagger} = -160(38)$ J K^{-1} mol^{-1} (Figure 4.6, open and filled black circles). Similarly, these results are within experimental error of Eyring parameters determined in the saturated $[H_2{}^{18}O]$ regime between 284 and 258 K, where $\Delta H^{\ddagger} = 26(3)$ kJ mol^{-1} and $\Delta S^{\ddagger} = -194(17)$ J K^{-1} mol^{-1} (Figure 4.6, open and filled red circles). Thus, analogous to the KIE results, the Eyring activation parameters for the OAE between $H_2{}^{18}O$ and **7** do not appear to change in a significant manner between the two $[H_2{}^{18}O]$ dependence regimes.

Different from **7**, complex **8** undergoes OAE with a rate that is independent of $[H_2{}^{18}O]$, as found for other nonheme oxoiron(IV) complexes supported by pentadentate ligands, **3 - 6**, which is likely due to saturation at very low $[H_2{}^{18}O]$ values (Figure 4.5, filled purple squares). Complex **8** exhibits an H_2O/D_2O KIE of 5.7 (Figure 4.6, top), similar to the KIE of 5.1 obtained for the pentadentate-ligand-supported oxoiron(IV) complex, **6**. This kinetic result once again suggests a large degree of O–H/O–D cleavage in the RDS.

However, in stark contrast, the reactions between $H_2{}^{18}O$ and **9**, where the oxoiron(IV) center is supported by an isomeric pentadentate variant of PyTACN,[35] exhibit OAE rates with a linear [$H_2{}^{18}O$] dependence (Figure 4.5, filled blue triangles), with a k_2 = 12(1) x 10^{-3} M^{-1} s^{-1} at 323 K, which does not appear to saturated even at high [$H_2{}^{18}O$], suggesting a different RDS from complexes **7** and **8**. In corroboration, H_2O/D_2O KIE experiments with **9** afford a value of 1.3 (Figure 4. 6, bottom), significantly smaller than the KIE of 5.7 measured for **8** (Figure 4.6, top). The difference in Eyring parameters for the OAE reactions of **8** and **9** also supports a difference in the RDS (Table 4.1, Figure 4.9). Specifically, the enthalpy of activation, $\Delta H^{\ddagger}$, for **8** is 22 kJ mol^{-1}, while that for **9** is over 75 kJ mol^{-1} higher, at 89 kJ mol^{-1}. Meanwhile, the entropy of activation, $\Delta S^{\ddagger}$, for **8** at -220 J K^{-1} mol^{-1} is quite large and negative, but that for **9** is near zero.

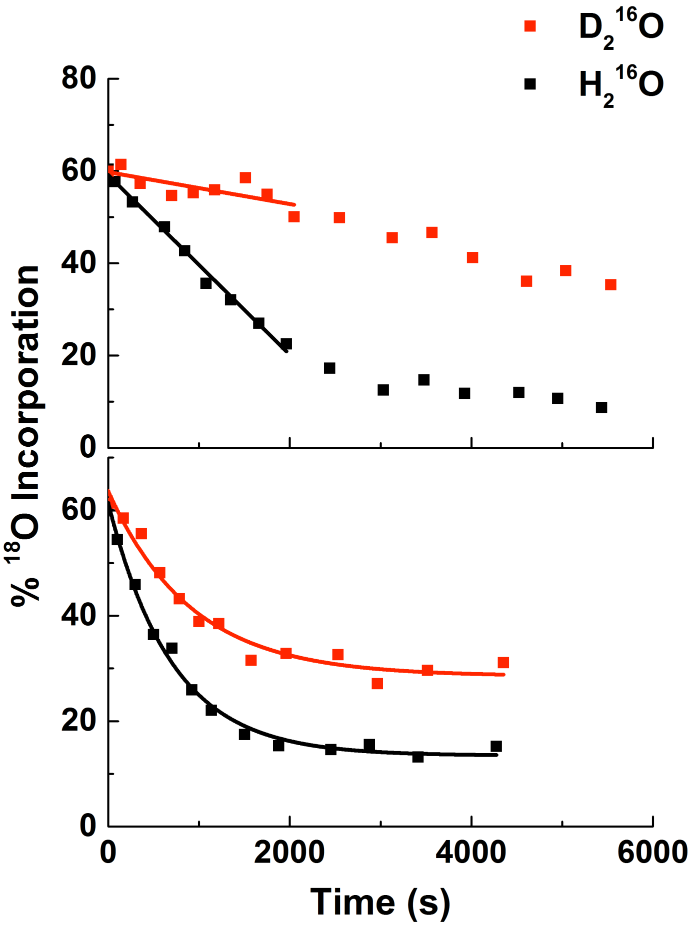

Figure 4.7. Top: Experiment between ^{18}O-labeled **8** (0.5 mM, generated from reaction of $[Fe^{II}(Me_2Py_2TACN)(MeCN)](OTf)_2$ and $PhI^{18}O$) and $H_2{}^{16}O$ (black, 0.37 M) and $D_2{}^{16}O$ (red, 0.37 M) at 45 °C, resulting in a KIE = 5.7. A ratio of the initial rates was used to calculate the KIE, where the initial rates are determined from the linear fit shown as solid lines. **Bottom**: Experiment between ^{18}O-labeled **9** (0.5 mM, generated from reaction of $[Fe^{II}(MePy_2TACN)(MeCN)](OTf)_2$ and $PhI^{18}O$) and $H_2{}^{16}O$ (black, 0.37 M) and $D_2{}^{16}O$ (red, 0.37 M) at 30 °C, resulting in a KIE = 1.3. Single exponential fits are shown as solid lines.

4.7 Mechanistic Considerations

Table 4.1 lists ten oxoiron(IV) complexes supported by polydentate ligands that have been investigated with respect to their propensity to undergo OAE with $H_2{}^{18}O$; of these, only one, complex **2**, does not undergo OAE under the conditions studied. The remaining nine complexes exhibit OAE rates that span a range of over two orders of magnitude when compared under identical reaction conditions, clearly demonstrating that the rates of OAE are modulated by the nature of the supporting polydentate ligand. Complexes **3** and **8** represent the complexes with the slowest OAE rates, while the BnTPEN-based complexes **4** – **6** comprise those with the fastest rates (Table 4.1). As reflected by their [$H_2{}^{18}O$] dependence, the reactions between $H_2{}^{18}O$ and these oxoiron(IV) complexes mainly fall into one of two distinct kinetic regimes. Subset A consists of nonheme oxoiron(IV) complexes with OAE rates that demonstrate a linear dependence on [$H_2{}^{18}O$], suggesting bimolecular RDS in which $H_2{}^{18}O$ binds to the Fe^{IV} center. On the other hand, subset B consists of nonheme oxoiron(IV) complexes that demonstrate no [$H_2{}^{18}O$] dependence on the OAE rate, presumably reflecting a RDS occurring after initial $H_2{}^{18}O$ binding in which proton transfer or tautomerization between the bound aqua and oxo ligands is likely occurring. Employing this classification, $[Fe^{IV}(O)(TMC)(MeCN)]^{2+}$ and complexes **1** and **9** belong to subset A, while complexes **3**, **4**, **5**, **6**, and **8** fall within subset B. Interestingly, complex **7** spans both subsets A and B, exhibiting a linear dependence on [$H_2{}^{18}O$] up to 0.6 M and saturation behavior beyond 0.6 M at 22 **°C**.

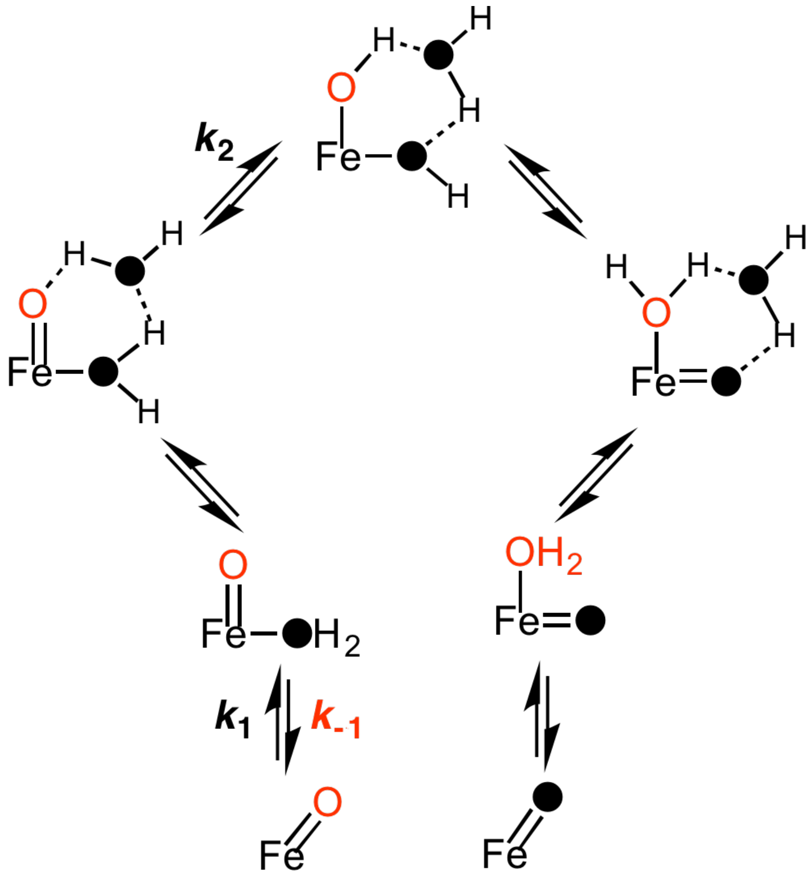

Scheme 4.4. Common mechanism for OAE between $H_2{}^{18}O$ and nonheme oxoiron(IV) complexes supported by tetradentate and pentadentate ligands.

The two kinetic regimes found within a common OAE mechanism are illustrated in Scheme 4.4.[45] For complexes in subset A, k_{-1}, $k_1 << k_2$, and $H_2{}^{18}O$ association to the iron complex must be the rate determining step to account for the observed linear dependence on $[H_2{}^{18}O]$, as previously reported for **1** and $[Fe^{IV}(O)(TPA)(NCMe)]^{2+}$, and found here for **7** at $[H_2{}^{18}O]$ values below 0.6 M and complex **9** (Figure 4.2).[12,43] Consistent with this mechanistic step, H_2O/D_2O KIEs of 1.3 – 1.6 were found in this study for **1**, **7** and **9**, reflecting some contribution of O-H/O-D bond cleavage upon binding $H_2{}^{18}O$ to the Fe^{IV} complex, likely due to the Lewis acidity of these high-valent iron centers. However, for subset B for which k_{-1}, $k_1 >> k_2$, a facile water binding pre-equilibrium is achieved and proton transfer becomes the rate determining step, so the observed OAE reaction rate is independent of [$H_2{}^{18}O$]. The latter results in the observation of quite large H_2O/D_2O KIEs of 5.1 and 5.7 for complexes **6** and **8**, respectively. These results represent the first direct experimental evidence for O–H bond cleavage in OAE reactions between $H_2{}^{18}O$ and oxoiron(IV) complexes. Notably, no H/D KIE was found in OAE studies between $H_2{}^{18}O$ and di-μ-oxo-dimanganese complexes by Brudvig and Crabtree.[27,28] However, there are some H/D KIE values known regarding proton-assisted O-O bond cleavage events with iron peroxo species, in which new O-H bonds are formed. Specifically, KIE values of 1.4 and 1.8 were observed for O-O cleavage in soluble methane monooxygenase, 1.7 for horseradish peroxidase, 2.0 for a synthetic porphyrin peroxoiron(III) complex, and 2.5 for a synthetic nonheme peroxoiron(III) complex. These values are quite similar to the H/D KIEs observed for complexes **1**, **7**, and **9**, but are much smaller than those observed for **6** and **8** (Table 4.2). For reasons that are not clear, the KIE of **7** remains unchanged in both of these kinetic regimes. Presumably, proton transfer in this step is substantially masked by at least one of the reactions that precede this step. For example, structural reorganizations within the water bound complex may account for this effect. Finally, the common mechanism also reflects the involvement of more than one H_2O molecule to facilitate intramolecular proton transfer, as proposed earlier for **7** by DFT calculations.[43]

An examination of the Eyring activation parameters for OAE between $H_2{}^{18}O$ and oxoiron(IV) complexes listed in Table 4.1 and derived from plots shown in Figure 4.14 Appendix, shows that, except for **9**, all the other oxoiron(IV) complexes have relatively small to moderate $\Delta H^{\ddagger}$ values (5 to 43 kJ mol^{-1}) and very large and negative $\Delta S^{\ddagger}$ values (-133 to -248 J K^{-1} mol^{-1}), despite the observation that these complexes fall under kinetic regimes or subsets as described earlier. This is mostly clearly illustrated by complex 7, which exhibits the same Eyring activation parameters, irrespective of being in a linear [$H_2{}^{18}O$] dependence regime or saturation regime (Figure 4.6). This suggests that the Eyring activation parameters are likely reflecting a combination of multiple steps in the mechanism, rather than an individual RDS. The large negative activation entropies observed, despite the fact that all the complexes are in principle octahedral coordinatively saturated species, are indicative of inner or outer-sphere water binding as the RDS or being involved in a facile equilibrium prior to the RDS. In addition, the Eyring parameters exhibit an apparent entropy-enthalpy compensation effect in the activation barriers observed across the series of complexes.[50] This observation gives further evidence for a shared mechanism of OAE between $H_2{}^{18}O$ and nonheme oxoiron(IV) complexes supported by tetradentate and pentadentate ligands, where the different [$H_2{}^{18}O$] dependence we observe reflect different kinetic regimes within the same mechanism.

The OAE behavior of **9** stands out from that of the other complexes in this study. Most notably it has an activation enthalpy twice as large as that of **3**, the complex with the second largest $\Delta H^{\ddagger}$ in Table 4.1. Moreover, OAE for **9** essentially exhibits zero activation entropy. These two observations are suggestive of a unimolecular RDS, such as the dissociation of a ligand arm from the oxoiron(IV) center prior to $H_2{}^{18}O$ binding.

Despite the near-zero $\Delta S^{\ddagger}$, a linear [$H_2{}^{18}O$] dependence and a small H_2O/D_2O KIE of 1.3 are nevertheless observed.

4.8 Discussion

We have undertaken a detailed study of OAE between $H_2{}^{18}O$ and a number of nonheme oxoiron(IV) complexes. In so doing, we have determined that the [$H_2{}^{18}O$]/[$H_2{}^{16}O$] ratio in solution is reflected by the extent of ^{18}O-atom incorporation into nonheme oxoiron(IV) complexes. These results suggest that every step in the nonheme OAE mechanism is reversible, allowing for formation of both ^{18}O and ^{16}O isotopomers. While this outcome may appear to contrast with Meunier's initial report on OAE between $H_2{}^{18}O$ and Mn- and Fe-based metalloporphyrin systems, where the ^{18}O-atom incorporation reaches a maximum of 50%,[8] the ^{18}O-atom incorporation in these systems was determined by the extent of ^{18}O-labeling in the epoxide product formed upon reaction of the unobserved high-valent metal-oxo species with olefin. Subsequent studies by Nam illustrated that the ^{18}O-labeling could exceed 50% if the concentration of olefin was low compared to the concentration of $H_2{}^{18}O$, thereby slowing the rate of olefin oxidation versus the rate of OAE with $H_2{}^{18}O$.[11]

Our mechanistic insights into the ligand dependence on rates of OAE between $H_2{}^{18}O$ and nonheme oxoiron(IV) complexes will be of intrinsic value not only for the indirect detection of oxoiron(IV) complexes in substrate oxidation reactions but also for generating the ^{18}O-isotopomer of nonheme oxoiron(IV) complexes for spectroscopic and reactivity studies. As a general rule of thumb, increasing $[H_2{}^{18}O]$ will increase the rate of OAE for oxoiron(IV) complexes that fall within subset A, where a linear $[H_2{}^{18}O]$ dependence is observed. In contrast, OAE rates may not be controlled by varying $[H_2{}^{18}O]$ for oxoiron(IV) complexes falling within subset B, suggesting that other experimental variables, such as temperature, must be used to control the rate of OAE. These data will also be of relevance to studies of oxoiron(IV) complexes generated in water or acetonitrile/water mixtures[51,52] that are becoming increasingly more common in the context of photocatalysis[35,53] and water oxidation.[54,55]

4.9 References

(1) Nam, W. *Acc. Chem. Res.* **2007**, *40*, 522–531.

(2) Meunier, B.; de Visser, S. P.; Shaik, S. *Chem. Rev.* **2004**, *104*, 3947-3980.

(3) Ortiz de Montellano, P. R. *Chem. Rev.* **2010**, *110*, 932-948.

(4) Costas, M.; Mehn, M. P.; Jensen, M. P.; Que, L., Jr. *Chem. Rev.* **2004**, *104*, 939-986.

(5) Kovaleva, E. G.; Lipscomb, J. D. *Nat. Chem. Biol.* **2008**, *4*, 186-193.

(6) Umena, Y.; Kawakami, K.; Shen, J.-R.; Kamiya, N. *Nature* **2011**, *473*, 55-60.

(7) Hashimoto, S.; Tatsuno, Y.; Kitagawa, T. *Proc. Natl. Acad. Sci. USA* **1986**, *83*, 2417-2421.

(8) Bernadou, J.; Fabiano, A.-S.; Robert, A.; Meunier, B. *J. Am. Chem. Soc.* **1994**, *116*, 9375-9376.

(9) Meunier, B.; Bernadou, J. *Struct. Bonding* **2000**, *97*, 1-35.

(10) Nam, W.; Valentine, J. S. *J. Am. Chem. Soc.* **1993**, *115*, 1772-1778.

(11) Lee, K. A.; Nam, W. *J. Am. Chem. Soc.* **1997**, *119*, 1916-1922.

(12) Seo, M. S.; In, J.-H.; Kim, S. O.; Oh, N. Y.; Hong, J.; Kim, J.; Que, L., Jr.; Nam, W. *Angew. Chem. Int. Ed.* **2004**, *43*, 2417-2420.

(13) Jensen, M. P.; Lange, S. J.; Mehn, M. P.; Que, E. L.; Que, L., Jr. *J. Am. Chem. Soc.* **2003**, *125*, 2113-2128.

(14) Rana, S.; Dey, A.; Maiti, D. *Chem. Comm.* **2015**, *51*, 14469-14472.

(15) Ottenbacher, R. V.; Talsi, E. P.; Bryliakov, K. P. *ACS Catalysis* **2015**, *5*, 39-44.

(16) Mitra, M.; Lloret-Fillol, J.; Haukka, M.; Costas, M.; Nordlander, E. *Chem. Comm.* **2014**, *50*, 1408-1410.

(17) Prat, I.; Gómez, L.; Canta, M.; Ribas, X.; Costas, M. *Chem. Eur. J.* **2013**, *19*, 1908-1913.

(18) Mikhalyova, E. A.; Makhlynets, O. V.; Palluccio, T. D.; Filatov, A. S.; Rybak-Akimova, E. V. *Chem. Commun.* **2012**, *48*, 687-689.

(19) Wang, B.; Wang, S.; Xia, C.; Sun, W. *Chem. Eur. J.* **2012**, *18*, 7332-7335.

(20) Wu, M.; Miao, C.-X.; Wang, S.; Hu, X.; Xia, C.; Kühn, F. E.; Sun, W. *Adv. Synth. Catal.* **2011**, *353*, 3014-3022.

(21) Makhlynets, O. V.; Das, P.; Taktak, S.; Flook, M.; Mas-Ballesté, R.; Rybak-Akimova, E. V.; Que, L., Jr. *Chem. Eur. J.* **2009**, *15*, 13171-13180.

(22) Lee, S. H.; Han, J. H.; Kwak, H.; Lee, S. J.; Lee, E. Y.; Kim, H. J.; Lee, J. H.; Bae, C.; Lee, S. N.; Kim, Y.; Kim, C. *Chem. Eur. J.* **2007**, *13*, 9393 – 9398.

(23) Chen, K.; Costas, M.; Kim, J.; Tipton, A. K.; Que, L., Jr. *J. Am. Chem. Soc.* **2002**, *124*, 3026-3035.

(24) Mekmouche, Y.; Ménage, S.; Toia-Duboc, C.; Fontecave, M.; Galey, J.-B.; Lebrun, C.; Pecaut, J. *Angew. Chem. Int. Ed.* **2001**, *40*, 949-952.

(25) Chen, K.; Que, L., Jr. *J. Am. Chem. Soc.* **2001**, *123*, 6327-6337.

(26) Chen, K.; Que, L., Jr. *Angew. Chem. Int. Ed.* **1999**, *38*, 2227-2229.

(27) Tagore, R.; Chen, H. Y.; Crabtree, R. H.; Brudvig, G. W. *J. Am. Chem. Soc.* **2006**, *128*, 9457-9465.

(28) Tagore, R.; Crabtree, R. H.; Brudvig, G. W. *Inorg. Chem.* **2007**, *46*, 2193-2203.

(29) Pestovsky, O.; Bakac, A. *Inorg. Chem* **2006**, *45*, 814-820.

(30) Rohde, J.-U.; In, J.-H.; Lim, M. H.; Brennessel, W. W.; Bukowski, M. R.; Stubna, A.; Münck, E.; Nam, W.; Que, L., Jr. *Science* **2003**, *299*, 1037-1039.

(31) Thibon, A.; England, J.; Martinho, M.; Young, V. G., Jr.; Frisch, J. R.; Guillot, R.; Girerd, J.-J.; Münck, E.; Que, L., Jr.; Banse, F. *Angew. Chem. Int. Ed.* **2008**, *47*, 7064-7067.

(32) Lubben, M.; Meetsma, A.; Wilkinson, E. C.; Feringa, B.; Que, L., Jr. *Angew. Chem. Int. Ed. Engl.* **1995**, *34*, 1512-1514.

(33) Kaizer, J.; Klinker, E. J.; Oh, N. Y.; Rohde, J.-U.; Song, W. J.; Stubna, A.; Kim, J.; Münck, E.; Nam, W.; Que, L., Jr. *J. Am. Chem. Soc.* **2004**, *126*, 472-473.

(34) Roelfes, G.; Vrajmasu, V.; Chen, K.; Ho, R. Y. N.; Rohde, J.-U.; Zondervan, C.; la Crois, R. M.; Schudde, E. P.; Lutz, M.; Spek, A. L.; Hage, R.; Feringa, B. L.; Münck, E.; Que, L., Jr. *Inorg. Chem.* **2003**, *42*, 2639-2653.

(35) Company, A.; Sabenya, G.; González-Béjar, M.; Gómez, L.; Clémancey, M.; Blondin, G.; Jasniewski, A. J.; Puri, M.; Browne, W. R.; Latour, J.-M.; Que, L., Jr.; Costas, M.; Pérez-Prieto, J.; Lloret-Fillol, J. *J. Am. Chem. Soc.* **2014**, *136*, 4624-4633.

(36) Wang, D.; Ray, K.; Collins, M. J.; Farquhar, E. R.; Frisch, J. R.; Gómez, L.; Jackson, T. A.; Kerscher, M.; Waleska, A.; Comba, P.; Costas, M.; Que, L. *Chem. Sci.* **2013**, *4*, 282-291.

(37) Saltzman, H.; Sharefkin, J. G.: In *Organic Syntheses*; Wiley: New York, 1973; Vol. V; pp 658.

(38) Schardt, B. C.; Hill, C. L. *Inorg. Chem.* **1983**, *22*, 1563-1565.

(39) Schatz, M.; Leibold, M.; Foxon, S. P.; Weitzer, M.; Heinemann, F. W.; Hampel, F.; Walter, O.; Schindler, S. *Dalton Trans.* **2003**, 1480-1487.

(40) Klinker, E. J.; Kaizer, J.; Brennessel, W. W.; Woodrum, N. L.; Cramer, C. J.; Que, L., Jr. *Angew. Chem. Int. Ed.* **2005**, *44*, 3690-3694.

(41) Cho, J.; Jeon, S.; Wilson, S. A.; Liu, L. V.; Kang, E. A.; Braymer, J. J.; Lim, M. H.; Hedman, B.; Hodgson, K. O.; Valentine, J. S.; Solomon, E. I.; Nam, W. *Nature* **2011**, *478*, 502-505.

(42) Prakash, J.; Rohde, G. T.; Meier, K. K.; Münck, E.; Que, L. *Inorg. Chem.* **2015**, *54*, 11055-11057.

(43) Company, A.; Prat, I.; Frisch, J. R.; Mas-Ballesté, R.; Güell, M.; Juhász, G.; Ribas, X.; Münck, E.; Luis, J. M.; Que, L., Jr.; Costas, M. *Chem. Eur. J.* **2011**, *17*, 1622-1634.

(44) Planas, O.; Clemancey, M.; Latour, J.-M.; Company, A.; Costas, M. *Chem. Comm.* **2014**, *50*, 10887-10890.

(45) A reviewer suggested an alternate mechanism in which residual Fe^{II} in the reaction mixture may accelerate OAE. We have tested this hypothesis with complex **1** and found no enhancement in OAE reate between $H_2{}^{18}O$ and **1** upon addition of $[Fe^{II}(TMC)(OTf)](OTf)$ to the reaction mixture (Figure 4.19 Appendix).

(46) a) Lee, S. Y.; Lipscomb, J. D. *Biochemistry* **1999**, *38*, 4423. b) Tinberg, C. E.; Lippard, S. J. *Biochemistry* **2009**, *48*, 12145.

(47) Dunford, H. B.; Hewson, W. D.; Steiner, H. *Can. J. Chem.* **1978**, *56*, 2844.

(48) a) Traylor, T. G.; Xu, F. J. *J. Am. Chem. Soc.* **1990**, *112*, 178. b) Groves, T. J.; Watanabe, Y. *J. Am. Chem. Soc.* **1988**, *110,* 8443.

(49) Oloo, W. N.; Fielding, A. J.; Que, L., Jr. *J. Am. Chem. Soc.* **2013**, *135*, 6438.

(50) Kryatov, S. V.; Chavez, F. A.; Reynolds, A. M.; Rybak-Akimova, E. V.; Que, L., Jr.; Tolman, W. B. *Inorg. Chem.* **2004**, *43*, 2141-2150.

(51) Lee, Y.-M.; Dhuri, S. N.; Sawant, S. C.; Cho, J.; Kubo, M.; Ogura, T.; Fukuzumi, S.; Nam, W. *Angew. Chem. Int. Ed.* **2009**, *48*, 1803-1806.

(52) Chantarojsiri, T.; Sun, Y.; Long, J. R.; Chang, C. J. *Inorg. Chem.* **2015**, *54*, 5879-5887.

(53) Kotani, H.; Suenobu, T.; Lee, Y.-M.; Nam, W.; Fukuzumi, S. *J. Am. Chem. Soc.* **2011**, *133*, 3249-3251.

(54) Fillol, J. L.; Codolà, Z.; Garcia-Bosch, I.; Gómez, L.; Pla, J. J.; Costas, M. *Nat. Chem.* **2011**, *3*, 807-813.

(55) Codolà, Z.; Gómez, L.; Kleespies, S. T.; Que Jr, L.; Costas, M.; Lloret-Fillol, J. *Nat. Comm.* **2015**, *6*.

(56) Draksharapu, A.; Li, Q.; Logtenberg, H.; van den Berg, T. A.; Meetsma, A.; Killeen, J. S.; Feringa, B. L.; Hage, R.; Roelfes, G.; Browne, W. R. *Inorg. Chem.* **2012**, *51*, 900-913.

4.11 Appendix

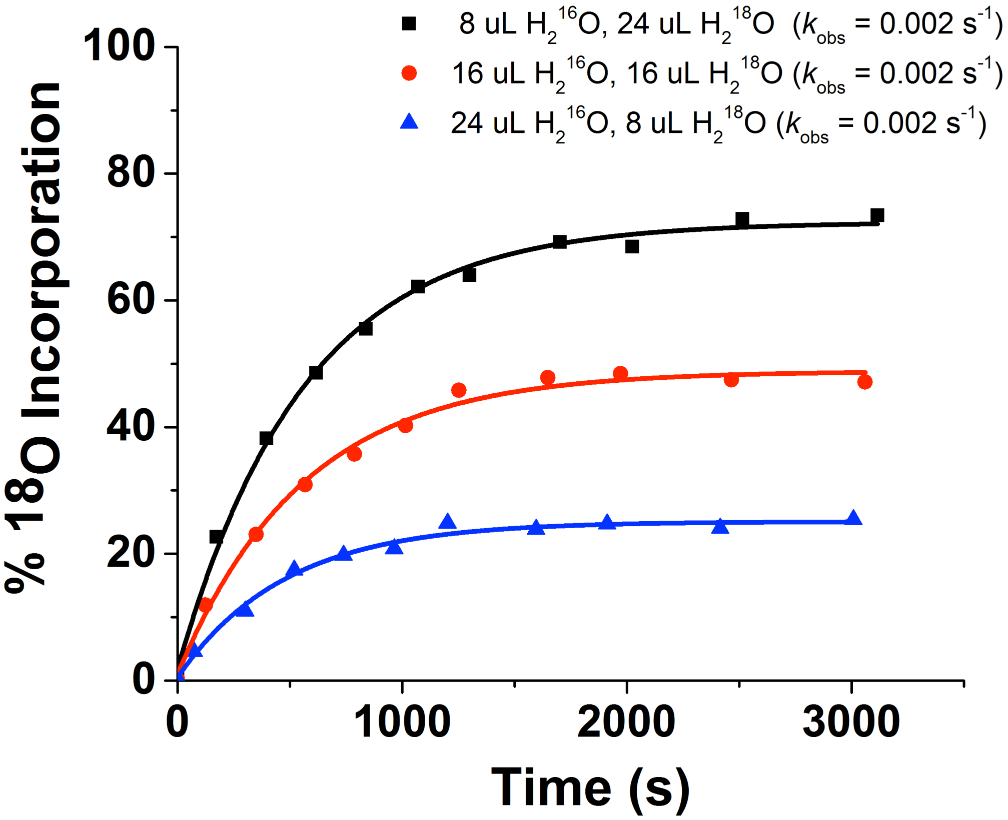

Figure 4.8. Plots of percent ^{18}O-atom incorporation against time for the OAE reaction between complex **1** and varying amounts of $H_2^{16}O/H_2^{18}O$ (1:3 in black squares, 1:1 in red circles and 1:3 in blue triangles), where the total H_2O volume is kept constant at 32 μL (0.59 M) in MeCN solution at 24 °C.

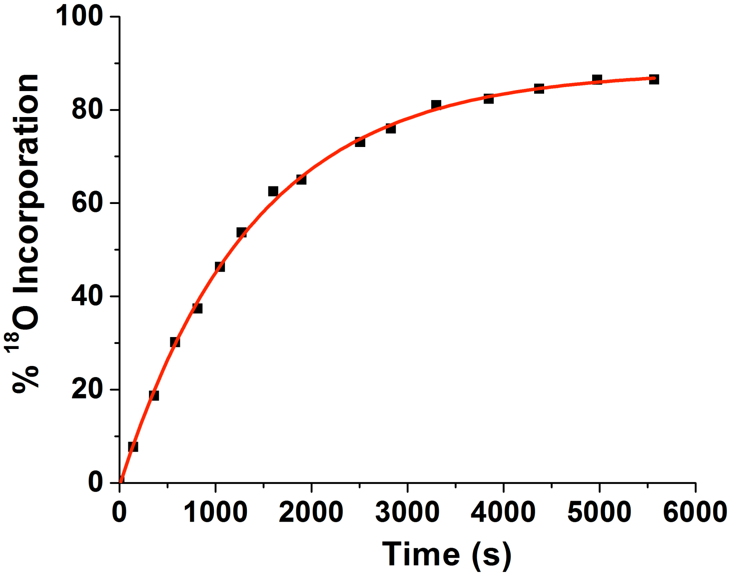

Figure 4.9. Plots of percent ^{18}O-atom incorporation against time for the OAE reaction between complex **1** (black squares, 0.5 mM) and $H_2{}^{18}O$ (0.19 M) in MeCN solution at 25 °C, demonstrating high overall ^{18}O-atom incorporation of ~80%. The single exponential fit is shown as a solid red line.

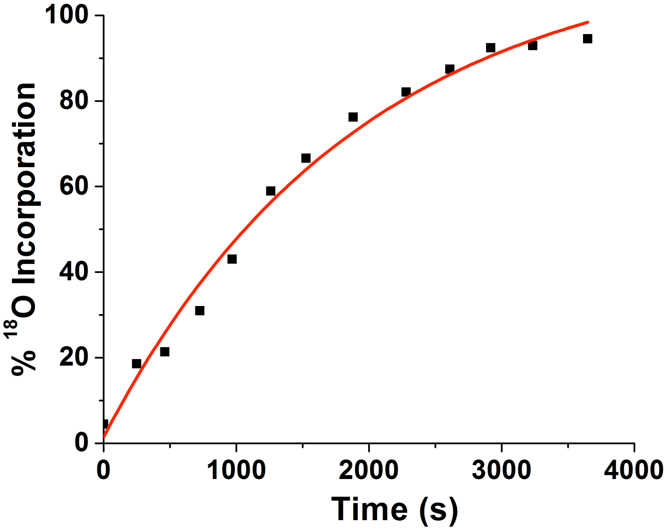

Figure 4.10. Plot of percent ^{18}O-atom incorporation against time for the OAE reaction between complex **3** (black squares, 2.0 mM) and $H_2{}^{18}O$ (1.48 M) in MeCN solution at 25 °C, demonstrating high overall ^{18}O-atom incorporation of ~90%. The single exponential fit is shown as a solid red line.

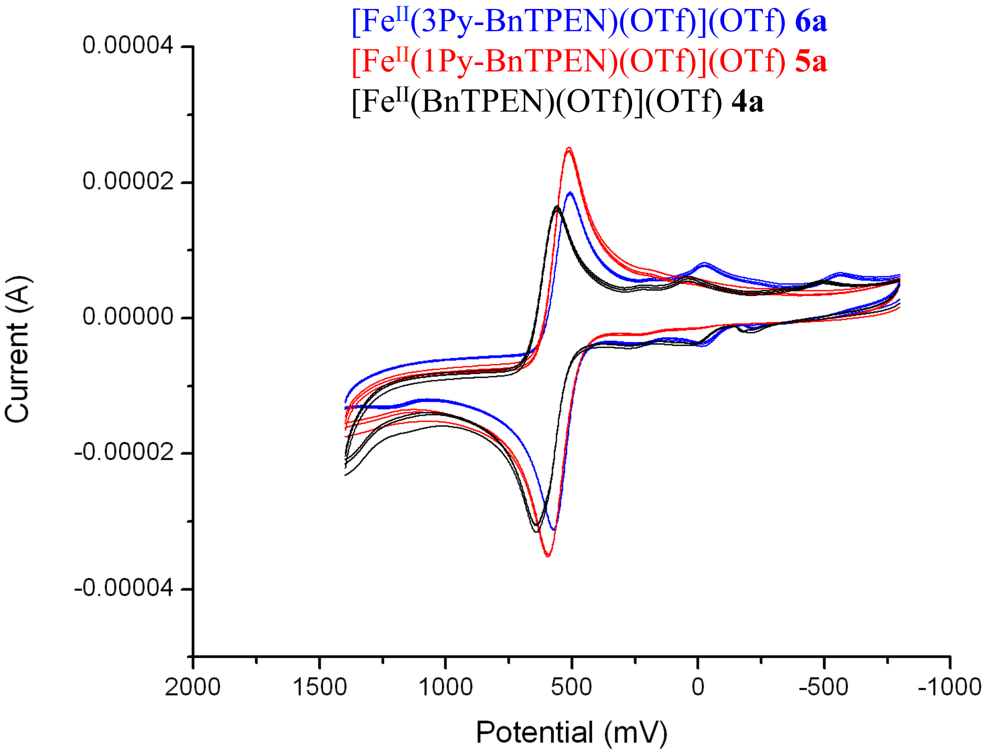

Figure 4.11. Cyclic voltammetry (CV) of **4a**, **5a** and **6a** in acetonitrile with 0.1 M TBAPF$_6$ at 25 °C with noted potential (mV) versus Fc/Fc$^+$. The smaller redox waves are likely due to a Fe^{II}/Fe^{III} redox couple of [Fe^{II}(L)(OH$_2$)]$^{2+}$ from residual H$_2$O in the acetonitrile, based on assignments made in ref 56.

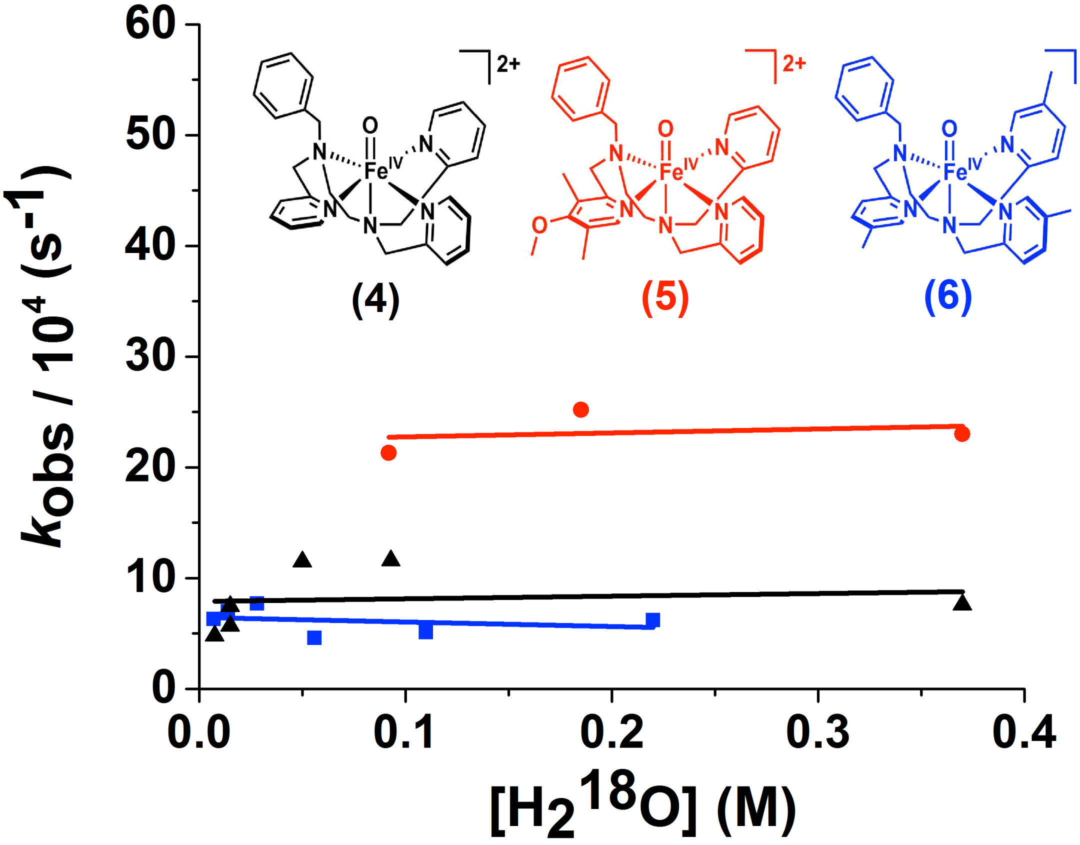

Figure 4.12. Plots of $H_2{}^{18}O$ concentration dependence for **4** (0.5 mM, black triangles) at -38 °C, **5** (0.5 mM, red circles) at 0 °C, and **6** (0.5 mM, blue squares) at 15 °C in a MeCN solution

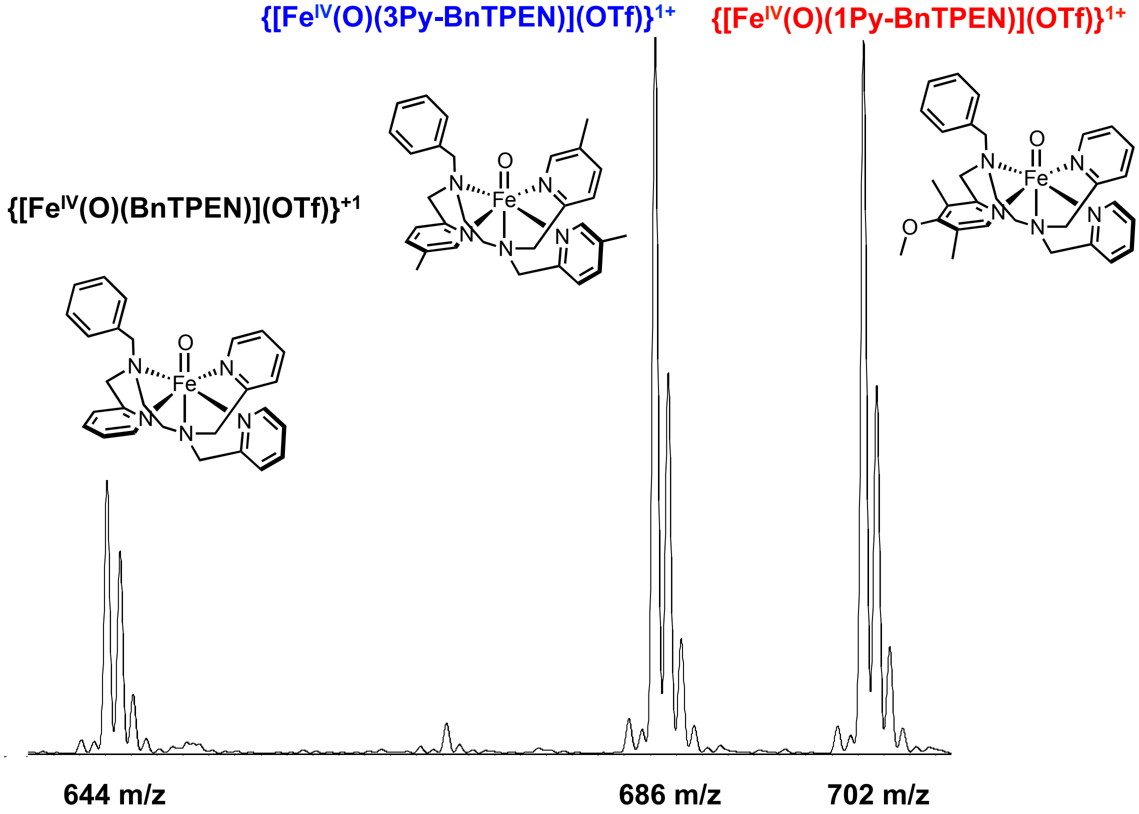

Figure 4.13. Sample ESI-MS spectrum of a combined solution of **4**, **5**, and **6**, showing sufficient spread of each cluster of peaks to monitor the OAE with $H_2{}^{18}O$ simultaneously for all three complexes.

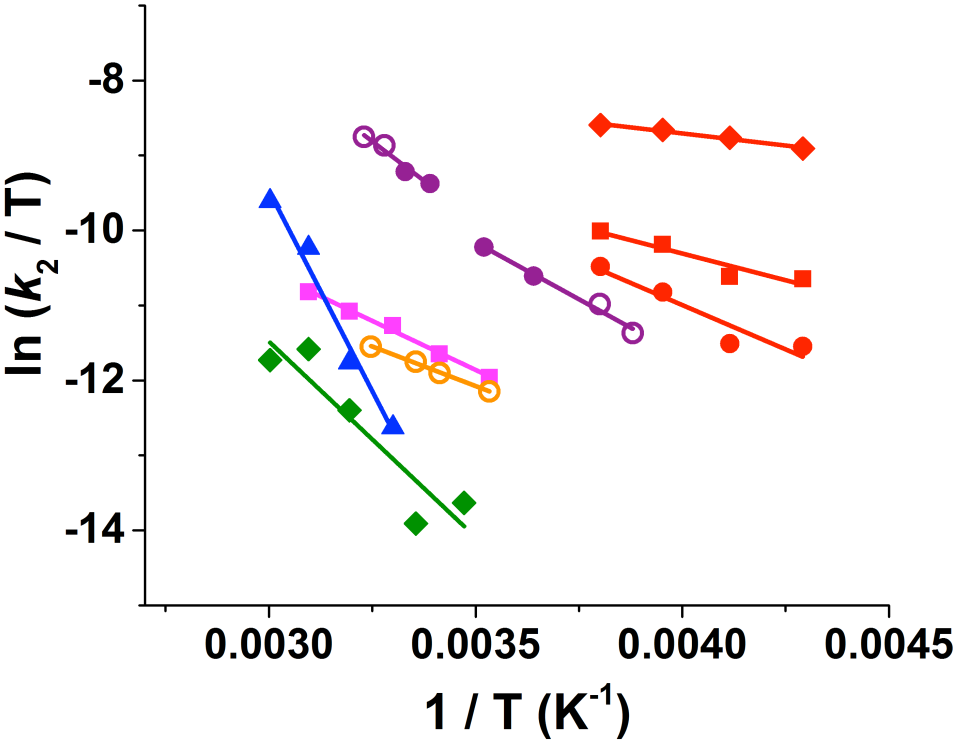

Figure 4.14. Eyring plots for **1** (previously reported in ref 12, open orange circles) with 0.37 M [$H_2{}^{18}O$], **3** (filled green diamonds) with 0.37 M [$H_2{}^{18}O$], **4** (filled red diamonds) with 0.28 M [$H_2{}^{18}O$], **5** (filled red squares) with 0.28 M [$H_2{}^{18}O$], **6** (filled red circles) with 0.28 M [$H_2{}^{18}O$], **7** (previously reported in ref 43 in filled purple circles, current work in open purple circles) with 0.20 M [$H_2{}^{18}O$], **8** (filled pink squares) at 0.74 M [$H_2{}^{18}O$], and **9** (filled blue diamonds) at 0.19 M [$H_2{}^{18}O$].

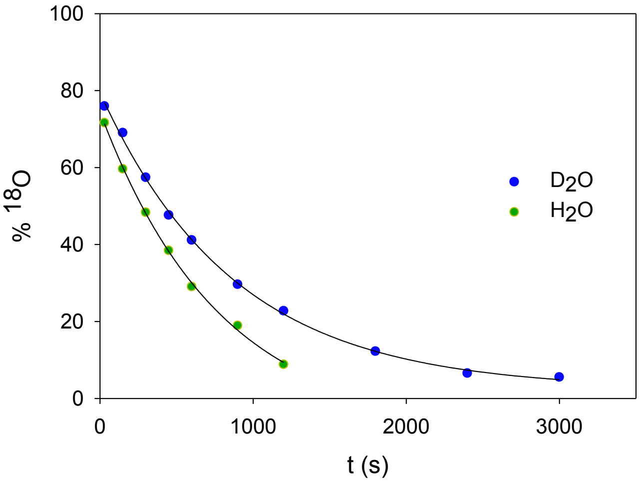

Figure 4.15. Experiments between ^{18}O-labeled **7** (generated from reaction of ^{16}O-labeled **7** and 0.14 M $H_2{}^{18}O$, 1.0 mM) and $H_2{}^{16}O$ (green, 1.57 M) or $D_2{}^{16}O$ (blue, 1.57 M) at 0 °C, resulting in a KIE = 1.5. The ^{18}O-incorporation was determined by quenching aliquots (0.4 mL, 0.4 mmol) of the reaction with thioanisole (5 μL, 42.7 mmol) and determining the ratio of ^{16}O and ^{18}O-methylphenylsulfoxide by GCMS, as previously described.[43]

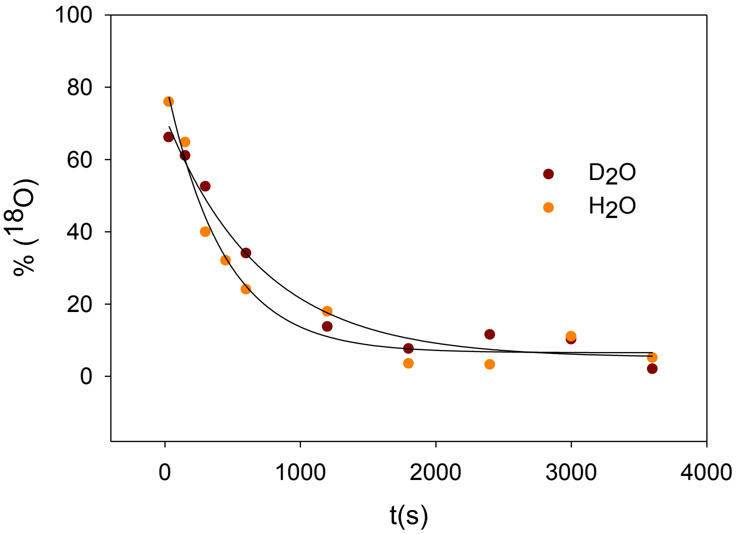

Figure 4.16. Experiments between ^{18}O-labeled **7** (generated from reaction of ^{16}O-labeled **7** and 0.14 M $H_2{}^{18}O$, 1.0 mM) and $H_2{}^{16}O$ (green, 0.74 M) or $D_2{}^{16}O$ (blue, 0.74 M) at 0 °C, resulting in a KIE = 1.7. The ^{18}O-incorporation was determined by quenching aliquots (0.4 mL, 0.4 mmol) of the reaction with thioanisole (5 μL, 42.7 mmol) and determining the ratio of ^{16}O and ^{18}O-methylphenylsulfoxide by GCMS, as previously described.[43]

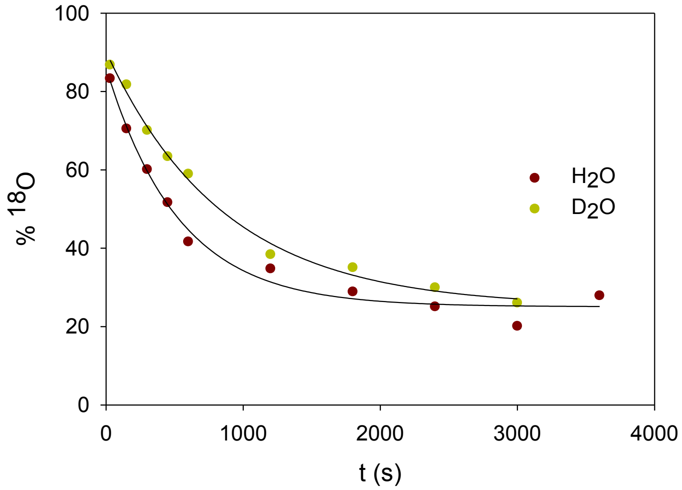

Figure 4.17. Experiments between ^{18}O-labeled **7** (generated from reaction of ^{16}O-labeled **7** and 0.14 M $H_2{}^{18}O$, 1.0 mM) and $H_2{}^{16}O$ (green, 0.42 M) or $D_2{}^{16}O$ (blue, 0.42 M) at 0 °C, resulting in a KIE = 1.6. The ^{18}O-incorporation was determined by quenching aliquots (0.4 mL, 0.4 mmol) of the reaction with thioanisole (5 μL, 42.7 mmol) and determining the ratio of ^{16}O and ^{18}O-methylphenylsulfoxide by GCMS, as previously described.[43]

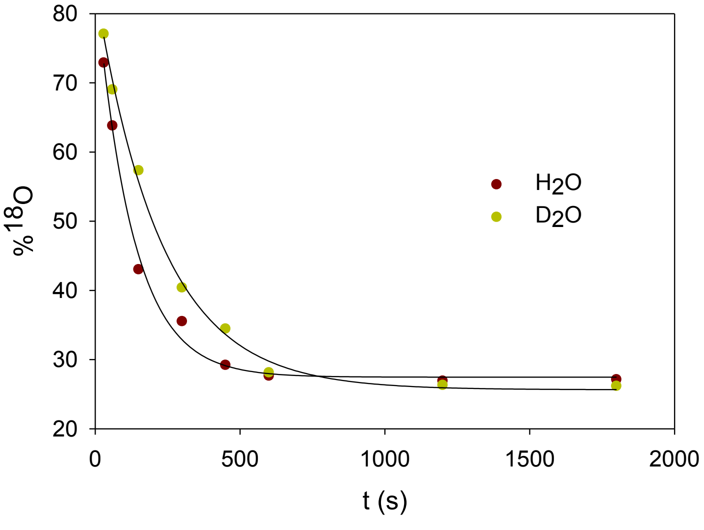

Figure 4.18. Experiments between ^{18}O-labeled **7** (generated from reaction of ^{16}O-labeled **7** and 0.14 M $H_2{}^{18}O$, 1.0 mM) and $H_2{}^{16}O$ (green, 0.42 M) or $D_2{}^{16}O$ (blue, 0.42 M) at 22 °C, resulting in a KIE = 1.8. The ^{18}O-incorporation was determined by quenching aliquots (0.4 mL, 0.4 mmol) of the reaction with thioanisole (5 μL, 42.7 mmol) and determining the ratio of ^{16}O and ^{18}O-methylphenylsulfoxide by GCMS, as previously described.[43]

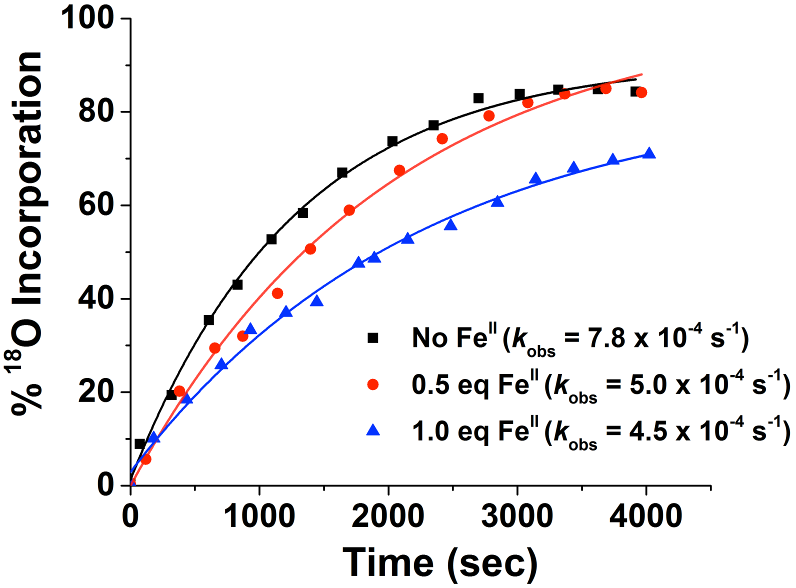

Figure 4.19. Plots of percent ^{18}O-atom incorporation against time for the OAE reaction between complex **1** (0.5 mM) and $H_2{}^{18}O$ (0.56 M) with no added [Fe^{II}(TMC)(OTf)](OTf) (black squares), 0.5 equivalent added [Fe^{II}(TMC)(OTf)](OTf) (red circles), and 1.0 equivalent added [Fe^{II}(TMC)(OTf)](OTf) (blue triangles), in MeCN solution at 22 °C. Single exponential fits are shown as solid lines.

Chapter 5:
Generation and Characterization of Six-coordinate Nonheme Imidoiron(IV) Complexes

5.1 Introduction

Nonheme imidoiron(IV) complexes are isoelectronic to oxoiron(IV) complexes and have been actively explored over the past decade, fueled in part by the desire to carry out amination and aziridination reactions that are analogous to the hydroxylation and epoxidation reactions which nonheme oxoiron(IV) complexes are well known for.[1,2,3,4,5,6] Importantly, the vast majority of nonheme imidoiron(IV) complexes reported to date adopt a four-coordinate pseudo-tetrahedral geometry,[7,8,9] with the only reported example of a six-coordinate pseudo-octahedral nonheme imidoiron(IV) complex being $[Fe^{IV}(NTs)(N4Py)]^{2+}$ (where Ts is tosylate).[10] A consequence of this difference in coordination geometry is that the pseudo-tetrahedral imidoiron(IV) complexes contain a formal Fe-N triple bond imparting remarkable stability to these species, whereas pseudo-octahedral six-coordinate imidoiron(IV) complexes contain a formal Fe-N double bond which often leads to a decrease in stability and an increase in reactivity (Figure 5.1).[5,10-11]

While there are some examples of four-coordinate nonheme imidoiron(IV) complexes capable of elegant intramolecular and intermolecular reactivity, such as Betley's $[Fe^{III}(pyrrol_2)(NC_6H_4\text{-}p\text{-}{}^tBu)]$ complex,[6,12] these are exceptions as they have an open-shell configuration with a formal Fe^{III} center and coordinated iminyl radical leading to an overall $S = 2$ ground spin state. Fully closed-shell six-coordinate nonheme imidoiron(IV) complexes are therefore rare and interesting synthetic targets, as these intermediates are more likely to be amendable to group-transfer and C-H bond activation studies under mild conditions compared to their four-coordinate analogues.[13]

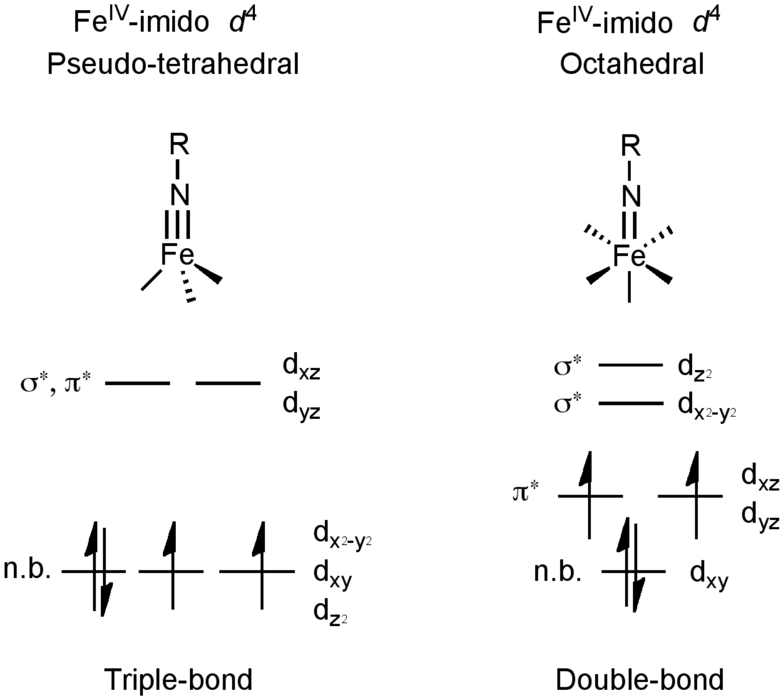

Figure 5.1. Qualitative d-orbital splitting diagrams for pseudo-tetrahedral imidoiron(IV) complexes (left) and pseudo-octahedral imidoiron(IV) complexes (right).[5,10]

Currently, the only published example of a six-coordinate nonheme imidoiron(IV) complex is $[Fe^{IV}(NTs)(N4Py)]^{2+}$ (**1**), where the $Fe^{IV}NTs$ center is supported by the pentadentate ligand, N4Py (Figure 5.2).[10] A similar N5 ligand, BnTPEN, has also been reported to stabilize the $Fe^{IV}NTs$ unit, $[Fe^{IV}(NTs)(BnTPEN)]^{2+}$ (**2**), although this data has remained unpublished (Figure 5.2).[14] These sole examples of six-coordinate nonheme imidoiron(IV) complexes employ pentadentate ligands, while there are no such examples containing tetradentate ligands, which would impart an open-coordination site for the binding of exogenous ligands, thereby increasing the potential scope for reactivity.

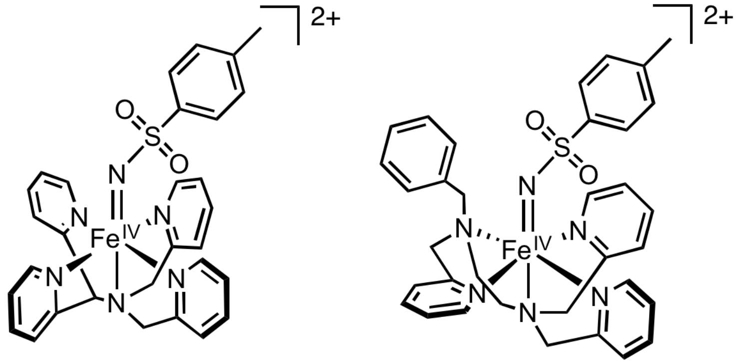

$[Fe^{IV}(NTs)(N4Py)]^{2+}$ (**1**) $[Fe^{IV}(NTs)(BnTPEN)]^{2+}$ (**2**)

Figure 5.2. Two reported examples of six-coordinate pseudo-octahedral imidoiron(IV) complexes.

Inspiration for designing a synthetic system in which a tetradentate ligand may support a six-coordinate nonheme imidoiron(IV) complex dates back to 2003, when Jensen reported the intramolecular *ortho*-hydroxylation and amination of a pendant phenyl ring of the tetradentate tripodal ligand, 6-PhTPA (where 6-PhTPA is 6-phenyl-2-pyridylmethyl)bis(2-pyridylmethyl)amine), upon reaction between $[Fe^{II}(6\text{-}PhTPA)(MeCN)_2]^{2+}$ and the hypervalent-iodine oxidants, PhIO (iodosylbenzene) and PhINTs (phenyl-N-tosylimidoiodinane), respectively (Figure 5.3).[15] The reactive intermediates in this transformation were proposed to be nonheme oxoiron(IV) and imidoiron(IV) species; however, these intermediates could not be directly trapped or characterized.[15b] Later in 2003, successful generation of the nonheme oxoiron(IV) complex was reported by removal of the pendant 6-phenyl group and utilization of the parent TPA ligand (Figure 5.4).[16] While the generation of the corresponding nonheme imidoiron(IV) complex supported by TPA has yet to be reported, the observed *ortho*-amination reactivity suggests that such a species should be possible to trap and characterize under the right conditions (Figure 5.4).

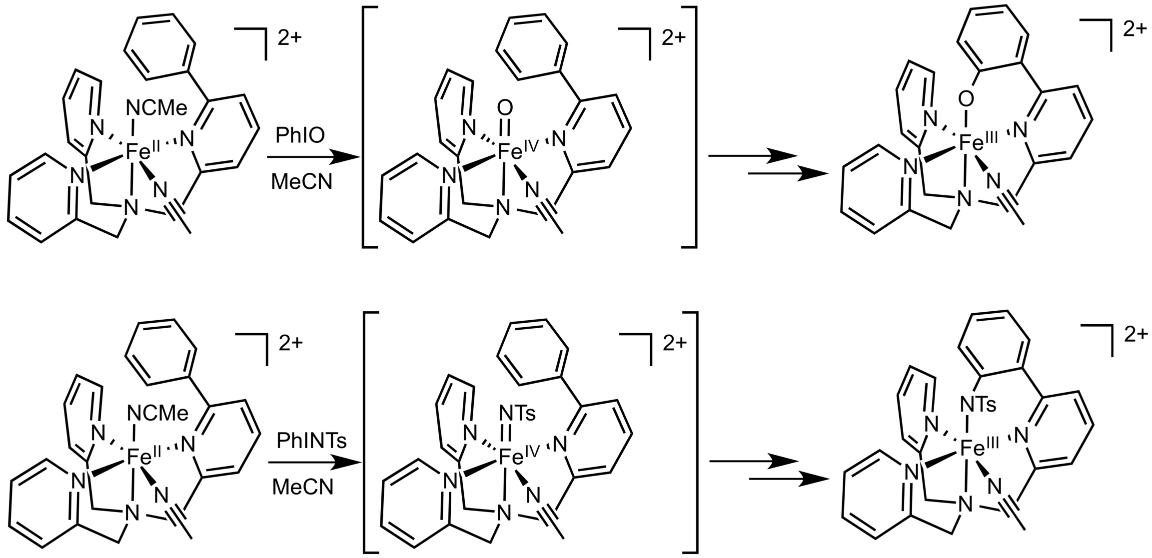

Figure 5.3. Previously reported intramolecular aromatic *ortho*-hydroxylation and amination utilizing PhIO and PhINTs with the $[Fe^{II}(6Ph\text{-}TPA)(MeCN)_2]^{2+}$ system, where the proposed oxoiron(IV) and imidoiron(IV) intermediates are shown in brackets.[15b]

Here the generation of a six-coordinate nonheme imidoiron(IV) complex supported by a tripodal tetradentate ligand, TPA*, is reported. This new species, $[Fe^{IV}(NTs)(TPA^*)(MeCN)]^{2+}$ (**3**), has been characterized by UV-Visible spectroscopy, ESI-MS, XAS, Mössbauer, and rRaman spectroscopies, and is compared against other nonheme imidoiron(IV) complexes in the literature.

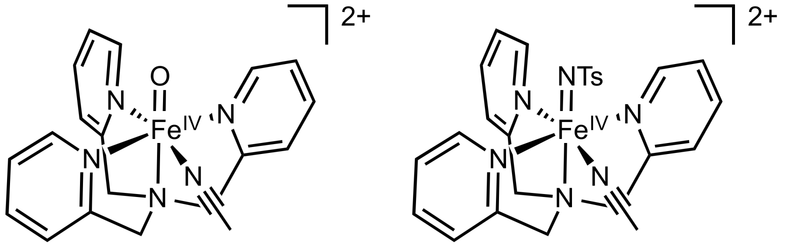

Que, 2003

Not reported

Figure 5.4. Reported oxoiron(IV) complex, $[Fe^{IV}(O)(TPA)(MeCN)]^{2+}$, and unreported imidoiron(IV) complex, $[Fe^{IV}(NTs)(TPA)(MeCN)]^{2+}$.

5.2 Experimental Details

Synthesis

The ligands, N4Py and TPA*,[17] corresponding Fe^{II} starting compounds, $[Fe^{II}(TPA^*)(MeCN)_2](OTf)_2$ and $[Fe^{II}(N4Py)(MeCN)](OTf)_2$, and nitrene transfer agents, PhINTs, PhINNs and MsINTs, were all synthesized according to published procedures.

$[Fe^{IV}(NTs)(TPA^*)(MeCN)](OTf)_2$ (3). The generation of **3** was carried out under inert atmospheric settings. 1.5 mL of a 1 mM solution of $[Fe^{II}(TPA^*)(MeCN)_2](OTf)_2$ in acetonitrile was cooled down to -20 °C. MsINTs or PhINTs was then dissolved in an appropriate amount of TFE and 2 equivalents (0.003 mmol) was added to the $[Fe^{II}(TPA^*)(MeCN)_2](OTf)_2$ stock solution, forming complex **3** within ~10 seconds. **NOTE**: Upon dissolution of MsINTs or PhINTs into TFE, the oxidant stock solution decomposes rapidly at room temperatures. Therefore, the oxidant stock solution should be made fresh and used immediately to ensure high yield of complex **3**.

$[Fe^{IV}(NNs)(N4Py)](OTf)_2$ (4). Complex **4** was generated at room temperature by dissolving $[Fe^{II}(N4Py)(MeCN)](OTf)_2$ (0.0015 mmol) in 1.5 mL acetonitrile and adding 1 - 2 equivalents PhINNs (0.0015– 0.003 mmol). The reaction mixture is stirred for 15 minutes and then filtered to yield **4**.

Physical methods.

All moisture and oxygen sensitive compounds were synthesized in a nitrogen-filled glove box. UV-vis spectra were recorded on a HP8453A diode array spectrometer equipped with a cryostat from Unisoku Scientific Instruments (Osaka, Japan).

Mössbauer spectra were recorded with home-built spectrometers using Janis Research Super-Varitemp dewars. Mössbauer spectral simulations were performed using the WMOSS software package (SEE Co., Edina, MN). Isomer shifts are quoted relative to Fe metal at 298 K.

Geometry optimizations and frequency calculations were carried out using the electronic structure code Turbomole V6.6. The TPSSh functional in combination with the def2-TZVPP basis set[18] was used and calculations were performed in the gas phase using an unrestricted Kohn-Sham formalism. Calculations were accelerated using the multipole accelerated resolution of the identity approximation (MARIJ) in combination with the appropriate fitting basis set def2-TZVPP/J. All calculations were performed without geometrical constraints and structures possess only real frequencies. Frequencies are used unscaled. All complexes are considered to be in an $S = 1$ ground state. The multiple grid *m5* was used throughout. The structure for complex **3** was constructed from a previously published X-ray structure of a diiron complex supported by the TPA* ligand framework.

Iron K-edge X-ray absorption spectra were collected on SSRL beam line 7-3 using a 30 element solid state Ge detector (Canberra) with a SPEAR storage ring current of ~500 mA at a power of 3.0 GeV. The incoming X-rays were unfocused using a Si(220) double crystal monochromator, which was detuned to 40% of the maximal flux to attenuate harmonic X-rays. Eight (8) scans were collected from 6882 eV to 8000 eV at a temperature (10 K) that was controlled by an Oxford Instruments CF1208 continuous flow liquid helium cryostat. An iron foil was placed in the beam pathway prior to I0 and scanned concomitantly for an energy calibration, with the first inflection point of the edge assigned to 7112.0 eV. A 6 μm Mn filter and a Soller slit were used to increase the signal to noise ratio of the spectra. Photoreduction was monitored by scanning the same spot on the sample twice and comparing the first derivative peaks associated with the edge energy during collection. The detector channels from the scans were examined, calibrated, averaged, and processed for EXAFS analysis using EXAFSPAK (G. George, 1990) with pre-edge analysis conducted between 7108 eV to 7119 eV using the Fityk program.

5.3 Strategies to Generate [Fe^{IV}(NTs)(TPA*)(MeCN)]$^{2+}$

Previously, stirring [Fe^{II}(N4Py)(CH$_3$CN)]$^{2+}$ or [Fe^{II}(BnTPEN)(OTf)]$^{1+}$ with the solid nitrene-transfer agents, PhINTs (phenyl-*N*-tosylimidoiodinane) or MsINTs (mesityl-*N*-tosylimidoiodinane), in acetonitrile solution at room temperature generated the corresponding nonheme imidoiron(IV) complexes, **1** and **2**, in high yields within minutes (Figure 5.4).[10, 14] However, the same synthetic strategy was unsuccessful in obtaining [Fe^{IV}(NTs)(TPA)(MeCN)]$^{2+}$, likely due to the decreased lifetime of this species at room temperature.

Two experimental strategies were employed to overcome this obstacle – first, it was discovered that PhINTs and MsINTs are both soluble in 2,2,2-trifluoroethanol (TFE), allowing these nitrene-transfer agents to be delivered as a stock-solution to the Fe^{II} starting material at low temperatures, thereby increasing the lifetime of the intermediate. Secondly, a variant of the TPA ligand, TPA*, which has electron-donating methyl groups in the 3 and 5 position of the pyridines rings and an electron-donating methoxy group in the 4 position, was utilized to provide an electron-rich alternative to TPA in order to stabilize this reactive species (Figure 5.5).[17b]

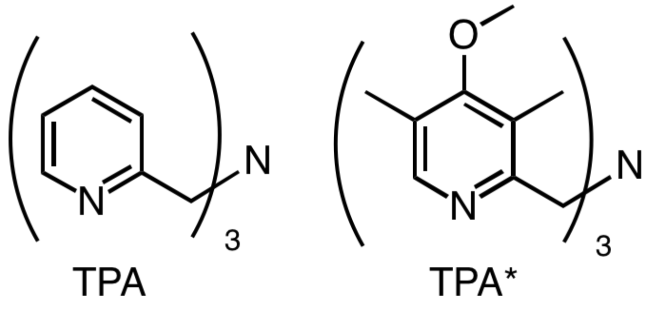

Figure 5.5. Structure of the tripodal tetradentate TPA and electron-rich TPA* ligands.[17b]

5.4 UV-Visible Spectroscopy of $[\mathrm{Fe^{IV}(NTs)(TPA^*)(MeCN)}]^{2+}$

Treatment of $[\mathrm{Fe^{II}(TPA^*)(MeCN)_2}]^{2+}$ with 2 equivalents of MsINTs or PhINTs, dissolved in TFE, at -20 °C in acetonitrile solution leads to the formation of $[\mathrm{Fe^{IV}(NTs)(TPA^*)(MeCN)}]^{2+}$ (**3**) within seconds. Complex **3** displays an intense UV feature at 440 nm ($\varepsilon = 5500\ \mathrm{M^{-1}\ cm^{-1}}$) and a broad NIR feature at 750 nm ($\varepsilon = 330\ \mathrm{M^{-1}\ cm^{-1}}$) (Figure 5.6). These absorption features correlate nicely with those observed for **1** and **2**, where intense UV peaks, tentatively assigned to the imido-to-$\mathrm{Fe^{IV}}$ charge-transfer bands, are found at 445 nm and 460 nm (Table 5.1).[10, 14]

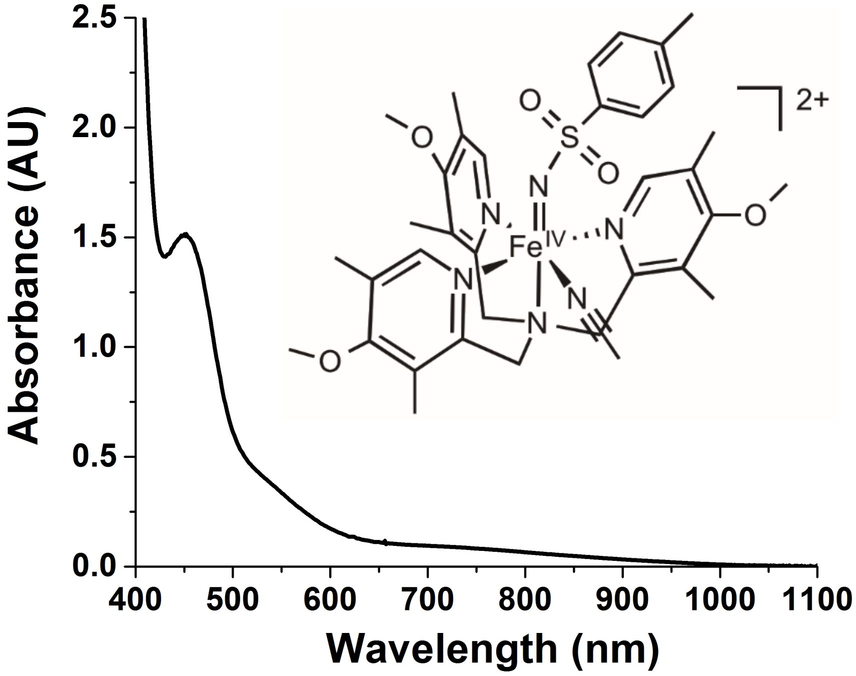

Figure 5.6. UV-visible absorption spectrum of $[\mathrm{Fe^{IV}(NTs)(TPA^*)(MeCN)}](\mathrm{OTf})_2$ (**3**) in acetonitrile solution at -20 °C.

Similarly, the weak and broad NIR feature observed for **3** at 750 nm is similar, albeit red-shifted, compared to the NIR features observed for **1** and **2** at 660 nm and 645 nm, respectively. While a more rigorous spectroscopic technique, such as MCD, will be required for the assignment of these bands, they likely correspond to d-d transitions, as is observed for the analogous nonheme oxoiron(IV) complexes.[19] Interestingly, the NIR feature of the corresponding oxoiron(IV) complexes, $[Fe^{IV}(O)(N4Py)]^{2+}$ (λ_{max} = 695 nm), $[Fe^{IV}(O)(BnTPEN)]^{2+}$ (λ_{max} = 739 nm), and $[Fe^{IV}(O)(TPA^*)(MeCN)]^{2+}$ (λ_{max} = 730 nm), do not follow the same trend, suggesting that the ligand framework interacts differently with the $Fe^{IV}O$ unit than it does with the $Fe^{IV}NTs$ unit (Table 5.1).

Table 5.1. Spectroscopic and structural properties of select nonheme oxoiron(IV) and imidoiron(IV) complexes.

Compound	**λ_{max} (nm) (M^{-1} cm^{-1})**	**δ (mm/s)**	**ΔE_Q (mm/s)**	**Fe=X (Å)**	**Fe=X (cm-1)**	**Edge (eV)**	**Pre-edge Area**	***$t_{1/2}$* (hrs)**	**Ref**
$[Fe^{IV}(NTs)(N4Py)]^{2+}$ **(1)**	445 (2700), 660 (250)	0.02	0.98	1.73	998 (-23)	7123.8	18	3 (25 ºC)	10
$[Fe^{IV}(NTs)(BnTPEN)]^{2+}$ **(2)**	460 (4100), 645 (330)	0.06	0.99	1.72	984 (-27)	7123.4	15	3 (25 ºC)	14
$[Fe^{IV}(NTs)(TPA^*)(MeCN)]^{2+}$ **(3)**	450 (5500), 750 (330)	0.05	1.02	1.69	974 (-28)	7126	12	>3 (-20 ºC)	
$[Fe^{IV}(NNs)(N4Py)]^{2+}$**(4)**	430, 660				978			1 (25 ºC)	
$[Fe^{IV}(NTs)(Me_2Py_2TACN)]^{2+}$	457, 736				1050 (-25)			7 (25 ºC)	
$[Fe^{IV}(NTs)(MePy_2TACN)]^{2+}$	462, 730				984 (-24)			0.5 (25 ºC)	
$[Fe^{IV}(O)(N4Py)]^{2+}$	695 (400)	-0.04	0.93	1.639(5)	841 (-35)	7124.0	25	60 (25	20

								ºC)	
$[Fe^{IV}(O)(BnTPEN)]^{2+}$	739 (400)	0.01	0.87	1.67	835 (-39)	7123.7	29	6 (25 ºC)	20
$[Fe^{IV}(O)(TPA^*)(MeCN)]^{2+}$	730	0.01	0.95	1.66	827 (-38)	7125	24	---	21

5.5 Mössbauer Spectroscopy of $[Fe^{IV}(NTs)(TPA^*)(MeCN)]^{2+}$

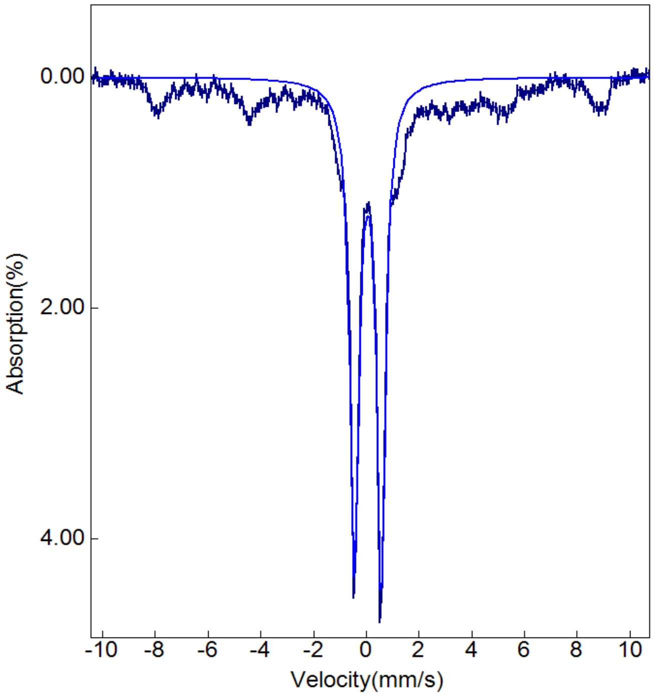

Figure 5.7. 4.2 K Mössbauer spectrum of $[Fe^{IV}(NTs)(TPA^*)(MeCN)]^{2+}$ (**3**) carried out under 0 kG parallel applied fields.

Further evidence for the generation of **3** comes from Mössbauer analysis, which under zero-field conditions reveals a single quadrupole doublet with an isomer shift of 0.05 mm/s and quadrupole splitting of 1.02 mm/s in 70% yield, confirming the presence of a $S = 1$ Fe^{IV} center (Figure 5.7). This is consistent with Mössbauer data for other $S = 1$ imidoiron(IV) and oxoiron(IV) complexes, including **1**, **2**, and $[Fe^{IV}(O)(TPA)(MeCN)]^{2+}$ ($\delta = 0.01$ mm/s and $\Delta E_Q = 0.92$ mm/s; Table 5.1). The remaining Fe in the sample (30%)

is associated with an unknown mononuclear ferric species, although it may be assigned to the mononuclear ferric decay product observed in the ESI-MS (*vide infra*).

5.6 ESI-MS of [Fe^{IV}(NTs)(TPA*)(MeCN)]$^{2+}$

The ESI-MS of **1** and **2** are challenging to obtain, with low dry-gas temperatures needed to observe the parent ions, [Fe^{IV}(NTs)(N4Py)(OTf)]$^{+}$ and [Fe^{IV}(NTs)(BnTPEN)(OTf)]$^{+}$.[14] In the case of **2**, a mixture of both [Fe^{IV}(NTs)(BnTPEN)(OTf)]$^{+}$ and the one-electron reduced decay product, [Fe^{III}(NHTs)(BnTPEN)(OTf)]$^{+}$, was observed.[14] Unfortunately, similar techniques were unsuccessful in observing the parent ion of **3**, despite using a low-temperature cooling bath and low dry-gas temperatures. Instead, a decay product of **3** was observed with a peak at 837.2 *m/z* (Figure 5.8), one mass-unit lower than the parent ion, [Fe^{IV}(NTs)(TPA*)(OTf)]$^{+}$, which is expected at 838.2 *m/z*. The decay product is proposed to be one in which the Fe^{IV}NTs unit has undergone intramolecular *ortho*-amination with one of the pyridine rings of the TPA* ligand to yield the ion, [Fe^{III}((*o*-TsN-$C_8H_{10}NO$)-TPA*)(OTf)]$^{+}$ (Figure 5.9). The experimental and simulated isotopic pattern for this species is displayed in Figure 5.8.

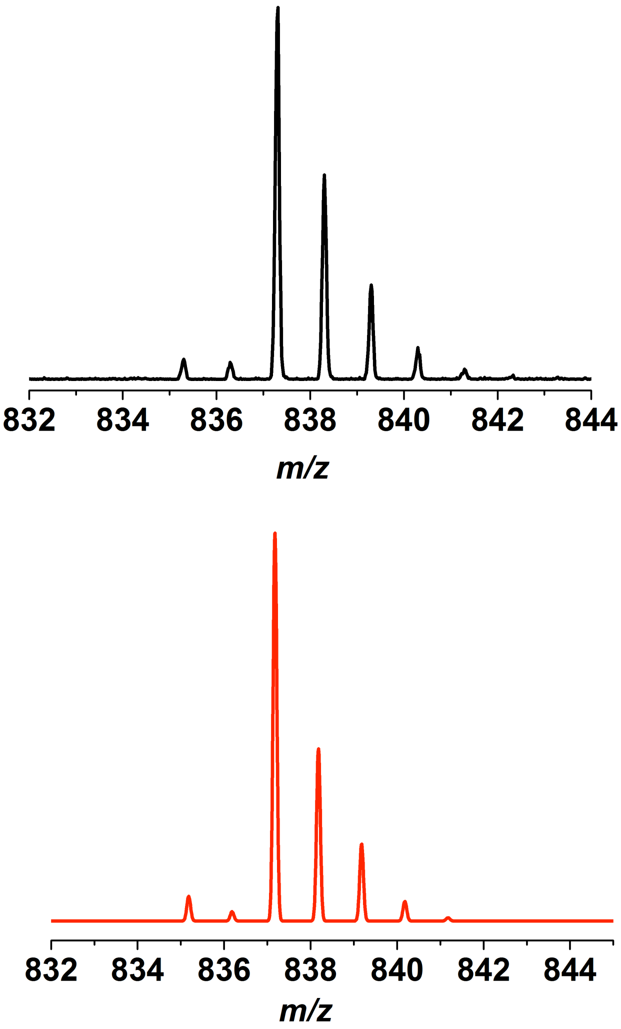

Figure 5.8. Experimental ESI-MS (top, black) of **3**, consistent with the formula of the decay product [Fe^{III}((*o*-TsN-$C_8OH_{10}N$)-TPA*)(OTf)]$^+$. Theoretical ESI-MS (bottom, red) of [Fe^{III}((*o*-TsN-$C_8OH_{10}N$)-TPA*)(OTf)]$^+$.

Further evidence that this decay product originates from **3** comes from isotopic labeling, where the same ESI-MS experiment was performed with **^{15}N-3**, which could be generated from the corresponding PhI^{15}NTs oxidant. As expected, the original ^{14}N-**3** decay product peak at *m/z* 837.2 is now upshifted by 1 mass unit to *m/z* 838.2 (Figure 5.10), confirming the presence of the tosylimido unit in the decayed species.

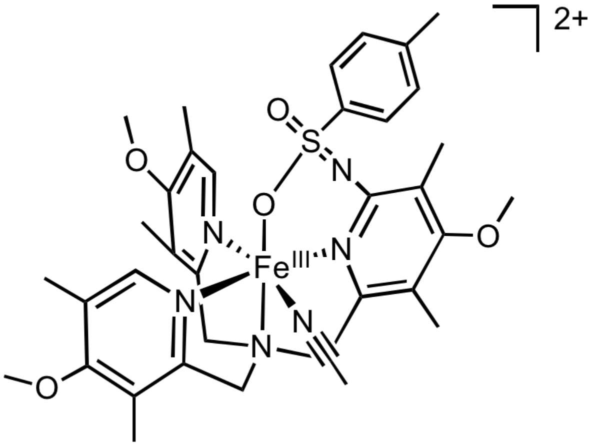

Figure 5.9. Proposed decay product of **3**, revealing an ESI-MS peak at *m/z* 837.2.

Isolation and characterization of this decay product has been unsuccessful, although Mössbauer spectroscopy has revealed the presence of a mononuclear ferric decay species that could possibly be assigned to this product. This type of a decay product would not be surprising, as *ortho*-amination is also observed upon reaction of PhINTs with $[Fe^{II}(6Ph\text{-}TPA)(MeCN)_2]^{2+}$.[15b]

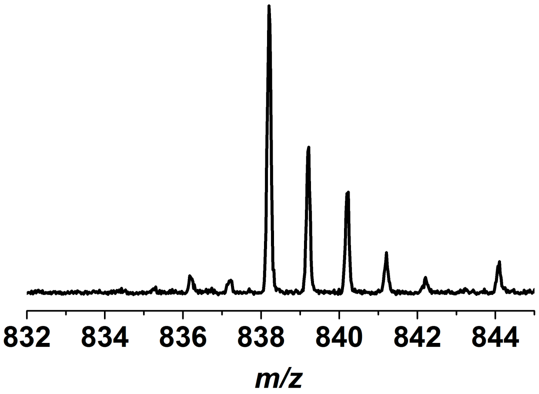

Figure 5.10. Experimental ESI-MS of **^{15}N-3**, consistent with the formula of the decay product $[Fe^{III}((o\text{-}Ts^{15}N\text{-}C_8OH_{10}N)\text{-}TPA^*)(OTf)]^+$, which is 1 unit up-shifted from the spectrum of **^{14}N-3** shown in Figure 5.8 (top).

5.7 XAS of [Fe^{IV}(NTs)(TPA*)(MeCN)]$^{2+}$

XAS was carried out to obtain additional electronic and structural information on **3**. However, due to the necessity of higher concentrations for the XAS experiments, the yield of **3** was only 50%. XANES measurements on **3** reveal an edge energy of 7126 eV, one unit higher than the edge energy of [Fe^{IV}(O)(TPA*)(MeCN)]$^{2+}$ at 7125 eV, and on the high end for Fe^{IV} species (Figure 5.11, Table 5.1). The pre-edge area of **3** was measured at 11.8 units, which is significantly smaller than the pre-edge area of 24.3 units measured for [Fe^{IV}(O)(TPA*)(MeCN)]$^{2+}$ (Figure 5.11, Table 5.1). A similar observation was noted when comparing the pre-edge areas of **1** and [Fe^{IV}(O)(N4Py)]$^{2+}$, 18 and 25 units, respectively, and **2** and [Fe^{IV}(O)(BnTPEN)]$^{2+}$, 9 and 29 units, respectively (Table 5.1).[14] The much smaller pre-edge area for the nonheme imidoiron(IV) complexes may be rationalized by the elongated Fe=NTs bond length versus the Fe=O bond length (*vide infra*), which increases the relative centrosymmetry of the imidoiron(IV) complexes and ultimately leads to a smaller pre-edge area.

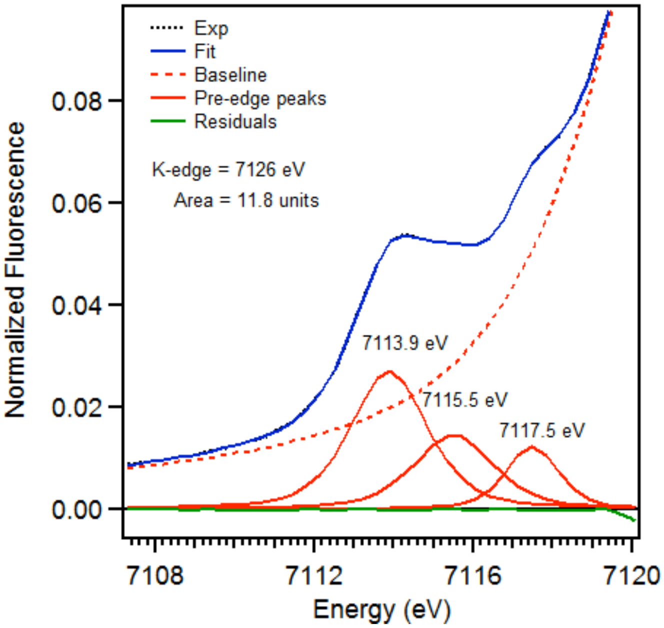

Figure 5.11. XANES spectrum of [Fe^{IV}(NTs)(TPA*)(MeCN)]$^{2+}$ (**3**) where the experimental data in shown in black dots and the fitting is shown in blue.

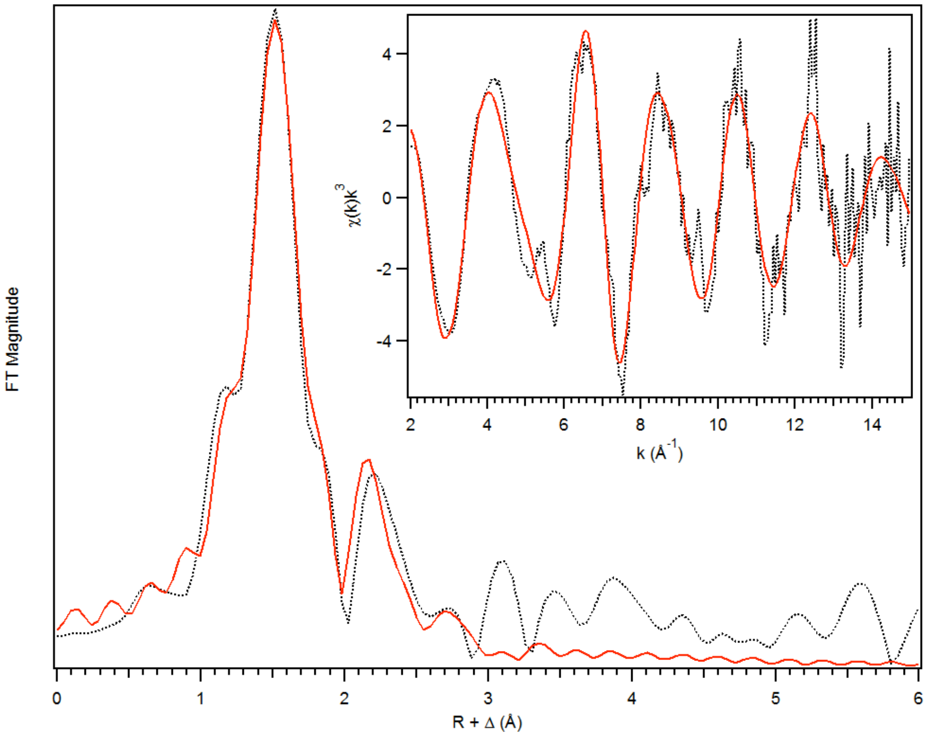

Figure 5.12. EXAFS spectrum of [Fe^{IV}(NTs)(TPA*)(MeCN)]$^{2+}$ (**3**) where the experimental data is in the black dotted line and the best fit is the red solid line. Unfiltered EXAFS data shown in the inset and the Fourier transform data in center.

EXAFS measurements on **3** reveal four shells, with a 0.5 nitrogen scatterer at 1.69 Å, 5 nitrogen scatterers at 1.94 Å, 3 carbon scatterers at 2.75 Å and 4 carbon scatterers at 2.89 Å (Figure 5.12, Fit 1 Table 5.2). The half-equivalency of the 1.69 Å scatterer is due to the substoichiometric yield of **3**. This 1.69 Å scatterer may be assigned to the Fe^{IV}=NTs distance, which is slightly shorter than the 1.73 Å distance measured for **1** but still elongated compared to the 1.65 Å Fe=O distance measured for a typical oxoiron(IV) complex (Table 5.1). The rationale for longer Fe=X bond in pseudo-octahedral imidoiron(IV) complexes versus oxoiron(IV) complexes was explained by Klinker *et al.* to be due to a weaker σ-interaction in imidoiron(IV) stemming from a poor interaction between the Fe d_{z2} orbital and N p_z orbital of the imido ligand.[10]

The 5 nitrogen scatterers at 1.94 Å are consistent with the Fe-N bonds of the TPA* ligand in complex **3**, slightly shorter than the 1.97 Å distance found for the Fe-N bonds in **1**. This contraction in Fe-N bond distance may be due to pyridine rings of the TPA* ligand being more electron-rich in nature.

Table 5.2. Fit parameters for complex **3,** unfiltered from k = 2 – 15 Å^{-1}

	Fe-N			**Fe-N**			**Fe•••C**			**Fe•••S**				**GOF**	
Fit	**N**	**R(Å)**	**σ^2(10^{-3})**	**N**	**R(Å)**	**σ^2(10^{-3})**	**N**	**R(Å)**	**σ^2(10^{-3})**	**N**	**R(Å)**	**σ^2(10^{-3})**	**E_o**	**F**	**F'**
1	**5**	**1.94**	**4.06**	**0.5**	**1.69**	**3.58**	**4**	**2.89**	**3.84**				**-6.58**	**232**	**405**
							3	**2.75**	**3.85**						
2	5	1.94	4.09	0.5	1.69	3.60	4	2.88	3.65	1	3.53	3.80	-6.45	219	395
							3	2.75	3.59						
3	5	1.94	3.77	1	1.72	11.47	4	2.88	3.88				-7.21	237	410

5.9 DFT Calculations on [Fe^{IV}(NTs)(TPA*)(MeCN)]$^{2+}$

DFT calculations were carried out on complex **3**, revealing the geometry optimized structure shown in Figure 5.13. This calculation confirms the pseudo-octahedral geometry of complex **3**, with a calculated Fe=N bond distance of 1.74 Å, which is notably elongated compared to the experimental distance of 1.69 Å measured from EXAFS. The deviation may be due to the purity of the EXAFS sample. It should also be noted that DFT calculations on **1** yielded slightly elongated Fe=N bond distances of 1.75 Å, compared to the experimental value of 1.73 Å derived from EXAFS, suggesting that DFT calculations may be overestimating the Fe=N bond length.[10] The second feature of the calculated structure of **3** is the bent Fe-N-S angle of 142°, which was also observed in the DFT-calculated structure of complex **1**. This bent angle is notably absent in the pseudo-tetrahedral nonheme imidoiron(IV) complexes, which display a nearly linear Fe-N-R unit owing to the Fe-N triple bond,[7-9] whereas the Fe-N double bond of the pseudo-octahedral imidoiron(IV) complexes leads to lone-pair character on the nitrogen-imido atom, ultimately causing a bending in the Fe-N-R angle.[10] Finally, the calculated Fe-S distance is 3.19 Å, significantly shorter than the proposed Fe-S distance of 3.53 Å from EXAFS, suggesting that Fit 2 in Table 5.2 is not the best fit for complex **3**.

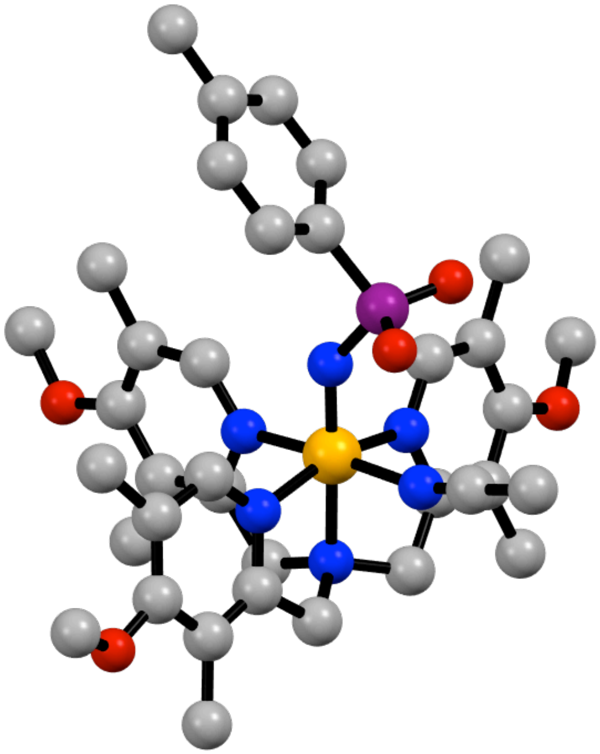

Figure 5.13 DFT calculated image of $[Fe^{IV}(NTs)(TPA^*)(MeCN)]^{2+}$ (**3**) corresponding to the lowest-energy geometry optimized structure, where orange = iron, blue = nitrogen, red = oxygen, purple = sulfur, grey = carbon. Hydrogen-atoms are omitted for clarity. Triflate counter-ions also omitted for clarity.

5.10 Resonance Raman Spectroscopy of $[Fe^{IV}(NTs)(TPA^*)(MeCN)]^{2+}$

Excitation of a frozen sample of **3** at 488 nm, reaching the tail-end of the imido-to-Fe^{IV} charge transfer band, leads the observation of a very intense vibration in the resonance Raman spectrum at 974 cm^{-1}, as well as a less intense vibration at 665 cm^{-1} (Figure 5.14). The 974 cm^{-1} peak downshifts by 28 cm^{-1} upon ^{15}N-labeling, while the 665 cm^{-1} vibration appears to be isotopically insensitive.

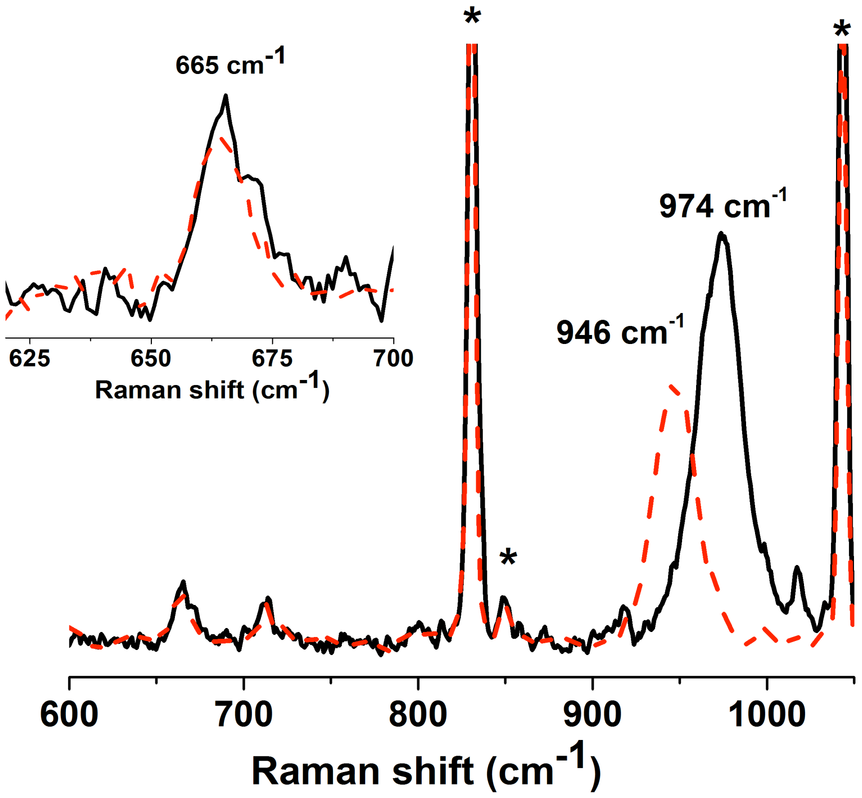

Figure 5.14. Resonance Raman spectrum of [Fe^{IV}(NTs)(TPA*)(MeCN)]$^{2+}$ (**3**) obtained with 488 nm excitation in frozen CD_3CN solution. Data corresponding to **^{14}N-3** shown in black solid line and **^{15}N-3** shown in red dashed line. Inset: Zoom of the isotopically insensitive peak at 665 cm^{-1}. Solvent peaks are marked with asterisks (*).

Hooke's law predicts a 26 cm^{-1} shift for an ideal Fe=N diatomic oscillator, which at first glance appears to be consistent with the experimental shift of 28 cm^{-1}. However, vibrational spectroscopy on metal-imido complexes in the literature has demonstrated that the –R unit of the imido ligand is strongly coupled to the metal-imido stretches. This is evident when you compare the Fe=N stretch of 974 cm^{-1} to the Fe=O stretch of 827 cm^{-1} for [Fe^{IV}(O)(TPA*)(MeCN)]$^{2+}$ (Table 5.1). Despite having somewhat comparable Fe=X bond distances as measured by EXAFS, the Fe=X vibrational frequencies of the nonheme imidoiron(IV) and oxoiron(IV) complexes are approximately 150 cm^{-1} different, suggesting a drastic perturbation of the Fe=N stretch the adjacent –R group of the imido unit.

This interesting vibrational spectroscopy is not unique for **3**. Similar stretches of 998 cm^{-1} and 984 cm^{-1} were measured for **1** and **2**, respectively (Table 5.1).[14] Upon labeling with ^{15}NTs, the observed stretch downshifts by 23 cm^{-1} and 27 cm^{-1}, respectively, close to the theoretical downshift of 27 cm^{-1} and 26 cm^{-1}. Currently it is not clear why the vibrations are consistent with the theoretical Hooke's law shift for a diatomic oscillator but the magnitude of the shifts are much larger than expected.
Work by Mehn, Peters and Que on the resonance Raman of nonheme imidoiron(III) complexes also confirm strong coupling of the –R group from the imido unit in the vibrational spectroscopy of these molecules, making it unrealistic to label the stretches as simple diatomic vibrations.[22] The value of these stretches, 1104 cm^{-1} for $[Fe^{III}(N^{t}Bu)(PhBP_3)]$ and 958 cm^{-1} for $[Fe^{III}(NPh)(PhBP_3)]$ are similar to those observed for **1** – **3**, despite having a formal Fe-N triple bond with much shorter distances of 1.65 Å.[22]

5.11 Tuning the Electronics of the –NR unit

From the resonance Raman spectra of **1** – **3**, it is clear that the –R group of the imido ligand (NR^{2-}) is strongly coupled in the observed vibrations of these interesting molecules. To probe the degree of coupling, we chose to vary the *para*-substituent of the aryl –R group of the imido unit from an electron-donating methyl group (tosylimido,

-NTs) to an electron-withdrawing nitro group (nosylimido, -NNs). Synthetically, the oxidant, PhINNs (phenyl-*N*-nosylimidoiodinane), could be obtained analogously to PhINTs, by treatment of iodosobenzene diacetate with *p*-nitrobenzenesulfonamide under basic conditions (Figure 5.15).

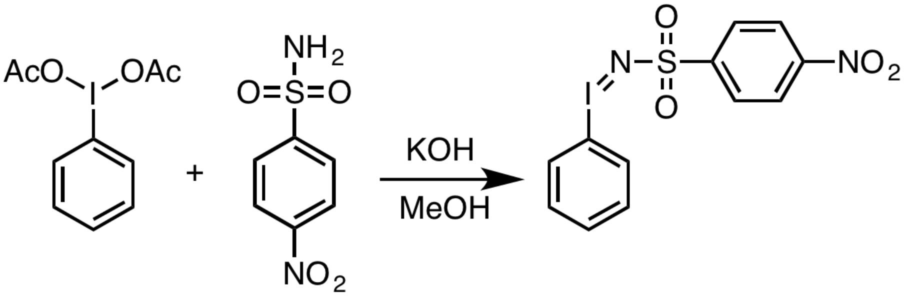

Figure 5.15. One-step synthesis of the PhINNs oxidant.

A new nonheme imidoiron(IV) species, $[Fe^{IV}(NNs)(N4Py)]^{2+}$ (**4**), could be accessed by reacting solid PhINNs (1 – 2 equiv.) with $[Fe^{II}(N4Py)(MeCN)]^{2+}$ in acetonitrile solution at room temperature. The solution color changed from orange to gold after 15 minutes, which was notably longer than the reaction between solid PhINTs and $[Fe^{II}(N4Py)(MeCN)]^{2+}$, which is completed within 2 – 3 minutes.

Similar to **1**, complex **4** demonstrates an intense UV feature at 430 nm, 15 nm blue-shifted compared to **1** (Figure 5.16). This blue-shift suggests the imido-to-Fe^{IV} charge transfer has increased in energy, a result rationalized by the electron-withdrawing $–NO_2$ substituent causing a decrease in energy of the imido-ligand HOMO. However, the NIR feature at 660 nm remains unchanged between **1** and **4**, suggesting that the electronic environment of the imido ligand does not dramatically perturb the d-d transitions.

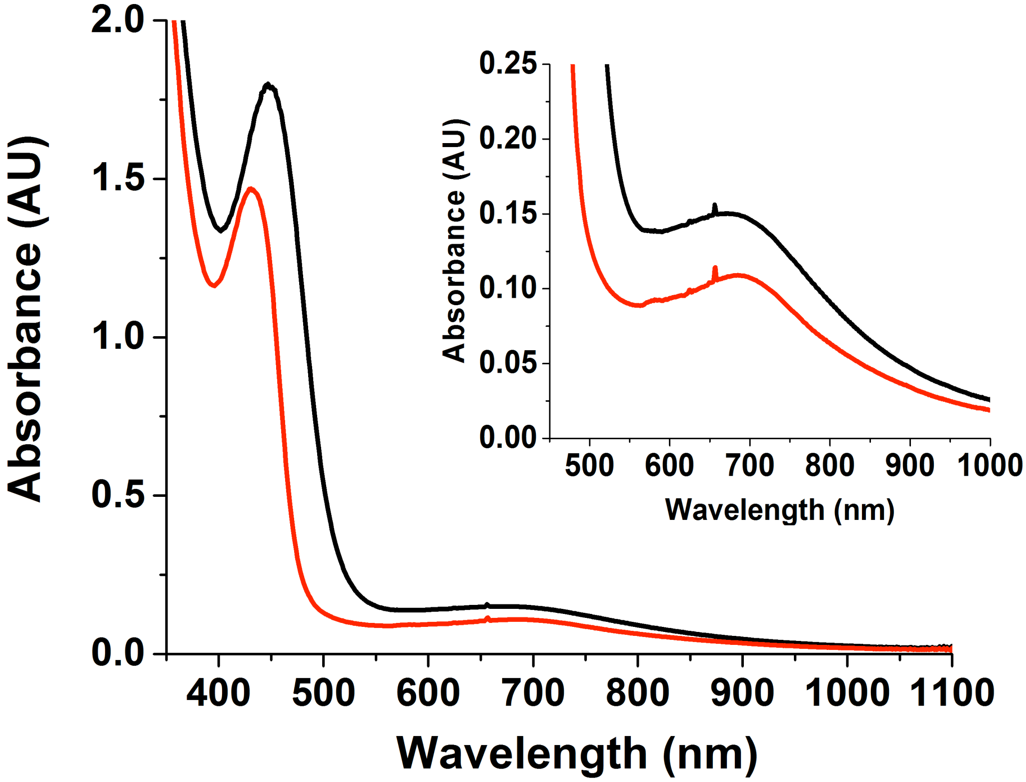

Figure 5.16. UV-visible absorption spectrum of 0.5 mM $[Fe^{IV}(NTs)(N4Py](OTf)_2$ (**1,** black) and $[Fe^{IV}(NNs)(N4Py](OTf)_2$ (**4**, red) in acetonitrile solution at 25 °C.

Upon excitation of a frozen sample of **4** at 488 nm, the resonance Raman spectrum demonstrates an intense band at 978 cm^{-1}, which is 20 cm^{-1} lower in energy than the band at 998 cm^{-1} reported for **1** (Figure 5.16). The magnitude of this shift is notable, as it is comparable to the shift observed from **1** to **3**, in which the supporting ligand architecture has changed from a pentandentate ligand to a tetradentate ligand. However in this case, **1** and **4** are supported by an identical ligand framework and the only difference is the electronics of the aryl group in the imido unit. This supports the notion that the observed stretch is not a simple Fe=N diatomic oscillator and that the –R group of the imido unit is coupled with this vibration.

In addition, **4** demonstrates a lower energy vibration at 660 cm^{-1} that is 5 cm^{-1} shifted from that observed in **1**. This vibration was found to be isotopically insensitive to ^{15}N labeling in **1**. The observation of a small 5 cm^{-1} shift when switching from the –NTs unit to the –NNs unit suggests that this may be a vibration associated with the aryl ring of the imido unit. A similar peak at 672 cm^{-1} was observed for the arylimidoiron(III) complex [Fe^{III}(NPh)(PhBP$_3$)], supporting this assignment.[22]

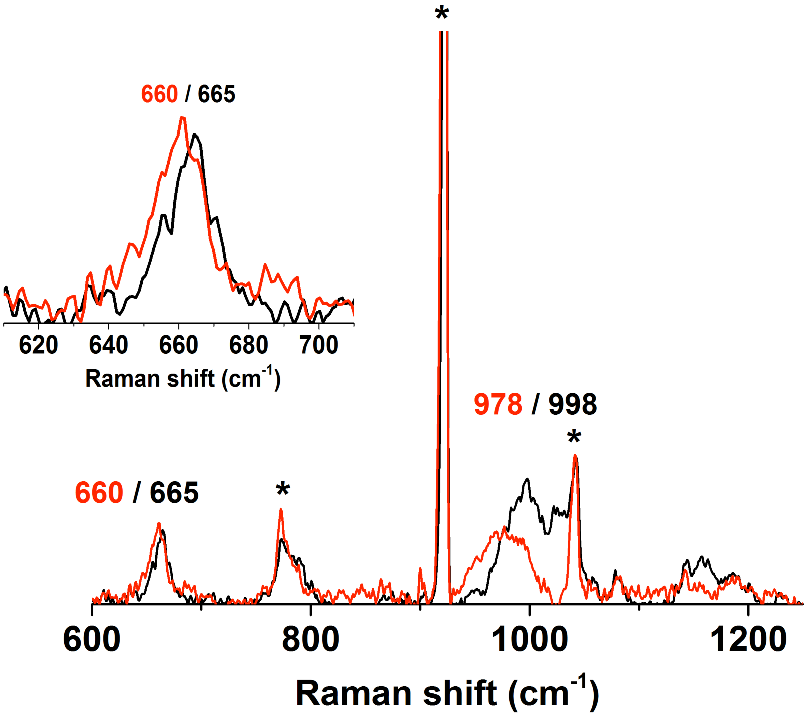

Figure 5.17. Resonance Raman spectrum of [Fe^{IV}(NTs)(N4Py)]$^{2+}$ (**1**, black) and [Fe^{IV}(NNs)(N4Py)]$^{2+}$ (**4**, red) obtained with 488 nm excitation in frozen CH$_3$CN solution. Solvent peaks are marked with asterisks (*). Inset: Zoom of peak at 665 cm^{-1}.

5.12 Discussion

Here we report the first example of a pseudo-octahedral imidoiron(IV) complex supported by a tetradentate ligand, **3**. This is a unique achievement, as the only other pseudo-octahedral imidoiron(IV) complexes reported are supported by pentadentate ligands. The key to its synthesis was the utilization of an electron-rich variant of the tripodal ligand TPA, called TPA*. In addition, dissolving the nitrene transfer agent, MsINTs or PhINTs, in TFE allowed for low-temperature delivery of this oxidizing agent, thus increasing the lifetime of complex **3**.

The spectroscopic properties of **3** is similar to those of complexes **1** and **2**, where an intense feature is observed at 450 nm, tentatively assigned to an imido-to-Fe^{IV} charge transfer band. The absorption spectrum also displays a weak NIR feature at 750 nm, which is reminiscent of the NIR bands observed in nonheme oxoiron(IV) complexes, assigned to d-d ligand field transitions. Excitation into the imido-to-Fe^{IV} charge transfer band with 488 nm laser elicits a resonance enhanced Raman vibration at 974 cm^{-1}, which downshifts by 28 cm^{-1} upon ^{15}N labeling. While the magnitude of this downshift is consistent with the Hooke's law calculation for an ideal Fe=N diatomic oscillator, the very large value of 974 cm^{-1} suggests that the R group of the imido unit must be coupling into this vibrational feature.

Complex **3** differs from the pseudo-octahedral nonheme imidoiron(IV) complexes in that the supported ligand is tetradentate in nature, leaving one open coordination site on the Fe^{IV} center. Currently there is no direct evidence for binding of the MeCN ligand to complex **3**. Attempts to induce a ligand exchange by treating **3** with halide sources, such as NBu_4Cl or NBu_4Br leads to immediate decay of **3**. This may not be surprising as pseudo-octahedral imidoiron(IV) complexes have been shown competent at long-range electron transfer and may be oxidizing these halide ligands. Ligand exchange with alternate ligands, such as pyridine-N-oxide and acetate, is currently be explored to confirm the presence of a labile coordination site in complex **3**.

Finally, this synthetic progress opens the door to explore the reactivity of complex **3** in the context of imido-group transfer and C-H bond activation chemistry. The rates of these reactions may then be compared to the analogous oxoiron(IV) complex, $[Fe^{IV}(O)(TPA^*)(MeCN)]^{2+}$, as well as the other two reported pseudo-octahedral nonheme imidoiron(IV) complexes, **1** and **2**.

5.13 Acknowledgements

Much of the work in this chapter was accomplished with the help of very talented collaborators. Williamson Oloo and Caleb Allpress are thanked for their donation of the TPA* ligand and the $[Fe^{II}(TPA^*)(MeCN)_2](OTf)_2$ starting material. Andy Jasniewski carried out and analyzed the XAS experiments on **3**. Ruixi Fan and Yisong (Alex) Guo carried out the Mössbauer experiments on **3**. Johannes Klein carried out DFT calculations on **3**.

5.14 References

1. Costas, M.; Mehn, M. P.; Jensen, M. P.; Que, L., Jr. *Chem. Rev.* **2004,** *104*, 939.

2. Nam, W. *Acc. Chem. Res.* **2007,** *40*, 522.

3. Que, L., Jr. *Acc. Chem. Res.* **2007,** *40*, 493.

4. Puri, M.; Que, L. *Acc. Chem. Res.* **2015,** *48*, 2443.

5. Mehn, M. P.; Peters, J. C. *J. Inorg. Biochem.* **2006,** *100*, 634.

6.King, E. R.; Hennessy, E. T.; Betley, T. A. *J. Am. Chem. Soc.* **2011,** *133*, 4917.

7.Verma, A. K.; Nazif, T. N.; Achim, C.; Lee, S. C. *J. Am. Chem. Soc.* **2000,** *122*, 11013.

8.Thomas, C. M.; Mankad, N. P.; Peters, J. C. *J. Am. Chem. Soc.* **2006,** *128*, 4956.

9.Nieto, I.; Ding, F.; Bontchev, R. P.; Wang, H.; Smith, J. M. *J. Am. Chem. Soc.* **2008,** *130*, 2716.

10.Klinker, E. J.; Jackson, T. A.; Jensen, M. P.; Stubna, A.; Juhász, G.; Bominaar, E. L.; Münck, E.; Que, L., Jr. *Angew. Chem. Int. Ed.* **2006,** *45*, 7394.

11.Saouma, C. T.; Peters, J. C. *Coord. Chem. Rev.* **2011,** *255*, 920.

12.Hennessy, E. T.; Betley, T. A. *Science* **2013,** *340*, 591.

13.(a) Vardhaman, A. K.; Barman, P.; Kumar, S.; Sastri, C. V.; Kumar, D.; de Visser, S. P. *Angew. Chem.* **2013,** *125*, 12514; (b) Kumar, S.; Faponle, A. S.; Barman, P.; Vardhaman, A. K.; Sastri, C. V.; Kumar, D.; de Visser, S. P. *J. Am. Chem. Soc.* **2014,** *136*, 17102.

14.Klinker, E. J., *High-valent iron compounds supported by pentadentate ligands*. ProQuest: 2007.

15.(a) Jensen, M. P.; Lange, S. J.; Mehn, M. P.; Que, E. L.; Que, L., Jr. *J. Am. Chem. Soc.* **2003,** *125*, 2113; (b) Jensen, M. P.; Mehn, M. P.; Que, L., Jr. *Angew. Chem. Int Ed.* **2003,** *42*, 4357.

16.Lim, M. H.; Rohde, J.-U.; Stubna, A.; Bukowski, M. R.; Costas, M.; Ho, R. Y. N.; Münck, E.; Nam, W.; Que, L., Jr. *Proc. Natl. Acad. Sci. USA* **2003,** *100*, 3665.

17.(a) Lubben, M.; Meetsma, A.; Wilkinson, E. C.; Feringa, B.; Que, L., Jr. *Angew. Chem. Int. Ed. Engl.* **1995,** *34*, 1512; (b) Xue, G.; Wang, D.; De Hont, R.; Fiedler, A. T.; Shan, X.; Münck, E.; Que, L., Jr. *Proc. Nat. Acad. Sci. USA* **2007,** *104*, 20713.

18.Weigend, F.; Ahlrichs, R. *Phys. Chem. Chem. Phys.* **2005,** *7*, 3297.

19.Decker, A.; Rohde, J.-U.; Klinker, E. J.; Wong, S. D.; Que, L., Jr.; Solomon, E. I. *J. Am. Chem. Soc.* **2007,** *129*, 15983.

20.Kaizer, J.; Klinker, E. J.; Oh, N. Y.; Rohde, J.-U.; Song, W. J.; Stubna, A.; Kim, J.; Münck, E.; Nam, W.; Que, L., Jr. *J. Am. Chem. Soc.* **2004,** *126*, 472.

21.Xue, G.; Fiedler, A. T.; Martinho, M.; Münck, E.; Que, L., Jr. *Proc. Nat. Acad. Sci. USA* **2008,** *105*, 20615.

22.Mehn, M. P.; Brown, S. D.; Jenkins, D. M.; Peters, J. C.; Que, L., Jr. *Inorg. Chem.* **2006,** *45*, 7417.

Chapter 6:
Conclusions and Perspectives

Parts of this chapter were published in:

1. Puri, M.; Que, L. Jr. Towards the Synthesis of More Reactive *S* = 2 Nonheme Oxoiron(IV) Complexes. *Acc. Chem. Res.*, **2015**, *48*, 2443 – 2452.

2. Biswas, A. N.; Puri, M.; Meier, K. K.; Oloo, W. N.; Rohde, G. T.; Bominaar, E. L.; Münck, E.; Que, L. Jr. Modeling TauD-J: A High-Spin Nonheme Oxoiron(IV) Complex with High Reactivity toward C-H Bonds. *J. Am. Chem. Soc.*, **2015**, *137*, 2428 – 2431.

3. Puri, M.; Biswas, A. N.; Fan, R.; Guo, Y.; Que, L. Jr. Modeling Non-heme Iron Halogenases: High-Spin Oxoiron(IV)-Halide Complexes that Halogenate C-H Bonds. *J. Am. Chem. Soc.* **2016**, *138*, 2484 – 2487.

4. Puri, M; Company, A.; Sabenya, G.; Costas, M.; Que, L. Jr. Oxygen-Atom Exchange Between H_2O and Nonheme Oxoiron(IV) Complexes: Ligand Dependence and Mechanism. *Inorg. Chem.* Manuscript Accepted.

6.1 Introduction

2003 marked a banner year in the bioinorganic chemistry of mononuclear nonheme iron enzymes. The first nonheme oxoiron(IV) intermediate (called ***J***) was trapped and characterized by Bollinger and Krebs in the catalytic cycle of taurine dioxygenase (TauD),[1] and the first crystal structure of a synthetic nonheme oxoiron(IV) complex was reported by Que and coworkers.[2] These results stimulated inorganic chemists to synthesize related oxoiron(IV) complexes to shed light on the electronic structures and spectroscopic properties of these novel intermediates and gain mechanistic insights into their function in biology.[3,4] All biological oxoiron(IV) intermediates discovered since 2003 have an $S = 2$ ground spin state, while over 90% of the sixty or so synthetic oxoiron(IV) complexes reported to date have an $S = 1$ ground spin state.[5] This difference in electronic structure has fueled an interest to model more accurately these enzymatic intermediates and synthesize $S = 2$ oxoiron(IV) complexes.[6]

Upon inspection of a qualitative d-orbital splitting diagram for a d^4 metal-oxo center, it becomes evident that the key to achieving an $S = 2$ ground state is to decrease the energy gap between the $d_{x^2-y^2}$ and d_{xy} orbitals. Chapter 1 describes synthetic strategies bioinorganic chemists have used to accomplish this task.[6] Chapter 2 then describes a new synthetic strategy in which the relatively strong-field pyridine donors of the well-known TPA ligand are systematically substituted for weaker-field quinoline donors, leading to a new tripodal ligand called TQA (Figure 6.1).[7] This has led to the synthesis and characterization of three new $S = 2$ nonheme oxoiron(IV) complexes supported by the TQA ligand framework (Figure 6.2). These species demonstrate spectroscopic signatures that are remarkably close to the nonheme oxoiron(IV) intermediates found in the enzymes TauD, CytC3 and SyrB2.[6,7]

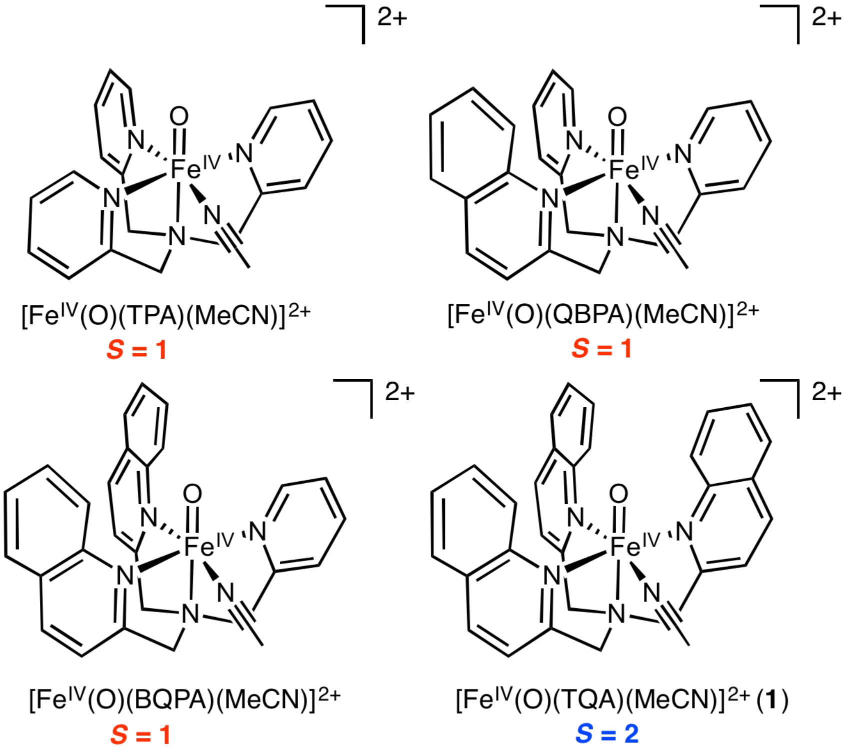

$[Fe^{IV}(O)(TPA)(MeCN)]^{2+}$
***S* = 1**

$[Fe^{IV}(O)(QBPA)(MeCN)]^{2+}$
***S* = 1**

$[Fe^{IV}(O)(BQPA)(MeCN)]^{2+}$
***S* = 1**

$[Fe^{IV}(O)(TQA)(MeCN)]^{2+}$ (**1**)
***S* = 2**

Figure 6.1 Systematically tuning the spin state of nonheme oxoiron(IV) complexes from $S = 1$ to $S = 2$ by replacing pyridine rings for weaker-field quinoline rings in a tripodal ligand framework.

In Chapter 3, the reactivity of these molecules is presented in the context of both hydrogen-atom transfer (HAT) and oxygen-atom transfer (OAT) reactions.[7] The mechanisms for C-OH and C-X (X = Cl or Br) bond formation are then evaluated and compared against the well-known rebound mechanism, prevalent in enzymatic and synthetic heme oxoiron chemistry. In Chapter 4, the reaction involving the oxygen-atom exchange between $S = 1$ nonheme oxoiron(IV) complexes and $H_2{}^{18}O$ is studied,[8] leading to mechanistic insights in the exchange process between nonheme oxoiron(IV) complexes supported by tetradentate and pentadentate ligands. Chapter 5 explores the chemistry of six-coordinate $S = 1$ nonheme imidoiron(IV) complexes,[9] which are analogous to the six-coordinate $S = 1$ nonheme oxoiron(IV) complexes described in the literature,[5] and provides spectroscopic evidence for the first six-coordinate nonheme imidoiron(IV) complex supported by a tetradentate ligand. This final section, Chapter 6, summarizes these results and provides a perspective on future challenges facing bioinorganic chemists.

6.2 Generation and Characterization of *S* = 2 Nonheme Oxoiron(IV) Complexes

$S = 2$ oxoiron(IV) species are often implicated in the mechanisms of nonheme iron oxygenases, their C–H bond cleaving properties being attributed to the quintet spin state.[10-14] However, the few available synthetic $S = 2$ nonheme oxoiron(IV) complexes supported by polydentate ligands do not cleave strong C–H bonds.[15-18] In Chapter 2, the synthetic tuning of the Fe^{IV} spin state from $S = 1$ to $S = 2$ is described, where the three pyridine rings of the tripodal tetradentate ligand, TPA,[19] are systematically substituted with weaker-field quinoline donors, eventually leading to the fully-substituted ligand, TQA.[7] This weak-field ligand allows for the synthesis and characterization of three new highly reactive $S = 2$ nonheme oxoiron(IV) complexes, including $[Fe^{IV}(O)(TQA)(MeCN)]^{2+}$ (**1**),[7] and its halide derivatives, $[Fe^{IV}(O)(TQA)(Cl)]^{1+}$ (**2**) and $[Fe^{IV}(O)(TQA)Br)]^{1+}$ (**3**) (Figure 6.2). A key factor in their synthesis was the use of a soluble oxo-transfer agent, ArIO,[20] which allowed the delivery of this oxidant at low-temperatures. In addition, the steric barriers of the TQA ligand likely helped limit comproportionation between the generated oxoiron(IV) species and residual Fe^{II} starting material.

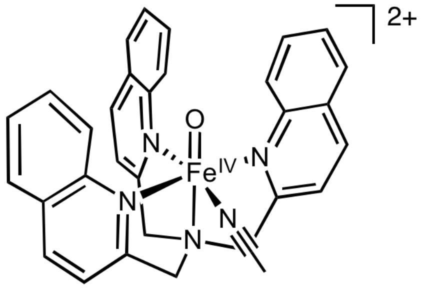

$[Fe^{IV}(O)(TQA)(MeCN)]^{2+}$ (**1**)
***S* = 2**

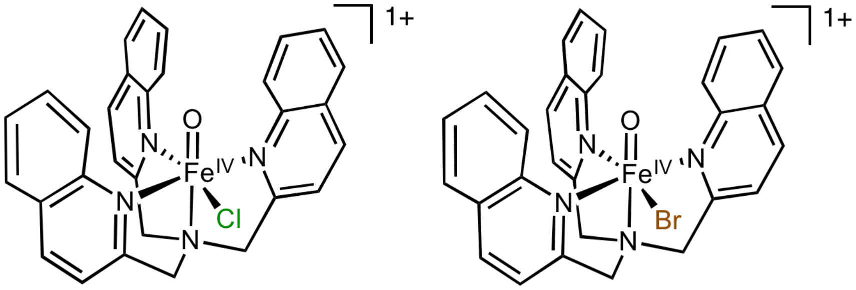

$[Fe^{IV}(O)(TQA)(Cl)]^{1+}$ (**2**)
***S* = 2**

$[Fe^{IV}(O)(TQA)(Br)]^{1+}$ (**3**)
***S* = 2**

Figure 6.2 Three new $S = 2$ nonheme oxoiron(IV) complexes reported in this thesis.

Compared with other $S = 2$ nonheme oxoiron(IV) complexes characterized thus far, the spectroscopic properties of **2** most closely resemble those of the enzymatic intermediates in TauD, CytC3 and SyrB2.[6] Specifically, these are the only three synthetic nonheme oxoiron(IV) complexes that have an isomer shift falling within the range observed for enzymatic nonheme oxoiron(IV) intermediates (0.22 mm/s – 0.30 mm/s), suggesting that they are the closest electronic model of these important bioinorganic species to date.[6]

6.3 Reactivity of *S* = 2 Nonheme Oxoiron(IV) Complexes

In Chapter 3, the reactivity of the three $S = 2$ nonheme oxoiron(IV) complexes, **1** – **3**, is reported. Complex **1** was found to oxidize both strong C–H bonds and C=C olefinic bonds with rapid rates at -40 °C.[7] In fact, the oxidation of cyclohexane by **1** occurs at a rate comparable to the oxidation of taurine by the TauD-***J*** enzyme intermediate, after adjusting for the different temperatures of measurement. Labeling studies with ^{18}O-**1** under an atmosphere of $^{16}O_2$ demonstrates a mixture of ^{16}O and ^{18}O-labeled oxidation products, suggesting a competitive mechanistic pathway for substrate oxidation involving both rebound and radical escape (Figure 6.3).

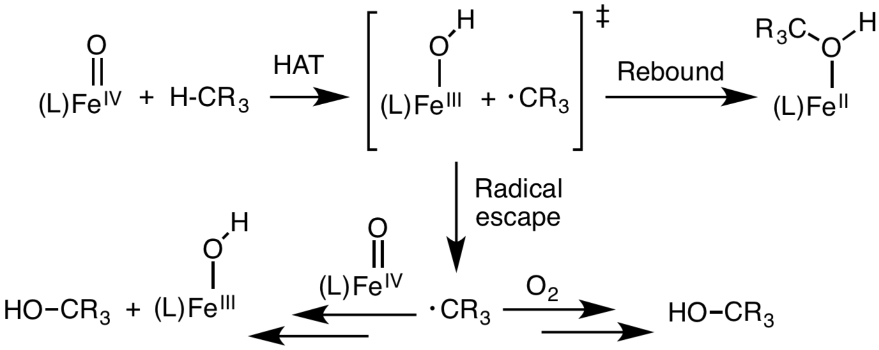

Figure 6.3 Possible C-H bond hydroxylation mechanistic pathways for nonheme oxoiron(IV) complexes.

In addition, the reactivity of the nonheme oxoiron(IV)-halide complexes, **2** and **3**, were examined in regards to cyclohexane and toluene oxidation. Notably, these are the first nonheme oxoiron(IV)-halide complexes to demonstrate the ability to convert C-H bonds to C-halogen bonds, with high selectivity for halogenation in cyclohexane oxidation. Interestingly, in contrast to the chemistry of **1**, the nascent substrate radical generated by these synthetic complexes is long lived and can be fully intercepted by O_2, preventing halogenation. These results suggest that the rate of halogen rebound, observed in **2** and **3**, is likely intrinsically slower than the rate of oxygen rebound, observed in **1**. More work is needed to establish the factors that control the chemoselectivity between halogenation and oxygenation in these systems.

Most importantly, the rate of oxygen and halogen-rebound observed in the reactivity of the nonheme oxoiron(IV) complexes **1** – **3** is slower than the rate of rebound observed in many synthetic and enzymatic heme systems. This may be due to the fact that the oxidizing intermediate in heme enzymes is formally an oxoiron(V) species, which will generate a hydroxoiron(IV) intermediate after abstraction of a hydrogen-atom. This hydroxoiron(IV) species will likely be a more potent oxidant than the corresponding hydroxoiron(III) species found in the majority of mononuclear nonheme systems, thereby leading to faster rebound.

6.4 Oxygen-atom Exchange Reaction between $H_2{}^{18}O$ and Nonheme Oxoiron(IV) Complexes

Chapter 4 involves a detailed study of oxygen-atom exchange (OAE) between $H_2{}^{18}O$ and synthetic nonheme oxoiron(IV) complexes supported by tetradentate and pentadentate ligands,[8] revealing that they proceed by a common mechanism but within two different kinetic regimes, with OAE rates that span two orders of magnitude. The first kinetic regime involves initial reversible water association to the Fe^{IV} complex, while the second kinetic regime involves a subsequent proton-transfer step between the bound aqua and oxo ligands. Reversible water association to the oxoiron(IV) unit is evidenced by OAE rates that are linearly dependent on [$H_2{}^{18}O$], while saturation behavior with [$H_2{}^{18}O$] and large H_2O/D_2O KIEs are evident of a rate-determining proton-transfer step. Both kinetic regimes, linear [$H_2{}^{18}O$] dependence at low water concentrations and saturation of [$H_2{}^{18}O$] at high water concentrations, are observed for the oxoiron(IV) complex, $[Fe^{IV}(O)(PyTACN)(MeCN)]^{2+}$, containing a tetradentate ligand. In contrast, a single regime entailing linear dependence on [$H_2{}^{18}O$] is observed for $[Fe^{IV}(O)(TMC)(MeCN)]^{2+}$ and also $[Fe^{IV}(O)(MePy_2TACN)]^{2+}$, both complexes demonstrating a small H_2O/D_2O KIE of 1.6, reflecting some degree of O-H / O-D bond cleavage contributing to the rate-determining step (RDS). Furthermore, OAE rates independent on water concentration, suggestive of very facile $H_2{}^{18}O$ saturation, are observed for complexes $[Fe^{IV}(O)(N4Py)]^{2+}$, $[Fe^{IV}(O)(BnTPEN)]^{2+}$, $[Fe^{IV}(O)(1Py\text{-}BnTPEN)]^{2+}$, $[Fe^{IV}(O)(3Py\text{-}BnTPEN)]^{2+}$ and $[Fe^{IV}(O)(Me_2Py_2TACN)]^{2+}$. These complexes exhibit very large H_2O/D_2O KIE values of 5 – 6 suggesting that proton-transfer is a major contributor to the RDS. Consistent with the proposed mechanism, these complexes exhibit large and negative activation entropies. One exception is complex $[Fe^{IV}(O)(MePy_2TACN)]^{2+}$, which has a near-zero activation entropy and is proposed to undergo ligand-arm dissociation during the RDS to accommodate $H_2{}^{18}O$ binding. These mechanistic insights are of relevance to studies of nonheme oxoiron(IV) complexes in water or acetonitrile/water mixtures for applications in photocatalysis and water oxidation chemistry.

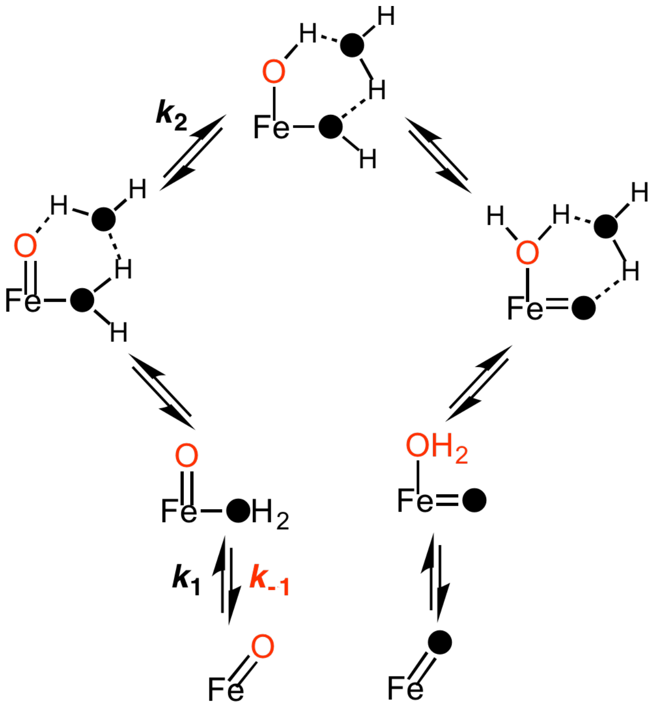

Figure 6.4 Proposed mechanism for OAE between nonheme oxoiron(IV) complexes and $H_2{}^{18}O$.

6.5 Generation and Characterization of Six-coordinate Nonheme Imidoiron(IV) Complexes

The generation and characterization of nonheme imidoiron(IV) complexes represent an important advance in inorganic chemistry,[21] as these species are proposed to be involved in the amination and aziridination of C-H and C=C bonds, analogous to the hydroxylation and epoxidation chemistry of nonheme oxoiron(IV) complexes.[22] More than 90% of the nonheme oxoiron(IV) complexes reported to date have a six-coordinate pseudo-octahedral geometry,[5] while only one out of the seven reported nonheme imidoiron(IV) complexes is six-coordinate,[9] with the remaining adopting four-coordinate geometries.[23-28] In order to accurately compare the chemistry of nonheme oxoiron(IV) and imidoiron(IV) complexes, it is important to maintain similar coordination numbers and geometries. For this reason, the synthesis and reactivity studies of six-coordinate pseudo-octahedral nonheme imidoiron(IV) species are of great importance and are discussed in Chapter 5.

The only published example of a six-coordinate nonheme imidoiron(IV) complex is $[Fe^{IV}(NTs)(N4Py)]^{2+}$,[9] where the Fe^{IV} center is supported by a pentadentate ligand. In contrast, the imidoiron(IV) equivalent of the nonheme oxoiron(IV) species, $[Fe^{IV}(O)(TPA)(MeCN)]^{2+}$,[19] where the Fe^{IV} center is supported by a tripodal tetradenate ligand, has not been reported (Figure 6.5). Through the use an electron-rich variant of TPA, known as TPA*,[29] and soluble nitrene-transfer agents, we report the generation and characterization of $[Fe^{IV}(NTs)(TPA^*)(MeCN)]^{2+}$. This species demonstrates spectroscopic signatures very similar to those of $[Fe^{IV}(NTs)(N4Py)]^{2+}$,[9] including a Fe=N vibrational feature in the resonance Raman spectrum that appears to be coupled to the tosylate group of the imido ligand. To test this hypothesis, the electron-donating $–CH_3$ group of the tosylate unit was converted to an electron-poor $–NO_2$ group, revealing a 20 cm^{-1} shift in the Fe=N vibrational stretch between $[Fe^{IV}(NTs)(N4Py)]^{2+}$ and $[Fe^{IV}(NNs)(N4Py)]^{2+}$, suggesting the electronic environment of the aryl ring impacts the Fe=N frequency, thus implying that the observed stretch is not a simple diatomic vibration.[30]

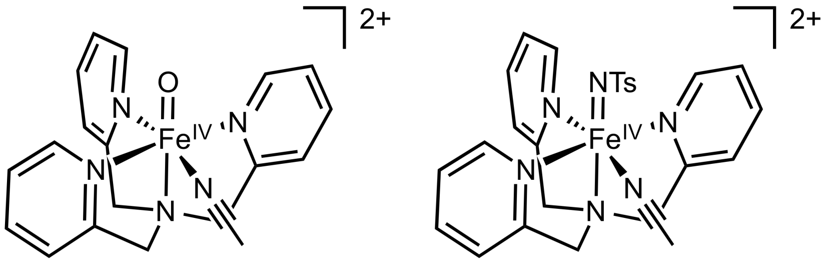

Que, 2003

Not reported

Figure 6.5 Reported oxoiron(IV) complex, $[Fe^{IV}(O)(TPA)(MeCN)]^{2+}$, and unreported imidoiron(IV) complex, $[Fe^{IV}(NTs)(TPA)(MeCN)]^{2+}$.

6.6. Future Challenges

The *S* = 2 nonheme oxoiron(IV) complexes, **1** – **3**, model both the spectroscopic features and reactivity of nonheme oxoiron(IV) enzymatic intermediates found in nature, representing a significant advance in bioionorganic chemistry. However, many unanswered questions remain about these synthetic complexes.

For example, **1** was found to be the most reactive nonheme oxoiron(IV) complex to date with respect to HAT, suggesting that the *S* = 2 ground spin state may contribute to its high reactivity.[7] However, a related nonheme oxoiron(IV) complex with an *S* = 1 ground spin state, $[Fe^{IV}(O)(Me_3NTB)(MeCN)]^{2+}$, was found to be capable of oxidizing organic substrates at similar rates to **1**.[31] This important observation reveals that two nonheme oxoiron(IV) complexes with different ground spin states can achieve comparable HAT reactivity.[6] This suggests that spin state may not be the underlying factor behind reactivity and opens the possibility for other factors to rationalize these observations.

One fundamental reactivity parameter that has been difficult to quantify for many nonheme oxoiron(IV) systems is the thermodynamic driving force of HAT reactions, which requires a knowledge of both the $Fe^{IV/III}$ $E_{1/2}$ of the oxoiron(IV) complex, as well as the pK_a of the resulting hydroxoiron(III) species.[32] In the absence of secondary-coordination sphere interactions,[33,34] these hydroxoiron(III) complexes have been notoriously challenging to isolate and characterize, making these thermodynamic parameters difficult to come across.[32] For this reason, synthetic bioinorganic chemists need to develop strategies to stabilize and isolate these hydroxoiron(III) species. Two possible routes to their synthesis include the one-electron oxidation of ferrous starting materials, which has been met with mixed success, or the two-electron oxidation of iron(I) compounds. While iron(I) chemistry is not common in the context of oxoiron systems, this approach has been used with success in synthesizing nonheme imidoiron(III) complexes.[35]

2 and **3** represent the first nonheme oxoiron(IV)-halide complexes capable of halogenating C-H bonds, with a high degree of halogenation selectivity observed in the oxidation of cyclohexane. However, the origin of this chemoselectivity is not clear. In order to determine the factors that may control this selectivity, such as sterics or electronics, additional nonheme oxoiron(IV)-halide complexes with a range of steric bulk about the bound halide and hydroxide ligands, and in both $S = 1$ and $S = 2$ spin states, are necessary to synthesize.[17,36,37] With these molecules in hand, it will then be important to determine which set of oxoiron(IV)-halide species halogenate C-H bonds and with what degree of chemoselectivity.

Relevant to Chapter 5 of this thesis, N4Py represents the only nonheme ligand framework in which both oxoiron(IV) and imidoiron(IV) complexes have been isolated.[9,38] This suggests that the corresponding nitridoiron(IV) species, $[Fe^{IV}(N)(N4Py)]^{1+}$, should also be obtainable. A synthetic strategy towards this complex would be treatment of $[Fe^{II}(N4Py)(Cl)]^{1+}$ with NaN_3, followed by photolysis, which has shown to be successful in the synthesis of four-coordinate nitridoiron(IV) species[39] and Wieghardt's six-coordinate nitridoiron(V)[40,41] and iron(VI)[42] complexes. Synthesis of $[Fe^{IV}(N)(N4Py)]^{1+}$ would be of great interest, as it would allow a systematic comparison of the Fe^{IV}-O, Fe^{IV}-NR, Fe^{IV}-N bond distances and spectroscopic features within a common ligand framework. Notably, the resonance Raman spectrum of $[Fe^{IV}(N)(N4Py)]^{1+}$ may help clarify the vibrational stretches associated with $[Fe^{IV}(NTs)(N4Py)]^{2+}$ and related six-coordinate nonheme imidoiron(IV) complexes,[43] as the nitridoiron(IV) species should give rise to a simple Fe-N diatomic stretch. Finally, further attempts should be made to crystallize $[Fe^{IV}(NTs)(N4Py)]^{2+}$,[9] as there has been no crystal structure of a six-coordinate nonheme imidoiron(IV) complex reported to date.

Finally, nonheme oxoiron(V) complexes represents an alluring frontier for future bioinorganic chemists. While there are more than sixty nonheme oxoiron(IV) complexes in the literature,[5] there are only a handful of nonheme oxoiron(V) species that have been reported[44-46] and none that have been crystallographically characterized. One synthetic strategy to reach these elusive species is treatment of ferric starting complexes, such as a hydroxoiron(III) species, with two-electron oxidants, such as PhIO or H_2O_2. This strategy has been remarkably successful in the conversion of ferrous starting materials to oxoiron(IV) complexes.[5] However, as discussed earlier, the lack of mononuclear hydroxoiron(III) compounds represents a major hurdle towards adopting this strategy. Alternatively, treatment of a nonheme oxoiron(IV) complex with a one-electron chemical oxidant may be a fruitful strategy for reaching a nonheme oxoiron(V) intermediate. Electrochemical methods may also be applied at low-temperatures to oxidize oxoiron(IV) species to an oxoiron(V) state. Finally, a vast number of currently reported nonheme oxoiron(IV) complexes are supported by nitrogen-rich neutral ligand sets.[5] Alternative ligand sets, such as monoanionic or dianionic ligands may be necessary to stabilize nonheme oxoiron(V) species, as made evident by the nonheme oxoiron(V) complexes supported by the tetraanionic TAML ligands.[44,46] Similar electronic complexities facing nonheme oxoiron(IV) systems, such as the difference in reactivity and spectroscopy between $S = 1$ and $S = 2$ ground spin states, will also be of concern to nonheme oxoiron(V) systems, where both $S = 1/2$ and $S = 3/2$ are possibilities. However, the ability to probe these non-integer spin states with EPR spectroscopy will likely aid in this endeavor.

I wish the best of luck to future synthetic bioinorganic chemists who decide to tackle these challenges. Go team!

6.7 References

(1) Price, J. C.; Barr, E. W.; Tirupati, B.; Bollinger, J. M., Jr.; Krebs, C. *Biochemistry* **2003**, *42*, 7497-7508.

(2) Rohde, J.-U.; In, J.-H.; Lim, M. H.; Brennessel, W. W.; Bukowski, M. R.; Stubna, A.; Münck, E.; Nam, W.; Que, L., Jr. *Science* **2003**, *299*, 1037-1039.

(3) Que, L., Jr. *Acc. Chem. Res.* **2007**, *40*, 493-500.

(4) Nam, W. *Acc. Chem. Res.* **2007**, *40*, 522–531.

(5) McDonald, A. R.; Que, L., Jr. *Coord. Chem. Rev.* **2013**, *257*, 414-428.

(6) Puri, M.; Que, L. *Acc. Chem. Res.* **2015**, *48*, 2443-2452.

(7) Biswas, A. N.; Puri, M.; Meier, K. K.; Oloo, W. N.; Rohde, G. T.; Bominaar, E. L.; Münck, E.; Que, L. *J. Am. Chem. Soc.* **2015**, *137*, 2428-2431.

(8) Seo, M. S.; In, J.-H.; Kim, S. O.; Oh, N. Y.; Hong, J.; Kim, J.; Que, L., Jr.; Nam, W. *Angew. Chem. Int. Ed.* **2004**, *43*, 2417-2420.

(9) Klinker, E. J.; Jackson, T. A.; Jensen, M. P.; Stubna, A.; Juhász, G.; Bominaar, E. L.; Münck, E.; Que, L., Jr. *Angew. Chem. Int. Ed.* **2006**, *45*, 7394-7397.

(10) Shaik, S.; Hirao, H.; Kumar, D. *Acc. Chem. Res.* **2007**, *40*, 532–542.

(11) Decker, A.; Rohde, J.-U.; Klinker, E. J.; Wong, S. D.; Que, L., Jr.; Solomon, E. I. *J. Am. Chem. Soc.* **2007**, *129*, 15983-15996.

(12) Bernasconi, L.; Louwerse, M. J.; Baerends, E. J. *Eur. J. Inorg. Chem.* **2007**, 3023-3033.

(13) Geng, C.; Ye, S.; Neese, F. *Angew. Chem. Int. Ed.* **2010**, *49*, 5717-5720.

(14) Shaik, S.; Chen, H.; Janardanan, D. *Nat. Chem.* **2011**, *3*, 19-27.

(15) England, J.; Martinho, M.; Farquhar, E. R.; Frisch, J. R.; Bominaar, E. L.; Münck, E.; Que, L., Jr. *Angew. Chem. Int. Ed.* **2009**, *48*, 3622-3626.

(16) Lacy, D. C.; Gupta, R.; Stone, K. L.; Greaves, J.; Ziller, J. W.; Hendrich, M. P.; Borovik, A. S. *J. Am. Chem. Soc.* **2010**, *132*, 12188-12190.

(17) England, J.; Guo, Y.; Van Heuvelen, K. M.; Cranswick, M. A.; Rohde, G. T.; Bominaar, E. L.; Münck, E.; Que, L., Jr. *J. Am. Chem. Soc.* **2011**, *133*, 11880–11883.

(18) Bigi, J. P.; Harman, W. H.; Lassalle-Kaiser, B.; Robles, D. M.; Stich, T. A.; Yano, J.; Britt, R. D.; Chang, C. J. *J. Am. Chem. Soc.* **2012**, *134*, 1536-1542.

(19) Lim, M. H.; Rohde, J.-U.; Stubna, A.; Bukowski, M. R.; Costas, M.; Ho, R. Y. N.; Münck, E.; Nam, W.; Que, L., Jr. *Proc. Natl. Acad. Sci. USA* **2003**, *100*, 3665-3670.

(20) Macikenas, D.; Skrzypczak-Jankun, E.; Protasiewicz, J. D. *J. Am. Chem. Soc.* **1999**, *121*, 7164-7165.

(21) Mehn, M. P.; Peters, J. C. *J. Inorg. Biochem.* **2006**, *100*, 634-643.

(22) Kleespies, S. T.; Oloo, W. N.; Mukherjee, A.; Que, L. *Inorg. Chem.* **2015**, *54*, 5053-5064.

(23) Verma, A. K.; Nazif, T. N.; Achim, C.; Lee, S. C. *J. Am. Chem. Soc.* **2000**, *122*, 11013-11014.

(24) Thomas, C. M.; Mankad, N. P.; Peters, J. C. *J. Am. Chem. Soc.* **2006**, *128*, 4956-4957.

(25) Nieto, I.; Ding, F.; Bontchev, R. P.; Wang, H.; Smith, J. M. *J. Am. Chem Soc.* **2008**, *130*, 2716-2717.

(26) King, E. R.; Hennessy, E. T.; Betley, T. A. *J. Am. Chem. Soc.* **2011**, *133*, 4917-4923.

(27) Searles, K.; Fortier, S.; Khusniyarov, M. M.; Carroll, P. J.; Sutter, J.; Meyer, K.; Mindiola, D. J.; Caulton, K. G. *Angew. Chem. Int. Ed.* **2014**, *53*, 14139-14143.

(28) Wang, L.; Hu, L.; Zhang, H.; Chen, H.; Deng, L. *J. Am. Chem. Soc.* **2015**, *137*, 14196-14207.

(29) Xue, G.; Fiedler, A. T.; Martinho, M.; Münck, E.; Que, L., Jr. *Proc. Nat. Acad. Sci. USA* **2008**, *105*, 20615-20620.

(30) Mehn, M. P.; Brown, S. D.; Jenkins, D. M.; Peters, J. C.; Que, L., Jr. *Inorg. Chem.* **2006**, *45*, 7417–7427.

(31) Seo, M. S.; Kim, N. H.; Cho, K.-B.; So, J. E.; Park, S. K.; Clémancey, M.; Garcia-Serres, R.; Latour, J.-M.; Shaik, S.; Nam, W. *Chem. Sci.* **2011**, *2*, 1039-1045.

(32) Usharani, D.; Lacy, D. C.; Borovik, A. S.; Shaik, S. *J. Am. Chem. Soc.* **2013**, *135*, 17090-17104.

(33) MacBeth, C. E.; Golombek, A. P.; Young, V. G., Jr.; Yang, C.; Kuczera, K.; Hendrich, M. P.; Borovik, A. S. *Science* **2000**, *289*, 938-941.

(34) Soo, H. S.; Komor, A. C.; Iavarone, A. T.; Chang, C. J. *Inorg. Chem.* **2009**, *48*, 10024-10035.

(35) Brown, S. D.; Betley, T. A.; Peters, J. C. *J. Am. Chem. Soc.* **2003**, *125*, 322-323.

(36) Rohde, J.-U.; Stubna, A.; Bominaar, E. L.; Münck, E.; Nam, W.; Que, L., Jr. *Inorg. Chem.* **2006**, *45*, 6435-6445.

(37) Planas, O.; Clemancey, M.; Latour, J.-M.; Company, A.; Costas, M. *Chem. Comm.* **2014**, *50*, 10887-10890.

(38) Kaizer, J.; Klinker, E. J.; Oh, N. Y.; Rohde, J.-U.; Song, W. J.; Stubna, A.; Kim, J.; Münck, E.; Nam, W.; Que, L., Jr. *J. Am. Chem. Soc.* **2004**, *126*, 472-473.

(39) Scepaniak, J. J.; Vogel, C. S.; Khusniyarov, M. M.; Heinemann, F. W.; Meyer, K.; Smith, J. M. *Science* **2011**, *331*, 1049-1052.

(40) Meyer, K.; Bill, E.; Mienert, B.; Weyhermüller, T.; Wieghardt, K. *J. Am. Chem. Soc.* **1999**, *121*, 4859-4876.

(41) Aliaga-Alcalde, N.; George, S. D.; Mienert, B.; Bill, E.; Wieghardt, K.; Neese, F. *Angew. Chem. Int. Ed.* **2005**, *44*, 2908-2912.

(42) Berry, J. F.; Bill, E.; Bothe, E.; George, S. D.; Mienert, B.; Neese, F.; Wieghardt, K. *Science* **2006**, *312*, 1937-1941.

(43) Klinker, E. J.: *High-valent iron compounds supported by pentadentate ligands*; ProQuest, 2007.

(44) Tiago de Oliveira, F.; Chanda, A.; Banerjee, D.; Shan, X.; Mondal, S.; Que, L., Jr.; Bominaar, E. L.; Münck, E.; Collins, T. J. *Science* **2007**, *315*, 835-838.

(45) Van Heuvelen, K. M.; Fiedler, A. T.; Shan, X.; De Hont, R. H.; Meier, K. K.; Bominaar, E. L.; Münck, E.; Que, L., Jr. *Proc. Nat. Acad. Sci. USA* **2012**, *109*, 11933-11938.

(46) Ghosh, M.; Singh, K. K.; Panda, C.; Weitz, A.; Hendrich, M. P.; Collins, T. J.; Dhar, B. B.; Sen Gupta, S. *J. Am. Chem. Soc.* **2014**, *136*, 9524-9527.

Bibliography

Publications

- **Puri, M.**; Biswas, A.; Zhou, A.; Fan. R.; Guo, Y.; Que, L. Jr. Modeling Nonheme Iron Halogenases: High-Spin Oxoiron(IV)-Halide Complexes that Halogenate C-H Bonds. *J. Am. Chem. Soc.* **2016**, *138*, 2484 - 2487.

- **Puri, M.**; Que, L. Jr. The Amazing High-Valent Nonheme Iron-Oxo Landscape. *Bull. Jpn. Soc. Coord. Chem.* **2016**, *67*, TBD.

- **Puri, M.**; Company, A.; Sabenya, G.; Costas, M.; Que, L. Jr. Oxygen-Atom Exchange Between H_2O and Nonheme Oxoiron(IV) Complexes: Ligand Dependence and Mechanism. *Inorg. Chem.* **2016**, *Manuscript Accepted*.

- **Puri, M.**; Que, L. Jr. Towards the Synthesis of More Reactive $S = 2$ Nonheme Oxoiron(IV) Complexes. *Acc. Chem. Res.*, **2015**, *48*, 2443 – 2452.

- Biswas, A. N.; **Puri, M.**; Meier, K. K.; Oloo, W. N.; Rohde, G. T.; Bominaar, E. L.; Münck, E.; Que, L. Jr. Modeling TauD-*J*: a High-Spin Nonheme Oxoiron(IV) Complex With High Reactivity Towards C-H Bonds. *J. Am. Chem. Soc.*, **2015**, *137*, 2428 – 2431.

- Company, A.; Sabenya, G.; Gonzalez-Bejar, M.; Gomez, L.; Clemancey, M.; Jasniewski, A; **Puri, M.**; Browne, W.; Latour, J-M.; Que, L. Jr.; Costas, M.; Perez-Prieto, J.; Lloret-Fillol, J. Triggering the Generation of an Iron(IV)-oxo Compound and its Reactivity Towards Sulfides by Ru^{II} Photocatalysis. *J. Am. Chem. Soc.,* **2014**, *136*, 4624 – 4633.

Presentations

- **Puri, M.**; Que, L. Jr. *The Chemistry of Synthetic Nonheme S = 2 Fe*^{IV}*(O) Complexes.* UMN Doctoral Dissertation Fellowship Symposium, Minneapolis, MN. 2015. (**Poster**)

- **Puri, M.**; Que, L. Jr. *The Chemistry of Synthetic Nonheme S = 2 Fe*^{IV}*(O) Complexes.* UMN Metalloprotein Interest Group (MPIG) – Invited Lecture, Minneapolis, MN. 2015. (**Talk**)

- **Puri, M.**; Biswas, A.; Meier, K.; Oloo, W.; Rohde, G.; Bominaar, E. L.; Münck, E.; Que, L. Jr. *The Chemistry of Synthetic Nonheme S = 2 Fe*^{IV}*(O) Complexes.* Gordon Research Conference: Inorganic Reaction Mechanisms, Galveston, TX. 2015. (**Poster**)

- **Puri, M.**; Que, L. Jr. *Mechanistic Insights into the Oxygen-Atom Exchange Reaction Between H2*^{18}*O and Non-heme Fe*^{IV}*(O) Complexes.* 248th American Chemical Society National Meeting, San Francisco, CA. 2014. (**Talk**)

- **Puri, M.**; Cen, J.; Rasheed, W.; Que, L. Jr. *Ligand Dependence on the Reactivity of Synthetic Non-heme Fe*^{IV}*(O) Complexes.* 248th American Chemical Society National Meeting, San Francisco, CA. 2014. (**Poster**)